

PLACE IN RETURN BOX to remove this checkout from your record.
TO AVOID FINES return on or before date due.
MAY BE RECALLED with earlier due date if requested.

DATE DUE	DATE DUE	DATE DUE
JUN 02 2000 03 05 03		

**THE EFFECT OF HEAT TREATMENTS ON MICROSTRUCTURES
AND PRIMARY CREEP DEFORMATION OF INVESTMENT
CAST TITANIUM ALUMINIDE ALLOYS AND
POLYSYNTHETICALLY TWINNED (PST) CRYSTALS**

By

Dong Yi Seo

A DISSERTATION

**Submitted to
Michigan State University
In partial fulfillment of the requirements
for the degree of**

DOCTOR OF PHILOSOPHY

Department of Materials Science and Mechanics

1998

ABSTRACT

THE EFFECT OF HEAT TREATMENTS ON MICROSTRUCTURES AND PRIMARY CREEP DEFORMATION OF INVESTMENT CAST TITANIUM ALUMINIDE ALLOYS AND POLYSYNTHETICALLY TWINNED (PST) CRYSTALS

By

Dong Yi Seo

Several heat treatments were developed and applied to several investment cast duplex (equiaxed+lamellar) TiAl alloys (Ti-45~47Al-2Nb-2Mn+0.8v%TiB₂XDTM, Ti-47Al-2Nb-2Mn+0.8TiB₂ XDTM with interstitial elements, Ti-47Al-2Nb-2Cr, and Ti-47Al-2Nb-1Mn-0.5W-0.5Mo-0.2Si) in an effort to enhance creep properties. Creep behavior in polysynthetically twinned (PST) crystals with different orientations was also investigated.

Primary creep resistance of W-Mo-Si alloys can be improved by about 10 times with heat treatment, and the XD alloys with additions of interstitials can be improved by about 7 times, and 47-2-2 can be improved by about 3 times, and the XD alloys can be improved slightly, or not at all when the Al level is lower. The variation in creep resistance with heat treatment can be explained by differences observed in the microstructures and textures produced by the various heat treatments. The XD alloys with high O show large lamellar volume fraction (40%), since oxygen is an α stabilizer. The addition of carbon in the XD alloys results in grain size refinement and improvement of primary creep resistance due to the formation of fine precipitates. These XD alloys show no additional benefit from carbon concentrations higher than 0.065 wt% C. Precipitates in the W-Mo-Si alloys nucleated and grew at a faster rate in the deformed part of the specimen, as compared to the grip section, and the precipitates were generally smaller

and more homogeneously dispersed. These observations indicate that strain assisted nucleation and/or growth of precipitates accounts for much of the excellent creep resistance of the W-Mo-Si alloy.

Quantitative microscopic comparisons were made between microstructures in undeformed and deformed regions using SEM and TEM techniques in the W-Mo-Si alloys. The lamellar spacing in lamellar grains systematically decreased by 15-35% with increasing stress, during the first 0.2-0.5% strain at the early stage of primary creep. More refinement of lamellar spacing occurs at lower temperature and higher stress. The refinement process is a consistent microstructural feature during primary creep deformation in all investment cast TiAl alloys. The refinement occurred by mechanical twinning (easy mode deformation) or/and α_2 shear transformation parallel to lamellar boundary. Primary creep in TiAl alloys is divided into two stages, an initial rapid process that refines lamellar spacing through strain levels between 0.2 and 0.5%, and a second primary creep process, where no lamellar refinement occurs.

The stress exponent and activation energy for creep in the lamellar microstructure depend on the direction of the stress tensor. In comparing activation energies of the early process in primary creep in the W-Mo-Si alloy with creep in the soft orientation in a PST crystal, the activation energies are small, near 150 kJ/mol. This indicated that the early stage deformation in TiAl alloys correlates closely with PST crystal creep in easy mode deformation. From simulations of lamellar refinement, computed local shear strains are similar or higher than effective shear strain. There are some correlations between the computed local shear strain and microstructural changes during primary creep deformation.

To My Parents

Ik-Soo Seo, Dong-Pil Kim, and Sangshin Suh

ACKNOWLEDGEMENTS

I would like to express my sincere appreciation to my academic advisor, Professor Thomas R. Bieler and to Dr. Sung-Uk An at Korean Institute Science and Technology (KIST) for their effective guidance and encouragement to finish this research.

I also wish to thank the members of my committee, Professor David Grummon, Professor Matrin A. Crimp, Department of Materials Science and Mechanics, and Professor F. William Cambray, Department of Geological Science. They have been provided many suggestions and comments on this work, and the facilities necessary to pursue this research.

Particularly, I would like to express my sincere appreciation to Howmet Corporation, Whitehall, Michigan for the financial and material support to make this research possible. I would like to express my thanks to Mr. D.E. Larsen and Mr. P.A. McQuay for their contributions in pursuing this research.

I would like to express my gratitude to my wife, Sooyun Chung, my son, Younghun (Freddie Y.) Seo, my family, Dr. Freddie L. Poston and Charlotte Poston, for their never-ending love, patient support and encouragement, during my entire graduate study.

Table of Contents

LIST OF TABLES-----	xi
---------------------	----

LIST OF FIGURES-----	xiii
----------------------	------

CHAPTER 1

1.1 INTRODUCTION-----	1
1.2 RESEARCH STRATEGY-----	4
1.2.1 Rationale and goals-----	5

CHAPTER 2: CREEP THEORY-----8

2.1 DEFINITION OF CREEP-----	8
2.2 STAGES OF CREEP-----	10
2.3 STRESS AND TEMPERATURE EFFECTS-----	12
2.4 POWER LAW RELATIONSHIP-----	14
2.4.1 Power law breakdown-----	16
2.4.2 Transitions in n value-----	18
2.4.3 Transitions in Q_c value-----	18
2.5 DIFFUSIONAL CREEP PROCESS-----	20
2.5.1 Nabarro-Herring Creep-----	22
2.5.2 Coble Creep-----	23
2.5.3 Diffusional Creep and Grain Boundary Sliding-----	26
2.6 DISLOCATION CREEP PROCESSES-----	28
2.6.1 Dislocation Glide Rate-controlled Creep-----	28
2.6.2 Dislocation Climb Rate-controlled Creep-----	30
2.7 DIFORMATION-INDUCED TWINNING-----	33
2.8 CREEP IN SOLID SOLUTION ALLOYS-----	35

2.9 STRESS AND TEMPERATURE CHANGE CREEP (TRANSIENT CREEP)-----	38
2.10 PRIMARY CREEP IN METALS-----	41
2.11 DEFORMATION MECHANISM MAP-----	44
CHAPTER 3: OVERVIEW OF TITANIUM ALUMINIDES-----	48
3.1 INTRODUCTION-----	48
3.2 TITANIUM ALUMINIDES-----	50
3.2.1 Crystal Structure and Microstructure-----	50
3.2.2 Dislocation Structure and Deformation Mode-----	56
3.2.3 Creep Behavior in Gamma Titanium Aluminides-----	66
3.2.3.1 Al-rich single phase gamma Titanium aluminides-----	67
3.2.3.2 Ti rich fully lamellar gamma Titanium aluminides-----	67
3.2.3.3 Ti rich duplex gamma Titanium aluminides-----	70
3.2.4 Precipitates and Alloying Additions-----	77
3.2.5 Primary creep behavior in TiAl-----	77
CHAPTER 4: EXPERIMENTAL PROCEDURE-----	81
4.1 COMPRESSION AND TENSION CREEP TESTS-----	81
4.1.1 Compression creep test (ATS creep tester)-----	81
4.1.2 Tension creep test-----	84
4.2 THE CREEP CURVE FITTING-----	86
4.2.1 The θ projection concept-----	86
4.2.2 Modification of θ -projection concept-----	89
4.2.3 Modification for this analysis-----	90
4.3 MEASUREMENT OF LAMELLAR SPACING-----	93
4.4 A STATISTICAL ANALYSIS OF MEASURED CHANGES IN LAMELLAR SPACING -----	95

CHAPTER 5: OVERVIEW OF RESEARCH	104
CHAPTER 6	116
THE CORRELATION OF PRIMARY CREEP RESISTANCE TO THE HEAT TREATMENT AND MICROSTRUCTURES IN INVESTMENT CAST Ti-Al GAMMA ALLOYS	
6.1 INTRODUCTION	116
6.2 MATERIALS AND EXPERIMENTAL PROCEDURE	117
6.3 RESULTS	120
6.3.1 Primary creep to 0.5% strain	120
6.3.2 Microstructures	120
6.4 DISCUSSION	138
6.5 CONCLUSIONS	141
CHAPTER 7	143
EFFECT OF INTERSTITIAL CONCENTRATION AND HEAT TREATMENT ON MICROSTRUCTURE AND PRIMARY CREEP OF INVESTMENT CAST Ti-47Al-2Nb-2Mn WITH 0.8 vol.% TiB ₂	
7.1 INTRODUCTION	143
7.2 EXPERIMENTAL	144
7.3 RESULTS AND DISCUSSION	145
6.3.1 Microstructures	146
6.3.2 Lamellar spacing	148
7.4 CONCLUSIONS	155
CHAPTER 8	156
CHANGES IN MICROSTRUCTURE DURING PRIMARY CREEP IN A Ti-47Al-2Nb-1Mn-0.5W-0.5Mo-0.2Si ALLOY	
8.1 INTRODUCTION	157
8.2 EXPERIMENTAL	158

8.3 RESULTS-----	163
8.3.1 Primary creep behavior-----	163
8.3.2 Microstructures-----	169
8.4 DISCUSSION-----	190
8.5 CONCLUSIONS-----	194
 CHAPTER 9-----	 196
SHEAR+COMPRESSION CREEP DEFORMATION IN POLYSYNTHETICALLY TWINNED (PST) Ti-47Al-2Nb-2Cr WITH <110> AND <112> ORIENTATIONS	
9.1 INTRODUCTION-----	197
9.2 EXPERIMENTAL DETAILS-----	198
9.2.1 Specimen preparation and Shear+Compression creep test-----	198
9.2.2 Data acquisition and analysis-----	201
9.3 RESULTS AND DISCUSSION-----	202
9.3.1 Creep behavior-----	202
9.3.2 Activation energy-----	205
9.3.3 Stress exponent-----	207
9.3.4 Microstructure and lamellar spacing-----	208
9.4 CONCLUSION-----	212
 CHAPTER 10-----	 214
THE EFFECT OF HEAT TREATMENTS ON MICROSTRUCTURES AND PRIMARY CREEP DEFORMATION OF FOUR INVESTMENT CAST TITANIUM ALUMINIDE ALLOYS	
10.1 INTRODUCTION-----	215
10.2 MATERIALS AND EXPERIMENTAL PROCEDURE-----	217
10.3 RESULTS AND ANALYSIS-----	219
10.3.1 Primary creep behavior-----	219
10.3.2 Microstructures-----	223
10.3.3 Lamellar spacing-----	232

10.3.4 Effect of Anisotropic Crystal Structure on Deformation-----	239
10.4 DISCUSSION-----	240
10.4.1 Lamellar refinement-----	240
10.4.2 Effects of Heat Treatment on Grain size and Lamellar Volume Fraction-----	242
10.4.3 Effects of Heat Treatment on Precipitation, and Dynamic precipitation-----	244
10.5 CONCLUSION-----	244
CHAPTER 11-----	246
THE EFFECT OF CARBON CONCENTRATION ON PRIMARY CREEP OF AN INVESTMENT CAST Ti-47Al-2Mn-2Nb+0.8vol.%TiB ₂ ALLOY	
11.1 INTRODUCTION-----	247
11.2 EXPERIMENTAL PROCEDURE-----	247
11.3 RESULTS AND DISCUSSION-----	249
11.3.1 Microstructures-----	249
11.3.2 Lamellar spacing-----	257
11.3.3 Primary Creep behavior-----	259
11.4 CONCLUSIONS-----	267
CHAPTER 12-----	269
MECHANISMS OF LAMELLAR REFINEMENT DURING PRIMARY CREEP OF NEAR-GAMMA DUPLEX TiAl	
CHAPTER 13-----	277
SUMMARY	
APPENDIX-----	281
PROGRAM CODES FOR SIMULATION OF LAMELLAR REFINEMENT	
REFERENCES-----	288

List of Tables

CHAPTER 2

Table 2.1 Characteristic features in Class I and Class II creep behavior-----	36
Table 2.2 Different Q_C values associated with dislocation and diffusion creep occurring with pure metals-----	47

CHAPTER 3

Table 3.1 Comparison of Gamma TiAl with Titanium alloy and Superalloy-----	49
Table 3.2 Creep data on TiAl alloys-----	72
Table 3.2 (cont'd)-----	73~76
Table 3.3 Alloying effects in gamma TiAl alloys-----	78

CHAPTER 6

Table 6.1 Observation of the effects of heat treatment on three TiAl alloys from optical microscopy-----	122
Table 6.2 Average and range of dimensions describing lamellar microstructures-----	137

CHAPTER 7

Table 7.1 Chemical compositions of investment cast Ti-47Al-2Nb -2Mn-0.8TiB ₂ XD TM -----	145
---	-----

CHAPTER 8

Table 8.1 Curve fit parameters in several experimental conditions-----	165
Table 8.2 Summary of Precipitate Composition and Shapes (at% of element)-----	182
Table 8.3 Diffusion distances of Ti in TiAl-----	192

CHAPTER 9

Table 9.1 The conditions for each Shear+Compression creep test-----	200
---	-----

CHAPTER 10

Table 10.1 Nominal chemical composition of investment cast TiAl alloys (at%)-----	218
---	-----

Table 10.2 Grain sizes of four investment TiAl alloys (unit: μm)-----	228
---	-----

Table 10.3 Average lamellar spacing and reduction % of TiAl alloys-----	237
---	-----

CHAPTER 11

Table 11.1 Al and C content in as-HIPed investment cast alloys-----	248
---	-----

Table 11.2 The lamellar volume fraction and grain size in TiAl alloys-----	252
--	-----

Table 11.3 Curve Fit Parameters in Creep tests shown in Figure 11.10-----	261
---	-----

List of Figures

CHAPTER 2

Figure 2.1 Creep curves at high and low temperatures. At high temperatures, creep deformation can cause considerable changes in dimensions and failure generally occurs after some time, t_f . In contrast, dimensional changes due to creep are usually extremely small and failure rarely occurs-----	9
Figure 2.2.a Schematic representation of creep stages at a high temperature creep curve-----	11
Figure 2.2.b Schematic creep strain rate versus creep strain curve at a high Temperature-----	11
Figure 2.3 (a) Temperature effect on creep curves (b) Log $\dot{\epsilon}$ vs. $1/T$ for Ni-67% Co- Al_2O_3 showing the variation in activation energy above and below $0.5 T_m$ -----	13
Figure 2.4 (a) Stress effect on creep curves (b) Log $\dot{\epsilon}$ vs. Log σ for aluminium and aluminium-magnesium alloys at 523 K showing the variation in stress exponent, n , values-----	15
Figure 2.5 The temperature-compensated secondary creep data (or Z) for Polycrystalline copper. The activation energy of 130 KJ/mole is used for this plot-----	17
Figure 2.6 A plot of the grain-size compensated secondary creep rate as a function of stress for polycrystalline copper-----	19
Figure 2.7 Schematic illustration of the transitions in n value occurring when the stress dependences of steady-state creep rate for pure metals at temperatures above $0.4 T_m$ are described using a power-law relationship-----	19
Figure 2.8 The variation with temperature of the activation energy for the creep of polycrystalline copper-----	21
Figure 2.9 The variation of the diffusion coefficient with temperature for the single crystals and the polycrystalline silver-----	21
Figure 2.10 Schematic diagram of (a) Nabarro-Herring creep and (b) Coble creep on an ideal grain-----	24

Figure 2.11 Accommodation of diffusional creep by GBS: (a) An original configuration of equiaxed grains. (b) The result of diffusional creep without participation of GBS. (c) Simultaneously with diffusional creep, GBS occurs as shown by the offset of a marker line-----	27
Figure 2.12 Sequence of events which may lead to boundary sliding and migration. S, slip spacing; C, subgrain diameter-----	27
Figure 2.13 Weertman's models of creep: (a) Dislocations form pile-ups, the leading dislocations of both pile-ups climb and annihilate. (b) Arrangement and motion of dislocations assumed in a future version of the model-----	32
Figure 2.14 Schematic diagram of twinning and slip after applied stress-----	34
Figure 2.15 Relationship between strain and strain rates for pure metals, solid solutions of Class I (dislocation-drag control), and solid solutions of Class II (substructure control)-----	37
Figure 2.16 Schematic drawings of the instantaneous elongation and contraction upon small changes in cases of (a) the free-flight glide, and (b) the viscous glide-----	40
Figure 2.17 Schematic version of a deformation map for a polycrystalline metal illustrating the stress/temperature regimes within which dislocation and diffusional creep processes may be expected to be dominant-----	46

CHAPTER 3

Figure 3.1 Phase diagram of binary Ti-Al system-----	51
Figure 3.2 Lattice structure of (a) $L1_0$ -TiAl and (b) DO_{19} -Ti ₃ Al-----	52
Figure 3.3 $\langle 110 \rangle_\gamma$ directions and the atomic arrangement on a (111) plane in $L1_0$ and $\langle 11\bar{2}0 \rangle_{\alpha_2}$ directions and the atomic arrangement on the basal plane (0001) in DO_{19} -----	54
Figure 3.4 The stereographic projection of $(111)_\gamma$ and $(0001)_{\alpha_2}$ show the six possible orientation variants of $\langle 110 \rangle_\gamma$ with respect to $\langle 11\bar{2}0 \rangle_{\alpha_2}$ matrix-----	54

Figure 3.5 (a) duplex and (b) fully lamellar (c) near-gamma microstructures in TiAl alloys-----	57
Figure 3.6 The thin twin morphology near the twin tip-----	59
Figure 3.7 The formation sequence of TiAl _{5F} , Ti ₃ Al, Ti ₃ Al _{5F} and TiAl _T due to high temperature deformation-----	60
Figure 3.8 (a) The maximum Schmid factor for deformation in a given crystal direction is plotted for ordinary and super dislocations, and for true twinning, which depends on deformation mode. (b) There are no operative ordinary dislocation or true twinning systems near <001] for tension, and none near <110] for compression-----	64
Figure 3.9 Yield stress of PST crystals as a function of angle between compression axis and the lamellar boundaries-----	65
Figure 3.10 Comparison of steady state creep data of TiAl with different microstructures-----	69
Figure 3.11 Primary creep curve of TiAl alloys-----	80
 CHAPTER 4	
Figure 4.1 The diagram of ATS creep tester with data acquisition system-----	82
Figure 4.2 Creep testing involves holding test specimens at constant load and temperature until some specific experimental parameter is met-----	85
Figure 4.3 The θ -projection concept envisages normal creep curves in terms of a decaying primary component (ϵ_p) and an accelerating tertiary component (ϵ_T)-----	88
Figure 4.4 Measurement of lamellar spacing in (a) backscattered electron image in scanning electron microscopy (SEM) mode and (b) bright field image in transmission electron microscopy (TEM) mode-----	94
Figure 4.5 Frequency of α_2 spacing with different number of bins (a) 10 bins, (b) 15 bins, (c) 20 bins in W-Mo-Si alloys -----	98
Figure 4.6 Frequency of α_2 spacing with different number of bins (a) 5 bins, (b) 10 bins for the natural logarithm scale in W-Mo-Si alloys-----	99

Figure 4.7 Normal and log-normal probability plots of W-Mo-Si alloy for undeformed and deformed cases -----	100
Figure 4.8 Frequency of γ thickness with different number of bins (a) 10 bins, (b) 15 bins, (c) 20 bins in Ti-47Al-2Nb-2Cr -----	101
Figure 4.9 Normal and log-normal probability plots of Ti-47Al-2Nb-2Cr alloy for undeformed case -----	102
Figure 4.10 Frequency of γ thickness with different number of bins (a) 5 bins, (b) 10 bins for the natural logarithm scale in Ti-47Al-2Nb-2Cr alloy -----	103
CHAPTER 5	
Figure 5.1 The α_2 spacing decreases with respect to increasing stress at similar strains at 650 °C-----	110
Figure 5.2 The amount of lamellar refinement (% reduction of α_2 spacing) increases with the volume fraction of lamellar grains-----	112
Figure 5.3 Higher lamellar fraction retards the strain rate at the transition between the early and later creep processes-----	112
Figure 5.4 Comparison of lamellar refinement history with primary creep rate shows that the early process operates by lamellar refinement, whereas the later process does not alter the lamellar spacing appreciably with known transition strain in the XD+C alloy-----	114
CHAPTER 6	
Figure 6.1 Phase diagram illustrating heat treatment and creep condition-----	119
Figure 6.2 Time to 0.5% creep strain with respect to heat treatment. The lines go through the average of 3 values, the high and low values are indicated by additional symbols-----	121
Figure 6.3 Optical microstructures of deformed Ti-45Al-2Nb-2Mn-0.8TiB ₂ a) as-HIPed, as polished, b) as-HIPed and etched, c) 900 °C/20hrs heat treatment, and d) two-step heat treatment-----	124
Figure 6.4 Backscattered electron images of Ti-45Al-2Nb-2Mn-0.8TiB ₂ a) as-HIPed undeformed, b) as-HIPed deformed, c) 900 °C/20hrs heat treatment, and d) two-step heat treatment-----	125

Figure 6.5 Bright field images of as HIPed Ti-45Al-2Nb-2Mn-0.8TiB ₂ after creep test a) Fine mechanical twins observed in α_2 grains, b) Fine mechanical twins observed in lamellar regions, c) dislocations interactions with a TiB ₂ particle-----	127
Figure 6.6 Optical microstructures of deformed Ti-47Al-2Nb-2Mn-0.8TiB ₂ a) as-HIPed, as polished, showing TiB ₂ particles, b) as-HIPed and etched, c) 900 °C/20hrs heat treatment, and d) two-step heat treatment-----	128
Figure 6.7 Optical microstructures of deformed Ti-47Al-2Nb-2Cr a) as-HIPed, as polished, b) as-HIPed and etched, c) 900 °C/20hrs heat treatment, and d) two-step heat treatment-----	130
Figure 6.8 Backscattered electron images of deformed Ti-47Al-2Nb-2Cr a) as-HIPed, b) 900 °C/20hrs heat treatment, and c) and d) two-step heat treatment-----	132
Figure 6.8 Low magnification backscattered electron images of Ti-47Al-2Nb-2Cr illustrate dendritic segregation of aluminum, e) as-HIPed undeformed, f) as-HIPed deformed, g) 900 °C/20hrs heat treatment, undeformed, and h) 900 °C/20hrs heat treatment, deformed-----	133
Figure 6.9 Bright field images of as HIPed Ti-47Al-2Nb-2Cr after creep test a) commonly observed relationship between coarser and finer lamellar regions exhibit a 170° about a <110> axis relationship, b) subgrain boundaries develop in larger γ regions-----	134
Figure 6.9 Bright field images of Ti-47Al-2Nb-2Cr after creep test c) α_2 lathes resist absorption in a boundary where an equiaxed γ grain is consuming a lamellar grains (900°C/20hrs heat treatment), d) particles are located at grainboundary, and e) inside a γ grain after two-step heat treatment-----	135
Figure 6.10 Refinement of lamellar feature was observed with increasing heat treatment conditions, and resulting from deformation-----	136
Figure 6.11 Inverse pole figures for 3 heat treatments a) Schmid factor, b) as-HIPed, c) 900 °C/20hrs heat treatment, d) two step heat treatment after creep test-----	139

CHAPTER 7

Figure 7.1 Time to 0.5% creep strain with respect to heat treatment. The lines go through the average of 3 values, high and low values are indicated by symbols-----	147
Figure 7.2 Strain rate-strain plot of the creep deformation for the specimen with the middle creep time-----	147
Figure 7.3 Optical microstructure of creep deformed (a) medium O and (b) high O alloys-----	149
Figure 7.4 Backscattered electron (BSE) images of after creep deformation of (a) medium O and (b) high O alloys-----	150
Figure 7.5 Lamellar spacing distribution of high O alloys before and after creep deformation-----	153
Figure 7.6 Plot of strain-rate ratio vs. % reduction in α_2 spacing and γ thickness in low and high O alloys-----	154
Figure 7.7 Relationship between fraction of specified lamellar spacing and time to 0.5% creep strain-----	154

CHAPTER 8

Figure 8.1 A Ti-Al phase diagram near the stoichiometric TiAl composition-----	159
Figure 8.2 Geometry of shear+compression deformation conditions-----	161
Figure 8.3 Primary creep strains are illustrated a) at low strains (0.2%) in as-HIPed shear+compression specimens, b) at larger strains (1%)-----	164
Figure 8.4 Primary creep strains to 0.5% in heat treated tensile specimens with different temperature and stress-----	166
Figure 8.5 Differentiated curve fits (strain rate vs. strain) of data in Figure 8.3 and 8.4-----	166
Figure 8.6 Microstructures of Ti-47Al-2Nb-1Mn-0.5W-0.5Mo-0.2Si: (a) As-HIPed condition before deformation (shear vector was subsequently horizontal), (b) Heat Treated tensile gage section deformed at 760 °C, 138 MPa-----	170

Figure 8.7 X-ray data obtained from the heat treated tensile gage section tested at 649 °C, 276 MPa-----	171
Figure 8.8 BSE image of Ti-47Al-2Nb-1Mn-0.5W-0.5Mo-0.2Si: (a) As-HIPed condition before deformation (b) Specimen tested at 760 °C, 138 MPa (1010 °C/50 hours heat treatment)-----	172
Figure 8.9 TEM image of lamellar and equiaxed grains from the specimen tested at 760 °C, 138 MPa (1010 °C/50 hours heat treatment)-----	174
Figure 8.10 Dislocation interactions with particles in lamellar regions. The below image is an enlargement of the precipitate (a) indicated by the arrow (760 °C and 138 MPa)-----	176
Figure 8.11 Precipitates in equiaxed grains are surrounded by dislocations (649 °C and 276 MPa), (b) an enlargement of the arrowed precipitate in (a)-----	177
Figure 8.12 BSE images of specimen a) undeformed, b) deformed at 760 °C, 138 MPa (1010 °C/50 hours heat treatment)-----	178
Figure 8.12 BSE images of specimen c) deformed at 760 °C,138 MPa (1010 °C/50 hours heat treatment) d) undeformed as-HIPed condition-----	179
Figure 8.13 Size distribution of precipitates in lamellar grains (tested at 760 °C, 138 MPa)-----	180
Figure 8.14 Lamellar refinement process is illustrated as indicated by arrows. Diffraction patterns in boxes a, b, and c illustrate true twin relationship----	183
Figure 8.15 Lamellar spacing was refined after creep deformation (760 °C and 138 MPa): (a) undeformed grip section and (b) deformed gage section-----	184
Figure 8.16 a), b) Distribution of α_2 spacing and γ thickness in 750 °C and 138 MPa, and c) α_2 spacing in 649 °C and 276 MPa specimens in undeformed grip and deformed gage section of heat treated tensile creep specimens-----	186
Figure 8.17 Average α_2 spacing and γ thickness in tensile creep specimens a) 760 °C and 138 MPa, and b) 649 °C and 276 MPa before and after creep deformation-----	187

Figure 8.18 a) Frequency of α_2 spacings based on about 500 counts in 25 lamellar regions after compression-shear deformation at 750 °C and 77 MPa, b) α_2 spacing resulting from different effective strains at 650 °C and 750 °C-----	188
---	-----

CHAPTER 9

Figure 9.1 Shear+Compression fixture used for creep deformation of 5x5x3 mm PST crystal bricks. PST crystal is shown in soft orientation-----	199
Figure 9.2 Creep deformation of <110> PST crystal in Ar (with curve fitting) (a) strain vs. time curve (b) strain vs. strain-rate curve-----	203
Figure 9.3 Creep deformation of <112> PST crystal in air (with curve fitting) (a) strain vs. time curve (b) strain vs. strain-rate curve-----	204
Figure 9.4 a) Temperature and b) Stress dependence of minimum creep rate for PST crystals. Numbers next to datum points refer to Figures 9.2 and 9.3-----	206
Figure 9.5 Backscattered electron images of deformed <112> PST crystal (1.38% shear strain at 760°C and 13 MPa)-----	210
Figure 9.6 (a) α_2 spacing distribution, and (b) average α_2 spacing and thickness with different primary creep strain levels in the <112> PST crystal-----	211

CHAPTER 10

Figure 10.1 Differentiated curve fits of creep data exhibit a decreasing strain rate to a saturation strain between 0.1 and 0.5% strain, whereafter the decrease in strain rate is less rapid-----	221
Figure 10.2 Microstructures of As HIPed 45Al XD (a) optical micrographs before creep test.-----	224
Figure 10.3 Volume fraction of lamellar grains in TiAl alloys with respect to heat treatment -----	226
Figure 10.4 (a) optical micrographs of As HIPed 47Al XD before creep test -----	226
Figure 10.5 Microstructures of As HIPed 47-2-2 (a) optical micrographs before creep test (b) BSE images after creep test -----	229

Figure 10.6 Distribution of α_2 spacing and γ thickness in TiAl alloys before and after creep deformation (a) high O (b) 47-2-2-----	234
Figure 10.6 Distribution of α_2 spacings and γ thickness in TiAl alloys before and after creep deformation (c) WMoSi alloys under tension mode -----	238
Figure 10.7 The plot of α_2 spacing respect to different effective strains and different loads at 650 °C and 760 °C -----	238
CHAPTER 11	
Figure 11.1 Optical macrographs of Ti-47Al-2Nb-2Mn+0.8 vol%TiB ₂ alloys having (a) Low carbon, (b) 0.065 wt% carbon, (c) 0.11 wt% carbon-----	250
Figure 11.2 Optical micrographs of Ti-47Al-2Nb-2Mn+0.8 vol%TiB ₂ alloys having (a,b) Low carbon, (c) 0.065 wt% carbon, (d) 0.11 wt% carbon-----	251
Figure 11.3 Backscattered electron images of Ti-47Al-2Nb-2Mn +0.8 vol%TiB ₂ alloys having (a) Low carbon, (b) 0.065 wt% carbon, (c) 0.11 wt% carbon. The arrows indicate the thin layers of α_2 phase-----	254
Figure 11.4 Distribution of thin α_2 layers surrounded by γ grains in TiAl alloys-----	255
Figure 11.5 a and b: Backscattered electron images of Ti-47Al-2Nb-2Mn +0.8 vol%TiB ₂ alloys having 0.065 wt% carbon-----	255
Figure 11.5 c: Precipitates along the grain boundaries of γ grains in creep tested Ti-47Al-2Nb-2Mn+0.8 vol%TiB ₂ alloys having 0.065 wt% carbon-----	256
Figure 11.6 Backscattered electron images of Ti-47Al-2Nb-2Mn+0.8 vol%TiB ₂ alloys having 0.11 wt% carbon-----	256
Figure 11.7 Dislocation activity near TiB particles in creep deformed Ti-47Al-2Nb-2Mn+0.8vol%TiB ₂ alloys having 0.065 wt% carbon. White arrows show bowing, and black arrows show pinning points-----	258
Figure 11.8 Distribution plot of α_2 spacing in undeformed grip and deformed gage section of tensile creep specimens-----	258

Figure 11.9 (a) Creep times to 0.2% and 0.5% strain as a function of carbon concentration for specimens deformed at three deformation conditions. (b) Creep strain to 0, 20, 30, 50, and 100 hours in Ti-47Al-2Nb-2Mn+0.8 vol%TiB ₂ alloys. Lines go through the average of 3 samples-----	260
Figure 11.10 Creep strain rate as a function of creep strain in Ti-47Al-2Nb-2Mn +0.8vol%TiB ₂ alloys-----	262
Figure 11.11 The relationship between lamellar vol. fraction and strain rates with carbon concentration. On this and subsequent plots, the size of the symbol represents carbon concentration-----	262
Figure 11.12 The relationship between lamellar vol. fraction and initial strain rates and strain rate at minimum and transition points. Symbol size represents carbon concentration (small, medium, and large size symbol: Low carbon, 0.065 wt%, and 0.110 wt% carbon)-----	264
Figure 11.13 α_2 spacing as function of creep strain-----	264
Figure 11.14 Lamellar refinement and strain rates at transition point as a function of lamellar vol. fraction-----	266
 CHAPTER 12	
Figure 12.1 The distribution of α_2 spacing is shifted to a greater fraction of finer spacing as a result of early stage primary creep deformation. A simulation based on the undeformed room temperature grip that generates 0.2 μm thick α_2 layers within thicker γ lamellae matches the deformed distribution-----	273
Figure 12.2 Lamellar laths configuration in undeformed and deformed case from simulation-----	274
Figure 12.3 The relationship between computed local shear strains and reduction of α_2 spacing-----	275
Figure 12.4 The relationship between computed local shear strains and strain rates at transition points-----	275
Figure 12.5 The relationship between computed local shear strains and volume fraction of lamellar grains-----	276
Figure 12.6 The relationship between strain rates and strains at transition point with volume fraction of lamellar grains-----	276

CHAPTER 1

1.1 INTRODUCTION

Gamma titanium aluminide (TiAl) based materials have been developed as candidates for high temperature structural applications, such as heat engines, turbine engine blades, aerospace and automobile components, because they have low density, low coefficients of thermal expansion (CTE), high thermal conductivities, high specific strengths and stiffness at elevated temperature, and high resistance to oxidation and creep. TiAl alloys are beneficial in the design of components operating at high temperature, because they are light weight, exhibit minimum thermal fatigue, and can operate at high temperatures with external cooling. However, these alloys have lower yield strengths, ultimate tensile strengths and room temperature ductilities than the current titanium alloys and superalloys used in these high temperature applications.

Several investment cast TiAl alloys (Ti-45Al-2Nb-2Mn+0.8TiB₂ XDTM, Ti-47Al-2Nb-2Mn+0.8TiB₂ XDTM, Ti-47Al-2Nb-2Mn+0.8TiB₂ XDTM with different amounts of interstitial elements (oxygen and carbon), Ti-47Al-2Cr-2Nb, and Ti-47Al-2Nb-1Mn-0.5W-0.5Mo-0.2Si alloy) have been developed by Howmet Corporation. Selected heat treatments and the addition of interstitial elements to the alloys have been used to reduce the costs of processing and to improve primary creep resistance, especially primary creep resistance as measured by the time to 0.5% creep strain. Most of these TiAl alloys have a duplex microstructures which have better ductility than lamellar structures. However, duplex h structures display poorer creep resistance than lamellar structures. Most studies of creep of TiAl alloys have focused on minimum creep rate conditions or stress-rupture

. The primary creep properties, however, are important in practical applications. On of ordinary and super-dislocations are the major deformation mechanisms in mechanical twinning, however, is also an important deformation mechanism at temperature. Limited research has been conducted on deformation behavior of TiAl early stage of creep, and the creep mechanisms of these alloys are not well d.

chapter two, the main creep mechanisms for pure metals and alloys at high are reviewed. In chapter three, titanium aluminides are reviewed in terms of structure, microstructure, deformation modes, deformation twinning, creep and alloying effects.

research methodology is presented in chapter four. An overview of research presented in chapter five, with the detail of these results being presented in ix through twelve.

chapter six, the primary creep resistance (time to 0.5% creep strain) is analyzed two-phase TiAl alloys. Two of the alloys containing TiB_2 particulates produced O^{TM} process and a third alloy without TiB_2 are compared. Because the nature of creep is affected by changes in the microstructure that arise from different heat s and compositions, the details of primary creep are explored.

the effect of interstitial concentration on the primary creep deformation and ctures of investment cast TiAl alloys is presented in chapter seven. The ctures and the primary creep deformation modes are analyzed in terms of grain ibution of α_2 and γ thickness, and α_2 thickness.

In chapter eight, microstructural changes during primary creep of Ti-47Al-2Nb-1Mn-0.5W-0.5Mo-0.2Si alloys as determined by analysis of the volume fraction of lamellar and equiaxed microstructures, the distribution of γ thickness and α_2 spacings, mechanical twinning, and precipitates are presented.

In chapter nine, stress and temperature change creep tests were carried out under a condition of combined compression and shear stress on carefully oriented PST crystals of Ti-47Al-2Cr-2Nb alloy with $\langle 110 \rangle$ and $\langle 112 \rangle$ directions parallel to the principle shear stress axis. Based on the measured stress exponents and activation energies, possible creep mechanisms are suggested. By understanding the fundamental mechanisms of creep deformation of polysynthetically twinned (PST) crystals, an understanding of the fundamental basis of deformation of the lamellar colonies present in polycrystalline TiAl alloys can be established.

The effects of different strengthening treatments on primary creep resistance of four alloys are presented in chapter ten. The changes in the different lamellar and equiaxed microstructures; γ thickness, α_2 spacing, mechanical twinning; interstitial levels, precipitate size, composition, and shape; and dislocation interactions with the precipitates are quantified for each alloy.

Ti-47Al-2Nb-2Mn+0.8TiB₂ XDTM alloys with higher interstitial element concentrations were developed for the enhancement of primary creep resistance and process cost reduction by Howmet Corp. The effect of carbon concentration on primary creep deformation and microstructures of investment cast and HIPed TiAl alloys with no further heat treatment are compared to the same alloy with low interstitial content in

chapter eleven. Grain size, distribution of α_2 spacing, and volume fractions of lamellar grains with respect to carbon concentration are also analyzed.

From previous studies have shown that the lamellar refinement is a common microstructural feature in the primary creep behavior of TiAl alloys. In chapter twelve, lamellar refinement is simulated using a set of lamellar spacings that represent an undeformed lamellar spacing frequency distribution. The lamellar spacing distribution obtained from the simulation is compared with the measurements of lamellar spacings in TiAl alloys. Local shear strains in the lamellar microstructure are computed to examine how different deformation histories affect the resulting deformed distribution.

In summary, the primary creep deformation behaviors of several TiAl alloys are characterized in terms of lamellar grain size, lamellar spacing, volume fraction of lamellar grains, and other factors. The primary creep mechanisms are suggested from all studies.

1.2 RESEARCH STRATEGY

This research focuses on primary creep in the duplex microstructure TiAl alloys, concentrations the relationship between creep deformation and microstructural characteristics: precipitates, twinning, lamellar spacing, dislocation activity, and volume fraction of lamellar and equiaxed grains. were applied to examine The effects of several heat treatments on primary creep resistance in five investment cast TiAl alloys were investigated. The effects of heat treatment on characteristics of precipitates, distribution of lamellar grains and equiaxed grains, lamellar spacing, volume fraction of lamellar and equiaxed grains, and orientation distribution of grains were examined. These variables in

turn effect the deformation process. By using stress and temperature change techniques, this investigation eventually lead to a phenomenological understanding of primary and secondary creep mechanisms at a particular stress condition and assisted in the development of alloy design criteria.

1.2.1 Rationale and goals

The substantial progress in understanding creep behavior of single or two-phase titanium aluminides has been made as summarized in the chapter three. Some important and interesting questions have emerged from previous work and these questions have to be answered in order to develop a better understanding of creep deformation. A brief summary of these is given.

1) If heat treatment gives better primary creep resistance in TiAl alloys, what kind of microstructural features can be influenced through the heat treatment? Some authors showed that the reduction of lamellar spacing leads to lower creep strain rate by blocking moving dislocations. Could the lamellar spacing be altered by heat treatment, and how sensitive is the lamellar spacing to alloy composition?

2) Addition of carbon in TiAl alloys resulted in improvement of creep properties. Therefore, understanding the relationship between interstitial concentration and heat treatment in the duplex TiAl alloys with respect to primary creep is important. The precipitates in the lamellar microstructure increase creep resistance. The mechanism by which the precipitates enhance primary creep resistance is not well understood. If precipitates grow during creep then models for strain assisted growth need to be examined.

3) Deformation twins were frequently observed in secondary or tertiary creep, and in some observations of primary creep, the amount of mechanical twinning strongly depends on stress and temperature. The role of deformation twins in the early stage of creep is not well understood. The deformation twinning parallel to lamellar planes is called easy mode deformation, but the twins that intersect lamellar boundaries are hard mode deformation. If easy mode twinning occurs in primary creep, it is necessary to determine the contribution of easy mode twinning to the early stage of creep strain with different stresses and temperatures.

4) The creep mechanism in PST crystals has not been examined. Thus it is important to determine the creep mechanism in PST crystals with different orientations, because the deformation mode of the lamellae is highly orientation dependent. By comparing creep in PST crystals and polycrystals in the same test conditions it is also helpful to understand how lamellar microstructures contribute to the creep mechanism. For example, if stress exponents or activation energies that govern PST deformation are also observed in polycrystals, then the role of deformation in lamellar microstructures on creep of duplex materials can be identified.

5) What kinds of deformation structures occur at the different levels of primary creep strain as function of strain, for example, 0.2%, 0.5%, 1.0% and 1.5%? Analyzing changes in the deformed microstructures is essential to understand primary creep mechanism.

Although primary creep is practically more important for many candidate applications for TiAl, most of the research has been focused on the secondary or tertiary creep in TiAl alloys. Thus, the goals of this research are to investigate the relationship between microstructure and primary creep mechanisms in TiAl alloys having different

compositions. First, the effect of composition, microstructure, lamellar spacing, and heat treatment on primary creep properties will be investigated. Next, the role of deformation twinning on primary creep deformation with different stress, temperature, and creep strain will be described by observation of deformed microstructures. Finally, creep behavior in PST crystals with different orientations will be compared to polycrystals in similar test conditions in order to understand the contribution of lamellar microstructures on duplex materials to the creep mechanism. Therefore, the primary creep mechanism in duplex TiAl alloys will be rationalized by analysis of experimental observations.

CHAPTER 2

CREEP THEORY

2.1 DEFINITION OF CREEP

There are many practical examples where materials are required to survive for long periods under load at high temperatures, such as turbine blades of jet engines and power generators. Thus when assessing the resistance of materials to deformation and failure over long times under load at high temperatures, particular attention must be given to a phenomenon known as “creep”. Creep may be defined as the process by which plastic flow occurs when a constant stress is applied to a material for a prolonged period of time.

As illustrated in Figure 2.1, the shape of a plot of creep extension versus time usually differs at low and high temperatures [1]. At low temperatures, dimensional changes due to creep are usually extremely small and failure rarely occurs. In contrast, at high temperatures, creep deformation can cause considerable changes in dimensions and failure generally occurs after some time. The time to fracture, t_F , decreases with increasing temperature and with increasing applied stress.

Under low-temperature creep conditions ($T < 0.3T_m$), for many different crystalline materials, it has been found that the creep strain increases with $\log(\text{time})$ as shown in Figure 2.1 [2]. On this basis, the increase in creep strain with time can be expressed as

$$\varepsilon = \varepsilon_{tot} - \varepsilon_0 = \alpha_1 \log_c(\alpha_2 t + 1) \quad (1)$$

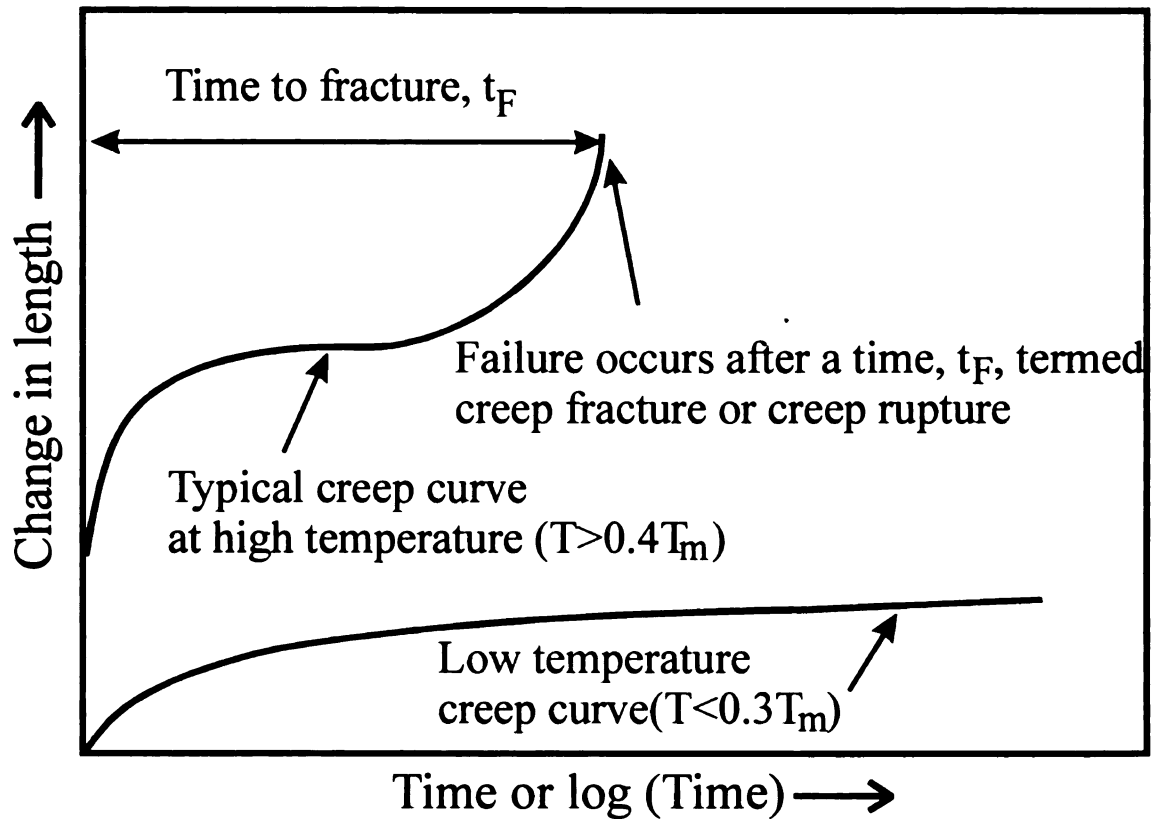


Figure 2.1. Creep curves at high and low temperatures. At high temperatures, creep deformation can cause considerable changes in dimensions and failure generally occurs after some time, t_F . In contrast, dimensional changes due to creep are usually extremely small and failure rarely occurs [1,2].

where ε_{tot} is total specimen strain, ε_0 is the virtually instantaneous strain, α_1 and α_2 are constants for the material which depend on stress and temperature, and t is time. [2]
Differentiating equation 1 gives the creep rate at any instant as

$$\dot{\varepsilon} = \frac{d\varepsilon}{dt} = \frac{\alpha_1 \alpha_2}{\alpha_2 t + 1} \quad (2)$$

which is consistent with the fact that the creep rate decreases continuously with increasing time during low-temperature tests [2].

2.2 STAGES OF CREEP

While the creep curves recorded at low temperatures are well described by equation (1), in the high-temperature regime ($T > 0.4T_m$), the creep curves are commonly described by reference to different regions of the curves in Figure 2.2.a [3]. After the initial strain on loading, the creep rate usually declines during the “primary stage” until an ostensibly constant creep rate is reached during the “secondary stage”, after which the creep rate increases again during the “tertiary stage” which leads to fracture. From Figure 2.2.b, the primary or transient stage, the creep rate continuously decreases with time; that is, the slope of the curve diminishes with time [4]. This indicates that the material experiences an increase in creep resistance or strain hardening. For the secondary stage, sometimes termed steady-state creep, the rate is constant; that is, the strain-time plot becomes linear. This is often the stage that is of the longest duration. The constant creep rate is explained on the basis of a balance between the competing processes of strain hardening and recovery (work softening). Recovery is the process whereby a material

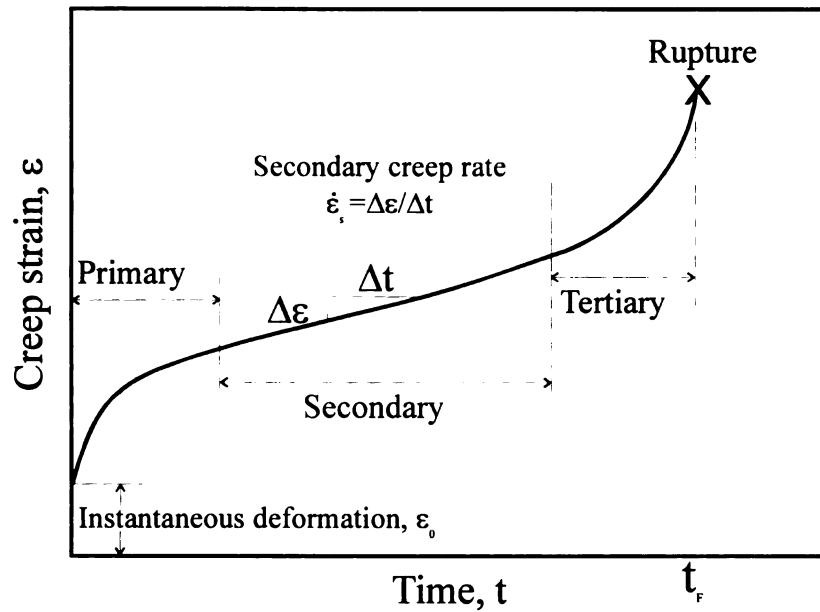


Figure 2.2.a Schematic representation of creep stages at a high temperature creep curve [3].

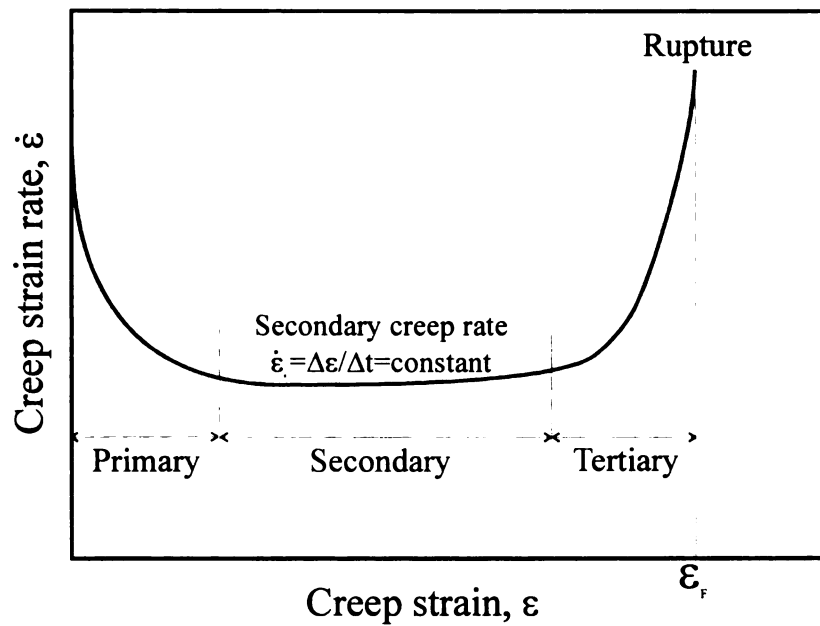


Figure 2.2.b Schematic creep strain rate versus creep strain curve at a high temperature [4].

becomes softer by various mechanisms, i.e. dislocation glide, climb, cross slip, etc. and acceleration of the strain rate retains its ability to experience deformation. Finally, in the tertiary stage, there is an acceleration of the strain rate and ultimate failure that is frequently termed rupture. Microstructural changes in the tertiary stage occurs such as grain boundary separation, the formation of internal cracks, cavities, voids, and neck formation in the tertiary stage. These all lead to a decrease in the effective cross-sectional area and an increase in strain rate.

2.3 STRESS AND TEMPERATURE EFFECTS

Figure 2.3.a shows the effect of temperature on the creep behavior at the same stress [5]. As the test temperature increases, the creep strain increases at the same creep time. When this kind of experiment is undertaken, it is usually found that a linear relationship is obtained by plotting $\ln \dot{\epsilon}_s$ against $(1/T)$ as shown in Figure 2.3.b [6]. Thus the secondary creep rate increases exponentially with temperature according to the equation

$$\ln \dot{\epsilon}_s \propto -\left(\frac{1}{T}\right) \quad (3)$$

where $\dot{\epsilon}_s$ is steady-state creep rate and T is temperature [7]. This form of temperature dependence is found for many thermally activated processes, including diffusion, oxidation and etc.. The creep rate can be defined to obeys Arrhenius's Law, so that

$$\dot{\epsilon}_s = K_1 \exp\left(-\frac{Q_c}{RT}\right) \quad (4)$$

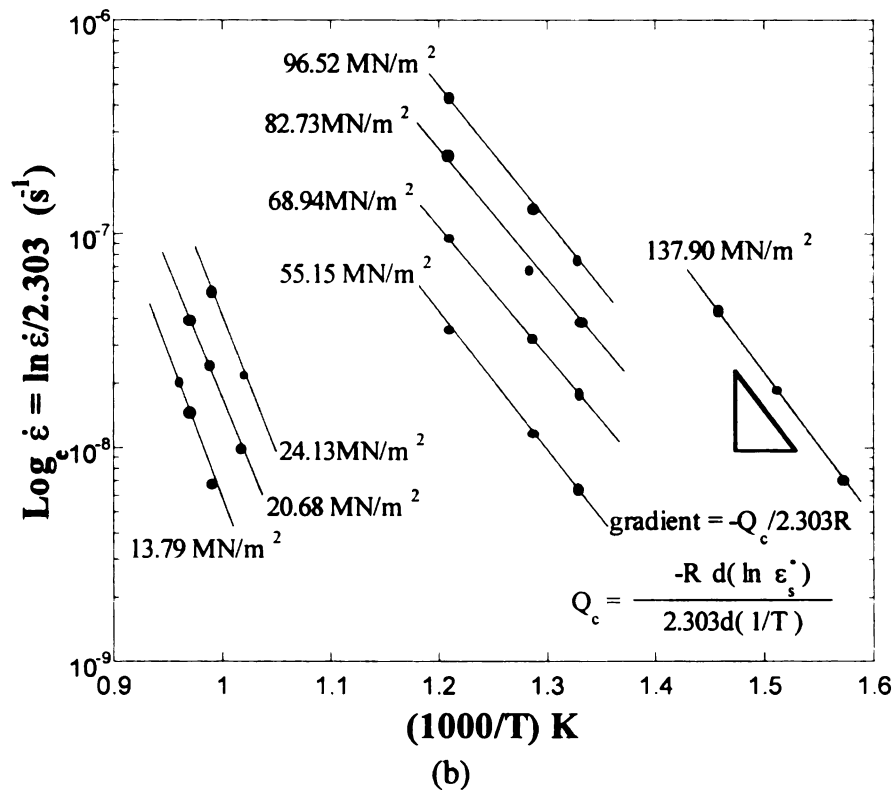
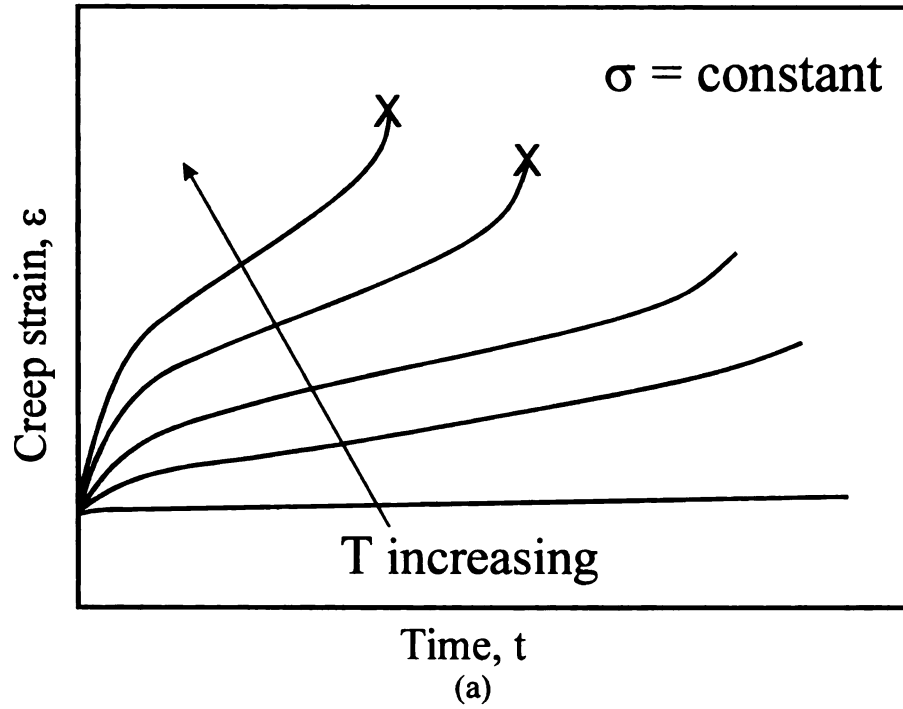


Figure 2.3 (a) Temperature effect on creep curves (b) Log $\dot{\epsilon}$ vs. $1/T$ for Ni-67% Co- Al_2O_3 showing the variation in activation energy above and below $0.5 T_m$ [5,6]

where K_1 is a constant, Q_c is called the activation energy for creep and R is the universal gas constant (8.31 J/mole K) [8]. From Figure 2.3.b, the magnitude of activation energy for creep can be evaluated from the slope of $\ln \dot{\epsilon}_s$ versus $(1/T)$ plot. From O.D. Sherby and P.M. Burke's study about the creep behavior of pure metals at high temperatures, the values of Q_c have frequently been found to be close to the activation energy for lattice self diffusion, Q_{SD} [9]. The fact that Q_c often equals Q_{SD} indicates how the important diffusion is for high-temperature creep conditions ($T > 0.4T_m$). The presence of diffusion accounts for the transition from low-temperature to high-temperature creep behavior.

A similar effect of different stress on creep behavior at the same temperature can be found in Figure 2.4.a [5]. Its dependence on stress can be written

$$\dot{\epsilon}_s = K_2 \sigma^n \quad (5)$$

where K_2 is a constant and n is material constant denoted as the stress exponent [10]. This expression, sometimes called Norton's Law, provides the basis for the "power law" relationships which have been widely used to describe high-temperature creep behavior. A plot of the $\log (\dot{\epsilon}_s)$ versus the $\log (\sigma)$ yields a straight line with slope of n as illustrated in Figure 2.4.b for aluminium and aluminium-magnesium alloys 523 K [11].

2.4 POWER LAW RELATIONSHIP

From the equations (4) and (5), steady strain rate, $\dot{\epsilon}_s$, varies with both stress and temperature. Thus steady state creep behavior can be described through their product by multiplying equations (4) and (5) together,

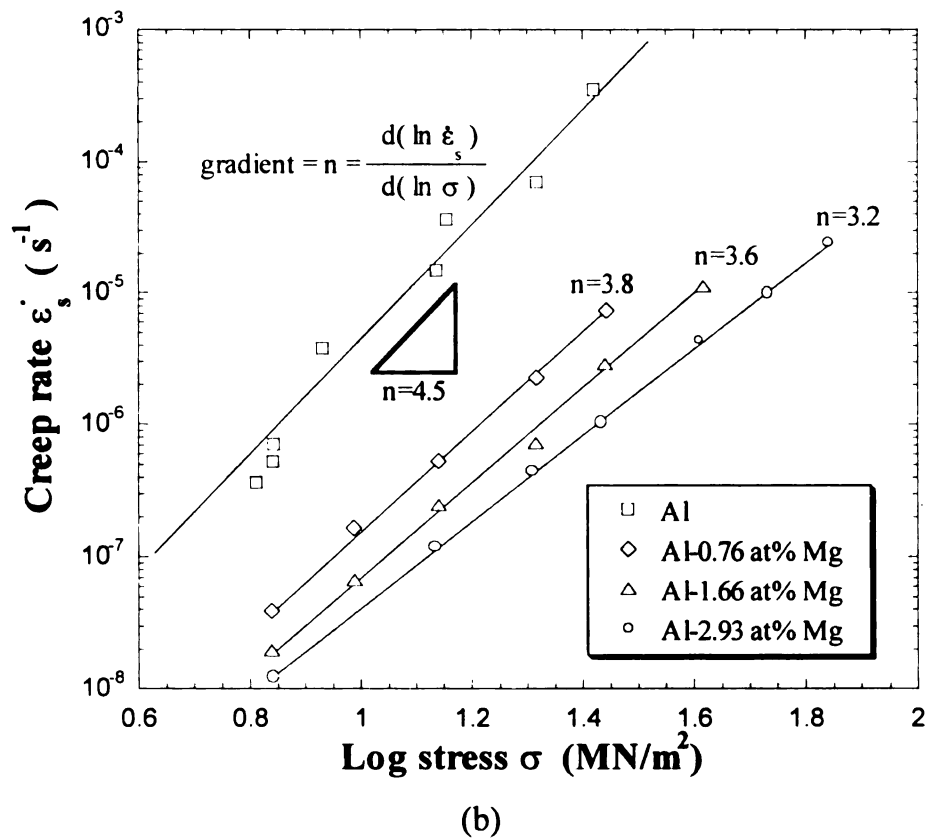
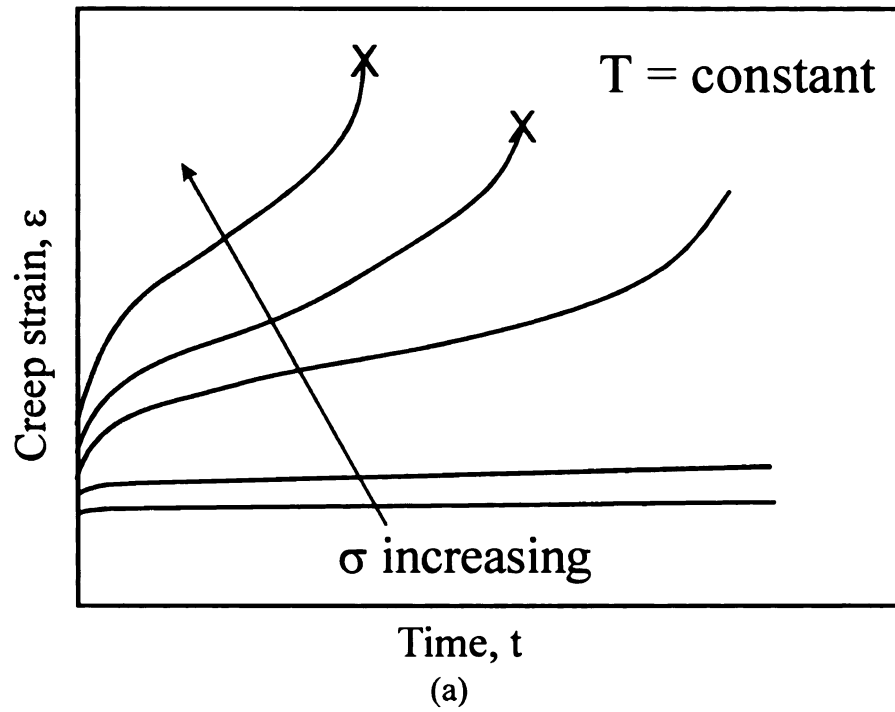


Figure 2.4 (a) Stress effect on creep curves (b) Log $\dot{\epsilon}$ vs. Log σ for aluminium and aluminium-magnesium alloys at 523 K showing the variation in stress exponent, n , values [5,11].

$$\dot{\epsilon}_s = K_1 K_2 \sigma^n \exp\left(-\frac{Q_c}{RT}\right) = A \sigma^n \exp\left(-\frac{Q_c}{RT}\right) \quad (6)$$

where A is a constant. In some cases, there is no steady-state rate region in the creep curve, and the minimum strain rate $\dot{\epsilon}_m$ is usually used instead of $\dot{\epsilon}_s$ [12]. This power law relationship appears to provide a good description of steady-state creep behavior. However, the values of n and Q_c can vary in different stress and temperature regions when the power law is used to describe steady state creep behavior.

2.4.1 Power law breakdown

By multiplying the first and third sides of equation (6) by $\exp(Q_c/RT)$,

$$\dot{\epsilon}_s \exp\left(\frac{Q_c}{RT}\right) = A \sigma^n = Z \quad (7)$$

The Z value is known as the Zener-Hollomon parameter [13] or the temperature compensated secondary creep rate [14,15]. In the plot of $\log[\dot{\epsilon}_s \exp(Q/RT)]$ against $\log(\sigma/E)$ as shown in Figure 2.5 [16], the curvature of the line (indicated by an arrow) at the highest stresses is observed. This nonlinear increase in n value with increasing stress in tests of very short duration is often referred to as “power-law breakdown”. Under power-law breakdown conditions, it shows an exponential dependence of the secondary creep rate on stress and temperature as

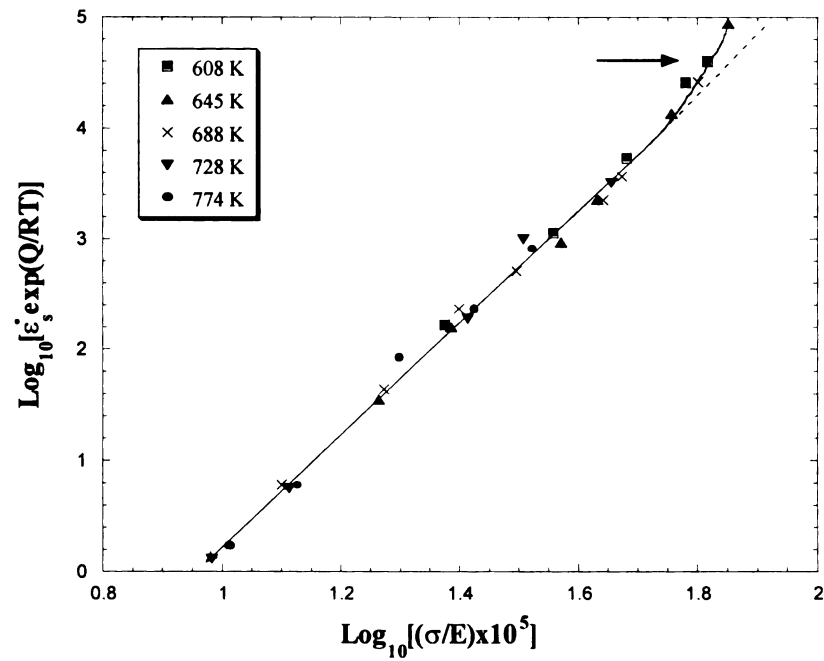


Figure 2.5 The temperature-compensated secondary creep data (or Z) for polycrystalline copper. The activation energy of 130 KJ/mole is used for this plot [16].

$$\dot{\epsilon}_s = B \exp - \frac{(Q_c - V'\sigma)}{RT} \quad (8)$$

Where $V' = VRT$ and B is constant [17]. It offers a good description of steady creep rate behavior in the power-law breakdown region.

2.4.2 Transitions in n value

Creep behavior with stress is well described by a power-law equation except for the power-law breakdown region at very high stresses. From B. Burton and G.W. Greenwood's research, Figure 2.6 shows a transition from $n=5$ to $n=1$ with decreasing stress in a plot of the grain-size compensated secondary creep rate as a function of stress for polycrystalline copper [18]. Figure 2.7 also indicates $n \sim 1$ low stress regime, at $n \sim 4,5$ at high stress regime, and power law breakdown at very high stress regime for pure metal at temperatures above $0.4T_m$ [19]. These different values of n are correlated with different deformation mechanisms (see Figure 2.2).

2.4.3 Transitions in Q_c value

A similar to transition in n value, transition in the activation energy, Q_c , occurs at different temperature regimes instead of different stress regimes. At a creep temperature around $0.4T_m$, the activation energy for creep of polycrystalline copper is close to that of lattice self diffusion, Q_{SD} . In contrast, at creep temperatures around $0.4T_m$ and just below, Q_c values are about half those for lattice self diffusion (see in Figure 2.8) [20]. Moreover, when the creep tests are conducted at high stresses when $n \cong 4-6$ or low stresses when $n \cong 1$, this transition from $Q_c \cong Q_{SD}$ to $Q_c \cong 0.5Q_{SD}$ has been found as the creep temperature is decreased toward $0.4T_m$ [21].

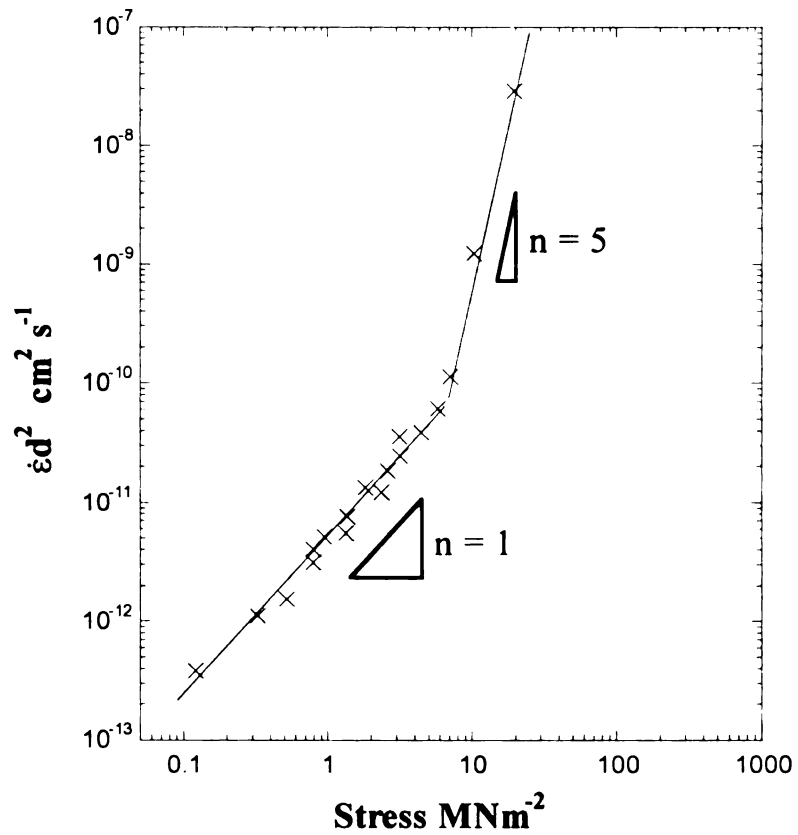


Figure 2.6 A plot of the grain-size compensated secondary creep rate as a function of stress for polycrystalline copper [18].

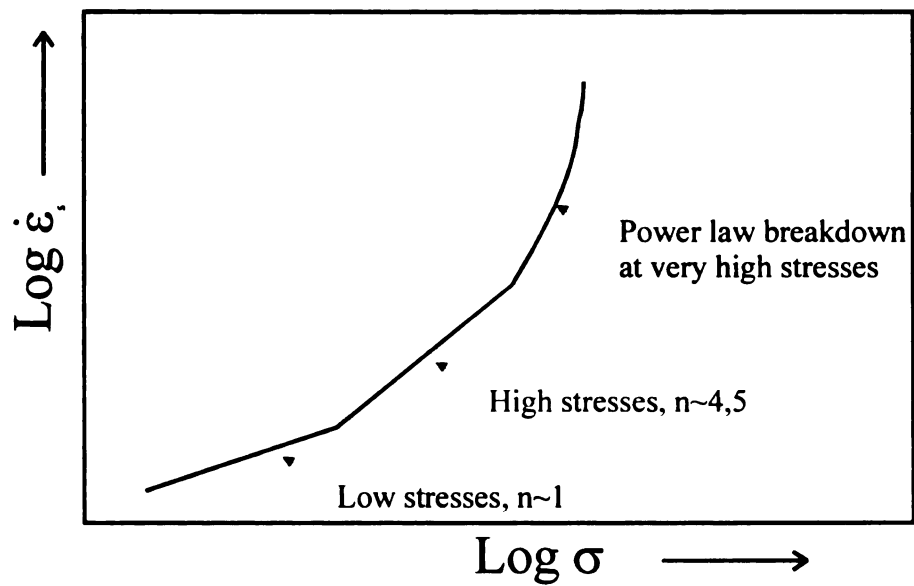


Figure 2.7 Schematic illustration of the transitions in n value occurring when the stress dependences of steady-state creep rate for pure metals at temperatures above $0.4 T_m$ are described using a power-law relationship [19].

These transitions in n and Q_c are commonly explained on the basis that different mechanisms determine creep behavior in different stress-temperature regimes. This suggests that a change in n and/or Q_c signifies a change in creep mechanism.

2.5 DIFFUSIONAL CREEP PROCESS

High-temperature creep behavior can be described by using a power law equation. The Q_c term in the power law can be correlated with diffusion process. Diffusion is clearly important in determining creep behavior, since diffusion normally occurs due to the presence of vacancies within the crystal lattice at high temperatures. Thus vacancy movement is the dominant diffusion mechanism in most metals and alloys. For example, the movement of vacancies in a pure metal by which copper atoms move in the copper lattice is called self-diffusion, and the activation energy for this process is the activation energy for self-diffusion, Q_{SD} . As mentioned before, the activation energy for creep is frequently found to be equal to or less than that of self-diffusion through low and high temperature ranges. The “preferential diffusion path” can explain why the magnitude of the activation energy for creep, Q_c , can be smaller in different temperature regimes. The magnitude of the activation energy for diffusion depends on the bond energies between the moving atom and its neighbors. Surfaces provide “easy paths” for diffusion, since surface atoms have fewer neighbors and therefore fewer bonds than the atoms in crystals. Similarly grain boundaries and dislocation cores should also offer rapid diffusion paths, characterized by activation energies lower than that for lattice diffusion. Figure 2.9 shows evidence for a lower activation energy in polycrystalline silver at different temperature ranges as compared to single crystals, due to the existence of grain boundaries [22].

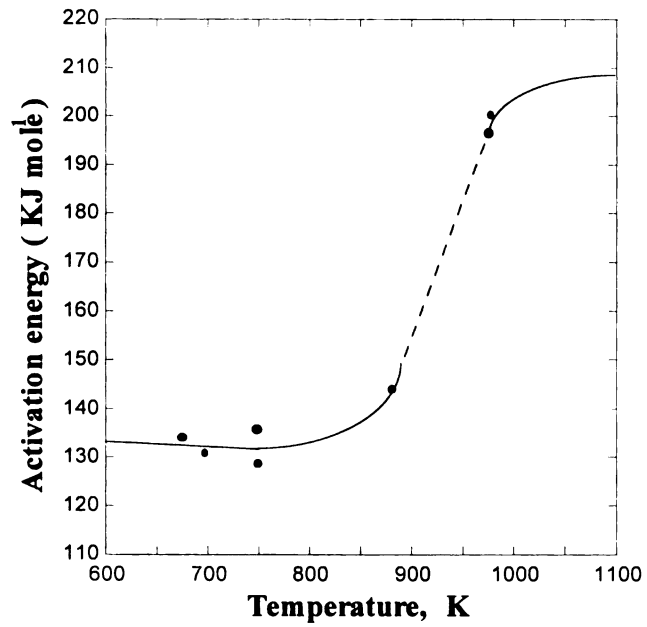


Figure 2.8 The variation with temperature of the activation energy for the creep of polycrystalline copper [20].

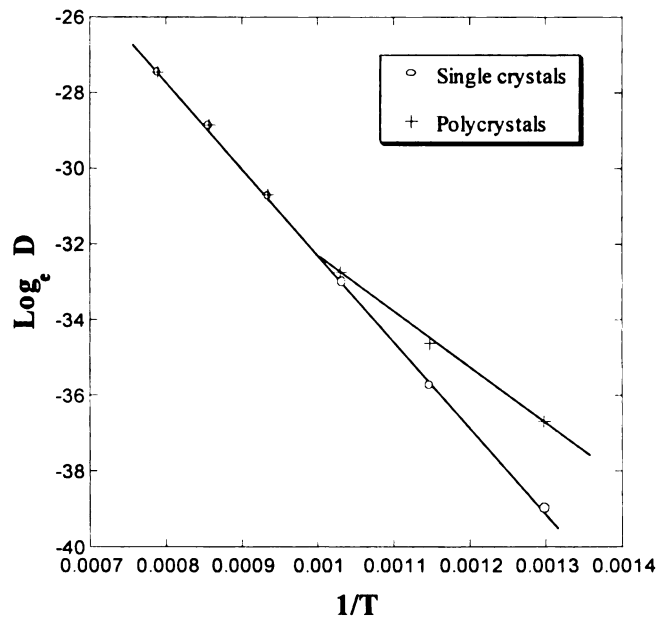


Figure 2.9 The variation of the diffusion coefficient with temperature for the single crystals and the polycrystalline silver [22].

2.5.1 Nabarro-Herring Creep

As shown in Figure 2.10.a [23], a stress is applied to a cube-shaped grain in a polycrystal deforming at high temperatures. If vacancies are moving away from boundaries experiencing tensile stress, these vacancies diffuse into the boundaries under compression. This results in a flow of vacancies toward compressive regions and a counter flow of atoms toward tensile regions. Continued vacancy transfer and counter flow of atoms causes time-dependent extension of the crystal in the tensile direction, simultaneously reducing the cross-sectional area of the grain at right angles to the tensile axis. This diffusional creep process is called Nabarro-Herring Creep. For Nabarro-Herring creep, the creep rate is given by [23,24]

$$\dot{\epsilon}_s = \frac{J_v}{d} = \alpha_{NH} \left(\frac{D_{SD}}{d^2} \right) \left(\frac{\Omega \sigma}{kT} \right) \quad (9)$$

where J_v is the flux of vacancies diffusing down the concentration gradient per second per unit area, d is the average grain diameter, α_{NH} is a geometrical constant (~ 10), D_{SD} is the lattice diffusion coefficient, Ω is the atomic volume, k is Boltzman's constant, and T is temperature.

The power law relationship, equation (6), is fully consistent with the form of equation (9) as indicated by

$$\dot{\epsilon}_s = A \sigma^n \exp\left(-\frac{Q_c}{RT}\right) = \alpha_{NH} \left(\frac{D_{SD}}{d^2} \right) \left(\frac{\Omega \sigma}{kT} \right) \quad (10)$$

By inspecting equation (10), $\dot{\epsilon}_s$ varies directly with the applied stress, i.e. in terms of the power law relationship, $n=1$ when creep occurs by stress-directed flow of vacancies through the crystal lattice. Furthermore, $\dot{\epsilon}_s$ depends on D_{SD} , the lattice self-diffusion coefficient, since D_{SD} is

$$\dot{\epsilon}_s \propto D_{SD} = D_0 \exp\left(-\frac{Q_{SD}}{RT}\right) \quad (11)$$

with D_0 being a constant and Q_{SD} the activation energy for self-diffusion in the crystal lattice. The Nabarro-Herring creep mechanism is dominant at higher temperatures and low stresses.

2.5.2 Coble Creep

Coble creep involves vacancy transfer from tensile boundaries to those under compression along the grain boundaries [25]. Sometimes Coble creep is named grain boundary diffusion creep. Consider the transfer of vacancies only along a narrow zone having a width δ_B to the grain boundary. The area of grain boundary zone intersecting a unit area of a polycrystal of average grain dimension, d , is given by (δ/d) . However, diffusion along this narrow grain boundary zone is determined not by lattice self-diffusion but by grain boundary diffusion. Under these conditions, the creep rate associated with Coble creep can be modified from equation (9) as given in equation (12)

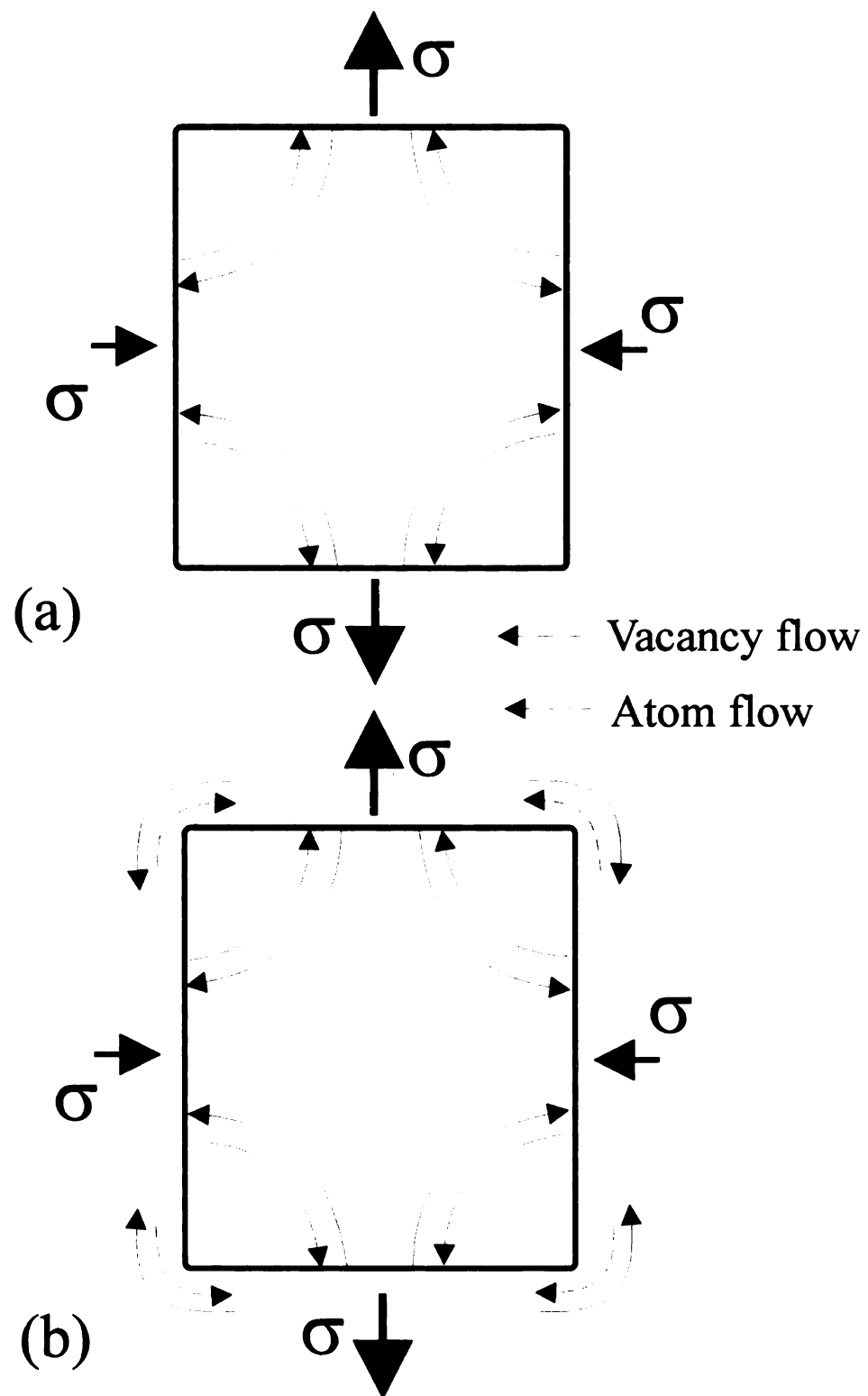


Figure 2.10 Schematic diagram of (a) Nabarro-Herring creep and (b) Coble creep on an ideal grain [23,25].

$$\dot{\epsilon}_s = K_2 \left(\frac{D_{GB}}{d^2} \right) \left(\frac{\delta_B}{d} \right) \left(\frac{\Omega \sigma}{kT} \right) = K_2 \left(\frac{D_{GB}}{d^3} \right) \left(\frac{\delta_B \Omega \sigma}{kT} \right) = \left(\frac{B_c}{\pi} \right) \left(\frac{D_{GB} \delta_B \Omega \sigma}{d^3 kT} \right) \quad (12)$$

where K_2 is a constant (~ 40), D_{GB} is the grain boundary diffusion coefficient, and B_c is a constant ($=148$) [25]. From equation (12) it follows that the creep rate again increases linearly with stress (i.e. $n \sim 1$ in equation (6)), and is inversely proportional to the cube of the mean grain diameter. The temperature dependence of the creep rate is practically identical to that of the grain boundary diffusion coefficient (i.e. $Q_c < Q_{SD}$). As illustrated in Figure 2.9, diffusion along grain boundaries (preferential paths) becomes important as lattice diffusion becomes progressively more difficult as the temperature decreases toward about $0.4 T_m$. When power law creep behavior leads to an n value of unity and an activation energy for creep which is less than the value of lattice self-diffusion in tests carried out at low stresses at temperatures around $0.4 T_m$, Coble creep can be considered to be the dominant creep process.

Both Nabarro-Herring and Coble mechanisms, operating in a parallel way, can contribute to the diffusional creep. The creep rate is then described by the equation

$$\dot{\epsilon} = \frac{B \sigma \Omega}{d^2 kT} D_{eff}, \quad D_{eff} = D_l \left(1 + \frac{\pi}{d} \frac{D_B \delta_B}{D_l} \right) \quad (13)$$

which expresses a sum of creep rates described by equation (11) and (12), and where D_{eff} is the effective diffusion coefficient, and the constant B is 14 [26]. The grain boundary diffusion will contribute to the creep rate to a greater extent, if the average grain diameter d is lower, and the ratio D_B/D_L is greater.

2.5.3 Diffusional Creep and Grain Boundary Sliding

As described in the diffusional creep of polycrystals, atoms are transported from boundaries subjected to compressive stress, to those subjected to tensile stresses. This results in changes in the shape of individual grains. Burton suggested a simple geometrical consideration as shown in Figure 2.11 [27]. Figure 2.11.a shows the original configuration of equiaxed grains. Diffusional creep without any participation of grain boundary sliding (GBS) results in the formation of voids due to incompatibility along longitudinal and horizontal the boundaries (Figure 2.11.b). For the compatibility to be preserved, GBS has to occur simultaneously with the diffusional elongation of individual grains (Figure 2.11.c), showing a shift of a marker line across a grain boundary. An experiment using a bi-crystal of tin explained the grain boundary movement during creep [28]. Gifkins also suggested that it is possible that grains slide past each other along their boundaries in addition to the climb of dislocations during secondary creep [29,30]. The sequence of events which may lead to grain boundary sliding and migration is shown in Figure 2.12 [30]. The dislocation pile-up and relaxation by climbing toward the boundary controls the rate of slip along the grain boundary, which is not constant with time. As a consequence of this process, the activation energy for grain boundary slip may be identified as that for steady-state creep. After climb, dislocations are able to give rise to grainboundary migration, which is proportional to the overall deformation when sliding has temporarily ceased.

The role of GBS in diffusional creep differs from that in dislocation creep. In the former, GBS is an indispensable pre-requisite of diffusion, while in the latter, dislocation creep, GBS need not occur at all if a sufficient number of glide and climb systems

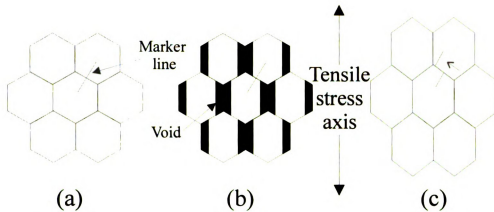


Figure 2.11 Accommodation of diffusional creep by GBS: (a) An original configuration of equiaxed grains. (b) The result of diffusional creep without participation of GBS. (c) Simultaneously with diffusional creep, GBS occurs as shown by the offset of a marker line [27].

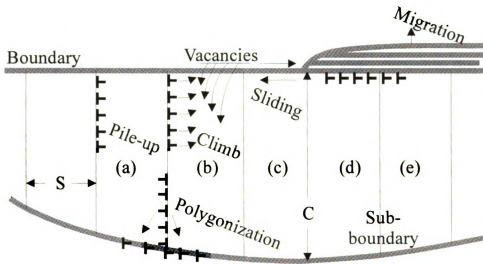


Figure 2.12 Sequence of events which may lead to boundary sliding and migration. S, slip spacing; C, subgrain diameter [30].

operate for the Von Mises criterion to be met. From several studies by Raj and Ashby [31], Beere [32], Speight [33] and Aigeltinger and Gifkins [29], diffusional creep can be considered as diffusion which is accommodated by GBS, or GBS which is accommodated by diffusion. Any consideration of mutually independent contributions of the GBS and the diffusion is meaningless [31].

2.6 DISLOCATION CREEP PROCESSES

When the temperature is between $0.4T_m$ and $0.7T_m$ and at intermediate/high stress levels ($10^{-4} < \sigma/G < 10^{-2}$), the dominant mechanism of creep is the rate of dislocation motion by glide or climb. This regime is known as dislocation creep. Dislocation creep processes start from two ideas of the processes that recovery is the creep rate controlling process, and that dislocation glide is the creep rate controlling process, respectively. Recovery aspects are related to nonconservative dislocation motion, e.g., dislocation climb, in which obstacles are circumvented and/or by which dislocations are annihilated. Work hardening aspects of creep are related to dislocation glide. Hardening mechanisms include dislocation interactions, dislocation pile-ups against barriers, and Kear-Wilksdorf (KW) locking by thermally activated cross slip of segments onto other slip planes observed in some ordered materials.

2.6.1 Dislocation Glide Rate-controlled Creep

In pure metals, a possible model of dislocation creep controlled by the glide of screw dislocations with jogs dependent on diffusion was first considered by Mott [34] and later by Raymond and Dorn [35], Barrett and Nix [36]. Barrett and Nix assumed that the non-conservative motion of jogs on screw dislocations can be connected with both the

emission and absorption of vacancies and that any screw segment contains either vacancy emitting or vacancy absorbing jogs [36]. Under this condition, the creep rate is determined from the following equation

$$\dot{\epsilon} = D_L 4\pi\beta l_j \frac{b^2}{a^3} \frac{Gb}{kT} \left(\frac{\sigma}{G} \right)^3 \quad (14)$$

where D_L is the coefficient of lattice self-diffusion, β is the number of atoms in the unit cell, a is the lattice parameter and l_j is the distance between jogs. This equation also predicts the dependence of the creep rate on the third power of the stress.

Weertman presented the first theory of creep controlled by viscous dislocation glide in solid solution alloys, and assumed not a specific type of interaction of solute atoms with dislocations [37]. Creep rate is described by the following equation,

$$\dot{\epsilon} \approx \frac{\sigma^3 b^2}{GAB} = \frac{2\pi(1-\nu)G}{A} \left(\frac{\sigma}{G} \right)^3 \quad (15)$$

where A is a constant dependent on temperature and on the mechanism of interaction of solute atoms with dislocations, $B = Gb^2/2\pi(1-\nu)$, b is the length of the Burgers vector, and σ is the applied stress. Thus, the creep strain rate depends on the third power of the stress.

Cottrell and Jaswon analyzed the dislocation creep involved in the drag of an atmosphere formed around a dislocation due to the elastic interaction between the dislocation and solute atoms [38]. From their analysis, the modified equation for the creep rate is expressed:

$$\dot{\epsilon} = \frac{2\pi(1-\nu)kTD_s}{Gb^5E_a^2C} \left(\frac{\sigma}{G} \right)^3 \quad (16)$$

where $E_a = (r - r_0)/r_0$ is the misfit parameter; r and r_0 are radii of solute and solvent atoms, respectively, D_s is the diffusion coefficient of the solute and $C = C_0 \exp[|W_M|/kT]$ is the solute concentration in the atmosphere; W_M is the solute atom-dislocation interaction energy.

2.6.2 Dislocation Climb Rate-controlled Creep

Weertman proposed a creep theory based on the assumption that dislocations form pile-ups, and the leading dislocations of pile-ups climb and annihilate in the pure metals as shown in Figure 2.13.a [39]. Under this assumption, the creep rate is expressed as

$$\dot{\epsilon} = A \frac{D_L}{b^{3.5} M^{0.5}} \frac{Gb^3}{kT} \left(\frac{\sigma}{G} \right)^{4.5} \quad (17)$$

where M is Frank-Read source density. The activation energy of creep is close to the activation enthalpy of lattice diffusion, and the creep rate depends on the 4.5-th power of applied stress. The theory predicts not only the usual temperature dependence but also the frequently observed stress dependence of steady state creep rate. With a different assumption in this theory, Weertman and Weertman modeled dislocations that do not form pile-ups, but climb in groups, and found the creep rate again proportional to the 4.5-

th power of applied stress [40]. Again, Weertman derived another version of model from the idea of dislocation motion and rearrangement in Figure 2.13.b [41,42]. The creep rate is presented as the following equation, which depends on the third power of stress [42].

$$\dot{\epsilon} = D_L A_C \frac{Gb}{kT} \left(\frac{\sigma}{G} \right)^3 \quad (18)$$

The previous Weertman creep models were considered based on the assumption that the creep rate is controlled by a recovery process dependent on dislocation climb occurring by means of lattice diffusion. In contrast, Nabarro considered individual links of the network as dislocation sources: while absorbing or emitting vacancies they bow out; the dislocation density increases due to this bowing [43]. The increase in dislocation density is compensated by the annihilation of links of opposite signs which meet during climb. The Nabarro analysis led to the equation,

$$\dot{\epsilon} = D_L A_N \frac{G\Omega}{b^2 kT} \left(\frac{\sigma}{G} \right)^3 \ln \left(\frac{4G}{\pi\sigma} \right)^{-1} \quad (19)$$

The value of the logarithmic term changes with stress very slightly, so that the creep rate practically varies with the third power of stress.

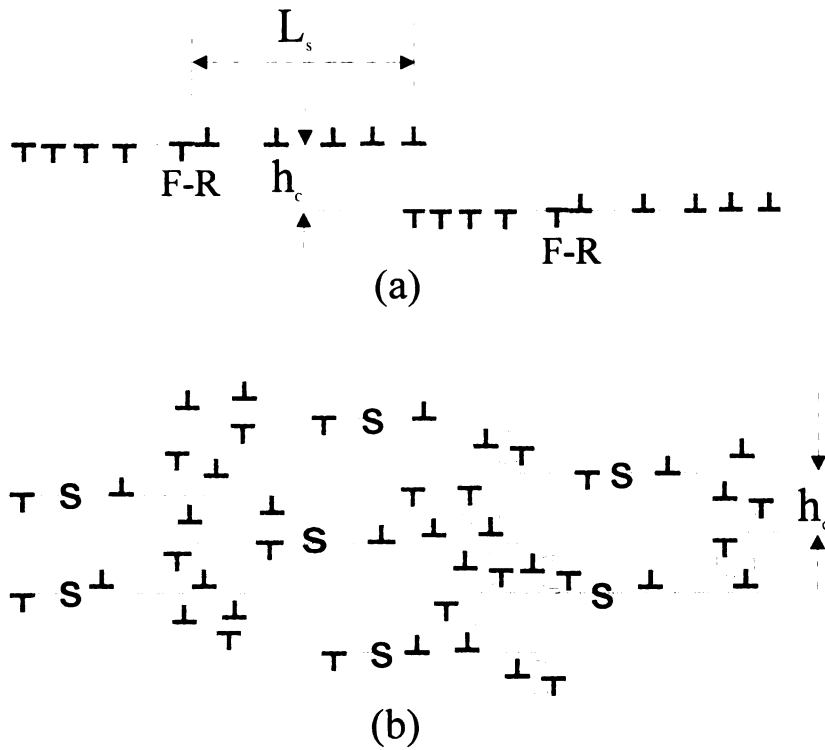


Figure 2.13 Weertman's models of creep: (a) Dislocations form pile-ups, the leading dislocations of both pile-ups climb and annihilate. (b) Arrangement and motion of dislocations assumed in a future version of the model [39,41].

2.7 DEFORMATION-INDUCED TWINNING

Deformation or mechanical twinning is a mode of plastic deformation that occurs by shear as the result of applied stresses. The shear associated with mechanical twinning is uniformly distributed over an entire deformed volume rather than localized on discrete slip planes. When a crystal deforms plastically by twinning, there occur atomic displacements, which give rise to rotated crystal bands within a grain. Hexagonal metals, such as Zn and Mg, behave in this way when deformed at ambient temperatures, while BCC metals, such as iron and Nb, show this behavior when deformed at subambient temperatures [44]. Deformation twins have been observed in a few FCC metals such as silver and copper-aluminium at low temperatures [45].

The results of plastic deformation by twinning are very different from that of slip. First, the twinned region of a grain has a mirror image of the original lattice with respect to the twin plane, while the slipped region has the same orientation as that of the original unslipped grain as shown in Figure 2.14. Second, twinning consists of uniform shear strain, while slip consists of a multiple shear displacement on a single slip plane. Third, the twinning direction is polar, while the slip direction can be positive or negative. In general, the stress necessary to form twins is greater than but less sensitive to temperature than that necessary for slip [44]. This stress for initiation of twinning is much larger than the stress necessary for its propagation [44].

In high temperature creep conditions, deformation twinning is rare, but it is observed in some ordered materials. Yamaguchi, Jin and Feng suggested that mechanical twinning is an important and common deformation mechanism at high temperatures in TiAl intermetallics [46,47,48,49,50], and sensitive to temperature, stress, strain rate, and

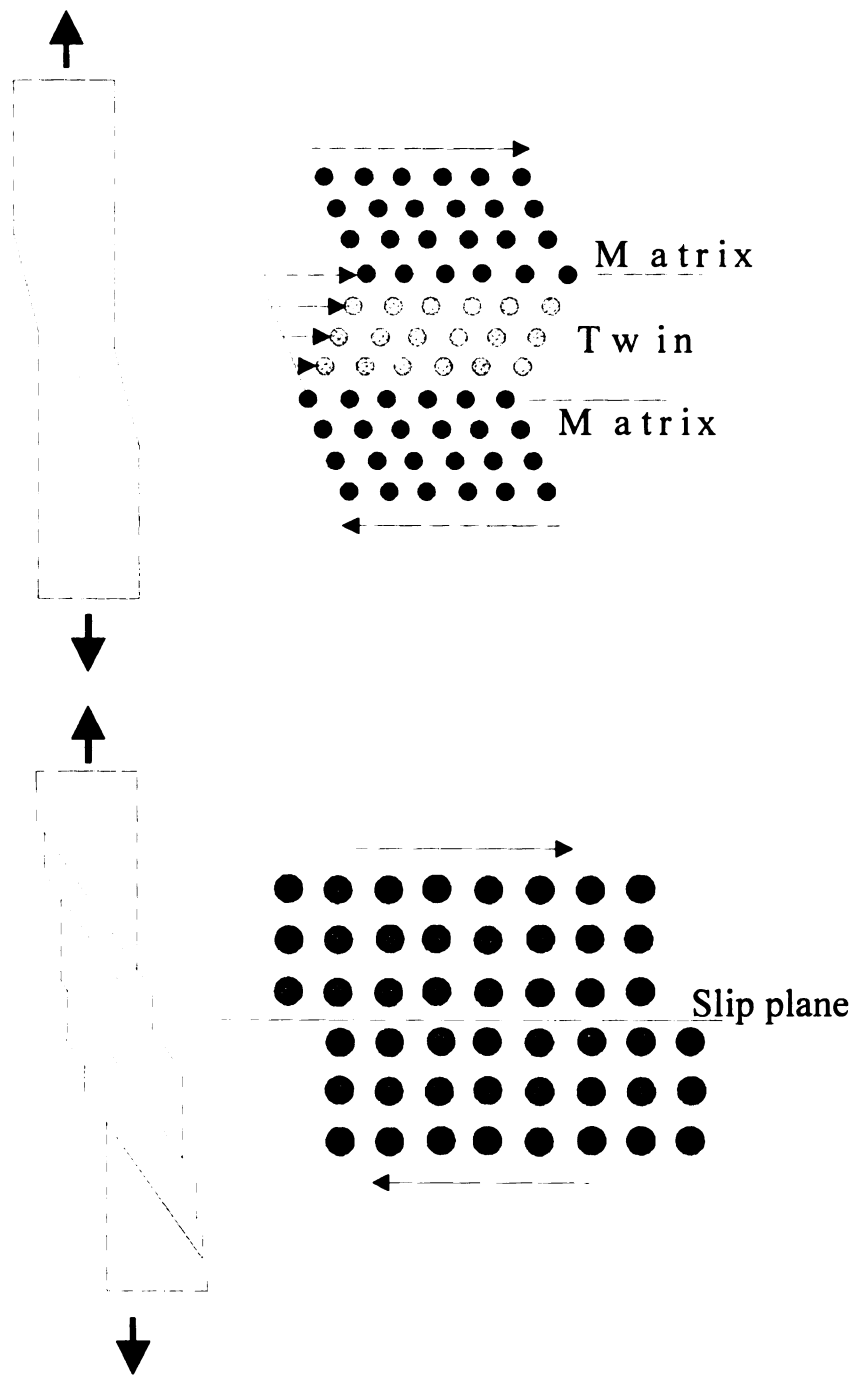


Figure 2.14 Schematic diagram of twinning and slip after applied stress.

crystal orientation [46,47,50].

2.8 CREEP IN SOLID SOLUTION ALLOYS

Sherby, Burke, and Langdon classified the solid solutions into two classes according to the value of stress exponent n of the steady state creep rate [51, 52]. For Class I alloys (class A), the movement of dislocations is controlled by the drag of solutes, and the parameter n is approximately 3. For Class II alloys (class M), the creep is controlled by climb of dislocations, as in the case of pure metals, and n is approximately 5. Other characteristic differences in Class I (A) and Class II (M) creep behavior are noted in Table 2.1 [53]. Figure 2.15 shows the different deformation behavior between strain and strain rate for pure metals, and Class I (A) and Class II (M) type in solid solution alloys [54]. In a pure metal, the initial creep rate is very high since the existing dislocations can freely move. The decrease in strain rate after some deformation is due to an increase density of dislocations. For Class I (A) alloys, the initial creep rate is low because there are a lot of solute atoms pinning each dislocation. As the deformation proceeds, the dislocation density increases and the number of solute atoms per unit length of dislocation decreases. Thus the creep rate increases with deformation. For Class II (M) alloys, a control of the dislocation drag by solutes is the initial process. However, dislocation climb becomes the main rate-controlling process after some deformation. Thus creep rates decrease after it reaches the peak.

Table 2.1 Characteristic features in Class I and Class II creep behavior [53]

Class I creep behavior	no instantaneous plastic strain after stress application 'inverse' primary creep behavior
	the higher creep rate after the stress reduction than the steady state creep rate
	the steady state creep rate not depend on or only slightly depends on the stacking fault energy
	no significant extent formation of dislocation substructure (cell or subgrain structure) during creep
	generally slightly curved, and homogeneously distributed dislocations, slight tendency of network formation
	dislocations with predominant edge orientation
Class II creep behavior	instantaneous plastic strain after stress application 'normal' primary creep behavior
	the lower creep rate after the stress reduction than the steady state creep rate
	the steady state creep rate strongly depend on the stacking fault energy
	well defined dislocation substructure (cell or subgrain structure) during creep, and not necessary well developed cell structure in the case of low stacking fault energy
	generally slightly curved, and homogeneously distributed dislocations, slight tendency of network formation
	random orientation of dislocations and not prevailed edge orientation

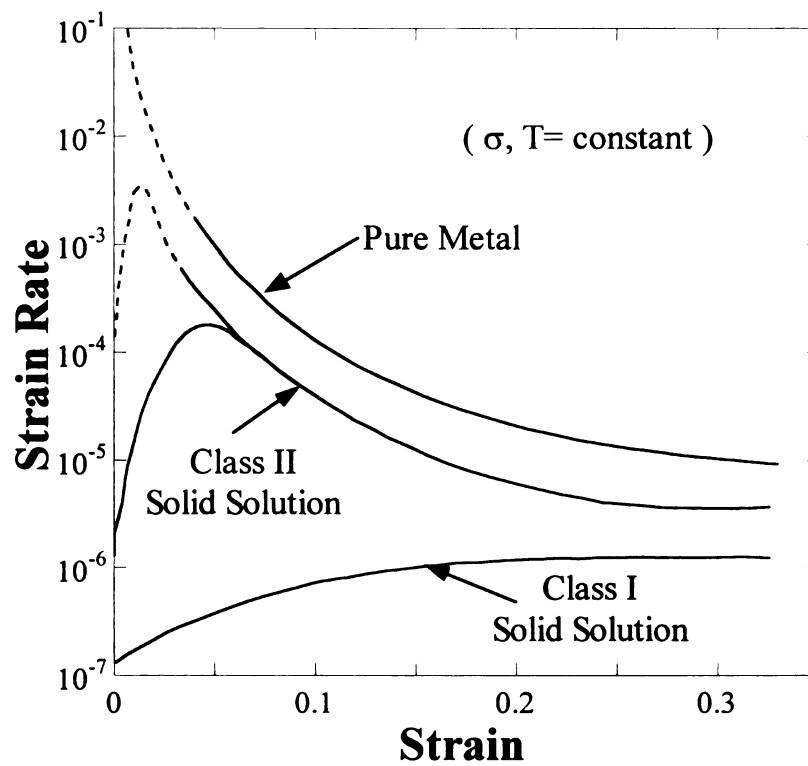


Figure 2.15 Relationship between strain and strain rates for pure metals, solid solutions of Class I (dislocation-drag control), and solid solutions of Class II (substructure control) [54].

2.9 STRESS AND TEMPERATURE CHANGE CREEP (TRANSIENT CREEP)

The transient creep behavior after stress changes generally depends on the material and on the amount and the sign of the stress change. The behavior during sudden stress changes during steady-state creep at high temperature is thought to depend on the type of glide motion of dislocations [55-57]. Oikawa and Sugawara suggested that there are two types of transient creep behavior in pure Al and Al alloys: the free-flight glide in which dislocations can glide freely and the viscous glide in which dislocations glide in a viscous manner [58]. Figure 2.16 shows the transient creep behavior of the pure metal and the alloy after increments and reduction of stress [59].

For the free-flight glide deformation in Figure 2.16.a, as stress increases, instantaneous strain is followed by transient deformation in which $d\epsilon/dt$ is much greater than the previous steady-state rate, and it decelerates to a new (higher) steady state value. This transient creep behavior consists of elastic and plastic components. But with a stress decrease, an instantaneous elastic contraction is followed by transient deformation in which $d\epsilon/dt$ is much less than the previous steady-state creep rate and accelerates to a new (lower) steady state stage. This type is known as 'normal' transient creep behavior. As indicated above, the transient creep behavior in a pure metal is governed by the dislocation climb processes, i.e. dislocation glide contributes strain but the creep rate is controlled by the rate of dislocation climb processes in which n is generally close to 5. These glide-climb creep processes which are associated with the formation of substructure allow rearrangement and annihilation of dislocations to occur. The effective stress (the difference between the applied stress and the internal stress; stress field around the dislocations due to the distortion of the crystal) causes dislocation movement after a

stress increment, and the substructure rearrangement and annihilation of dislocations associated with the decrease of effective stress causes deceleration of the creep rate. On the other hand, after a stress reduction, the coarsening of the dislocation substructure results in an increase of the effective stress for thermally activated glide that causes acceleration of the creep rate.

For the viscous glide deformation in Figure 2.16.b, instantaneous plastic strain does not occur when the applied stress is increased suddenly, and the instantaneous strain is elastic behavior. In contrast to free-flight dislocation glide, dislocations remain homogeneously distributed with no formation of subgrain structure during the primary creep in this type and the dislocation glide becomes the slowest process due to the viscous drag of mobile dislocations by the solute atmosphere, where n is equal to 3. Thus the solute-drag model can explain the inverse of normal primary creep behavior. The creep rate is limited by the mobile dislocation density which is low prior to creep. As subsequent stress increases, the mobile dislocation density increases gradually and therefore it leads to a higher creep rate. After a stress decrease, the mobile dislocation density is higher than the equilibrium level, but the excess dislocations have not yet glided to annihilation sites so the strain rate decelerates to the steady state value. Weertman presented a glide-controlled model which assumes that the creep rate depends on the mobile dislocation density and the average dislocation velocity that is determined by the rate at which the solute atoms can move along with the dislocations [60, 61].

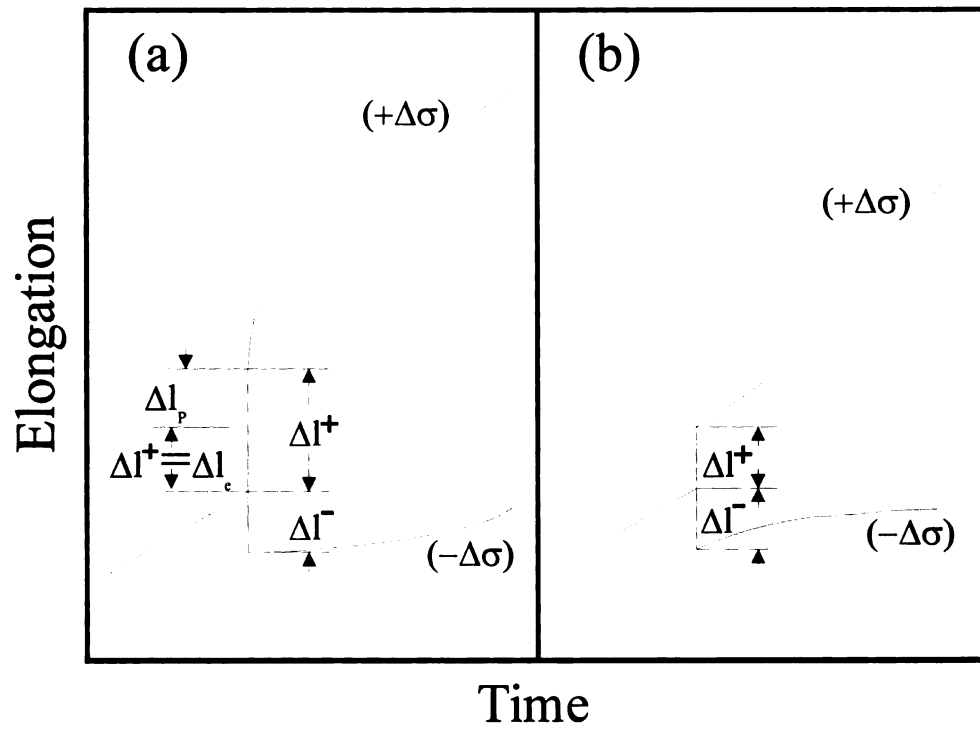


Figure 2.16 Schematic drawings of the instantaneous elongation and contraction upon small changes in cases of (a) the free-flight glide, and (b) the viscous glide [59].

2.10 PRIMARY CREEP IN METALS [62]

Primary creep has not been studied as extensively as secondary creep. Since the investigation of primary creep is complicated by variations in the initial loading process, which is very dependent on operator and machine variables. Primary creep is commonly modeled with equations of the form

$$\varepsilon = \varepsilon_0 + \alpha_1 \log_e(\alpha_2 t + 1) \text{ or}$$

$$\varepsilon = \varepsilon_0 + At^a \text{ or}$$

$$\varepsilon = \varepsilon_0 + e(1 - \exp(-rt)) \quad (20)$$

at lower and higher temperatures, respectively, where ε_0 represents the initial strain upon loading. Quantity of ε_0 can not be measured or defined easily, since it represents a combination of elastic and rapid plastic deformation. Primary creep is closely connected to microyielding [63], anelasticity [64-66], and viscoplasticity [67-69]. Andrade and Jolliffe [70] observed that the exponent a is near 1/3 in the middle equation above for many materials. Alternatively, stochastic approaches to modeling heterogeneous deformation in materials have been proposed by Daehn [71] and by Bagley [72], that reproduces the empirical nature of various primary creep models.

In a study of room temperature primary creep in Ti alloys, correlations between microstructural features and changes in the rate constant a have been identified for one and two phase alloys [73, 74]. When loaded at about 80-90 % of the yield stress, a one phase alloys exhibit three stages with increasing strain and time. The a value is initially close to 0.2, which correlates with rapid dislocation motion across grains optimally

oriented for easy slip as slip bands on the primary slip system. And then a value for the second stage increases to 0.4 near a strain of 0.1%, where slip transfer across grain boundaries is observed. Exhaustion of slip bands resulting from slip transfer accounts for the return of the a value to 0.2 at a strain near 0.5%. In two phase Ti alloys [74], the initial a value is 0.8, and it decreases to a value of 0.2 after a strain near 0.5%. The initially high value is attributed to the much smaller size of the microstructure, where slip transfer must occur at a lower overall strain. These observations indicate that when slip transfer is precluded, primary creep strains are dependent on the slip distance to a barrier, and that this strain process will be in the range between 0.1- 0.5%.

At elevated temperatures, the role of diffusion further complicates the details of dislocation motion, creation, and annihilation. With higher temperatures, diffusion affects primary creep behavior by processes of anelasticity and dislocation creep processes identified in steady state creep investigations. Anelastic flow is complex, and rheological modeling is commonly used [64]. Primary creep strains are commonly in the range of 0.01-0.05, with lower values being observed at lower temperatures [67]. In low stress diffusion creep conditions, one study suggests that primary creep strain may be completely anelastic with a value of about 5 times the elastic strain [65]. Primary creep strains were shown to be anelastic, as unloading resulted in recovery of the primary creep strain (similar to pure FCC metals where the activation energy implies diffusion controlled deformation [75]). With larger strains in the steady state regime, anelastic recovery was greater than the primary creep strain.

In a study of an austenitic stainless steel, dislocation densities measured as a function of strain indicated that the dislocation density increases and then decreases as

secondary creep is approached [76]. The geometrical perfection of dislocation networks increases with greater strains. Internal friction measurements on single crystal Al at $0.5 T_m$ indicate a similar result [77]. Argon and Bhattacharya [78] identified two stages of primary creep in pure Ni deformed between 0.54 and $0.62 T_m$, the first related to dynamic recovery with a time constant of about 100 s, followed by a static recovery process with a time constant of about 10^4 s. The internal stress was found to increase with strain to a plateau value at strains larger than the value where minimum creep was observed. They developed scaling laws that provided results consistent with Andrade's observed $t^{1/3}$ law. The composite model has been developed for primary creep [79, 80], in which the back stress is not constant, but evolves to the steady state value.

Primary creep strains and creep strength are very sensitive to orientation [81]. The deceleration of the creep rate and the evolution of dislocation structure is the result of Orowan bowing and dislocation pileups imposed by the geometry of the reinforcements [82]. When solid solution strengthening is present (e.g. Inconel 617 [83]), inverse creep followed by a normal creep transient is observed, reflecting interactions between solute atom drag effects on initial dislocation multiplication, and development of dislocation substructure. In contrast to the relatively large primary creep strains in single crystal superalloys, primary creep strains in aluminum strengthened with incoherent reinforcements are less than 20% of the values measured in pure aluminum [84].

Heat treatment can affect primary creep significantly. If precipitation occurs, it can remove solute atoms from solution that alters primary creep kinetics [85]. A smaller particle spacing is beneficial, particularly when the distance between them becomes small

enough to prevent Orowan looping, which significantly reduces primary creep strain, and causes incubation times before primary creep strains are observed [86].

As mentioned above, it is apparent that a wide variety of phenomena have been observed in primary creep. Though much of it can be rationalized in terms of known deformation mechanisms and microstructural observations, it is apparent that composition and processing history have a large impact on the processes of primary creep. Also, the details are commonly specific to the specific class of materials in which they are observed.

2.11 DEFORMATION MECHANISM MAP

As described before, the dominant creep mechanism depends on stress and temperature conditions. Thus the deformation mode will change and cause different creep behaviors under different stress and temperature conditions. Information about which creep mechanism controls deformation under various conditions can be obtained from construction of ‘Deformation Mechanism Map’ with two main creep mechanisms; dislocation creep and diffusion creep (Coble creep and N-H creep). The deformation mechanism maps, first introduced by Weertman [87] and Ashby [88], are a graphical description of creep, representing the ranges in which the various deformation modes are rate-controlling steps in the stress versus temperature space. Figure 2.17 shows a simple deformation map for a pure polycrystalline metal [89]. The boundaries are formed by setting two equations for different creep mechanisms equal to each other.

In general, the dislocation and diffusion creep are considered as an independent process, and both of them contribute to the overall creep rate. Under different stress and

temperature conditions, one of these processes will dominant in creep deformation. This creep process is defined as dominant mechanism, and a different dominant creep mechanism results in different values of stress exponent n and activation energy Q_C as indicated in Table 2.2 [90].

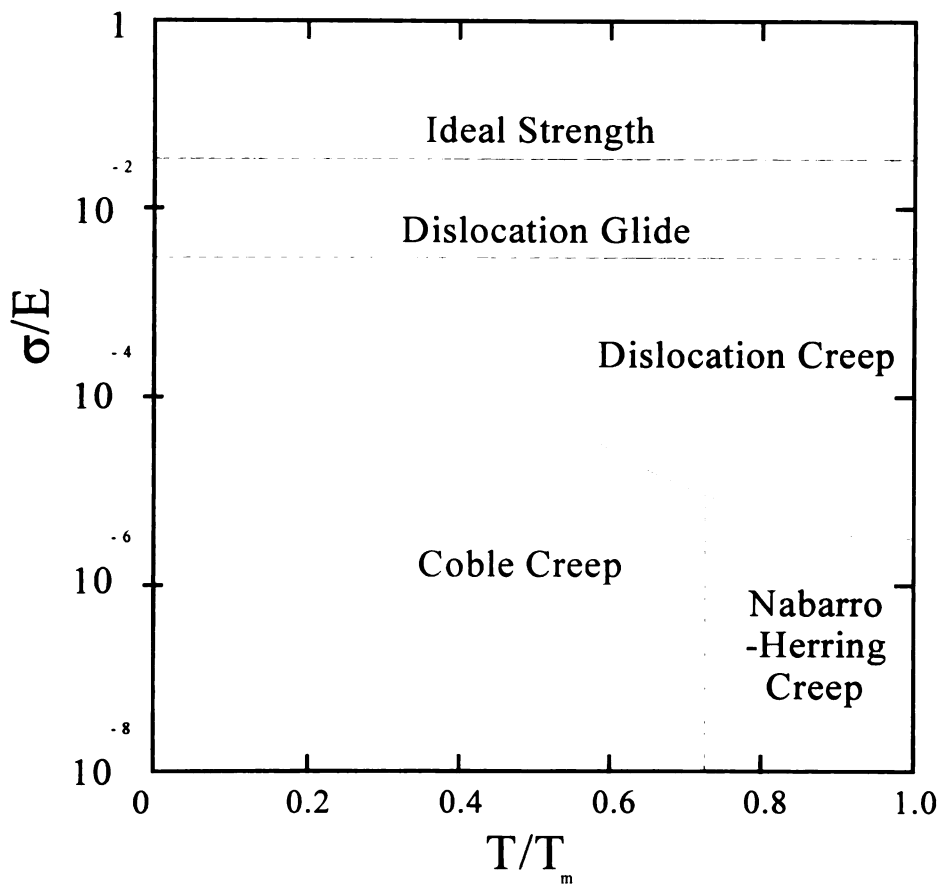


Figure 2.17 Schematic version of a deformation map for a polycrystalline metal illustrating the stress/temperature regimes within which dislocation and diffusional creep processes may be expected to be dominant [89].

Table 2.2 Different Q_C values associated with dislocation and diffusion creep occurring with pure metals [90].

Creep process	Temperature	Stress	n values	Q_C value
high temperature dislocation creep	above $\sim 0.7T_m$	Intermediate/ high	>3	$\sim Q_{SD}$
low temperature dislocation creep	~ 0.4 to $0.7T_m$	intermediate/ high	>3	Q_{CORE}
high temperature diffusion creep (Nabarro-Herring)	above $\sim 0.7T_m$	low	~ 1	Q_{SD}
low temperature diffusion creep (Coble creep)	~ 0.4 to $0.7T_m$	low	~ 1	Q_{GB}

Q_{SD} : the activation energy for self diffusion

Q_{CORE} : the activation energy for self diffusion along dislocation core, often termed pipe diffusion

Q_{GB} : the activation energy for grain boundary diffusion

CHAPTER 3

OVERVIEW OF TITANIUM ALUMINIDES

3.1 INTRODUCTION

Titanium Aluminide intermetallic compounds have been studied and developed for use as structural materials at high temperatures, such as heat engines, turbine engine blades, aerospace and automobile components, since it has a high specific strength at high temperatures [91-93]. From the comparison of properties provided in Table 3.1 [94,95] it is evident that near gamma TiAl alloys are better than current Titanium alloys and superalloys in terms of density, oxidation, and creep properties. The melting temperatures of the two materials are essentially the same and γ -TiAl has a distinct advantage when comparing density, coefficient of thermal expansion (CTE), and thermal conductivity, but it has a lower yield strength, ultimate tensile strength and room temperature ductility. Having lower density, CTE, and thermal conductivity are all advantages in the design of jet engines since they give light weight components, minimum thermal fatigue and allows higher operating temperatures with external cooling.

In the first part of chapter three, titanium aluminides will be reviewed in terms of crystal structure, microstructure, deformation mode, deformation twinning, creep behavior, and alloying effects. Then a proposed research plan will be presented with the research goal of determining the effect of heat treatments on microstructures and primary creep deformation of four investment cast titanium aluminide alloys, and to

Table 3.1 Comparison of Gamma TiAl with Titanium alloy and Superalloy [94,95].

Property	Ti-Alloy	γ -TiAl	Ni-base superalloy
Melting Point ($^{\circ}\text{C}$)		1440	1450
Crystal structure		tetragonal (f.c.t.), P4/mmm $a=0.4 \text{ nm}$, $c/a=1.02$	f.c.c. matrix + L12 precipitates
Density	4.54	3.7–3.9	8.3
Young's Modulus (GPa)		160–180	206
Poisson's ratio		0.27	0.29
Yield Strength (MPa)		275–380	850
Ultimate Strength (MPa)		360–500	1000
Stiffness (GPa)	110	176	207
Max T - Creep ($^{\circ}\text{C}$)	540	900	1090
Max T - Oxidation ($^{\circ}\text{C}$)	590	815	1090
Ductility - Room T (%)	15	1-3	3-10
Ductility - Oper. T (%)	15	5-12	10-20
Coefficient of Thermal Expansion ($10^{-6}/^{\circ}\text{C}$)		10.8	14.8
Thermal Conductivity ($\text{Wm}^{-1} \text{K}^{-1}$)		22	11

compare primary creep deformation in these alloys with creep in polysynthetically twinned (PST) Crystals.

3.2 TITANIUM ALUMINIDES

3.2.1 Crystal Structure and Microstructure

In general, there are two basic lattice structures (phases) found in Ti-Al alloy system near the stoichiometric composition in Figure 3.1[96,97]. One is the γ phase of TiAl and the other is α_2 phase of Ti_3Al . As indicated in Figure 3.2.a [98], the γ -TiAl has $L1_0$ lattice crystal structure where the titanium and aluminum atoms alternately stack in the sequence of ABCABC on (002) planes and it is a face-centered tetragonal structure in which c/a ratio is 1.02. The anisotropic crystal structure causes more complicated slip system in the $L1_0$ lattice [99]. From Figure 3.2.b [100], the α_2 (Ti_3Al) has DO_{19} crystal lattice structure where the stacking sequence is ABABAB and it is the hexagonal closed-packed structure (HCP) with a larger value of basal plane axis ($2a$). The system is often off-stoichiometric with Al atoms in Ti sites and therefore, this results in a slightly disordered lattice structure.

TiAl has a wide composition range, but mainly on the Al-rich side of the stoichiometric composition as shown in Figure 3.1. The microstructure of Ti-rich contains a large volume fraction of Ti_3Al (α_2 phase) and a small volume fraction of TiAl (γ phase). Therefore, as Al concentration increase, the volume fraction of TiAl increases and the volume fraction of Ti_3Al decreases in the equilibrium condition. With higher concentration of Al (> 50 at%), an equiaxed type of microstructure with single phase (γ phase) can be obtained. In Ti-rich two-phase microstructures, the volume fraction of each

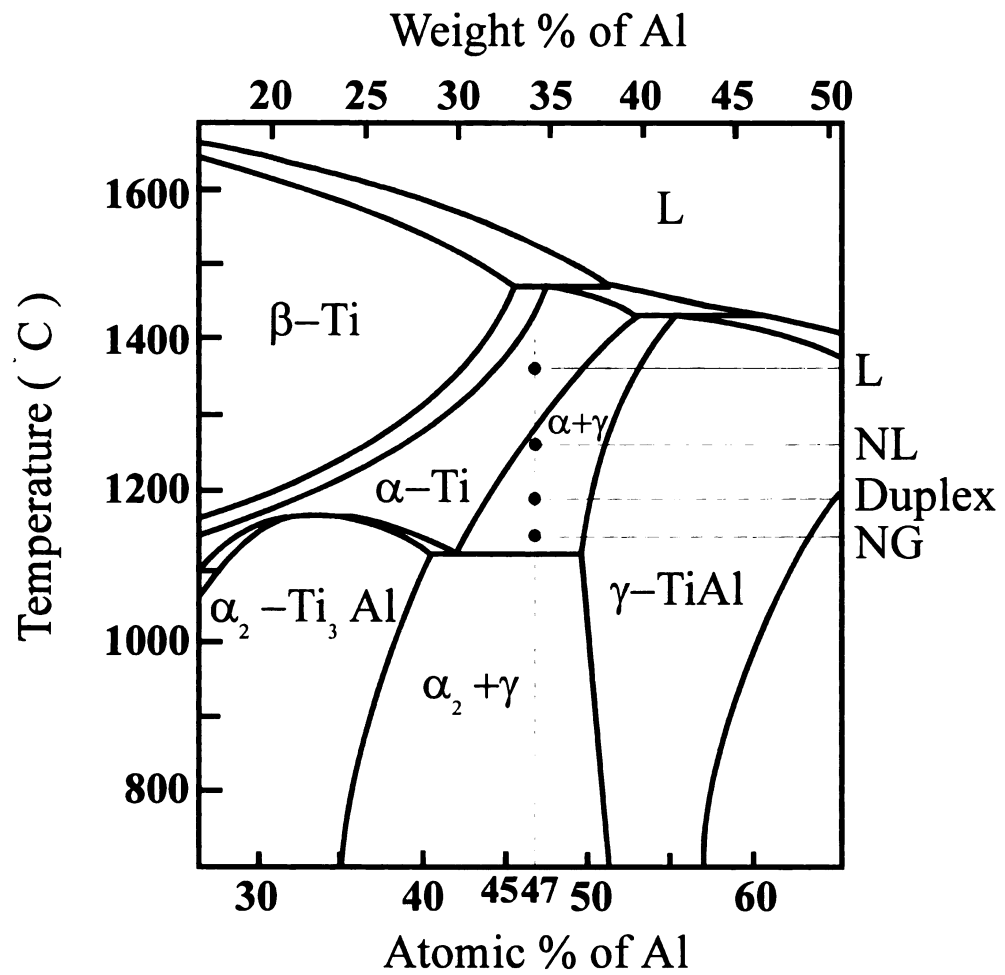


Figure 3.1. Phase diagram of binary Ti-Al system [96,97].

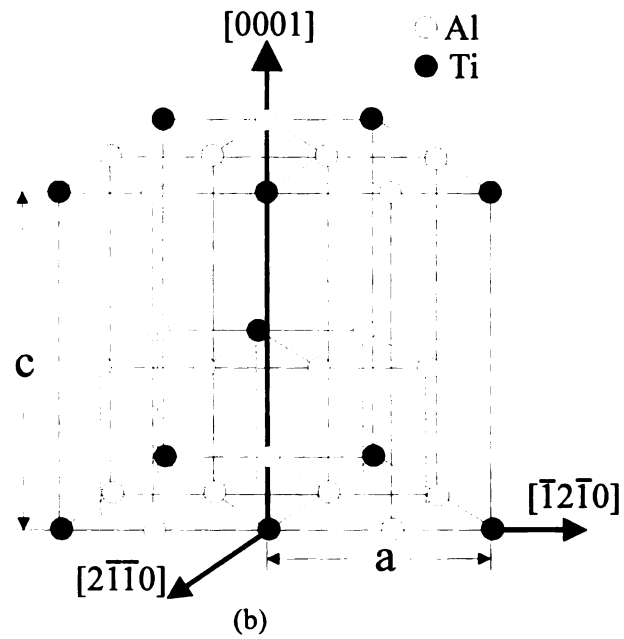
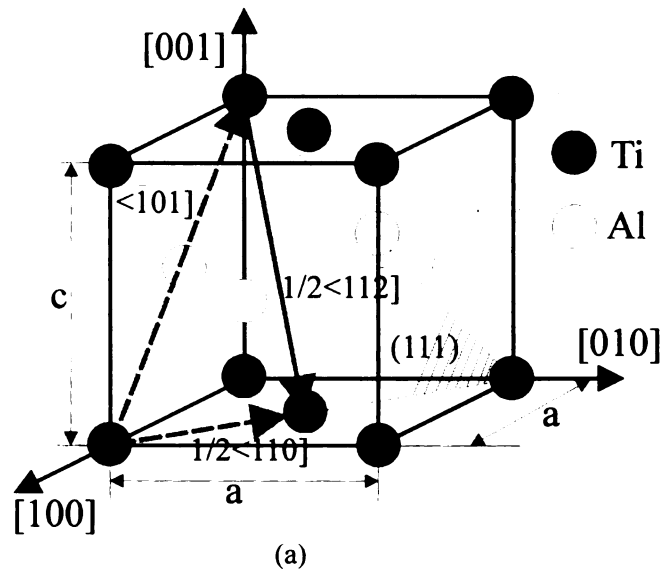


Figure 3.2 Lattice structure of (a) $L1_0$ -TiAl and (b) DO_{19} -Ti₃Al [98,100].

phase depends on composition and processing history. Upon solidification of stoichiometric or Ti-rich composition, a two phase microstructure having a lamellar microstructure develops from the α phase. Three types of lamellar structures, called type I, II and III (see below), have been identified through several microstructural development studies [48,49,101].

$$\text{TYPE I: } \alpha \rightarrow \alpha + \gamma_p \rightarrow L(\alpha / \gamma) \rightarrow L(\alpha_2 / \gamma)$$

$$\text{TYPE II: } \alpha \rightarrow \alpha_2 \rightarrow \alpha_2 + \gamma_{pt} \rightarrow \alpha_2 + \gamma_p \rightarrow L(\alpha_2 / \gamma)$$

$$\text{TYPE III: } \gamma_m + \alpha_2' \xrightarrow{\text{heating}} \gamma_m + \alpha_p' \rightarrow \gamma_m + \alpha_p \rightarrow L(\gamma / \alpha) \xrightarrow{\text{cooling}} L(\alpha_2 / \gamma)$$

$$\gamma_m \xrightarrow{\text{heating}} \gamma_m + \alpha_{pt} \rightarrow \gamma_m + \alpha_p \rightarrow L(\gamma / \alpha) \xrightarrow{\text{cooling}} L(\alpha_2 / \gamma)$$

The type I and II lamellar structure is typically formed by the growth of γ (TiAl) plates into the α or α_2 (Ti_3Al) phase in two phase regions such as $\alpha + \gamma$ and $\alpha_2 + \gamma$ (see Figure 3.1). The transformation proceeds by TiAl plates that form on the basal plane of the Ti_3Al and then thicken at the expense of the Ti_3Al phase. This phase transformation causes the lamellar structure, composed of alternating laths of TiAl and Ti_3Al phases. The orientation relationships between the γ (TiAl) phase and the α_2 (Ti_3Al) phase are $\{111\}_{\text{TiAl}} // (0001)_{\text{Ti}_3\text{Al}}$, $\langle 110 \rangle_{\text{TiAl}} // \langle 11\bar{2}0 \rangle_{\text{Ti}_3\text{Al}}$ as shown in Figure 3.3 [102,103]. The type III lamellar structure is formed by Ti_3Al plate growing into TiAl phase. This lamellar structure has the same orientation relationship between the TiAl and Ti_3Al as type I and II. However, since all $\langle 11\bar{2}0 \rangle$ directions in Ti_3Al are equivalent to one

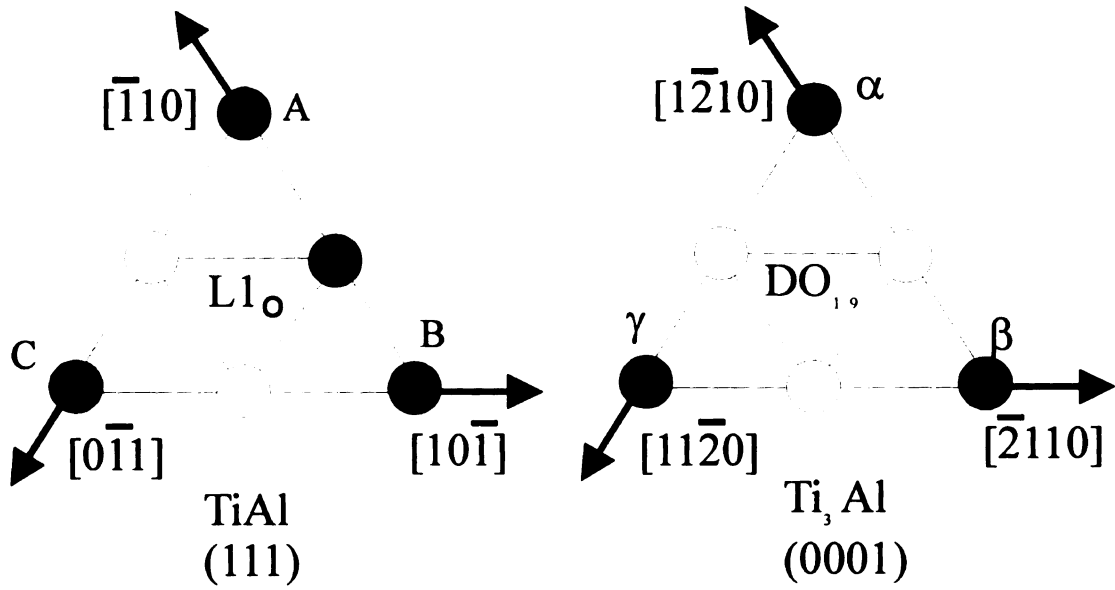


Figure 3.3. $\langle 110 \rangle_\gamma$ directions and the atomic arrangement on a (111) plane in $L1_0$ and $\langle 11\bar{2}0 \rangle_{\alpha_2}$ directions and the atomic arrangement on the basal plane (0001) in DO_{19} [103].

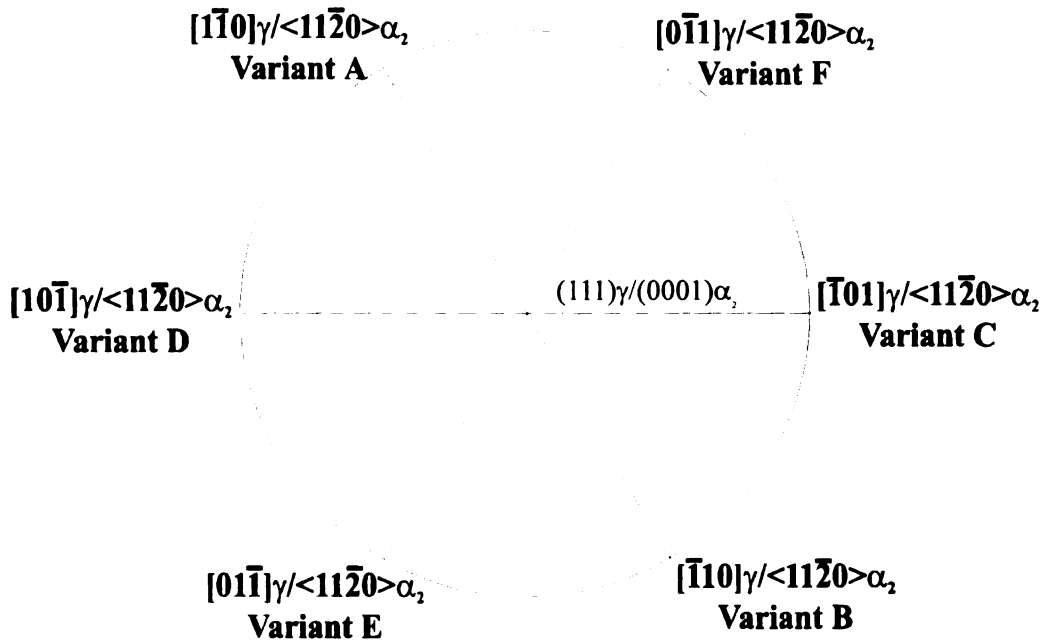


Figure 3.4. The stereographic projection of (111) $_\gamma$ and (0001) $_{\alpha_2}$ show the six possible orientation variants of $\langle 110 \rangle_\gamma$ with respect to $\langle 11\bar{2}0 \rangle_{\alpha_2}$ matrix [18].

another (see Figure 3.3), γ plates have the same crystal orientations within a grain in the type III, and γ plates crystal orientations in the type I and II vary from plate to plate. The TiAl lamellae are often twinned. Yamaguchi showed that there are six possible orientation variants corresponding to the six possible orientations of $[110]$ on (111) in the gamma phase with respect to $\langle 11\bar{2}0 \rangle$ on (0001) in the α_2 phase as shown in Figure 3.4 [104-106]. TiAl/TiAl or TiAl/Ti₃Al/TiAl lamellar interfaces with the $\{111\}\langle 11\bar{2} \rangle$ true twinning relation are found with greater frequency than those with orientation relationships other than the true twinning [107]. True twinning-type lamellar interfaces are more energetically favorable than interfaces of other types during the $\alpha \rightarrow \gamma$ transformation. Domains within a gamma plate can have any of the 6 orientations. The factors controlling the lamellar structure are (1) thickness of TiAl lamellae, (2) size of domains in TiAl lamellae, (3) the volume fraction, distribution and thickness of Ti₃Al lamellae, (4) size of equiaxed gamma grains and lamellar grains, (5) the volume fraction and distribution of lamellar grains [108,109]. These factors are closely related to strength, ductility, and creep properties in TiAl with Ti-rich and near stoichiometric compositions.

By processing and heat treatment conditions various microstructures in gamma alloys can be achieved. Four types of microstructures have been classified: i) near-gamma, ii) duplex, iii) nearly lamellar, and iv) fully lamellar microstructures [110]. The near- γ structure is obtained by an annealing heat treatment at temperatures just above the eutectoid temperature (see Figure 3.1) after a hot-working process and is normally characterized by coarse gamma grains and banded regions consisting of fine γ and α_2 grains [110]. The fine duplex microstructure, which is composed of fine γ grains, fine lamellar grains and some fine α_2 particles, can be obtained through a combination of hot-

working and subsequent heat treatment at temperatures where the volume fractions of equiaxed and lamellar microstructures are roughly equal. The nearly lamellar and fully lamellar microstructures are composed of coarse lamellar grains and a small volume fraction of fine γ grains that can be obtained by heat treatment of as-cast ingots near the alpha transus [110]. A typical near gamma, duplex and fully lamellar microstructure of TiAl alloys are shown in Figure 3.5 [111,112].

In zone melting growth of crystals of TiAl with a nearly stoichiometric composition, if the crystal growth rate is appropriate, crystals consisting of a single set of lamellae can be grown [113]. These crystals are called as polysynthetically twinned crystals or PST crystals, since as-grown crystals contain numbers of thin parallel twin lamellae having only six orientations. PST crystals can be used to investigate the nature of deformation behavior in lamellar TiAl microstructures with a single lamellar orientation.

3.2.2 Dislocation Structure and Deformation Mode

As mentioned before, the ordered intermetallic compound TiAl has a face centered tetragonal structure (f.c.t.: an $L1_0$ -type superlattice). It consists of alternating titanium and aluminum (002) planes stacked normal to the c-axis as shown in Figure 3.2.a. At the stoichiometric composition, the c/a ratio is 1.02, and tetragonality increases up to 1.03 as aluminum concentration increase and decreases to 1.01 with decreasing aluminum concentration [114-116]. As indicated in the Figure 3.2.a the slip planes in gamma TiAl are the $\{111\}$ close packed planes and the possible slip directions are $\langle 110 \rangle$, $\langle 112 \rangle$ and $\langle 101 \rangle$. The nomenclature $\langle 101 \rangle$ indicates that the first two indices can be

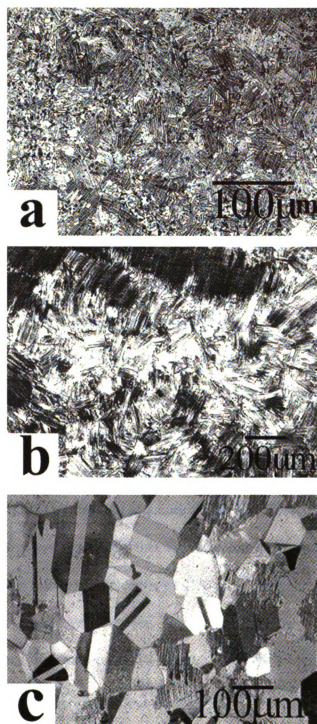
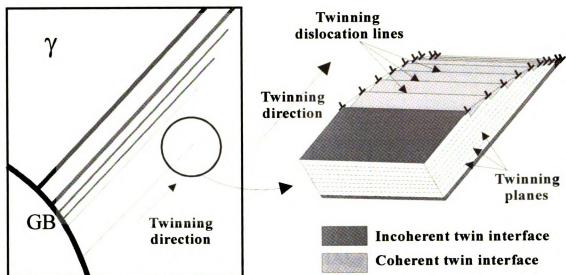


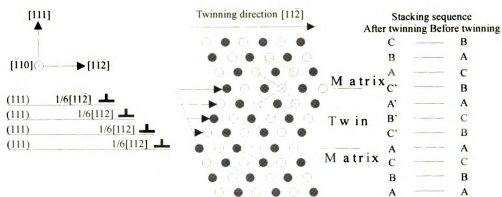
Figure 3.5. (a) duplex, (b) fully lamellar, (c) near-gamma microstructures in TiAl alloys [111,112].

reversed to get a similar crystallographic direction, but the third indice must remain in the third position. The $1/2\langle 110 \rangle$ dislocations in this slip system are called ordinary dislocations. $\langle 101 \rangle$ dislocations are superdislocations because they can be dissociated into two $1/2\langle 101 \rangle$ super-partial dislocations. $1/2\langle 112 \rangle$ dislocations are superdislocations whose Burgers vector is the second shortest of the Burgers vectors lying on $\{111\}$ planes.

Twinning is an important deformation mechanism in TiAl. Only true twinning on $\{111\}\langle 11\bar{2} \rangle$ can occur since the $L1_0$ structure is no longer preserved by twinning on $\{111\}\langle 12\bar{1} \rangle$ [117-119]. Some studies indicated that the mechanical twins nucleated at grain boundaries of triple points and propagated by emission of $1/6\langle 11\bar{2} \rangle$ partial dislocations [120-122]. Unlike normal or super dislocations, a twin leaves a stacking fault behind that is as long as the twinning dislocation has traveled as shown in Figure 3.6 [123]. Thus, the microstructure is refined by increasing the area of twin interfaces as twinning deformation proceeds. Shechtman et al. reported that TiAl_{SF} (SF: stacking faults) form at an early stage of deformation and develop into twins [124]. Since TiAl_{SF} and $\text{Ti}_3\text{Al}_{\text{SF}}$ have the equivalent stacking sequence to the Ti_3Al structure (DO_{19}) and TiAl ($L1_0$) structure, respectively, this suggests that TiAl_{SF} could act as the nucleation sites for the Ti_3Al and $\text{Ti}_3\text{Al}_{\text{SF}}$ be source of nucleation of $\text{TiAl}_{\text{matrix}}/\text{TiAl}_{\text{Twin}}$ [124-126]. This leads to the formation of the Ti_3Al layers between $\text{TiAl}_{\text{Matrix}}$ and $\text{TiAl}_{\text{Twin}}$ during deformation [125,126]. The sequence of formation of Ti_3Al layer between $\text{TiAl}_{\text{matrix}}$ and $\text{TiAl}_{\text{twin}}$ are shown schematically in Figure 3.7 [125]. These observations suggest that Ti_3Al can be formed by mechanical twinning during deformation. Jin and Seo also showed that α_2 (Ti_3Al) layers form between deformation twins after creep deformation [47,127].



(a)



(b)

Figure 3.6. The thin twin morphology near the twin tip [123].

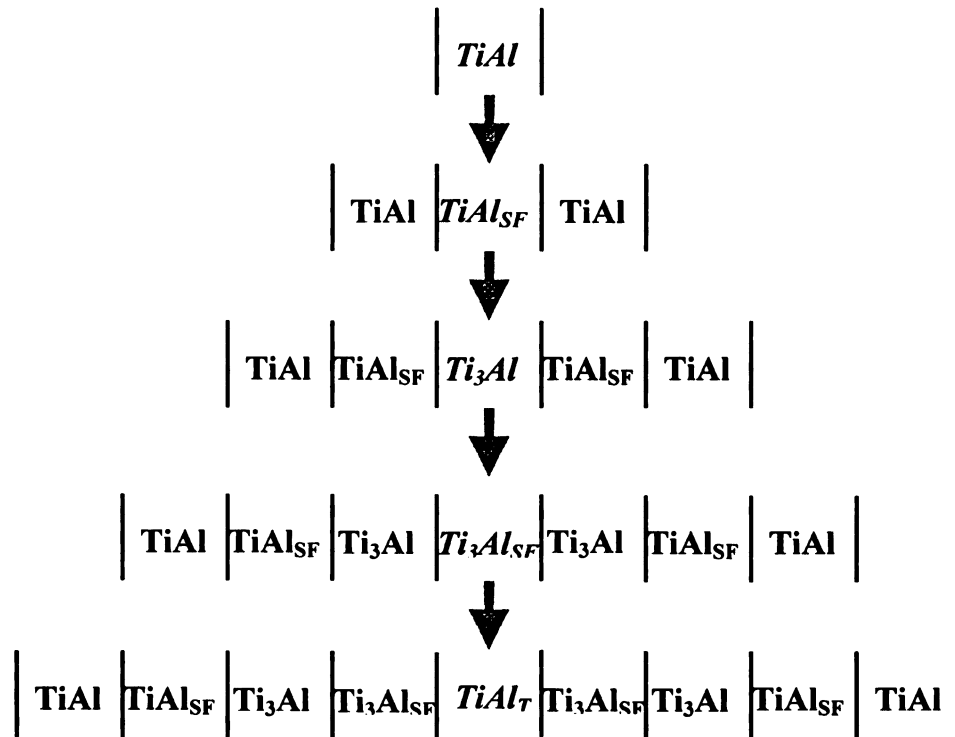


Figure 3.7. The formation sequence of TiAl_{SF} , Ti_3Al , $\text{Ti}_3\text{Al}_{\text{SF}}$ and TiAl_{T} due to high temperature deformation [125].

From several TEM studies [124,128-132], ordinary $1/2\langle 110 \rangle$ dislocations are much more active than $\langle 101 \rangle$ super dislocations up to 700 °C. The motion of many of $\langle 101 \rangle$ super dislocations has been reported to be impeded by the pinning of the trailing $1/6\langle 112 \rangle$ partial by an intrinsic pinning mechanism. The pinning of $\langle 101 \rangle$ superdislocation makes them sessile dissociations due to forming superlattice intrinsic stacking fault (SISF) and superlattice extrinsic stacking fault (SESF) which leads to formation of faulted dipoles and loops [129,130]. These dipoles and loops are commonly observed not only in Al-rich binary compounds, but also in Al-rich ternary TiAl alloys [132].

The most significant differences in deformation mode between TiAl coexisting with Ti_3Al and Al-rich TiAl, are the amount of twinning activity and the difference in mobility of $1/2\langle 110 \rangle$ dislocations. Twinning on $\{111\}\langle 11\bar{2} \rangle$ systems in Al-rich TiAl becomes the most active mode of deformation only at temperatures higher than 800 °C, while the $\{111\}\langle 11\bar{2} \rangle$ twinning is active even at room temperature in the Ti-rich two-phase compounds. Although dislocations with $1/2\langle 110 \rangle$ are observed in the single phase (Al-rich) compounds and in the two-phase compounds (Ti-rich), Vasudevan et al.[133] indicated that the increase in mobility of $1/2\langle 110 \rangle$ normal dislocations that are observed in Ti-rich TiAl arise from fewer impurities or interstitials in the γ matrix. The non-stoichiometric Ti_3Al apparently absorbs interstitials and impurities that interfere with normal dislocation motion [133], since the solubility of these elements in Ti_3Al is much larger than in TiAl. This is one reason why two phase compositions have better ductility. Thus the presence of the α_2 phase in TiAl has an important effect on deformation mechanisms.

The anomalous hardening behavior in single crystal and polycrystalline forms of single phase Al rich gamma Ti-Al alloys have been investigated by several researchers [134-140]. Three regimes are characterized by soft and hard mode deformation, and the data between (273 K~1073 K) is identified with the anomalous hardening. Both $\langle 101 \rangle$ superdislocations and $1/2\langle 110 \rangle$ ordinary dislocations exhibit anomalous hardening as well as orientation dependence. This anomalous hardening can be explained by the dissociation process and cross-slip reaction of $\langle 101 \rangle$ type superdislocations from primary slip plane onto other octahedral slip planes below 650 K (an octahedral lock mechanism), whereas between 650 K and 1073 K, cross slip occurs from the primary octahedral plane onto a cube plane [135-140]. The nature of hardening by ordinary dislocation is not understood yet. However, the pinning point and cusp formation mechanism and a local pile-up is probably due to the presence of immobile dislocations which lie in multiple slip planes as suggested by Viguier [137,138] and Whang [135].

The effect of crystal orientation on deformation mode was examined by Bieler and Seo using an analysis of the Schmid factor for $\langle 110 \rangle$ ordinary dislocations, $\langle 101 \rangle$ super dislocations, and true $\langle 112 \rangle$ twinning deformation systems as shown in Figure 3.8 [141]. In tension, orientations close to $\langle 441 \rangle$ (near tail of arrow) are likely to twin. They indicated that in the twinned orientation, the Schmid factor for ordinary dislocations is small, and only superdislocations have a high Schmid factor, so twinning increases the volume fraction of crystals where only super dislocations can operate. Luster and Morris observed that superdislocations were active only in crystals having a Schmid factor greater than 0.35, and they only nucleated from interfaces where efficient slip transfer from neighboring crystals was possible [142]. Ordinary dislocations and true twinning

were observed in grains where the Schmid factor was larger than 0.25. From these criteria indicated above, deformation in tension has only 19 vol% of a set of randomly oriented crystals with 4 Schmid factors operative, while in compression, 28 vol % have 4 systems active, as described in Figure 3.8.b.

From deformation behavior of PST crystals studied by Yamaguchi, Inui, and colleagues [143-147], yield strength and tensile elongation at the room and high temperature strongly depend on the angle ϕ , where ϕ is the angle between lamellar planes and the loading axis. When the lamellar boundaries are parallel or perpendicular to the loading axis, the yield stress is high, but it is very low for intermediate orientations as described in Figure 3.9 [147]. For parallel or perpendicular orientations, shear deformation proceeds on $\{111\}$ planes that intersect the lamellar boundaries (the hard-type of deformation). For intermediate orientations, shear deformation occurs parallel to the lamellar boundaries (easy-type of deformation) and hence large strains can be obtained. Thus the strength of TiAl with lamellar structure is thought to be related to the hard mode of deformation, i.e. shear deformation across the lamellar boundaries, and its ductility must be associated with the easy mode of deformation, i.e. shear deformation parallel to the lamellar planes. At room temperature, deformation of PST crystals occurs by $\{111\}\langle 11\bar{2}\rangle$ ordered twinning and slip on $\{111\}\langle 110\rangle$. These twinning and slip systems are still operative at high temperatures. However, the tendency for deformation twinning was found to decrease at high temperatures [144]. Few $\langle 101\rangle$ superdislocations are observed in PST crystals of TiAl deformed at room temperature, while at 800 °C $\langle 101\rangle$ super dislocations are frequently observed. This is indicative of an increased activity of $\langle 101\rangle$ slip at high temperatures. Dislocations with $1/2\langle 112\rangle$ are found in PST

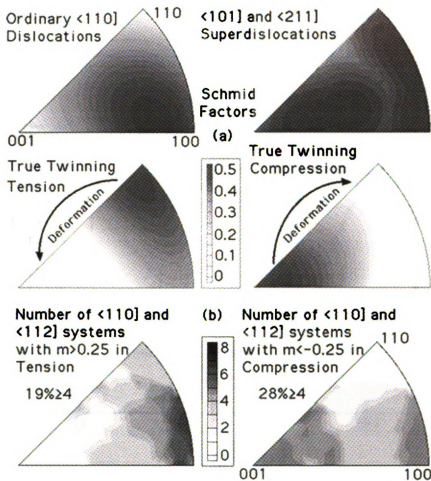


Figure 3.8. (a) The maximum Schmid factor for deformation in a given crystal direction is plotted for ordinary and super dislocations, and for true twinning, which depends on deformation mode. (b) There are no operative ordinary dislocation or true twinning systems near $\langle 001 \rangle$ for tension, and none near $\langle 110 \rangle$ for compression [141].

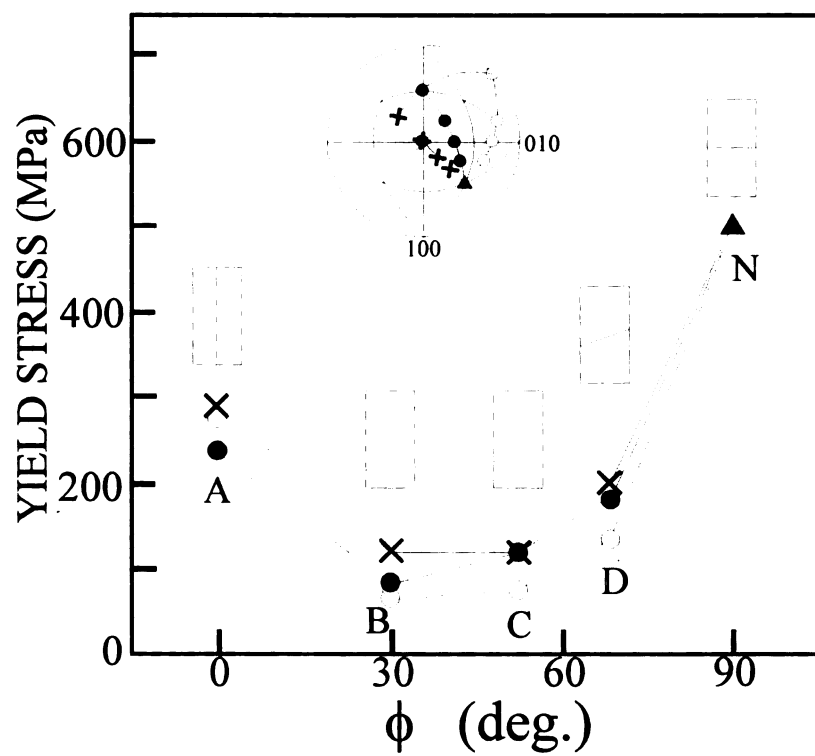


Figure 3.9. Yield stress of PST crystals as a function of angle between compression axis and the lamellar boundaries [147].

crystals deformed at room and high temperatures, however their contribution to deformation is not high even at 800 °C. The activity of all these dislocations depend highly on the orientation of given domain with respect to the stress axis [145,146,148].

From this review of deformation behavior in Al-rich, Ti-rich 2-phase, and PST crystals (lamellar structure), possible deformation systems are $1/2<110]$ ordinary dislocations, deformation twinning with $1/6<11\bar{2}]$ dislocations, $<101]$ super dislocations, and $1/2<112]$ super dislocations. The dominant deformation system strongly depends on the concentration of Al, the presence of Ti_3Al phase, service temperatures, domain orientations, stress level, and lamellar plane orientations during plastic deformation. The deformation behavior at high temperature with constant loads for a long term, that is creep deformation, is not as comprehensively explored in the literature, as the next section shows.

3.2.3 Creep Behavior in Gamma Titanium Aluminides

Creep is commonly analyzed using an empirical equation which relates the stress and creep strain rate by $\dot{\epsilon} = A\sigma^n \exp(-Q/RT)$ where A is constant depending on microstructure, Q is the activation energy of the rate limiting process, and n is the stress exponent which has particular values that are commonly associated with well described mechanisms. Creep in gamma titanium aluminides strongly depends upon microstructure and alloying compositions. From these two points of view, creep behavior in gamma titanium aluminides is reviewed based on three categories: (1) Al-rich single phase or Ti-rich near equiaxed gamma Titanium aluminides, (2) Ti-rich lamellar gamma Titanium aluminides, (3) Ti rich duplex gamma Titanium aluminides.

3.2.3.1 Al-rich single phase gamma Titanium aluminides

The creep behavior in these alloys shows different behavior under high, intermediate, and low stresses as shown in Figure 3.10 [149]. The stress exponent, $n = d \log \dot{\epsilon}_{\min} / d \log \sigma$, is the slope in Figure 3.10. For Ti-50-53Al, it changes from 3.5 to 7.5 to 4.7 with increasing σ . Creep in TiAl commonly exhibits a minimum strain rate at a strain below 5%, which is used in the empirical equation. Oikawa [150] reported that in the high stress regime (251 MPa), the activation energy for creep varies between 350-600 kJ/mole for different stress ranges, which is much larger than the 150 kJ/mole value for inter-diffusion reported by Ouchi. Lu and Hemker also reported that activation energy for creep in single phase Ti-51Al-2Mn is about 440 ± 15 kJ/mol which can be ascribed to either diffusion-related climb or the thermally activated motion of ordinary dislocations [151]. He mentioned that the fraction of grains containing twins increase with creep strain at 550 °C under an applied stress of 550 MPa.

3.2.3.2 Ti rich fully lamellar gamma Titanium aluminides

The creep behavior of forged Ti-49Al-1V-0.12O-0.07C (at%) with three different microstructures was investigated by Worth et al. [152]. Creep strain at 760-815 °C in air with a constant load of 87.5 MPa is highest in the duplex microstructure, intermediate in the near equiaxed gamma microstructure, and lowest in the fully lamellar microstructure for identical conditions. The stress exponents were found to be 3 to 5 for all microstructures, indicating that possible creep mechanism under this condition is dislocation controlled. Most creep studies on Ti-rich TiAl have been focused on the fully lamellar microstructure. Since they provide the best creep resistance as shown in Figure

3.10 [149,153,158,159,160]. Creep of fully lamellar Ti-48Al alloys was studied by J. Triantafillou et al. [153] at 760 °C in air under 240 MPa using stress increment tests. In Figure 3.10 the stress increment tests for fully lamellar structures exhibit an increasing stress exponent with increasing stress from $n=1$ at low stresses to $n=10$ at high stresses, suggesting a transition from diffusional controlled creep at low stress to dislocation climb controlled creep or power law breakdown (dislocation glide creep) at high stress. He also suggested that the reduction of lamellar spacing may be the microstructural parameter controlling dislocation creep as evidenced by the bowing of dislocations between adjacent lamellae and leading to a lower creep strain rate as indicated in Figure 3.10. In Ti-48Al-2W alloys with $\sim 330 \mu\text{m}$ lamellar grain size, a similar stress dependence on the stress exponent was found ($n=0.6-8.2$) [154]. In a ternary Ti-48Al-2Cr alloy crept at 800 °C in air under stresses of 145 to 330 MPa for 100 to 500 hours, the lamellae were deformed by twinning and dislocations which consist of tangled screw dislocations and curved ordinary dislocations, but the contribution of superdislocations appears to be marginal [155,156]. The creep deformed microstructure consisted of subgrain boundaries found in the equiaxed grains which is thought to trigger dynamic recrystallization observed at the tertiary creep stage.

The effect of grain size on creep behavior of fully lamellar Ti-48Al-2Cr-2Nb was studied using uniaxial compression tests at 850 °C with a true stress of 250 MPa [157]. The creep rate of the fully lamellar gamma TiAl alloy is independent of grain size in the region where dislocation creep is the dominant deformation mechanism. The major microstructural variable influencing the creep resistance of a fully transformed gamma

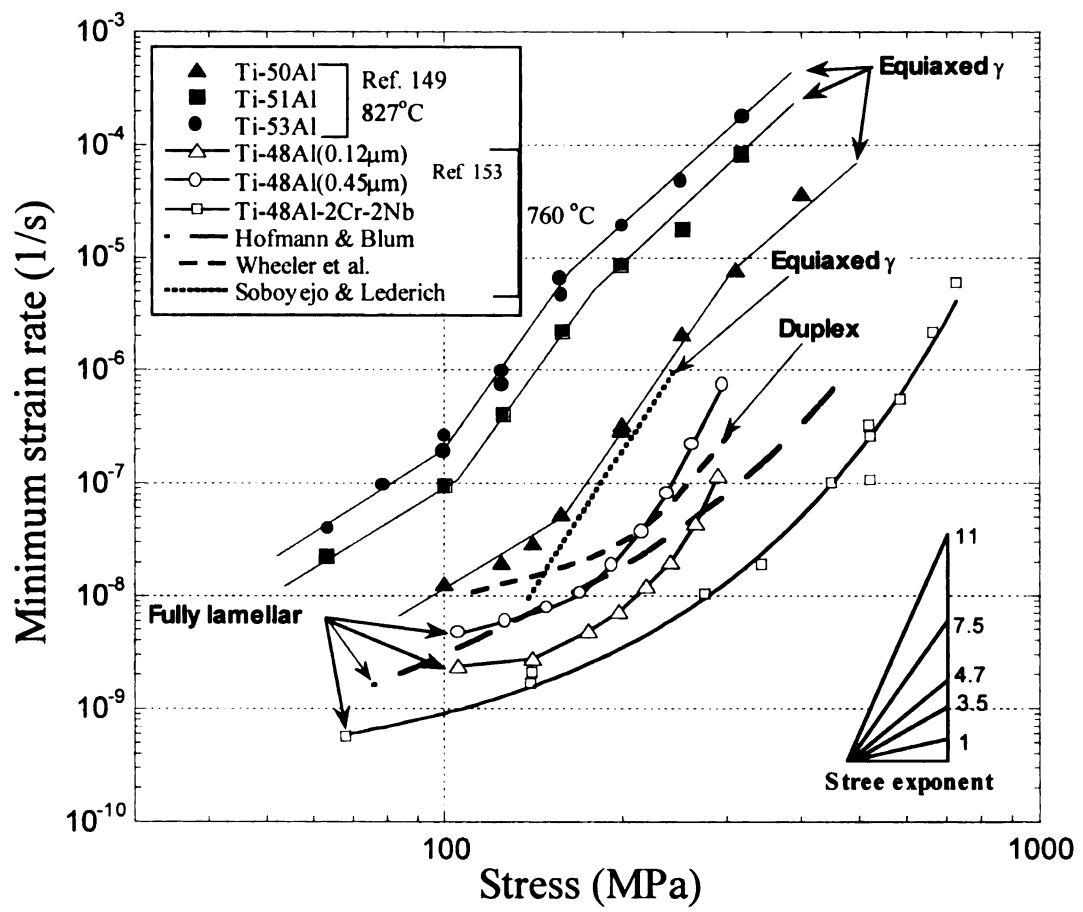


Figure 3.10. Comparison of steady state creep data of TiAl with different microstructures [149,153,158,159,160].

TiAl alloy is the α_2/γ lath spacing. Hoffmann and Blum have reported that the lamellar microstructure transforms dynamically into a globular one in many parts of the sample with softening in Ti-48Al-2Cr-2Nb at high temperatures [158].

Nieh and Wang studied creep behavior of Ti-47Al-2Cr-2Nb alloy with a fine grained fully lamellar structure at 760 °C, 140 MPa single or multiple stress increases [159,160]. For a given temperature, the higher the applied stress, the greater is the primary creep strain. Creep data from Nieh suggested that the creep of the alloy at 760 °C may be glide-controlled in the high stress region (>250 MPa) but recovery-controlled in the low stress region (<250 MPa). When deformed subsequently in the low stress region, creep would not commence for a certain period of time. This prestraining effect is believed to be related to a slow recovery process which controls the deformation in the low stress region. They suggested that that prestraining technique could be used effectively to reduce primary creep of TiAl alloys for engineering applications.

Huang and Kim [161] investigated creep in Ti-47Al-1Cr-1V-2.5Nb alloy at nominal stresses of 138, 207 and 276 MPa in air. The stress exponents range from 4.5 to 5.7. The results indicated that deformation took place in almost all cases in the gamma phase only and the α_2 plates were almost inert. A dislocation cell structure is also developed in gamma grains during deformation which led to dynamic recrystallization.

3.2.3.3 Ti rich duplex gamma Titanium aluminides

Creep in two phase gamma Titanium aluminides with duplex microstructure has not been investigated as much as in TiAl with lamellar microstructure [47,152,157,162-164], since the creep resistance of the duplex microstructure is always inferior to that of

lamellar microstructure. From the study of microstructural effects on creep in Ti-48Al-2Cr-2Nb, Ti-49Al-1V and Ti-48Al-1V-0.3C, the creep resistance with a fully lamellar structure was higher than that with a duplex microstructure [152,157,164]. This suggests that the decrease in creep resistance of the duplex structure might be due to an increase in dislocation mobility in the gamma phase.

Bieler et al. [165] showed that stress exponents in Ti-47.4Al-2.2Cr-1.9Nb are 3 in the low stress region (<200 MPa), and 8 in the high stress region (> 200 MPa). In compression+shear mode, creep in Ti-47Al-2Cr-2Nb, the stress exponent 3 at 760~774 °C and the activation energy 257 kJ/mole (in Ar) and 574 kJ/mole (in air) were found by stress and temperature change experiments. The low stress exponent and the high activation energy suggest that dynamic recrystallization occurs, and dislocation networks form, but glide is rate limiting [166].

The differences in creep behaviors between Al-rich single phase TiAl and Ti-rich two phase TiAl alloys can be easily seen in Figure 3.10. Al-rich alloys creep much faster, and well defined transitions are evident. There are two transition points in the stress exponent in Al-rich TiAl. On the contrary, in Ti-rich TiAl alloys, the stress exponent increases smoothly as stress increases until power law breakdown region is reached. Although some creep mechanisms were suggested, no systematic view in the creep mechanisms has been developed, and the role of deformation twinning has not been examined, other than in the work of Jin [47,120,121]. The creep properties of several TiAl alloys having different compositions and microstructures are summarized in Table 3.2 [138,152,154,155,158,159,161,162-164,167-189].

Table 3.2 Creep data on TiAl alloys [138,152,154,155,158,159,161,162-164,167-189].

Alloy(at%)	Microstructure/Condition	Stress (MPa)	Temp (°C)	n	Q (kJ/mole)	comment	Ref
Ti-(50~53.4mol%)Al/ compression creep	Al-rich single phase	158 ~251	677 ~827	4.5~5 8	350 ~400 600	recovery climb of dislocations and dynamic recrystallization found $\dot{\epsilon}_m$ exists	138
Ti-(34~49mol%)Al	single γ phase single α_2 phase lamellar	100 ~700	707 ~857	7.8 5.5 5.4	435 352 407	higher minimum creep rates in Single-phase Ti ₃ Al than single-phase TiAl	167
Ti-(50mol%)Al	lamellar + γ at colony boundaries	100 ~251	677 ~877	7.9	359	Better creep in homogenized and the most coarse-grained alloy	168
Ti-50.3Al/PM /hot extrusion at 1413°C+HT	lamellar + γ $d_\gamma=60\mu\text{m}$; colony=50~100 μm	103 ~241	700 ~850	4	300		169
Ti-(53.4 mol%)Al/ compression creep	equiaxed γ	80~40 0	677 ~927	8(L) 4.5(H)	600 360		170, 171
Ti-(50 mol%)Al/ compression creep	equiaxed γ $d_\gamma=32\sim 170 \mu\text{m}$	126 ~398	927	6(32 μm) ~8(170 μm)		minimum creep rate decreases with increasing grain size	172

Table 3.2 (cont'd).

Ti-51.5Al/ compression creep	equiaxed γ , $d_\gamma=22\sim40\ \mu\text{m}$	80~400	677 ~927	7.4(L σ) 4.8(H σ)	427 380		173
Ti-(50mol%)Al/ compression creep	equiaxed γ , $d_\gamma=32\sim170\ \mu\text{m}$	80 ~400	627 ~927	7.1(L s) 4.6(H s)	460 350		174
Ti-54Al/ compression creep	T>800°C no twinning T<800°C twinning no change in λ due to twin	30~200 30~200	750 900	4.6 3.7			175
Ti-49Al-1V- 0.12O-0.07C	Forged at 1107~1177°C, Duplex (DP), Equiaxed (G), Fully lamellar (FL)	87.5	760 815	3.7(DP) 3.4(G) 5.1(FL) 4.5(DP) 4.1(G) 5.2(FL)		dislocation controlled $\dot{\epsilon}_m$ was observed	152
Ti-49.5Al-2.5Nb- 1.1Mn/cast+HIP	equiaxed γ , $d_\gamma=125\ \mu\text{m}$	75~200	850 ~1377		411		176
Ti-48Al	extruded+HT (900°C/24hrs, NL) extruded+HT (1350°C/5hrs+900°C/6hrs)	105 ~241 105 ~241	768 ~815 768 ~815	4.8 (768,815°C) 4.6 (at 768°C)	278 350		177
Ti-48Al- 1Nb(0.09wt%O)	Duplex	103.4 ~241.3	704 ~850	5 (704°C) 4.9 (750°C) 4.7 (800°C) 4.46 (850°C)	317.5 (137.8MPa) ~341 (206.8MPa)		178

Table 3.2 (cont'd)

Ti-48Al-1Nb	Duplex	103.4 ~206.8	704 ~850		326.4	climb controlled existence of primary creep	162
Ti-48.4Al-1.9W	FL	172 ~300	760	0.6 (L s) 8.6 (H s)		transition of creep mechanism, power law breakdown	154
Ti-48.7Al-2.2W	P/M+extrusion+HT lamellar	172.4 ~310.3	750 ~950	5.5 (at 850°C)	750~950		169
Ti-48Al-1.5Cr	NL d=200μm	70 ~400	700 ~900	2.3~3.5 (L σ) 8.6~14 (H σ)	292 (200MPa)		179
Ti-48Al-2Cr	FL/500μm~1mm grain size surrounded by single-phase γ grains	145 ~330	800	7.6 larger than 5 for most fcc metals		subgrains boundaries, deformed by twinning, and tangled screw dislocations and curved ordinary dislocations	155, 180
Ti-48Al-2Cr/ compression creep	duplex	330	800	4.3	460		181
Ti-48Al +5 vol% TiB ₂	As-forged As-forged/HT					bulk diffusion controlled (L σ). a climb process dislocation glide with (intermediate σ). twinning (intermediate σ with high Q _c , and H σ).	182
Ti-48Al +10 vol% TiB ₂	As-forged	20 ~600	649 ~871	1 (<80MPa) 4 (80~300MPa) 7 (>300MPa)	350 (L σ) 470 (H σ)		

Table 3.2 (cont'd)

Ti-48Al-1V-0.3C	equiaxed γ , duplex, FL	150	760 ~815	4.2 for low carbon 2.5 for high carbon		creep resistance FL>equiaxed>Duplex dislocation glide	164
Ti-48Al-2Mn-2Nb	fine grained lamellar (FL)	69.4 ~310	760 ~871	4.8 (760°C) 5 (815°C) 4.5 (843°C)	335	localized shear bands within the lamellar grain interiors. void formation and dynamic recrystallization	183
Ti-48Al-2Cr-2Nb	Duplex d=25 μ m	70 ~400	700 ~900	12.5 (700°C) 7.2 (800°C) 4.7 (900°C)	513~630		179
Ti-48Al-2Cr-2Nb	Duplex HIP/1350°C/0.5hrs/ 1300°C/10hrs/GFC	103 ~300	705 ~815	3 (L) 7 (H)	300 (L) 410 (H)	Stress-assisted diffusion creep at low stresses, dislocation creep at high stresses	163
Ti-48Al-2Cr-2Nb	FL d=30~250 μ m	200 ~550	827 ~927	3~6 for 100~550 MPa		the transformation of the fully lamellar structure into the globular structure by dynamic recrystallization	158
Ti-48Al-2Cr-2Nb	ingot+HIPed+homogenize d+extruded-stress rupture	105 ~550	540 ~870		320		184
Ti-48Al-1.5Cr- (0.26~0.65)Si	FL	200	800	6.4 (Si free) 8 (0.26Si) 10.3 (0.65Si)		ppt Ti ₅ Si ₃ type: retard the slow dislocation motion	185

Table 3.2 (cont'd)

Ti-47Al/ Compression creep	Spray-formed FL, d=60 μ m	180 ~320	780 ~850	4.3	342 (300MPa)		186
Ti-47Al	P/M equiaxed d=4 μ m	34~138	600 ~900	1.9	340 \pm 31		187
Ti-47Al +6 vol% TiB ₂	I/M equiaxed d=8~18 μ m	34~138	600 ~900	3~3.5	340 \pm 31		
Ti-47Al +7vol% (TiB ₂ +Ti ₂ AlN)	as extruded	138~ 276	760	2.4 (760°C)	480		188
Ti-47Al-2Cr-2Nb	Nearly fully lamellar	140, 138 ~655	760	7 (H s) 1.6(L s)		climb controlled (<250 MPa) glide control (>250 MPa)	159
Ti-47Al-1Cr-1V- 2.5Nb	FL	138, 207, 276	900	5.8			161
Ti-46Al- 2V+6.6vol%TiB ₂	extruded+1200°C/16hrs +1000°C/5hrs	69~241	760 ~840	1.9(760°C) ~3.5	330	exhibit a very small primary creep strain	188
Ti-43Al/ Compression strain rate change test	equiaxed d=5 μ m, superplastic	35~400	1000 ~1100	2 (L s) 4 (H s)	380~390	slip controlled by lattice diffusion	189

3.2.4 Precipitates and Alloying Additions

The alloying effects observed in gamma alloys are described in Table 3.3 [190]. The most important alloying elements for creep deformation are Al, Si, W, Ta, B, C, and O. With less Al, more α_2 phase is produced, which results in poorer creep resistance [40]. The formation of silicides by the addition of Si in Ti-47Al-1Cr-1Mn-1.5Nb-0.2 alloys led to high creep strength [191]. In Ti-48Al-1V containing C, the creep resistance is higher in the high carbon alloy than those of the low carbon alloys, and the influence of carbon on creep is pronounced in the equiaxed and duplex microstructures [164]. The addition of W and B refined the microstructure and reduced the defects such as low angle grain boundaries, misoriented and kinked lamellae which is related to thermal instability prior to aging [192]. In general, the precipitates act as barriers to dislocation gliding as well as dislocation rearrangement. The interface between the matrix and precipitates act as sinks or sources for vacancies.

3.2.5 Primary creep behavior in TiAl

The primary creep deformation may be defined as a transient deformation and an alloy hardening period before reaching the minimum creep rate. Compared with secondary (or minimum) or tertiary creep studies in TiAl, few studies concerning primary creep behavior in TiAl alloy have been conducted. Here are some results of primary creep behavior from the past investigations [47,152,155,164,193,194,195]: Seo and Bieler et al. reported that transition point of creep curve (indicated by an arrow) was observed at the very early stage of primary creep (~0.25% strain) with different stress and temperature conditions as shown in Figure 3.11 [195]. Hsiung and Nieh [193] investigated the

Table 3.3 Alloying effects in gamma TiAl alloys [190]

Elements	Reported effects
Al	It strongly affects ductility by changing the microstructure. Best ductility occurs in the range of 46-50 at%
B	Add >0.5 at% refines grain size, and improve strength and workability.
C	Carbon-doping increases creep resistance and reduces ductility
Cr	Add 1-3 at% increases the ductility of duplex alloys Add >2 at% enhances the workability and superplasticity Add >8 at% greatly improves the oxidation resistance
Er	Changes the deformation substructures and increase the ductility of single-phase gamma
Fe	Increases fluidity, but also the susceptibility to hot cracking
Mn	Add 1-3 at% increases the ductility of duplex alloys
Mo	Improves the ductility and strength of a fine-grained material Improves the oxidation resistance
Ni	Increases fluidity
Nb	Improves greatly the oxidation resistance and creep resistance slightly
P	Improves oxidation resistance
Si	Add 0.5-1 at% improves the creep and oxidation resistance Improves fluidity, but reduces the susceptibility to hot cracking
Ta	Improves the creep and oxidation resistance Increases the susceptibility to hot cracking
V	Add 1-3 at% increases the ductility of duplex alloys and reduces the oxidation resistance
W	Greatly improves the oxidation resistance Improves the creep resistance
O	stabilize α phase

deformation structure of crept Ti-47Al-2Cr-2Nb alloy at 760 °C using stresses of 138 and 518 MPa. The deformed structure from a stress of 138 MPa shows dislocations in soft lamellar grains at interfaces and in {111} slip planes. On the other hand, the deformed structure from a stress of 518 MPa includes mechanical twins and dense boundary dislocations in both soft and hard grains. It appears that both twins and boundary dislocations are barrier to the moving dislocations. Es Souni et al. [155] reported subgrain boundaries in equiaxed gamma grains in Ti-48Al-2Cr deformed at 800 °C, 145 MPa to a strain of 0.05, which supports the climb-controlled model. Worth et al. [65,77] also reported that the dislocations in the lamellar layers were pinned by the lamellar boundaries in the Ti-49Al-1V alloy deformed at 815 °C, 87.5 MPa to a strain of 0.04. Jin [47,194] showed that very fine mechanical twins in equiaxed grains triple points and subboundaries in equiaxed and lamellar grains were observed in Ti-47.4Al-2.2Cr-1.9Nb alloy deformed to a strain close to the end of primary creep, and that a possible deformation mechanism is low temperature dislocation climb controlled creep.

The primary creep process in gamma titanium aluminides is not well understood. The possible creep mechanisms suggested by various authors include recovery controlled, climb controlled, stress-assisted diffusional creep mechanism at low stresses, and glide-controlled plus twinning and dislocation creep mechanisms at high stresses. The role of deformation twinning in primary or secondary creep behavior is still not well described.

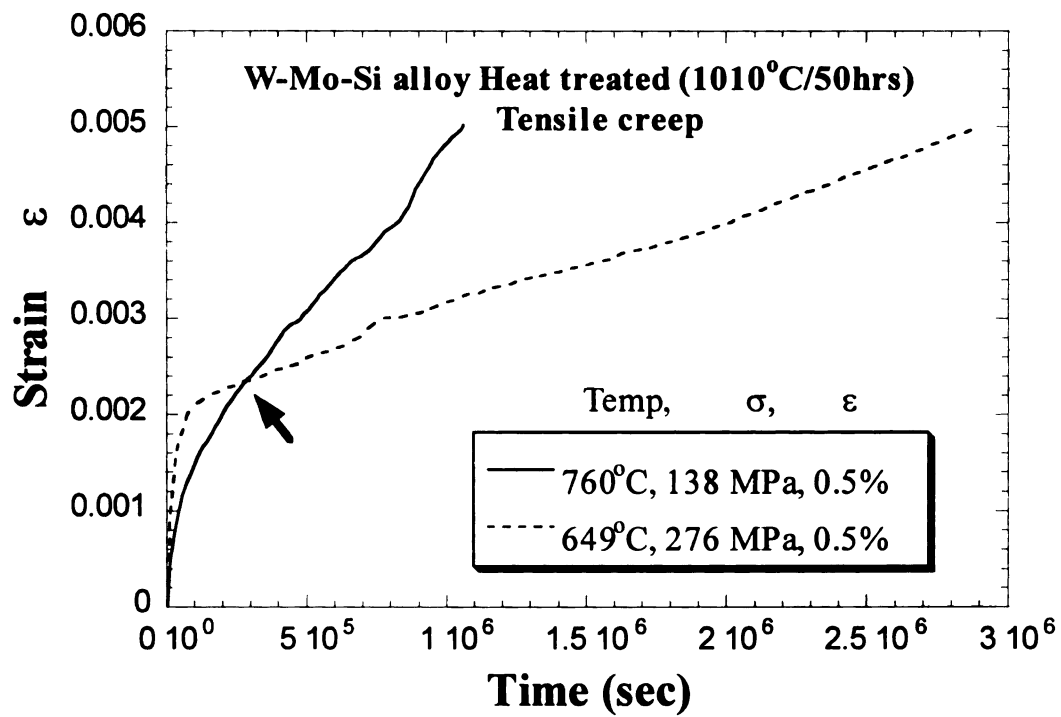


Figure 3.11. Primary creep curve of TiAl alloys [195].

CHAPTER 4

EXPERIMENTAL PROCEDURE

4.1 COMPRESSION AND TENSION CREEP TESTS

Creep tests of polycrystalline TiAl (Ti-47Al-2Nb-1Mn-0.5W-0.5Mo-0.2Si) alloys and polysynthetically twinned (PST) crystals were conducted on an ATS series 2710 creep test machine with a PC based data acquisition system. All tensile creep tests were conducted in the creep laboratory at Howmet Research Corporation, Whitehall, MI.

4.1.1 Compression creep test (ATS creep tester)

The ATS system is designed to perform either creep testing (constant load) or stress relaxation testing (constant strain). The machine has a lever arm ratio of 20:1 to provide a high load capacity and loading rate. As shown in Figure 4.1, the creep machine consists of three main control systems, which are the creep frame control system, the furnace control system, and the data acquisition system. A load signal and displacements from two transducers, A and B, are conditioned in the ATS control system. Temperatures can be adjusted by controlling three heating zones through the furnace control system. Data are collected from the automated data acquisition system consisting of a computer and data acquisition board (DAB).

The creep frame controller unit, which was made by ATS and Electronics Instrument Research Corp. (EIR), allows automatic or manual control mode for constant load or stress creep test. The three furnace heating zones are controlled by a furnace

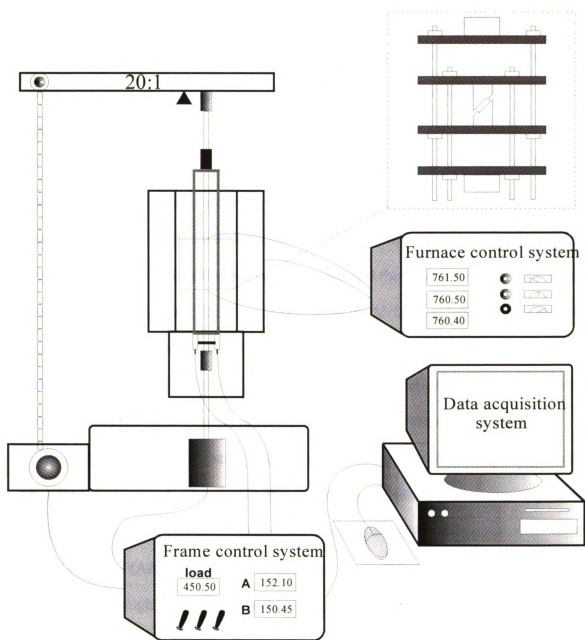


Figure 4.1 The diagram of ATS creep tester with data acquisition system.

control unit (LFE model 2010). The furnace is designed to reach a maximum temperature of 1200 °C and the temperature gradient between top and bottom of the chamber can be controlled by adjusting the three heat zones. K-type thermocouples were used for temperature measurement, and the temperatures are displayed on the panel of the furnace control unit. The one analog output channel from the unit is monitored by the data acquisition system.

The strain is measured by linear variable capacitance transducers (LVCT) which perform precise and stable specimen gaging. A small change in displacements in the transducer causes a change in capacitance. Two LVCTs were connected to the specially designed extensometer for compression creep tests, and they directly measure the change in length during creep test. The measurement from the LVCT and load cell are input into the control unit and show on a display panel. The analog outputs of strain and load transfer to the data acquisition system through the control unit, and are limited on -10~+10 V and the initial position of LVCT is adjusted to be within this limit.

The data acquisition system consists of a PC computer and a National Instruments AT-MIO-16L-25 board. This is a high-performance multifunction analog, digital and timing I/O board for a PC. Five analog input channels are scanned to monitor the values of displacements (A&B), temperatures of the top and bottom of the specimen, and loads are recorded through the data acquisition program developed by Wu [196]. A sampling rate for the testing is 5000 pts/sec for 5 channels, i.e. 1000 pts/sec-channel. The noise effect caused by fluctuations of loading or other noise is smoothed by two levels of averaging, first by averaging 1000 points acquired in a second, and then about 20 such points are averaged, and the datum point is kept if it differs from the datum that was most

recently kept. The details of hardware and software in this system are explained in reference [197].

4.1.2 Tension creep test [198]

Every tension creep test was conducted at the Howmet Corporation, Whitehall, MI. In 1995, Howmet installed a creep test system with a closed-loop control system for one of its highest volume activities, creep-and-stress-rupture testing. An example of data from Howmet is shown in Figure 4.2. The closed-loop system includes an IBM-Pentium-compatible host computer and an OPTO G4LC32SX Mystic Model 200 local computer to control and monitor all facets of the testing process. Both units are configured to allow interaction with the operator. The local computer controls multiple test stands, and is linked to individual stands by G4 brick I/O data-acquisition interfaces.

To eliminate the risk of losing data because of a local computer failure, the host computer backs up all test data at present intervals. The main windows from the host computer displays real time data for all 96 test stands supported by the system. The local computers are connected to all of the extensometer inputs from the creep test stands, and temperatures inputs. The local computers are also linked to end-of-test inputs, weight raising relays, and temperature controllers. The host and local systems exchange data through RS 422 communication lines.

The creep testers are designed to permit experiments at temperatures ranging from 540 to 1100°C (1000 to 2000°F), and stresses ranging from 100 to 1030 MPa (15 to 150 ksi). Resistance-heated tube or split furnaces are used to ease loading and unloading of the specimens. Two thermocouples are connected to the top and bottom of the specimens

Test Number: **T2 08426** **2** **HOWMET CORPORATION**
Creep / Stress Rupture Report
 Heat Number: **TI-AL**
 ThermoCouple Batch Number: **081497**
 Plant Number: **T2**
 Machine Number: **15** Setup Time: **09:14:27 10/12/1997**
 Test Temperature (F): **1208** Test Start Time: **10:29:32 10/12/1997**
 Stress Level (KSI): **40** Test Stop Time: **19:00:00 11/10/1997**
 Machine Load (LBS): **79.3**
 Adj. Gauge Length (in): **1.811**
 Technician: **CJM**
 Initial Width (in): **0.8008**
 Initial Thickness (in): **0.8008**
 Initial Bar Diameter (in): **0.2018** Final Bar Diameter (in): **0.2018**
 Original Length (in): **1.784** Final Length (in): **1.704**
 Loading Plastic Creep (%): **0.31**
 Total Loading Creep (%): **0.32**
 Creep At 20 hours (%): **0.11**
 Creep At 23 hours (%): **0.12**
 Creep At 36 hours (%): **0.13**
 Creep At 60 hours (%): **0.15**
 Time At 100 hours (%): **0.17**
 Time to 0.1% Creep (hrs): **12.0**
 Time to 0.2% Creep (hrs): **130.8**
 Time to 0.5% Creep (hrs): **n/a**
 Time to 1.0% Creep (hrs): **n/a**
 Time to 2.0% Creep (hrs): **n/a**
 Reduction of Area (%): **0.0**
 Elongation (%): **0.0**
 Final Actual Creep (%): **0.42**
 Time to Failure (hrs): **896.5**
 Suffix **DF** Material Term ☐ Terms ☐ ☐ ☐
 Upload Number 1 2 3 4 5 6 7 8 9
 Stress (KSI) 40.0
 Load (LBS) 79.3
 Start Hours 0.0
 End Hours 896.5
 Life At Stress (Hours) 896.5

All creep percentages are corrected by dividing their displacements by their Adjusted Gauge Length per ASTM E-139 section 18.2.3

HOWMET CORPORATION

Test Number: **T2-08426** **2** Stress: **40 KSI** Temp: **1208 F**

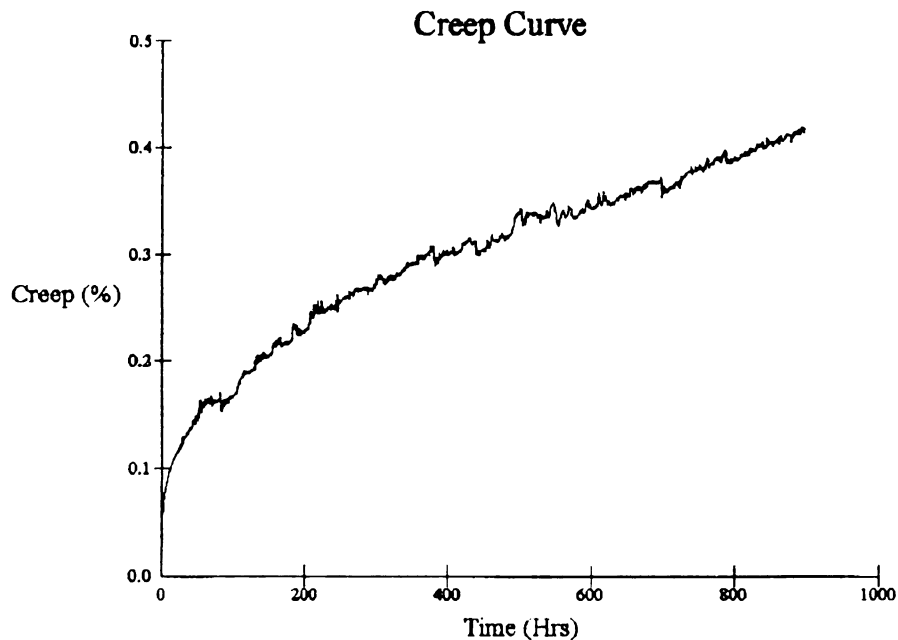


Figure 4.2 Creep testing involves holding test specimens at constant load and temperature until some specific experimental parameter is met.

to monitor the test temperature. Extensometers are used to measure the strain (or creep), and measurements are collected and recorded every 15 minutes after the applied load is reached

4.2 THE CREEP CURVE FITTING

In order to predict a long term creep behavior from short term creep data, some constitutive equations are used, such as the power law equation which relates $\dot{\epsilon}_s$ (steady state strain rate) to stress and temperature by the power law relationship and polynomial expressions which have proposed by Conway [199]. However, in the power law equation different values of n and Q are observed as the test conditions are varied, and it is difficult to interpret the polynomial coefficients in terms of physical meaning in the polynomial equations. Evans and Wilshire have proposed the θ -projection concept, which can not only accurately describe the shape of the creep curve but it also has some relation to the physical meaning of creep deformation [200].

4.2.1 The θ projection concept

Based on the micromodelling of the dislocation processes occurring at high temperatures in primary and secondary stages, the following constitutive equation is described as

$$\epsilon = \epsilon_i + \theta_1 \{1 - \exp(-\theta_2 t)\} + \dot{\epsilon}_s t \quad (1)$$

where ϵ_i is the initial strain upon loading, and the second and third terms describe

primary and secondary creep stages, respectively [200]. $\dot{\epsilon}_s$ is the secondary (or minimum) creep rate, and the parameters θ_1 and θ_2 are determined by curve fitting.

Differentiation then shows that the creep rate decays as

$$\dot{\epsilon} = \theta_1 \theta_2 \exp(-\theta_2 t) + \dot{\epsilon}_s \quad (2)$$

And the primary creep rate can be rearranged as

$$\dot{\epsilon}_p = \theta_1 \theta_2 \exp(-\theta_2 t) = \theta_2 (\theta_1 - \epsilon_p) \text{ where } \dot{\epsilon}_p = (\dot{\epsilon} - \dot{\epsilon}_s). \quad (3)$$

Equation (3) indicates that the primary creep rate ($\dot{\epsilon}_p$) decays linearly with increasing primary creep strain (ϵ_p) under the rate constant given by the parameter. θ_2 . θ_1 is a parameter of the strain-like quantity, and θ_2 is a rate parameter as shown in Figure 4.3.a [201]. From Equation (1), a creep curve is described as a continuously decaying creep curve, i.e. a curve characterized by a creep rate which decreases gradually until a steady state creep rate is eventually attained ($\dot{\epsilon}_s$) at very long times as the primary strain approaches θ_1 .

In a similar way it is possible to define a tertiary strain ϵ_T as $\epsilon - \epsilon_p$ where

$$\epsilon_T = \epsilon - \epsilon_p = \theta_3 \{ \exp(\theta_4 t) - 1 \} \quad (4)$$

and by differentiating equation (4), the tertiary creep strain rate is given by

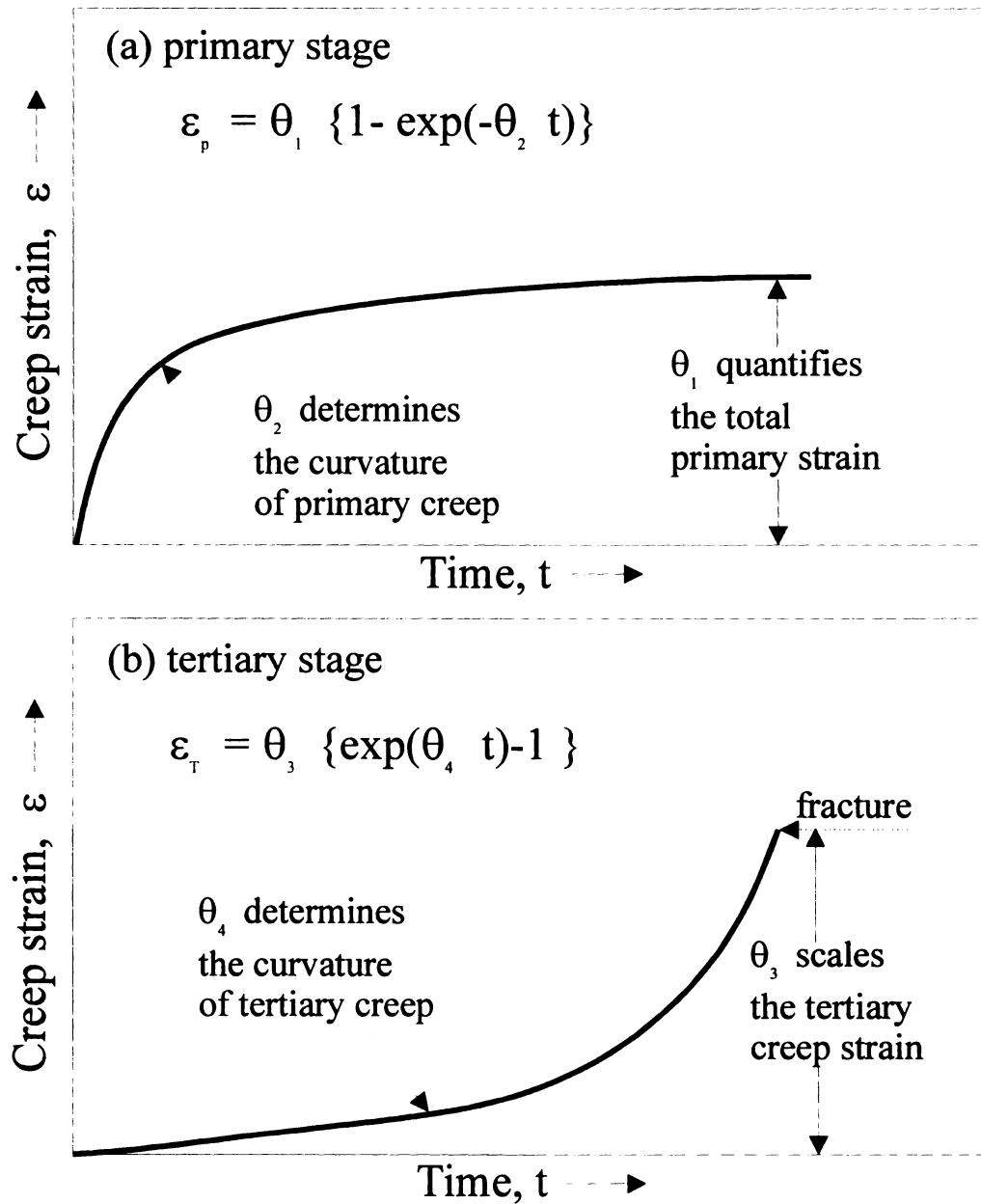


Figure 4.3 The θ -projection concept envisages normal creep curves in terms of a decaying primary component (ε_p) and an accelerating tertiary component (ε_T) [201].

$$\dot{\varepsilon}_T = \theta_3 \theta_4 \exp(\theta_4 t) = \theta_4 (\theta_3 + \varepsilon_T) \quad (5)$$

The tertiary creep rate ($\dot{\varepsilon}_T$) increases nearly linearly with increasing creep strain (ε_T) indicating that the tertiary stage also obeys first-order reaction-rate kinetics, with θ_4 being the rate constant. The meanings of the tertiary parameters θ_3 and θ_4 are also indicated in Figure 4.3.b [201].

All of the creep curve including primary and tertiary stages can be described by the following equation [199],

$$\varepsilon = \varepsilon_i + \theta_1 \{1 - \exp(-\theta_2 t)\} + \theta_3 \{\exp(\theta_4 t) - 1\} \quad (6)$$

where θ_1 and θ_3 define the strain magnitude with respect to time, and θ_2 and θ_4 describe the curvatures of primary and tertiary stages of creep, respectively. The second term in this equation represents the strain hardening term that dominates in primary creep, and the third term describes the strain weakening term that dominates in tertiary creep. The secondary stage is explained on the basis of a balance between the competing processes of strain hardening and strain weakening. It agrees qualitatively with theoretical interpretation of creep deformation by dislocation motion. However, since the secondary stage is only a transition between primary and tertiary creep processes, a true steady state creep rate can not be estimated by this equation.

4.2.2 Modification of θ -projection concept

The accurate measurement of initial strain, ε_i , is not easy even when high-precision test methods are used. It is because ε_i is determined by calculating only the

difference in strain immediately before loading and immediately after loading. Therefore, Maruyama *et al.* [202,203] presented the same equation as the θ -projection concept in order to get a better interpretation but with the variables having a different meaning.

$$\varepsilon = \varepsilon_0 + A\{1 - \exp(-\alpha t)\} + B\{\exp(\beta t) - 1\} \quad (7)$$

ε_0 is an adjustable parameter instead of initial strain in the original θ -projection model. A, α , B and β are the parameters for curve fitting. α represents the rate constant of the strain hardening process and β represents the rate constant of strain weakening process. Maruyama and Oikawa [203] have also proposed a modified and simplified equation of the form,

$$\varepsilon = \varepsilon_0 + A\{1 - \exp(-\alpha t)\} + B\{\exp(\alpha t) - 1\} \quad (8)$$

and ε_0 , A, B and α are parameters to be determined by the regression analysis. It has only one rate constant α instead of the two rate constants in equation (7). Actually, equation (7) having two rate constants, α and β , may be more suitable for all materials due to the complicated mechanisms during creep deformation. Microstructural changes often lead to changes in the rate-controlling mechanism during the creep process.

4.2.3 Modification for this analysis

For the experiments described here, only the primary and secondary stage of TiAl creep deformation have been considered, but especially the primary stage creep. The

tertiary stage creep and rupture life are beyond the scope of this research. The primary creep tests under shear+compression and tensile modes were conducted to examine primary creep behavior in detail. The initial elastic and plastic strain components were not recorded, since zero time represents the time when the creep load is reached. Therefore, only the second term of equation (1) as the constitutive equation was used for analyzing creep curves of the primary stage by using a modified mathematical model in the form of

$$\varepsilon_{primary\ creep} = e(1 - \exp(-rt)) \quad (13)$$

which describes a process with a rate constant r that slows exponentially with time to reach a saturation strain of e . Most of the experiments showed a transition in the downward curvature that suggested a change in the dominant deformation mechanism. If the transition in deformation phenomena results from two process that slow down exponentially at different rates, where one saturates earlier than the other, then these two process may be independent and therefore additive, and thus represented by

$$\varepsilon_{primary\ creep} = e_1(1 - \exp(-r_1t)) + e_2(1 - \exp(-r_2t)) \quad (14)$$

This equation was used as a fitting function using *KaleidaGraphTM* software to represent the experimental data in a form that can be easily differentiated. The parameters for e_1 and r_1 were determined for the experiments deformed at a given stress and temperature to the lowest strains, and these parameters were used as initial values in the least square fitting process for the larger strain experiments.

In stress and temperature change experiments for polycrystalline and PST TiAl alloys, another modified equation from equation (1) was used to account for various starting times for a particular deformation condition following a stress or temperature change [204]. The modified equation for transient creep after stress and temperature increase is

$$\varepsilon = \varepsilon_0 + A\{1 - \exp(-\alpha(t - t_0))\} + \dot{\varepsilon}_s(t - t_0) \quad (15)$$

where ε_0 is an adjustable reference strain parameter, t_0 is the starting time for a particular loading condition. $\dot{\varepsilon}_s$ is the steady state (or minimum) strain rate, A and α are curve fitting parameters. In the case of transient creep after stress and temperature decrease, the constitutive equation is

$$\varepsilon = \varepsilon_0 + B \exp(-\beta(t - t_0)) + \dot{\varepsilon}_s(t - t_0) \quad (16)$$

Differentiating equations (15) and (16),

$$\dot{\varepsilon} = A\alpha \exp(-\alpha(t - t_0)) + \dot{\varepsilon}_s \quad \text{for positive temperature or stress changes} \quad (17)$$

and

$$\dot{\varepsilon} = -B\beta \exp(-\beta(t - t_0)) + \dot{\varepsilon}_s \quad \text{for negative temperature or stress changes} \quad (18)$$

Equation (17) implies that the creep rate during the primary stage decreases gradually towards a “steady state” value, $\dot{\varepsilon}_s$, with times greater than t_0 , and equation (18) indicates a gradual increase in creep rate towards a “steady state value”.

4.3 MEASUREMENT OF LAMELLAR SPACING

Scanning electron microscopy (SEM) and Transmission electron microscopy (TEM) were used for measuring lamellar spacing in TiAl alloys before and after deformation. In the SEM (25 kv accelerating voltage, 9mm working distance), the backscattered electron technique was used for imaging in order to measure the α_2 lamellar spacing as shown in Figure 4.4.a. The γ thickness and α_2 thickness were measured by using the dark field method in the TEM (by tilting the foil to so that a $\langle 110 \rangle$ direction in a lamellar plane was parallel to the electron beam). For example, after α_2 laths were indentified by using the diffraction spots diffracted from α_2 under the Dark field mode, these α_2 were sketched on the Lab notebook. Then bright field images were taken at the beam direction very close to the $\langle 110 \rangle$ as indicated in Figure 4.4.b and the α_2 can be marked on the micrograph for the measurement. A ruler was put across the micrograph perpendicular to the lath boundaries as shown in Figure 4.4. The distance from one α_2 lath to the next α_2 lath is denoted as α_2 spacing, and the distance from one γ interface to the next γ interface or α_2 lath is called as the γ interface spacing. The average values of α_2 spacing measured in SEM before and after creep deformation were computed from 250-500 α_2 spacing counts in more than 20 lamellar regions. The average values of γ interface and α_2 thickness before and after creep deformation were computed from at least 100 γ interfaces, and about 50 α_2 laths in about 6 different regions near grain boundaries. The α_2 measurements are upper bounds of the actual spacing, since the lamellar plane normal direction was not determined to make the parallax correction needed to determine the actual α_2 spacing. Despite this systematic error, however, this method provided a way to compare α_2 spacing in specimens with similar microstructures.

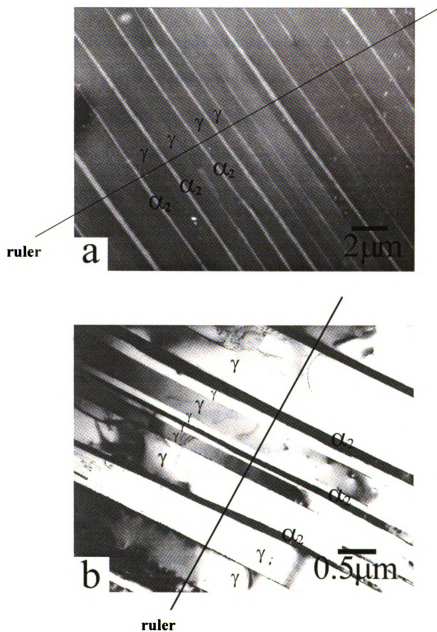


Figure 4.4 Measurement of lamellar spacing in (a) backscattered electron image in scanning electron microscopy (SEM) mode and (b) bright field image in transmission electron microscopy (TEM) mode.

After these measurements, distribution curves of lamellar spacing were plotted with the same bin sizes using *KaleidaGraph*TM software.

4.4 A Statistical Analysis of Measured Changes in Lamellar Spacing

In this section, a statistical analysis of the raw data from the measurement of α_2 spacing and γ thickness is examined using data shown in Figures 8.16.c and 10.9.b. These two figures show the smallest changes in lamellar spacing, so if these can be shown to be statistically reliable, then all other plots are also statistically reliable. These data are used to illustrate how variations in statistical presentation affect the perception of the lamellar spacing distribution. Also, an analysis of the average spacing is presented. The statistical analysis was conducted using MINITABTM software.

As shown in Figure 4.5, a different number of bins results in a different distribution curves for lamellar spacing. Figure 4.5.b shows that using a line curve is a better way to present the lamellar spacing distribution than a histogram, since relative differences in area under the curve for different bin sizes make changes easy to see. Thus all other plots use the line type presentation. Using a larger number of bins causes a bimodal type of lamellar spacing to be presented as shown in Figure 4.5.c. Although different bin sizes show different distribution curves, the higher frequency in the smaller bin size and the lower frequency in larger bin size after deformation is evident regardless of the number of bins. This indicates that more finer lamellar spacings are formed after deformation. The difference of average lamellar spacing before and after deformation is about 0.15 μm (see also Figure 8.16.c). There is a 95% chance that the change in the average value was between 0.1 and 0.2 mm from a confidence interval computation.

In Figure 4.6, the natural logarithm of every lamellar spacing was taken and plotted in a similar way. Depending on the number of bins, different distribution curves before and after deformation can be seen in Figure 4.6.a. Similar to Figure 4.5.c, a bimodal type of distribution curve with the log scale can be obtained with a higher number of bins.

From the comparison of two probability plots in Figure 4.7, both normal and log normal descriptions of this distribution provide a linear relationship, but the normal distribution plot has more outlying data at small spacings. In the log-normal plot, the reduction of lamellar spacing after deformation can be seen by a translation of the deformed distribution (marked by gray lines in Figure 4.7.b) to the left, indicating a systematic shift to smaller thicknesses. Except at very low spacings, the 95% confidence levels do not overlap, indicating that the shift in lamellar spacing is statistically certain.

In one case of change in γ thickness, there is 4% reduction of lamellar spacing after deformation (see Figure 10.9). As with the α_2 distribution, a different number of bins affects the appearance of the distribution, but a shift toward finer spacings is apparent in all three variations in Figure 4.8. In Figure 4.8.c, a bimodal type distribution can be seen in a γ thickness with a larger number of bins, which is similar to the effect in the α_2 spacing distribution. In the normal probability plot in Figure 4.9.a for γ thickness distribution, there is no linear relationship. The same data obey a linear relationship in the lognormal probability plot (see Figure 4.9.b). The γ thickness distributions using the natural logarithm of the γ thickness is plotted in Figure 4.10, and there is no obvious difference in the distribution before and after deformation

The 95% confidence interval for the average values of the undeformed and deformed 47-2-2 γ thickness included zero, indicating that a change in the lamellar spacing for this specimen is statistically insignificant. However, no other specimen showed such a small change in lamellar spacing. The distribution data presented in every chapter is reliable, since the reduction of lamellar spacing after deformation was similar to or greater than the example analyzed for the 18% in α_2 spacing. This statistical analysis shows that the data are better described using a log-normal distribution.

The plots shown in chapters (6-11) use a linear scale and a rather small number of bins, but the above analysis shows that the trends that are apparent in these plots are statistically reliable.

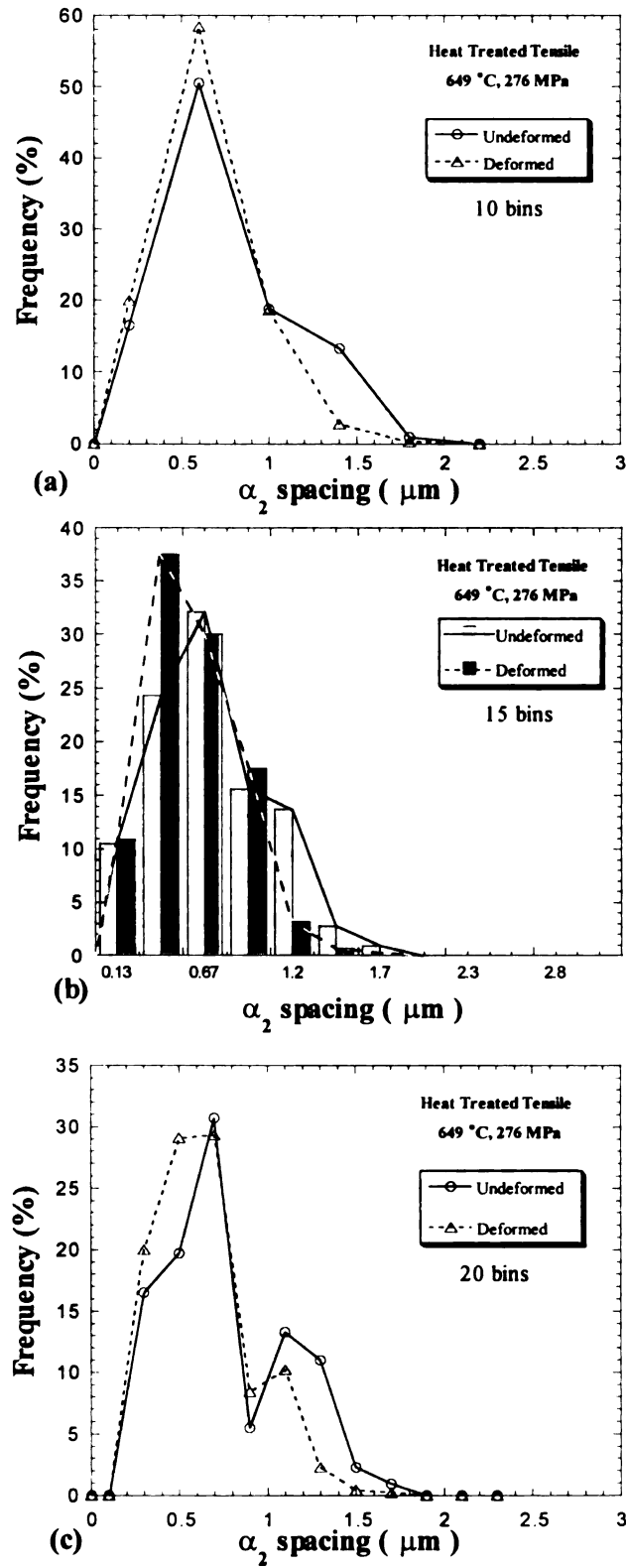


Figure 4.5 Frequency of α_2 spacing with different number of bins (a) 10 bins, (b) 15 bins, (c) 20 bins in W-Mo-Si alloys.

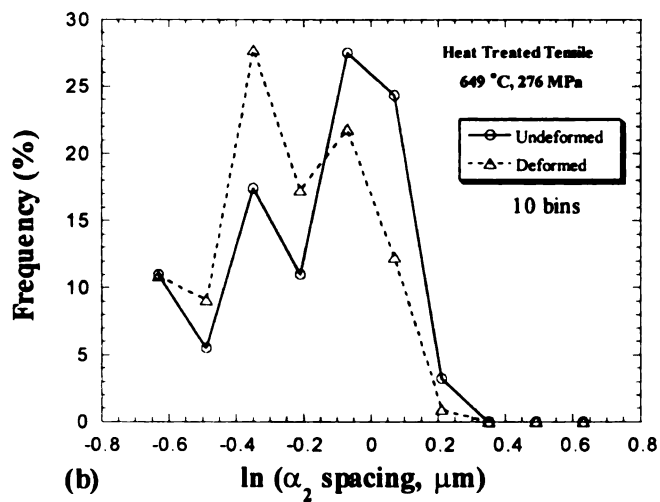
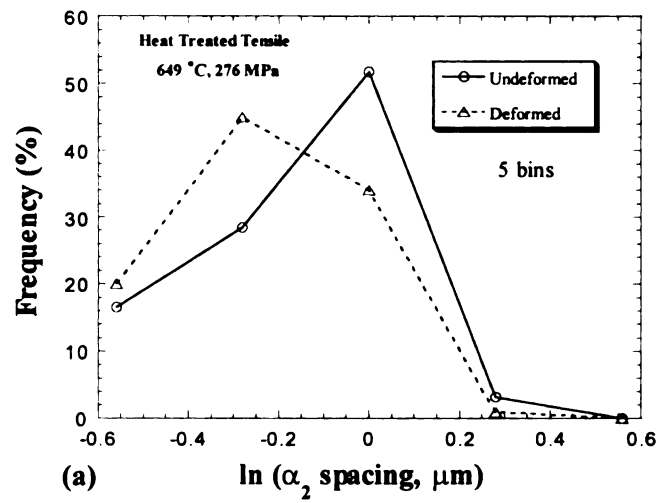
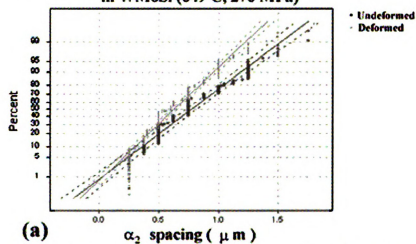


Figure 4.6 Frequency of α_2 spacing with different number of bins (a) 5 bins, (b) 10 bins for the natural logarithm scale in W-Mo-Si alloys.

**normal probability plot for undeformed & deformed
in WMoSi (649°C, 276 MPa)**



**lognormal probability plot for undeformed & deformed
in WMoSi (649°C, 276 MPa)**

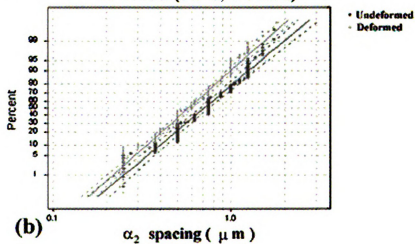


Figure 4.7 Normal and log-normal probability plots of W-Mo-Si alloy for undeformed and deformed cases.

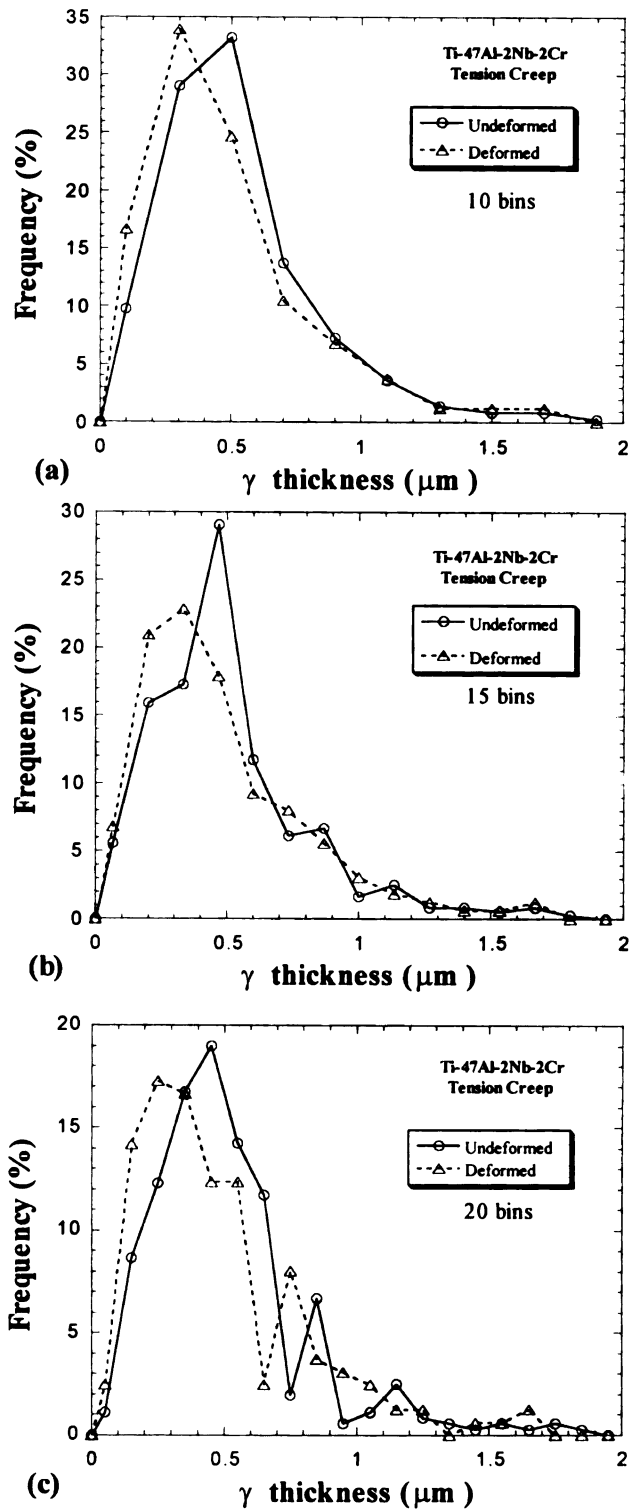


Figure 4.8 Frequency of γ thickness with different number of bins (a) 10 bins, (b) 15 bins, (c) 20 bins in Ti-47Al-2Nb-2Cr.

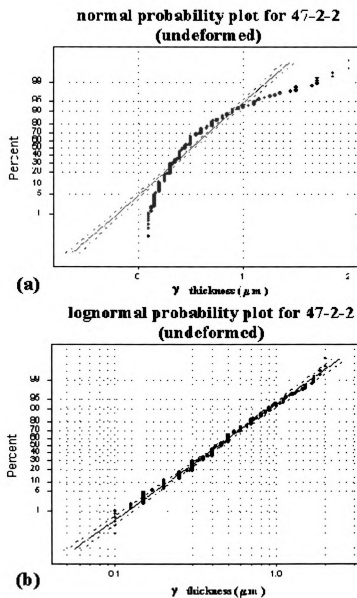


Figure 4.9 Normal and log-normal probability plots of Ti-47Al-2Nb-2Cr alloy for undeformed case.

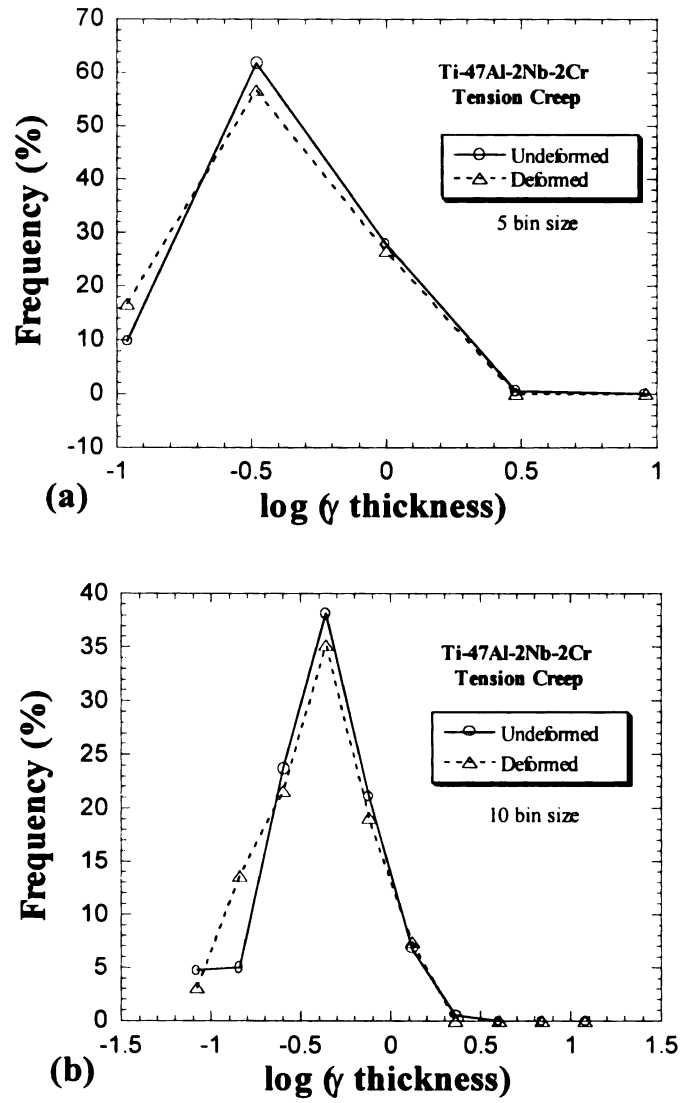


Figure 4.10 Frequency of γ thickness with different number of bins (a) 5 bins, (b) 10 bins for the natural logarithm scale in Ti-47Al-2Nb-2Cr alloy.

CHAPTER 5

OVERVIEW OF RESEARCH

In this chapter, an overview of the research results from chapter 6 to 12 is presented. Gamma TiAl based alloy has been developed for high temperature structural applications, since it has low density, low coefficient of thermal expansion (CTE), high thermal conductivity, high specific strength and stiffness at elevated temperature, and high resistance to oxidation and creep [94,95].

Yamaguchi, Inui, and colleagues [143-147] show orientation dependence (the angle ϕ between lamellar planes and the loading axis) of yield strength and tensile elongation at room and high temperature in PST crystals. For deformation parallel or perpendicular to lamellar planes, shear deformation proceeds on $\{111\}$ planes that intersect the lamellar boundaries (the hard-type of deformation that causes a high yield stress). At intermediate orientations, shear deformation occurs parallel to the lamellar boundaries (easy-type of deformation that causes a low yield stress) and hence large strains can be obtained for intermediate orientations (see Figure 3.9). Twinning is an important deformation mechanism in TiAl. Some studies reported that TiAl stacking faults form at an early stage of deformation and develop into twins during deformation [124]. TiAl stacking faults could act as the nucleation sites for formation of the Ti_3Al and Ti_3Al stacking faults are sources of nucleation of $TiAl_{matrix}/TiAl_{Twin}$ [124-126]. These observations suggest that Ti_3Al can be formed by a process similar to mechanical twinning during deformation.

Luster and Moris suggest that deformation modes are restricted to twinning or dislocation motion parallel to the lamellar interface in lamellae thinner than about 0.5 μm , and superdislocation is nucleated from interfaces when efficient slip transfer from neighboring crystals was possible [142].

The differences in creep behaviors between Al-rich single phase TiAl and Ti-rich two phase TiAl alloys can be easily seen in Figure 3.10. Al-rich alloys creep much faster, and well defined transitions are evident. There are two transition points in the stress exponent in Al-rich TiAl (n changes from 3.5 to 7.5 to 4.7 with increasing σ) [149]. On the contrary, the stress exponent increases smoothly as stress increases until power law breakdown region is reached in Ti-rich TiAl alloys [153]. Most of the studies in creep have focused on minimum creep rate conditions or stress-rupture properties. However, primary creep property is important for practical applications. Only limited research has been accomplished concerning deformation behavior in the early stage of creep on TiAl and there are still many mysteries regarding the creep mechanisms of TiAl. Thus, the goals of this research are to investigate the relationship between microstructure and primary creep mechanisms in TiAl alloys having different compositions. By comparing creep in PST crystals with different orientations and polycrystals in similar test conditions, the contribution of deformation in lamellar microstructures to the creep mechanism on duplex materials can be examined. The primary creep mechanisms in duplex TiAl alloys can be rationalized by analysis of experimental observations.

For the research, several investment cast TiAl alloys (Ti-45Al-2Nb-2Mn+0.8TiB₂ XDTM, Ti-47Al-2Nb-2Mn+0.8TiB₂ XDTM, Ti-47Al-2Nb-2Mn+0.8TiB₂ XDTM with different amounts of interstitial elements (oxygen and carbon), Ti-47Al-2Cr-2Nb and Ti-

47Al-2Nb-1Mn-0.5W-0.5Mo-0.2Si alloy) have been developed and tested at Howmet Corporation. All cast investment TiAl alloys were HIPed at 1260 °C/172 MPa for 4 hours, and then several kinds of heat treatments were applied. Conventional tensile and compression+shear creep tests were conducted at various temperatures, stress, and strain conditions. For study of deformation in lamellar microstructure, PST crystals with different orientations were creep deformed with stress and temperature changes creep. The creep behavior of these alloys and the influence of heat treatment are summarized, and details of these studies are found in chapter 6-12.

Ti-45Al-2Nb-2Mn-0.8TiB₂ did not show much difference in primary creep resistance after various heat treatments because no difference in the microstructures was caused by heat treatment. The creep resistance was poor, due to very fine microstructures and large angular α_2 grains (see Figure 6.4). Some limited improvement in the Ti-47Al-2Nb-2Mn-0.8TiB₂ alloy with low O was obtained with heat treatment. The lamellar volume fraction was about 25%, and this correlated with a smaller decrease in creep rate upon loading. Having 40% lamellar grains (see Figures 7.3 and 7.4), and less angular α_2 grains in The Ti-47Al-2Nb-2Mn-0.8TiB₂ alloy with high O resulted in better creep resistance than low and medium O alloys. The heat treatments (especially the two step HT) significantly improved the creep resistance of the Ti-47Al-2Nb-2Cr alloy. This heat treatment led to the smallest volume fraction (18%) of lamellar grains, a homogeneous microstructure, the least amount of pockets of small equiaxed grains, large equiaxed grains, and precipitation of some small particles (see Figures 6.7 and 6.9), all of which correlated with better primary creep resistance, in this alloy, and similar effects were observed in other alloys, too. Texture analysis indicates that the desirable texture to

minimize mechanical twinning is to have crystals oriented with the tensile axis near 001 and away from 441 (see Figure 6.11). This texture is strengthened with heat treatment and it may contribute to the excellent creep resistance obtained from the two-step heat treatment. Ti-47Al-2Nb-1Mn-0.5W-0.5Mo-0.2Si alloys show the best creep resistance (~300 hrs to 0.5% creep strain) due to presence of precipitates (see Figures 8.12. b and c). The precipitates (including Ti_5Si_3 , but also precipitates rich in Mo and W atoms) were nucleated by heat treatment, and they grow with the assistance of strain or transformation of α_2 to γ . The precipitates vary in size from 0.05 to 2 μm , and larger precipitates are found in the equiaxed regions. The nucleation and growth of these precipitates interferes with dislocation motion, and they harden the microstructure. This precipitation hardening mechanism accounts for much of the excellent creep resistance of this alloy when it was heat-treated. Similar to W-Mo-Si alloys, the primary creep resistance of investment cast Ti-47Al-2Nb-2Mn-0.8TiB₂ was improved by the addition of some limited amount of carbon. Fine precipitates ranging from 0.08 μm to 0.2 μm are observed preferentially in α_2 layers of lamellar laths, in equiaxed α_2 grains, and near grain boundaries of equiaxed grains and in lamellae (see Figure 11.5). The precipitates can be a barrier to moving dislocations during high temperature deformation, and their presence in α_2 may impede slip transfer through the α_2 phase. The addition of carbon in this alloy results in a grain size refinement, and the lamellar volume fraction is reduced from 70% to 30% by adding more than 0.065 wt% C (see Figures 11.1 and 11.2). In 0.110 wt% C alloys, thick layers of α_2 are observed, which are similar to angular α_2 grains that correlate with degraded creep resistance, compared to the 0.065 wt% C alloy (see Figure 11.3).

Two kinds of creep tests (tensile and compression+shear) were conducted, and they show similar creep curves in different loading condition at the early stage of creep. An empirical equation was used in a curve fitting process to characterize the data in a convenient functional form, as follows [200,204].

$$\varepsilon = e_1(1 - \exp(-r_1 t)) + e_2(1 - \exp(-r_2 t)) \text{ (tensile creep)}$$

$$\varepsilon = \varepsilon_0 + A\{1 - \exp(-\alpha(t - t_0))\} + \dot{\varepsilon}_s(t - t_0) \text{ (for stress and temperature increase)}$$

$$\varepsilon = \varepsilon_0 + B \exp(-\beta(t - t_0)) + \dot{\varepsilon}_s(t - t_0) \text{ (for stress and temperature decrease)}$$

Creep strain rate vs. strain was obtained by differentiating the curve fit equations (see Figures 8.3, 8.4, 8.5, 9.2, 9.3, 10.2, and 11.10). All creep tests show a 2-step primary creep process. The transition points or saturation points (where the first and faster deformation process is exhausted) can be seen in any strain rate vs. strain plot of creep data. The strains at the transition point depend on the temperature and stress. A higher stress at the same temperature or a higher temperature with same stress cause the saturation strain to shift toward smaller strain. The transition strain and strain rate at the transition strain also depend on composition and microstructure features such as lamellar volume fraction and deformation twinning (see Figures 11.10, 11.12, and 11.14).

The α_2 spacing and γ thickness (>200 and 100 measurements for α_2 and γ , respectively) were measured from more than 20 and 6 different regions near grain boundaries, respectively, before and after deformation. As shown in distribution plots (see Figures 7.5, 8.16, 8.18, 9.6, 10.9, and 11.8), there is a shift of the frequency distribution toward higher frequencies at lower spacing values due to small creep strains

in every case. For example, the average α_2 spacing in 0.065 wt% C changed from 1.17 to 0.84 μm due to a small creep strain of 0.42% (see Figure 11.8). This reduction of α_2 spacing can be explained indirectly by easy mode deformation twinning parallel to lamellar boundaries or/and strain assisted transformation to α_2 that occurs by a process similar to mechanical twinning. The average α_2 spacing is plotted with respect to effective strain and stress in Figure 8.18.b. There is about 23% reduction in the α_2 lamellar spacing with strain that saturates at effective strains between 0.2 and 0.5%, whereafter the spacing remains relatively constant, or increases slightly. More refinement of lamellar spacing occurs at lower temperature and higher stress (the amount of refinement at 750 °C is about half of the amount that occurred at 650 °C). For example, The amount of refinement at 650 °C increases with increasing stresses (Figure 5.1). The refinement process at the early stage of creep results in rapid drop of creep rate, because refinement of lamellar spacing will reduce the probability of dislocation motion on $\{111\}$ planes not parallel to the lamellar interface [142].

As shown in Figure 3.8 [141], in tension, orientations close to $\langle 441 \rangle$ (near tail of arrow) are likely to twin. This figure indicates that in the twinned orientation, the Schmid factor for ordinary dislocations is small, and only superdislocations have a high Schmid factor, so twinning increases the volume fraction of hard orientations where only super dislocations can operate. Therefore, twinning can orientational hardening in addition to hardening that results from refinement.

The relationship between the initial strain rate, the strain rate at the transition point, and minimum strain rate and lamellar volume fraction is shown in Figure 11.12. All of these creep strain-rates decrease linearly as the volume fraction of lamellar grains

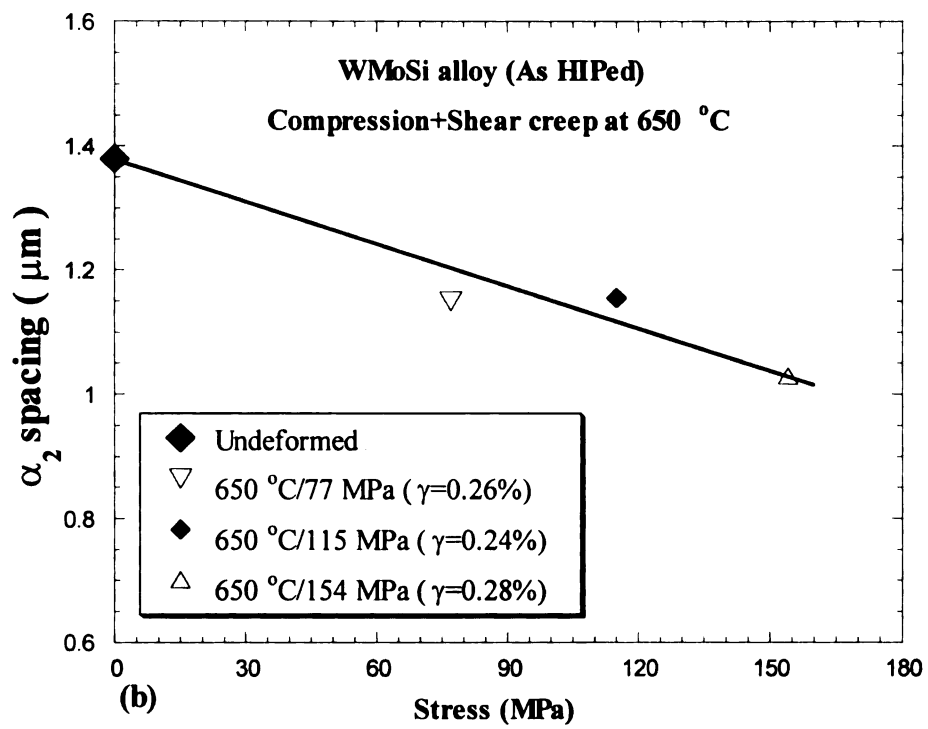


Figure 5.1 The α_2 spacing decreases with respect to increasing stress at similar strains at 650 °C [205].

increases. As shown in Figure 5.2, more lamellar spacing refinement occurs with a higher volume fraction of lamellar grains and with lower temperature and higher stress. Figure 5.3 shows how the strain rate at the transition between the early and later processes (when the early process is exhausted) correlates closely with the volume fraction of lamellar grains [62]. The best primary creep resistance occurs when the transition occurs at a lower strain rate. This set of studies shows that microstructural variance has a large impact on primary creep resistance, but that the lamellar refinement process occurs similarly in all microstructural variations. Thus a higher volume fraction of lamellar grains is beneficial for creep resistance because a larger volume fraction of lamellar interfaces will block overall dislocation motion during deformation.

From the investigation of PST crystals with different orientations ($\langle 110 \rangle$ and $\langle 112 \rangle$), the orientation dependence of the activation energy for creep and the stress exponent was examined. The activation energy was near 135 kJ/mol, when shear deformation occurred in the $\langle 110 \rangle$ direction and it was higher, near 185 kJ/mol for the $\langle 112 \rangle$ direction. These values are about half of the 290 kJ/mol activation energy measured for Ti diffusion, so mechanisms dependent on pipe diffusion or grain boundary diffusion are plausible. Furthermore, the amount of primary creep strain was several times larger in the $\langle 112 \rangle$ direction than in the $\langle 110 \rangle$ direction (see Figure 9.4.a), and this greater amount of strain occurred at a much lower stress. The stress exponent of $n=5.3$ at higher shear stress regions (see Figure 9.4.b) in both directions suggest that viscous dislocation glide ($n=3$) controlled by pipe diffusion ($n=2$) in this microstructure and lamellar orientation. Similar to the lamellar refinement in TiAl alloys, refinement of lamellar spacing of 13 and 23 % reduction during a strain of 0-1.4 % creep was also

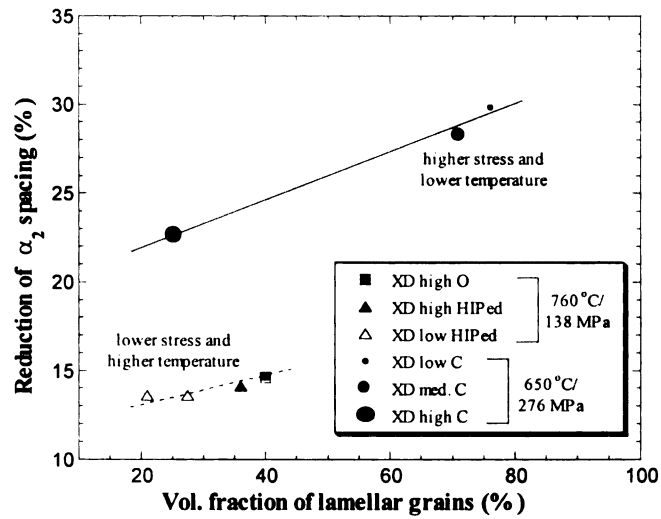


Figure 5.2 The amount of lamellar refinement (% reduction of α_2 spacing) increases with the volume fraction of lamellar grains.

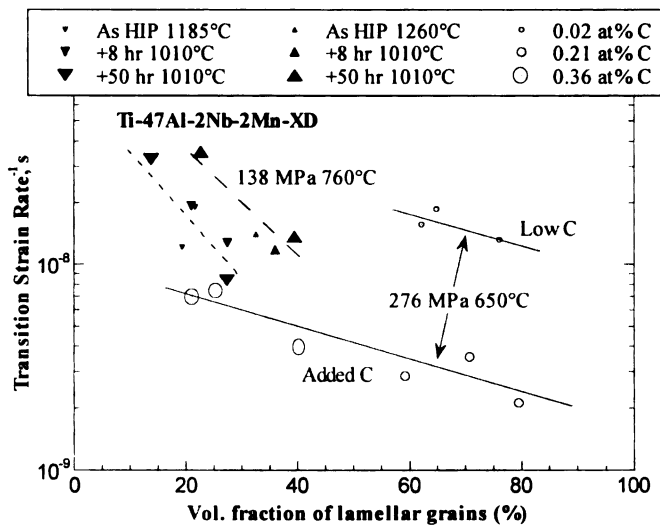


Figure 5.3 Higher lamellar fraction retards the strain rate at the transition between the early and later creep processes [62].

observed. The reduction of lamellar spacing contributes to strain in the early primary stage, and it also hardens the crystal. Near 1.38% shear strain, hard mode deformation (cross twinning) was activated in some lamellar laths (see Figure 9.5).

Some specimens of as-HIPed W-Mo-Si were deformed in the same manner as the PST crystals, but with monotonic loading histories (see Figure 8.2). The lamellar spacing was measured in the polycrystals as a function of strain. A strong correlation between exhaustion of the early primary creep process and the exhaustion of lamellar refinement is evident in Figure 5.4 (note that the strain scales for the creep rate and lamellar spacing are the same). In comparing activation energies of the early process in primary creep experiments in the W-Mo-Si alloy with creep in the soft orientation in a PST crystal ($Q_c=140$ and $137\sim185$ kJ/mole in the W-Mo-Si, and PST crystals, respectively), the activation energies are similar, near 150 kJ/mol (see Figure 8.5). The second process has an activation energy close to 300 kJ/mol that is similar to values observed in minimum creep conditions [206]. This suggests that early mechanism at the primary creep in polycrystals is correlated with creep kinetics of easy deformation in PST crystals that causes lamellar refinement.

The lamellar refinement process has been simulated to determine how much twinning or shear transformation contributed to the reduction of lamellar spacing after deformation. The thickest lamellae are subdivided in a manner that changes the frequency distribution to match the deformed distribution by assuming that strain induced α_2 shear transformations with a thickness of $0.2\ \mu\text{m}$ occur. When several variation of the detailed deformation histories are considered, the resulting deformed distribution, and the resulting local strains in the lamellar microstructure are computed. As shown in Figure

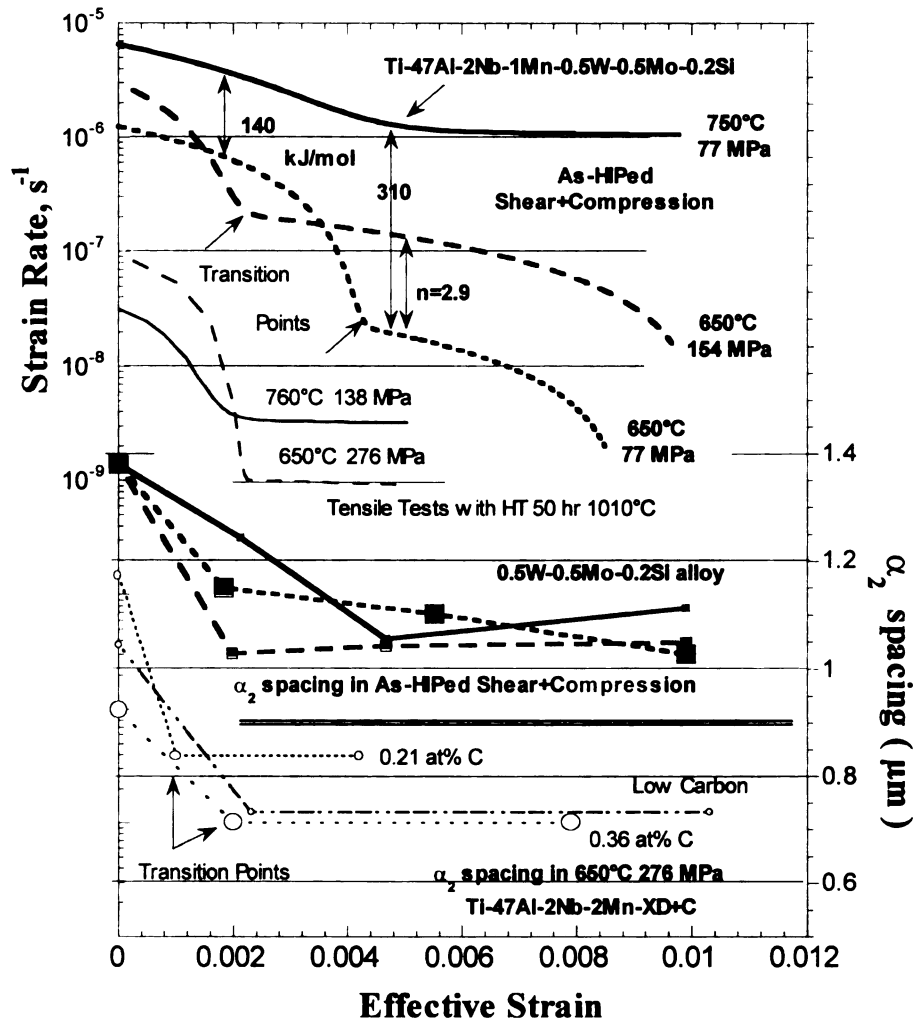


Figure 5.4 Comparison of lamellar refinement history with primary creep rate shows that the early process operates by lamellar refinement, whereas the later process does not alter the lamellar spacing appreciably with known transition strain in the XD+C alloy [62].

12.1, the simulated lamellar spacing distribution was quite close to the actual spacing distribution from the measurements. The computed local strains (0.7%) in lamellar microstructure were higher than the specimen (0.5%). There is a correlation between the computed local shear strain and the lamellar volume fraction, creep strains, and strain at transition points in most TiAl alloys. Higher lamellar volume fraction results in a lower calculated shear strain, which leads to more lamellar refinement and then lower creep strain.

From this research, primary creep properties depend on the composition, heat treatment, and microstructural features such as lamellar volume fraction, lamellar spacing, grain size, and the presence of precipitates. There are two stages between the transition point in primary creep, such as early and later stage, where creep rate is dropped rapidly, and slow down, respectively. There is a strong correlation between exhaustion of the early primary creep process and the exhaustion of lamellar refinement due to mechanical twinning parallel or/and α_2 shear transformation to lamellar planes (easy mode deformation). The early stage deformation in TiAl alloys correlates closely with PST crystals creep in easy mode deformation. There are some correlations between the local shear strain in lamellar microstructures with primary creep behavior, such as resulting from lamellar refinement are about 30% larger than the measured global strains, indicating that lamellar microstructures are softer than the equiaxed grains during the early stage of primary creep.

CHAPTER 6

THE CORRELATION OF PRIMARY CREEP RESISTANCE TO THE HEAT TREATMENTS AND MICROSTRUCTURES IN INVESTMENT CAST Ti-Al GAMMA ALLOYS

ABSTRACT

Cast gamma titanium aluminides are gaining acceptance as replacements for superalloy and steel components in aerospace, automotive and industrial applications. Components cast from these alloys can operate at temperatures up to 815 °C at half the weight of the components they replace. Most applications of cast gamma components require good creep resistance to meet component life requirements. Four heat treatments were developed and applied to investment cast Ti-45Al-2Nb-2Mn+0.8v%TiB₂ XDTM, Ti-47Al-2Nb-2Mn+0.8v%TiB₂ XDTM, and Ti-47Al-2Nb-2Cr alloys in an effort to enhance creep properties with a decrease in heat treatment time compared to current methods. Results show that the creep resistance of Ti-47Al-2Nb-2Cr alloys can be significantly altered, up to 3 times, through heat treatment. Some improvement was obtained in Ti-47Al-2Nb-2Mn+0.8v%TiB₂ XDTM and heat treatment had no effect on Ti-45Al-2Nb-2Mn+0.8v%TiB₂ XDTM alloy. The variation or lack of variation, in creep resistance with heat treatment can be explained by differences observed in the microstructures and textures produced by the various heat treatments.

6.1 INTRODUCTION

Gamma titanium aluminide can be heat treated to obtain four types of

microstructures [110]. The best creep resistance has been observed in fully lamellar microstructures, but the duplex microstructure provides desirable room temperature ductility [92,161]. The effect of alloying elements such as Cr, Nb, V, Mn, W, Mo, and Si on the properties of two phase Ti-Al alloys has been investigated [143,188,207-210]. Most of this research has focused on minimum creep rate conditions or stress-rupture properties. However, the primary creep resistance is important for practical applications. Gamma based TiAl exhibits primary creep strains that are typical for metals, where the minimum creep rate is reached after about 1% strain. In an effort to decrease the creep rate during primary creep deformation, additions of W, Mo, and Si have increased the time to reach 0.5% strain due to a dynamic precipitation process [211,212]. In related studies, observations of lamellar refinement were made that suggest that primary creep consists of a significant amount of mechanical twinning that occurs as an easy mode of deformation that hardens the microstructure at low strains [50,165,212,213]. In this chapter, the primary creep resistance (time to 0.5% creep strain) was analyzed in three two phase TiAl alloys that do not rely on the refractory elements for primary creep resistance. The nature of primary creep strain in these materials is explored in terms of microstructural changes that arise from different heat treatments. Two alloys containing TiB₂ particulate produced by the XDTM process and a third alloy without TiB₂ are compared.

6.2 MATERIALS AND EXPERIMENTAL PROCEDURE

Three investment cast gamma TiAl alloys, such as Ti-45~47Al-2Nb-2Mn-0.8TiB₂ (0.8 TiB₂ refers to volume fraction) and Ti-47Al-2Nb-2Cr, were cast. All cast materials

were then hot isostatically pressed (HIPed) at 1260 °C for 4 hours at 172 MPa (2300 °F, 25 ksi) in order to eliminate casting porosity. The heat treatments used were in the $\alpha_2+\gamma$ phase field at 900 or 1010 °C (1650 or 1850 °F) for 10 or 20 hours, and these alloys were cooled under the static argon atmosphere (SAC). A two step heat treatment was also used consisting of 1177 °C (in the $\alpha+\gamma$ phase field) for 5 hours and then in the $\alpha_2+\gamma$ field for 10 hours at 1010 °C (2150 and 1850 °F), respectively, and cooled in static argon. These heat treatments are illustrated on the phase diagram in Figure 6.1 [96,97]. The phase boundaries are not accurate for the quaternary alloys of this study. The specimens were subjected to room temperature tensile tests and creep tests at 760 °C, 138 MPa (1400 °F, 20 ksi). The creep specimens were cooled under load once 0.5 % strain was reached.

For optical and SEM analysis, deformed samples were obtained from the gage section of the creep deformed specimens. Some undeformed samples were also cut from the grip section of tensile test specimens. The samples were mounted, mechanically polished, and etched in Kroll's reagent (2ml HF, 6 ml HNO₃, and 92 ml H₂O). For TEM investigation, 0.7 mm thick slices were cut such that the sample normal was parallel to the tensile axis. 3mm diameter discs were cut from the slices using an electrodischarge machining (EDM) and ground to about 0.1 mm thick. The disks were thinned using a twin jet electropolishing system with a 10% sulfuric acid and methanol solution at -25°C and 20 volts. These foils were examined in a Hitachi H-800 transmission electron microscope operated at 200kV. For SEM analysis, a Cam Scan 44FE SEM was used at 25kV to obtain backscattered electron images that show phase contrast. Texture measurements were made on selected specimens and analysis was made using the popLA software [214].

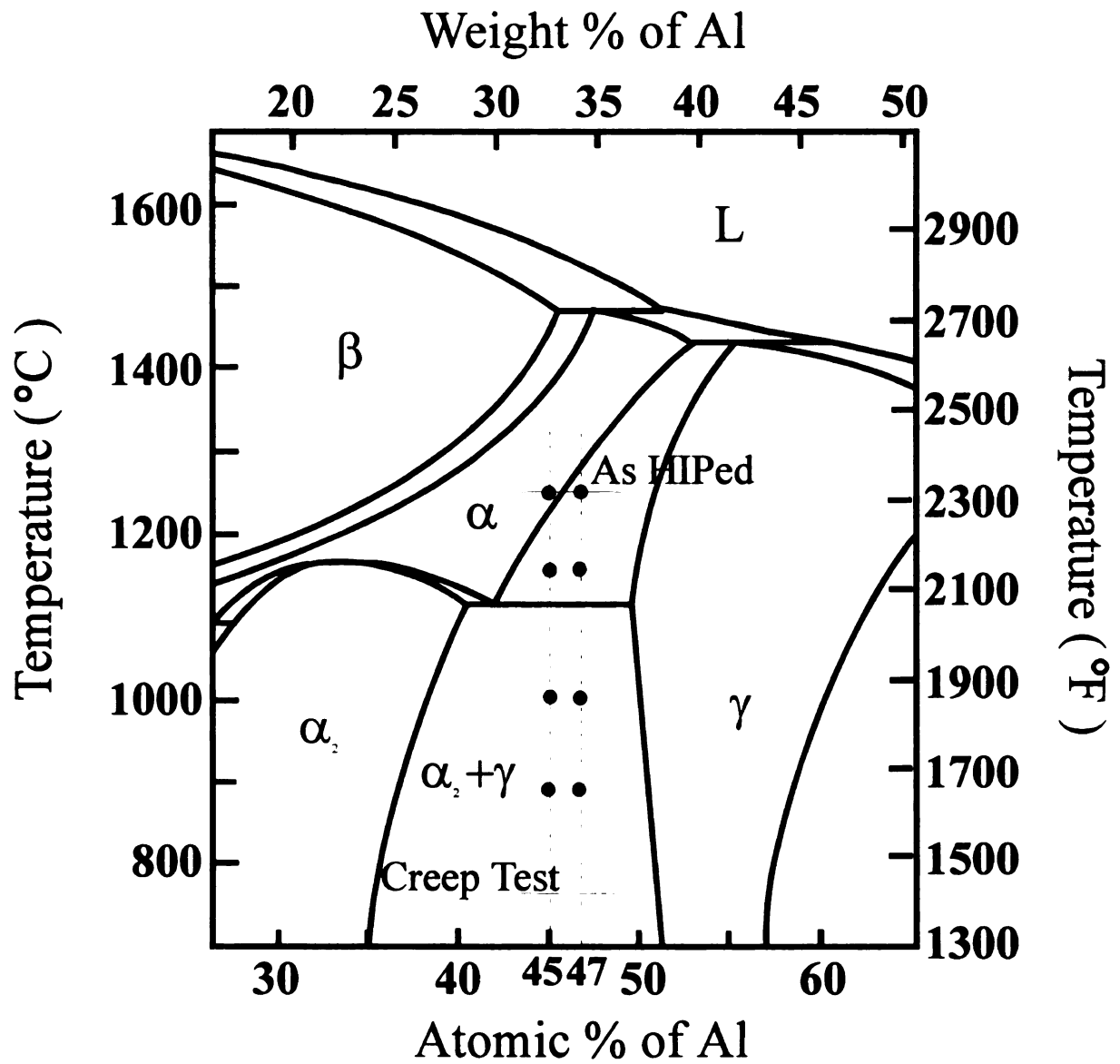


Figure 6.1 Phase diagram illustrating heat treatment and creep condition [96,97].

6.3 RESULTS

6.3.1 Primary creep to 0.5 % strain

The time to 0.5 % creep of the three titanium aluminide alloys varies with heat treatment as shown in Figure 6.2. The average value of three samples is plotted with the line, and high and low values are also plotted. From this plot, it is apparent that the 45Al composition is insensitive to heat treatment. The 47Al samples exhibit different responses to heat treatment. With TiB₂, the heat treatment for 10 hours at 900 °C is damaging to primary creep resistance, but otherwise there is no significant improvement with increasing time at temperature in heat treatment, other than a smaller range of values with the two step heat treatment. For the alloy without TiB₂, the creep resistance is substantially improved with increasing amounts of time and temperature in heat treatment, but the variability in the samples is not significantly improved with heat treatment.

6.3.2 Microstructures

The samples chosen for microstructural observation were the middle performance specimens. The microstructural variations in these specimens are summarized in Table 6.1. Details of the microstructure for each combination of composition and heat treatment are described in more detail below.

Ti-45Al-2Nb-2Mn-0.8TiB₂

As shown in Figure 6.3.a, optical micrographs of the crept specimen show that many TiB₂ particles (indicated by arrow) are distributed randomly. There are several types of particles such as equiaxed, needle, and irregular shaped precipitates with spacing

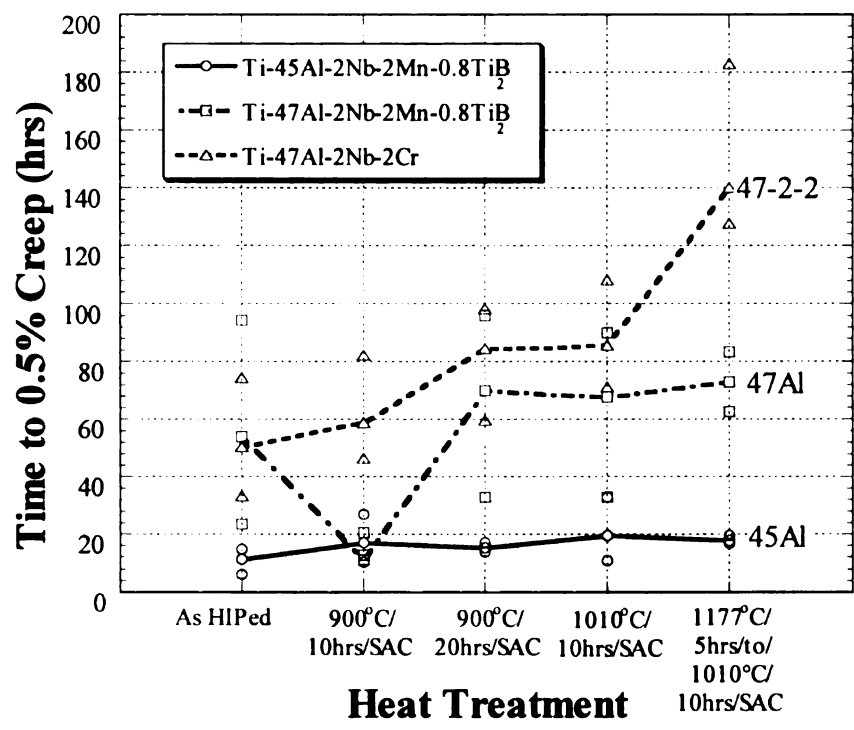


Figure 6.2 Time to 0.5% creep strain with respect to heat treatment. The lines go through the average of 3 values, the high and low values are indicated by additional symbols.

Table 6.1 Observation of the effects of heat treatment on three TiAl alloys from optical microscopy.

	As HIPed	900 °C/10hrs/SAC	900 °C/20hrs/SAC	1177 °C/5hrs to 1010 °C /10hrs/SAC
Ti-45Al-2Nb- 2Mn-0.8TiB ₂	Lamellar % & grain size	25%	39%	37%
		30 µm	50~70 µm	50~100 µm
	equiaxed % & grain size	75%	61%	63%
		15 µm	20~30 µm	20~30 µm
	TiB ₃	30~50 µm spacing	gray phase observed	
Ti-47Al-2Nb- 2Mn-0.8TiB ₂	characteristics	Lam patches	Lam patches	
	Lamellar % & grain size	21%	16%	56%
		50~200 µm	50~150 µm	100~200 µm
	equiaxed % & grain size	79%	84%	44%
	TiB ₂	10~40 µm	10~40 µm	10~40 µm
Ti-47Al-2Nb-Cr		30~50 µm spacing	similar	10~40 µm spacing
	characteristics	Heterogeneous	Homogeneous	Large Lam. grains
	Lamellar % & grain size	51%	43%	18%
		50~400 µm	40~150 µm	50~150 µm
	equiaxed % & grain size	49%	57%	82%
		5~150 µm	5~150 µm	5~150 µm
	characteristics	Heterogeneous	Less Heterog	Homogeneous

of 30-50 μm . As the annealing time increased no distinct change in the particles was observed, but in the case of two-step heat treatment there appeared to be fewer particles. From the micrographs of etched samples, a very fine duplex microstructure was observed in all specimens, regardless of heat treatment. There is a homogeneous distribution of 20-30 μm equiaxed and 30-100 μm lamellar grains. The volume fraction of lamellar grains increases slightly after heat treatment from as-HIPed to 900 °C/20hrs, but no difference between the 900 °C/20hrs and the two-step heat treatment was observed.

From analysis of backscattered images of undeformed and deformed specimens obtained in SEM, there are no distinguishable changes in the microstructure resulting from creep deformation (Figure 6.4.a and b). TiB_2 particles are distributed randomly, and they are located inside gamma grains, in grain boundaries between gamma (dark phase) and α_2 (bright phase) grains and in lamellar grains, but not inside α_2 grains, as shown in Figure 6.4. Single phase γ and α_2 grains represent about 40% of the volume fraction. The α_2 grains have large and angular shapes, but the γ grains tend to be more round and equiaxed. This indicates that equiaxed γ grains nucleate in several places in a given parent α grain, and that some of the parent α grains transform into lamellar grains, but others do not. Very fine mechanical twins are observed in some α_2 grains in both deformed and undeformed specimens (see arrows in Figure 6.4). These finely twinned regions also exhibit contrast indicating formation of extremely fine lamellar microstructures consisting of both α_2 and γ lathes. Since they are much finer than the obvious lamellar grains, they are not likely to have resulted from thermally induced transformation, so they are more likely to be a result of local stress concentrations [47,50,213]. These mechanical twins were observed in all heat treatments.

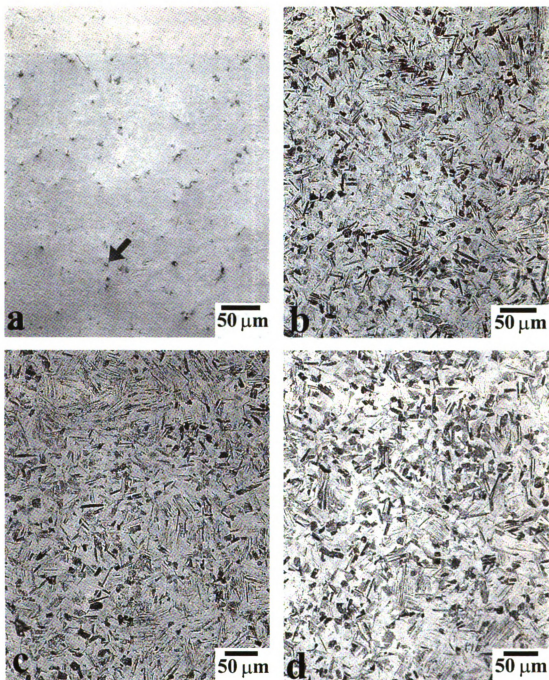


Figure 6.3 Optical microstructures of deformed Ti-45Al-2Nb-2Mn-0.8TiB₂ a) as-HIPed, as polished, b) as-HIPed and etched, c) 900 °C/20hrs heat treatment, and d) two-step heat treatment.

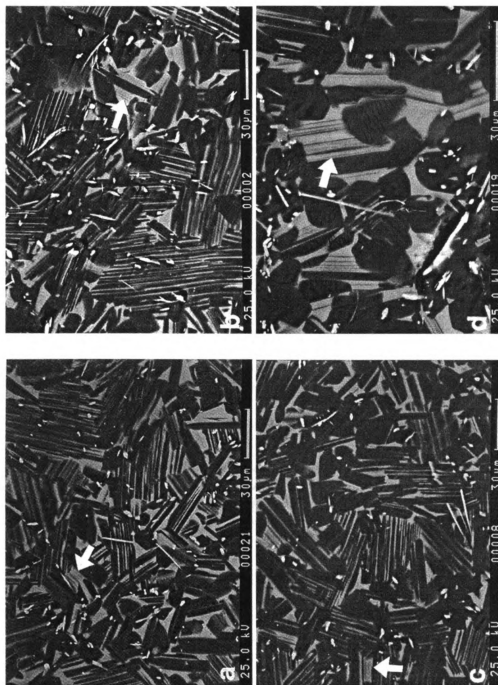


Figure 6.4 Backscattered electron images of Ti-45Al-2Nb-2Mn-0.8TiB₂ a) as-HIPed undeformed, b) as-HIPed deformed, c) 900 °C/20hrs heat treatment, and d) two-step heat treatment.

Since the α_2 grains have an angular shape, stress concentrations are more likely to be focused at triple points in α_2 grains, where the fine mechanical twinning is most often observed. The fine twinned regions are also observed in TEM images. They occur in the angular shaped α_2 grains, as illustrated in Figure 6.5.a. Regions of extremely fine mechanical twinning are also observed in some lathes of the lamellar grains (Figure 6.5.b). The width of the mechanically twinned region appears to be larger in regions with a higher stress concentration. Dislocations are also observed in the vicinity of TiB_2 particles, in Figure 6.5.c.

Ti-47Al-2Nb-2Mn-0.8TiB₂

The TiB_2 particles in the as-HIPed alloy Figure 6.6.a appear larger (10-70 μm) than in the 45 Al specimen in Figure 6.3.a, but they have a similar spacing. Microstructures of as-HIPed specimens after creep deformation exhibit a heterogeneous microstructure illustrated in Figure 6.6.b. There are clusters of small equiaxed grains in some regions where there are fewer lamellar grains, and conversely, few fine γ grains are observed in regions containing lamellar grains. After heat treatment in Figure 6.6.c and d the microstructures exhibit fewer small grain clusters. The volume fraction of equiaxed grains changes, and after the two step heat treatment, the lamellar volume fraction becomes largest. The maximum grain size of lamellar grains is about 200 μm . As time and temperature of heat treatment increase, microstructures became more homogeneous. The equiaxed grain size distribution becomes more homogeneous, and fewer clusters of finer γ grains were observed.



Figure 6.5 Bright field images of as HIPed Ti-45Al-2Nb-0.8TiB₂ after creep test a) Fine mechanical twins observed in α_2 grains, b) dislocations interactions with a TiB₂ particle, c) Fine mechanical twins observed in lamellar regions.

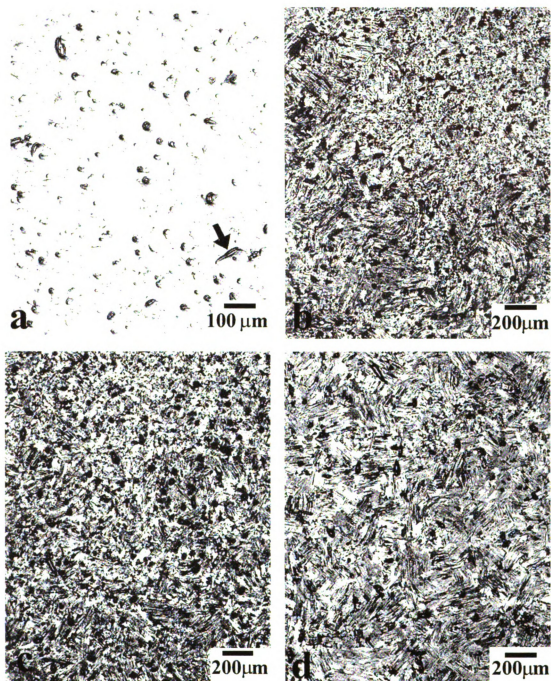


Figure 6.6 Optical microstructures of deformed Ti-47Al-2Nb-2Mn-0.8TiB₂ a) as-HIPed, as polished, showing TiB₂ particles, b) as-HIPed and etched, c) 900 °C/20hrs heat treatment, and d) two-step heat treatment.

Ti-47Al-2Nb-2Cr

Although no TiB_2 is present in this alloy, there are second phases present (Figure 6.7.a). However, in contrast to the microstructures containing TiB_2 , the as-HIPed microstructure exhibits very large 300-400 μm lamellar grains and about 200 μm pockets of equiaxed 10-20 μm grains (Figure 6.7.b). The microstructure is extremely heterogeneous, and it exhibits some of the same types of heterogeneities (clusters of small equiaxed grains) observed in Figure 6.6.b. With heat treatment, the volume fraction of the lamellar grains decreases with increasing time and temperature, and the microstructure becomes less heterogeneous. The pockets of equiaxed grains become fewer and there are fewer fine grains in the pockets.

In the backscattered electron SEM images of this alloy there is a smaller volume fraction of angular equiaxed α_2 grains between gamma grains and α_2 laths are thinning in lamellar grains (Figure 6.8). The very fine mechanical twins seen in the 45 Al sample (Figure 6.4) were not observed in the smaller α_2 equiaxed grains in the 47 Al specimens. Very small bright phases can be seen either in α_2 equiaxed grains or boundaries of gamma grains (indicated by arrows) and these phases are β_2 phase which is produced by addition of Cr [215]. They have an orientation relationship of $(0001)\alpha_2//\{111\}\gamma//\{110\}\beta_2$, and $\langle 11\bar{2}0 \rangle_{\alpha_2} // \langle 1\bar{1}0 \rangle_{\gamma} // \langle \bar{1}11 \rangle_{\beta_2}$ [215]. Since Cr is known to strengthen the α_2 and γ phases, this may account for the lack of mechanical twinning observed in the α_2 phase in the Ti-47Al-2Nb-2Cr alloy [215]. There appears to be a decrease in the amount of β_2 phase with the increasing amounts of heat treatment (Figure 6.8.c and d). At lower magnifications, the distribution of large equiaxed grains correlates with lower aluminum

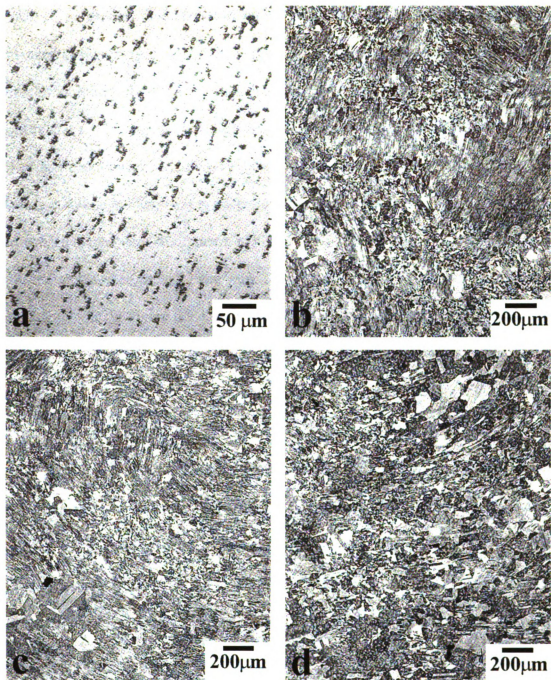


Figure 6.7 Optical microstructures of deformed Ti-47Al-2Nb-2Cr a) as-HIPed, as polished, b) as-HIPed and etched, c) 900 °C/20hrs heat treatment, and d) two-step heat treatment.

content regions (which are darker in Figure 6.8.e). With deformation, some dynamic growth of α_2 regions drain the surrounding region of titanium, in the lamellar region illustrated in Figure 6.8.f. Also there appears to be less segregation since there are fewer dark(alumium rich) regions after creep deformation (Figure 6.8.e~h). TEM investigations indicate that a 170° angle relationship between lamellae is frequently observed in the as-HIPed and heat treated conditions. Typically, one of the two lamellar lathes has a finer spacing as shown in Figure 6.9.a. Subgrains developed in larger regions of lamellar grains during high temperature deformation in Figure 6.9.b. No subgrains had developed fully in equiaxed grains even though there were regions exhibiting a dislocation density greater than $2 \times 10^{12}/\text{m}^2$ in Figure 6.9.e. From Figure 6.9.c, it appears that an equiaxed grain is consuming a lamellar region, but the α_2 lamellae resist consumption. After the two-step heat treatment, dynamic precipitation was observed in grain interiors and interfaces in Figure 6.9.e, and this may account for some the exceptional creep resistance.

By using the dark field method and tilting techniques, the spacing of γ thickness, α_2 spacing and the thickness of α_2 laths in several lamellar grains were measured. The data was obtained by measuring about 100-350 laths and taking the average as shown in Figure 6.10 and Table 6.2. The spacing generally decreases with more heat treatment. In the case of γ thickness, there was not much reduction of spacing from heat treatment, only about 8%. However, a 4% reduction of γ thickness after creep test was observed in the 900 °C/20hr heat treated alloy. The refinement of the lamellar spacing could result from mechanical twinning parallel lamellar boundaries since this is an easy mode of deformation against loading. Measured α_2 spacing shows that on the contrary to the previous case, the spacing decreases about 5% and 18% from the As HIPed condition

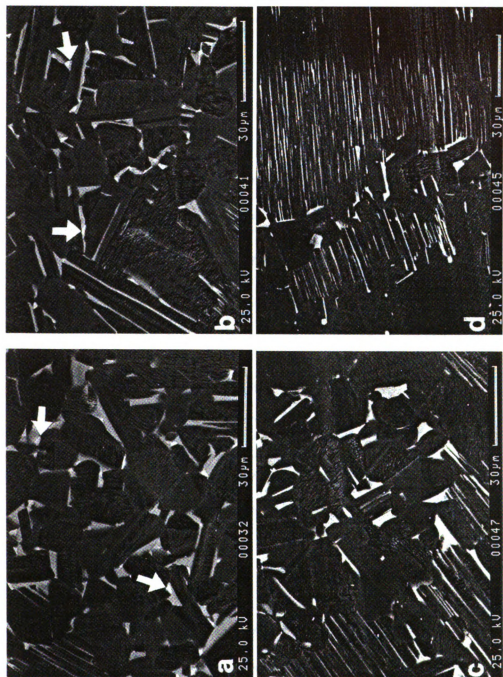


Figure 6.8 Backscattered electron images of deformed Ti-47Al-2Nb-2Cr a) as-HIPed, b) 900 °C/20hrs heat treatment, and c) and d) two-step heat treatment.

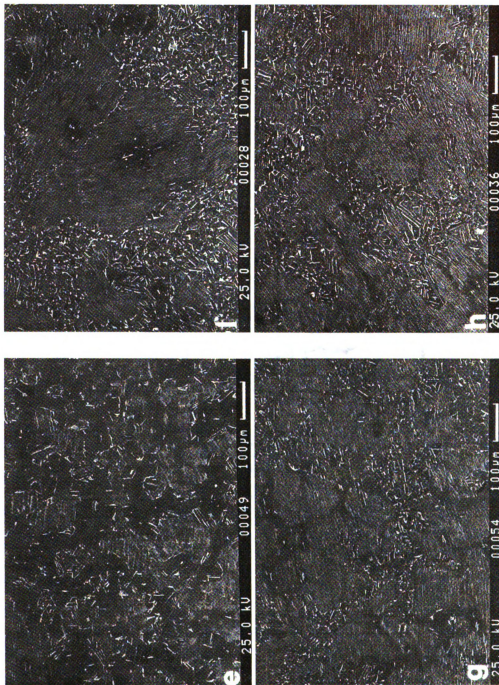


Figure 6.8 Low magnification backscattered electron images of Ti-47Al-2Nb-2Cr illustrate dendritic segregation of aluminum, e) as-HIPed undeformed, f) as-HIPed deformed, g) 900 °C/20hrs heat treatment undeformed, and h) 900 °C/20hrs heat treatment deformed.

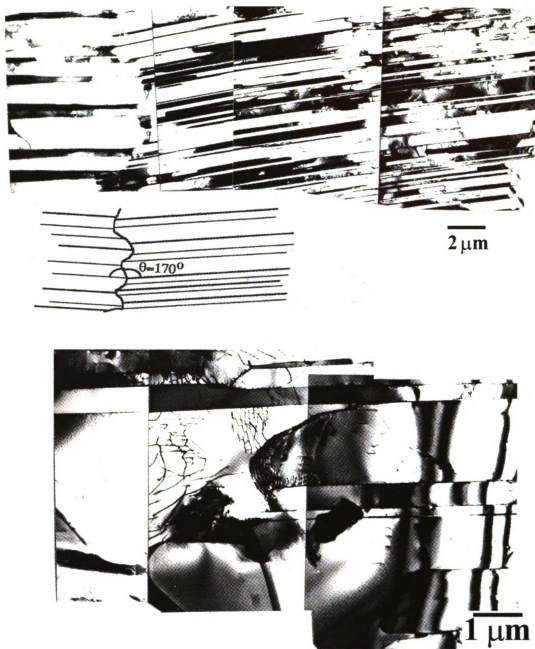


Figure 6.9 Bright field images of as HIPed Ti-47Al-2Nb-2Cr after creep test a) commonly observed relationship between coarser and finer lamellar regions exhibit a 170° about a $\langle 110 \rangle$ axis relationship, b) subgrain boundaries develop in larger γ regions.

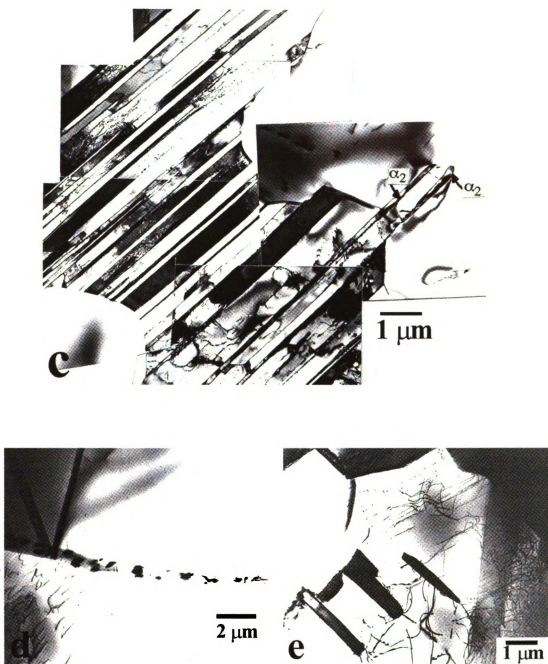


Figure 6.9 Bright field images of Ti-47Al-2Nb-2Cr after creep test c) α_2 lathes resist absorption in a boundary where an equiaxed γ grain is consuming a lamellar grains (900 °C/20hrs heat treatment), d) particles are located at grainboundary, and e) inside a γ grain after two-step heat treatment.

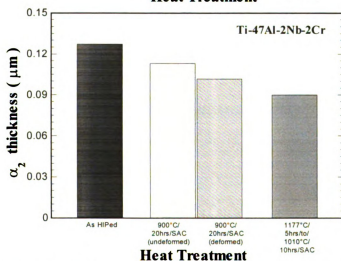
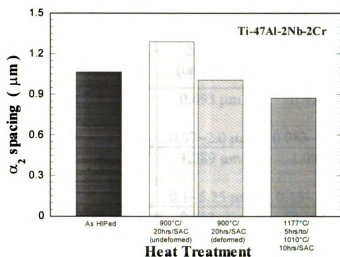
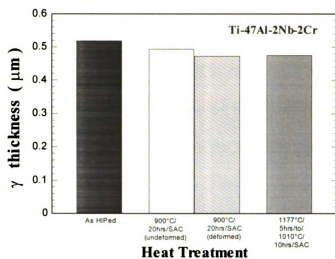


Figure 6.10 Refinement of lamellar feature was observed with increasing heat treatment conditions, and resulting from deformation.

Table 6.2 Average and range of dimensions describing lamellar microstructures.

Ti-47Al-2Nb- 2Cr	As HIPed	900 °C/ 20hrs/SAC (undeformed)	900 °C/ 20hrs/SAC (deformed)	1177 °C/ 5hrs/to/ 1010 °C/ 10hrs/SAC
γ thickness	0.518 μm	0.493 μm	0.475 μm	0.473 μm
	0.05~2.43 μm	0.07~2.0 μm	0.083~1.65 μm	0.125~1.98 μm
α_2 spacing	1.064 μm	1.289 μm	1.007 μm	0.874 μm
	0.55~1.68 μm	0.1~5.25 μm	0.15~2.41 μm	0.25~2.42 μm
α_2 thickness	0.127 μm	0.113 μm	0.102 μm	0.090 μm
	0.04~0.415 μm	0.04~0.25 μm	0.06~0.166 μm	0.01~0.15 μm

to the one and two-step heat treatments, respectively. After deformation, there was a 22% reduction of the α_2 spacing, and a 10% reduction in the α_2 thickness. This may result from nucleation of new α_2 lamellae initiated by mechanical twinning, since a mechanical twin has the crystal structure of the α_2 phase for three layers in each interface [213]. The heat treatment and creep deformation cause the lamellar scale to become more refined. Figure 6.11 shows inverse pole figures for 3 heat treatments. Figure 6.11.a shows that mechanical twinning has a low schmid factor near 001, and increasing heat treatment tends to increase crystal orientations that are hard to twin.

6.4 DISCUSSION

Ti-45Al-2Nb-2Mn-0.8TiB₂

As shown in Figure 6.2, primary creep resistance does not improve much and only a slight increase occurs after heat treatment from the as-HIPed condition. There is also no appreciable change in microstructure. The poor primary creep resistance can be most clearly correlated with the large amount of fine mechanical twinning observed in the microstructure, particularly in the α_2 grains. Heat treatment did not affect the rate of generation of these fine mechanical twins. The fine microstructures can also account for poor creep resistance, since diffusional processes are accelerated with more interfacial area.

Ti-47Al-2Nb-2Mn-0.8TiB₂

The as-HIPed condition gives more creep resistance than the 45Al composition, but after heat treatment at 900 °C for 10 hours the creep resistance decrease substantially.

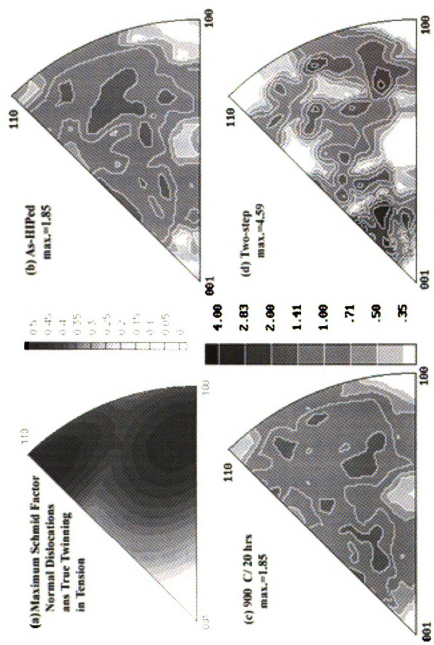


Figure 6.11 Inverse pole figures for 3 heat treatments a) Schmid factor, b) as-HIPed, c) 900 °C/20hrs heat treatment, d) two step heat treatment after creep test.

Heat treatment for 20 hours at the same temperature and the two step heat treatment provides slightly improved creep resistance. The microstructure of this alloy has a larger scale and the (TiB₂) particles are bigger and are more evenly distributed than in the 45Al alloy as shown in Figures 6.3 and 6.6. The particles were often observed with dislocation tangles nearby. Thus the primary creep resistance in all heat treatments are slightly improved except for the 900 °C/10hrs case, where the only explanation is a less homogeneous microstructure and a higher lamellar volume fraction. With further heat treatment, the microstructure becomes more homogeneous and the number of small equiaxed grains decreases. However, it appears that the benefit gained by reducing the number of small grains was offset by the increasing the lamellar volume fraction after the two-step heat treatment.

Ti-47Al-2Nb-2Cr

This alloy shows the best primary creep resistance due to the fact that heat treatment provides substantial benefits (Figure 6.2). As time and temperature of heat treatment increase the creep resistance increases. The two-step heat treatment provides the best 0.5% creep resistance of about 140 hours. This microstructure has the smallest volume fraction (18%) of lamellar grains, a homogeneous microstructure, the least amount of pockets of small equiaxed grains and bigger equiaxed grains, which all correlate with better primary creep resistance. In general, the lamellar microstructure gives a lower minimum creep rate [161]. However, this is not true for primary creep resistance, where initial deformation occurs easily in the lamellar microstructure. By comparing Figure 6.8 with 6.4, fine mechanical twins are found in the angular equiaxed

α_2 grains, but not in the α_2 regions in the 47Al material. One difference is that the α_2 grains in the 45 Al material are larger and more complicated in shape, and this may lead to larger stress concentrations and a geometrical condition that permits mechanical twinning to accommodate the stress concentration. Figure 6.11 shows that resistance to mechanical twinning occurs when crystals are oriented near 001 and away from 441, and this desirable texture is strengthened with heat treatment. The increased volume fraction in a hard orientation for twinning may contribute to the excellent creep resistance resulting from the two-step heat treatment. Figure 6.10 shows that lamellar grains were refined after deformation. The correlation of refined lamellar spacing with better creep resistance indicates that the contribution of the lamellar microstructure to the strength can arise from a Hall-Petch relationship that reduces slip distances, and/or from a sub-grain strengthening effect, if a twin interface can be considered effectively similar to a low-angle subgrain boundary. Since the Hall-Petch effect is associated with a low temperature strengthening mechanism, and the large equiaxed grain size is consistent with better diffusion creep resistance, then the primary creep resistance at 760 °C arises from a particular mixture of low and high temperature strengthening mechanisms. Consequently, deformation at a different temperature may result in a different balance of strain arising from low and high temperature mechanisms.

6.5 CONCLUSIONS

The effect of different heat treatments on primary creep resistance in three investment cast TiAl alloys were studied. Ti-45Al-2Nb-2Mn-0.8TiB₂ did not show much difference in primary creep resistance because of no difference in the microstructures

resulted after various heat treatment. The creep resistance was poor, due to very fine microstructures and very fine mechanical twinning observed in α_2 grains. Some limited improvement in the Ti-47Al-2Nb-2Mn-0.8TiB₂ alloy was obtained with heat treatment. However, the heat treatments and especially the two step case significantly improved the creep resistance of the Ti-47Al-2Nb-2Cr alloy. This heat treatment led to the smallest volume fraction (18%) of lamellar grains, a homogeneous microstructure, the least amount of pockets of small equiaxed grains, and large equiaxed grains, which all correlate with better primary creep resistance. Texture analysis indicates that the desirable texture to minimize mechanical twinning is to have crystals oriented near 001 and away from 441. This texture is strengthened with heat treatment and it may contribute to the excellent creep resistance obtained from the two-step heat treatment.

CHAPTER 7

EFFECT OF INTERSTITIAL CONCENTRATION AND HEAT TREATMENT ON MICROSTRUCTURE AND PRIMARY CREEP OF INVESTMENT CAST Ti-47Al-2Nb-2Mn WITH 0.8vol.% TiB₂

ABSTRACT

Most research about creep has focused on minimum creep rate or stress rupture properties, but primary creep is important for practical applications. In this chapter, we compare how interstitial content and heat treatments of shorter duration than used in past studies affect the microstructure and primary creep resistance of a particular alloy containing TiB₂ particles. More time and temperature in heat treatment homogenizes the microstructure and reduces the scatter of creep times to 0.5% strain. Increasing interstitial content increases the time to 0.5% creep, and it stabilizes the α_2 phase. Preliminary evidence for large mechanical twinning strains parallel to lamellar interfaces shortly following loading is provided.

7.1 INTRODUCTION

Most research on TiAl alloys has focused on room temperature mechanical properties, oxidation resistance, and yield strength [133,216-220]. Not many studies have been made on the effect of interstitials (hydrogen, nitrogen, carbon, and oxygen) on creep properties of TiAl. These interstitials strongly affect mechanical properties and microstructure development, and consequently, deformation mechanisms [221].

Investment cast Ti-47Al-2Nb-2Mn+0.8TiB₂ XDTM alloys are under development at Howmet Corp. Several less expensive heat treatments have been investigated, yielding some improvement in primary creep resistance [127]. Alloys with higher interstitial element concentrations were also investigated to examine effects on primary creep and cost reduction. In this chapter, the effect of interstitial concentration on primary creep deformation and microstructures of investment cast TiAl alloys is examined and compared to heats of the alloy with lower interstitial content. Microstructures and primary creep deformation mode were analyzed in terms of grain size, distribution of α_2 spacing and γ thickness and α_2 thickness.

7.2 EXPERIMENTAL

Three heats of investment cast near- γ TiAl with the nominal composition of Ti-47Al-2Nb-2Mn-0.8TiB₂XDTM were used with low interstitial contents typical of normal production capability, and higher interstitial compositions (denoted hereafter as low, medium and high O, as shown in Table 7.1). All materials were hot isostatically pressed (HIPed) at 1260 °C for 4 hours at 127 MPa (2300 °F, 25 ksi) to eliminate casting porosity and to establish the duplex microstructure. The alloys with higher interstitial content were subsequently heat treated using a standard schedule of 1010 °C for 50 hours and cooled in a static argon atmosphere (SAC). The low O alloys were heat treated using several shorter times and/or different temperatures indicated in Figure 7.1 (2-step is 5 hr. 1177 °C, then 10 hr. 1010 °C, details in [127]). These specimens were then subjected to creep tests at 760 °C, 138 MPa (1400 °F, 20 ksi). Data were collected in 15 minute intervals following

application of load. The creep specimens were cooled under load once 0.5% creep strain was reached.

Samples for microscopy were obtained from the grip section of a deformed room temperature tensile specimen (for the undeformed microstructure) and the gage section of creep deformed specimen for the deformed microstructure. A modified Kroll's reagent were used for etching [222]. Microscopy was conducted in a Neophot-21 optical microscope equipped with a LECO 2001 image analysis system, a JSM 6400V scanning electron microscope (SEM) operated at 25 kV, and a Hitachi H-800 transmission electron microscope (TEM) operated at 200 kV. TEM specimens were sliced from the specimens and the final thinning process was performed in a double jet electropolishing system using a 10% sulfuric acid + methanol solution at -20°C. All microscopy samples were prepared so that the sample normal was parallel to the tensile axis.

Table 7.1 Chemical compositions of investment cast Ti-47Al-2Nb-2Mn-0.8TiB₂XDTM

(at%)	Ti	Al	Nb	Mn	B	Cr	Si	Fe	O	N	H
Low O	48.54	46.19	1.87	1.86	1.15	0.02	0.04	0.07	0.203	0.026	0.012
Medium O	48.55	45.43	2.02	1.95	1.14	0.02	0.04	0.10	0.227	0.032	0.012
High O	47.66	47.16	1.81	1.88	1.07	0.02	0.04	0.03	0.289	0.037	0.012

7.3 RESULTS and DISCUSSION

The time to 0.5% strain for the three alloys varies with heat treatment as shown in Figure 7.1. The average value of three samples is plotted with the line, and high and low values are plotted with symbols. The heat treatment for 10 hours at 900 °C apparently damaged primary creep resistance but there was an improvement with longer heat treatment time and/or higher temperature. A smaller range of creep times is obtained with

the two step heat treatment. For the high O alloys, creep resistance is significantly improved with increasing amounts of O.

The alloys with medium and high O exhibit creep times to 0.5% that are more than twice as long. The scatter is similar in magnitude for all alloys except the low O alloy after the two-step heat treatment. Figure 7.2 shows a power law curve fit of the creep data. All alloys exhibit a rapid decrease in strain-rate up to about 0.1. The creep rates of the higher O alloys were lower and decreasing more rapidly at 0.5% strain. At low strains, the creep curves for both higher O alloys cross at a strain of 0.1%, indicating that the high O alloy had a faster initial creep rate.

7.3.1 Microstructures

Figure 7.3 shows optical micrographs of alloys with medium and high O. The microstructures of low O alloys are similar to that of the medium O alloy [127]. The medium O alloy has a lower volume fraction of lamellar grains than the high O alloy (22% and 40%) which is contrary to the common observation that lower aluminum (note Table 7.1) causes more lamellar grains. The average lamellar volume fraction of low O alloys is about 25%. This result is consistent with the observation that oxygen is an alpha phase stabilizer in Ti alloys [143,223]. The alloy with high O has 100-200 μm lamellar grain sizes and 25-100 μm equiaxed grain sizes. The low O alloys have 20-200 μm lamellar grains and 10-50 μm equiaxed grains [127]. The higher O levels have fewer small grains, which correlates with improved creep resistance [127].

Backscattered electron (BSE) images of the higher O alloys after creep deformation in Figure 7.4 illustrate differences in α_2 morphology (white phase, see

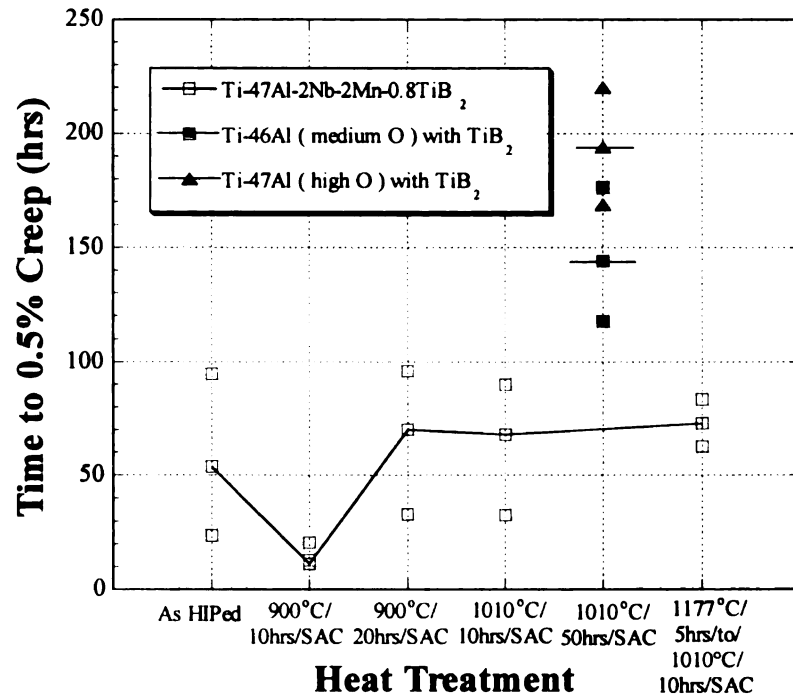


Figure 7.1 Time to 0.5% creep strain with respect to heat treatment. The lines go through the average of 3 values, high and low values are indicated by symbols.

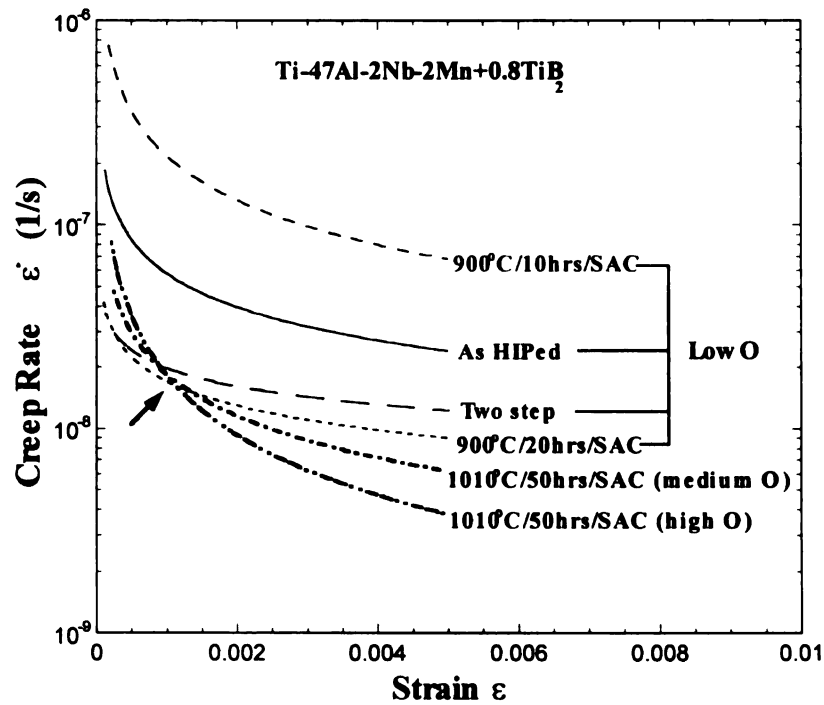


Figure 7.2 Strain rate-strain plot of the creep deformation for the specimen with the middle creep time.

arrows). The largest α_2 regions in the high O alloy are similar to the scale of the lamellar microstructure, but angular shaped 3-7 μm α_2 grains (arrow) were commonly observed in the medium O alloy (it also has lower aluminum). Angular α_2 grains correlate with faster primary creep [127].

In the three alloys, two types of boride particles were found, needle and round. They have dark halos in Figures 7.3 and 7.4; the round type is 1.5-3.5 μm , and the needle type is 3-60 μm long. The needle particles have been identified as TiB and equiaxed particles as TiB₂ [224]. The heat treatment or interstitial content did not affect the size and distribution of these particles. From analysis of SEM BSE images and TEM images, these particles appear to provide nucleation sites for lamellar lathes (fine lamellar colonies were frequently found near particles), and they also block and entangle dislocations.

7.3.2 Lamellar spacing

The α_2 spacing was measured by using BSE imaging and about 400 α_2 laths were used to characterize the spacing. These measurements are upper bounds of the actual spacing, since the lamellar plane normal direction was not determined to make the parallax correction needed to determine the actual α_2 spacing. However, this is a systematic way to compare α_2 spacings in specimens with similar microstructures. The TEM was used for measuring the true γ thickness and α_2 thickness (by tilting the foil to so that a $\langle 110 \rangle$ direction in a lamellar plane was parallel to the beam) and more than 100 laths for γ thickness and 50 α_2 laths were counted in several lamellar grains or regions

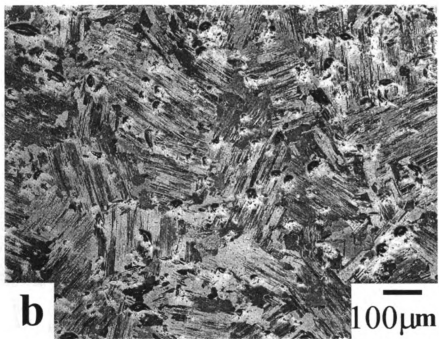
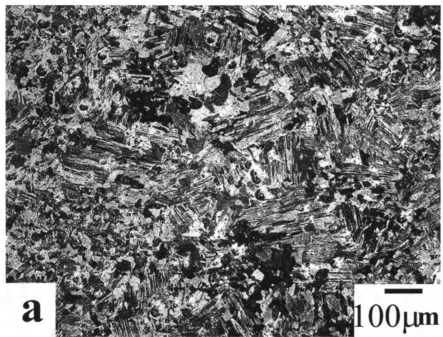


Figure 7.3 Optical microstructure of creep deformed (a) medium O and (b) high O alloys.

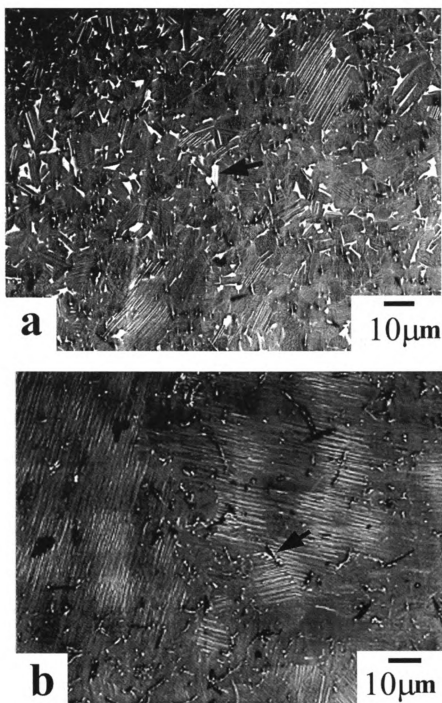


Figure 7.4 Backscattered electron (BSE) images of after creep deformation of (a) medium O and (b) high O alloys.

for this measurement.

The α_2 spacing was reduced in these alloys after creep deformation and this reduction varies with heat treatment and interstitial content [127]. The average α_2 spacing before deformation in the alloy with high O is 1.37 μm , which is nearly as large as the 1.57 μm spacing of the low O alloy which showed the poorest creep resistance. The average α_2 thickness is larger (0.2 μm) in the high O alloy than the low O alloy (0.15 μm). This also suggests that oxygen stabilizes the α_2 phase.

The distribution of α_2 spacing and γ thickness before and after creep deformation are shown in Figure 7.5. From the two plots, the reduction of the α_2 spacing and γ thickness after deformation at the early stage of creep can be easily visualized since the dashed line shows the highest frequency of lamellae with fine spacing. The reduction in γ thickness is greater than the α_2 spacing. An easy mode of deformation twinning parallel to lamellar boundaries accounts for the lamellar refinement. Mechanical twinning will rotate the crystal to a hard orientation where only superdislocations are operative [141]. The reduction of α_2 spacing could occur by nucleation of α_2 laths in deformation twin interfaces [120], and/or due to a strain induced phase transformation [125].

During the first 0.5% strain, more reduction in the strain-rate correlates with more reduction in lamellar spacing in the low O alloy (Figure 7.6). The high O alloy does not follow the same relationship between the reduction in spacing and the reduction in strain-rate: The high O alloy exhibits a larger reduction in strain-rate, and a greater amount of reduction in the γ thickness. The high O alloy exhibits more reduction of γ thickness than the alloy heat treated at 900 °C for 10 hours, which gave poor creep

resistance. If the reduction in lamellar spacing occurs by mechanical twinning, then more twinning appears to cause a greater amount of strain at early times. The effect of the high O is that more refinement in the γ thickness occurs in primary creep, but it occurs more slowly.

From the TEM investigation, several regions of tangled dislocations were observed in equiaxed grains and wider γ lamellar laths. Luster and Morris showed that several slip systems were activated in thicker lamellar laths, but that only twinning or slip parallel to the lamellae occurred in thinner laths [142]. From our TEM observations, dislocation density was very low in lamellar laths smaller than 0.5 μm wide. Thus lamellar laths less than 0.5 μm were defined as “thin”, and laths and between 0.5 and 1.0 μm as “thicker” in the plot in Figure 7.7, which indicates that before deformation, more laths with finer spacing gave better primary creep resistance, and conversely, more of the thicker laths result in poorer creep resistance. Dislocation motion is apparently hindered by more lath boundaries in the finer lamellar laths during the initial part of primary creep deformation. However the relationship in Figure 7.7 is not observed in the high O alloys or in the low O alloy with poor creep resistance. It appears that interstitials also act strongly as obstacles to generation of dislocations or to dislocation motion. If so, then this may force a greater amount of strain to be accomplished by mechanical twinning, as indicated by the greater amount of refining of the γ thickness in the high O material.

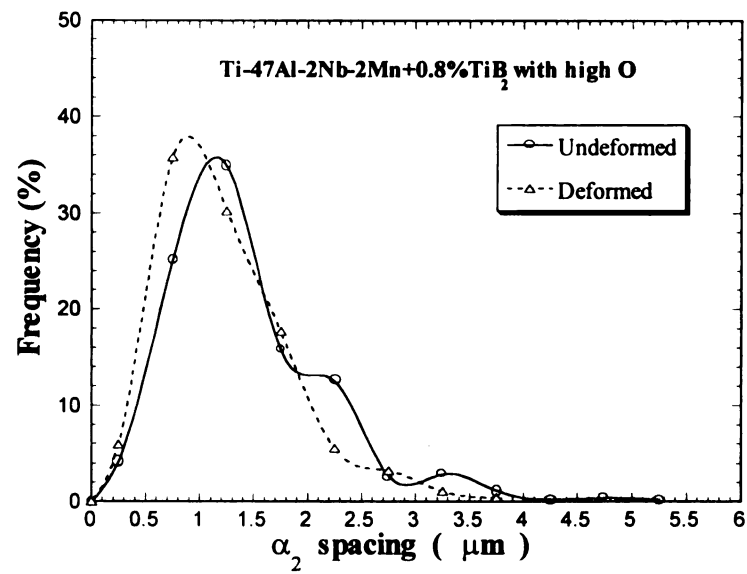
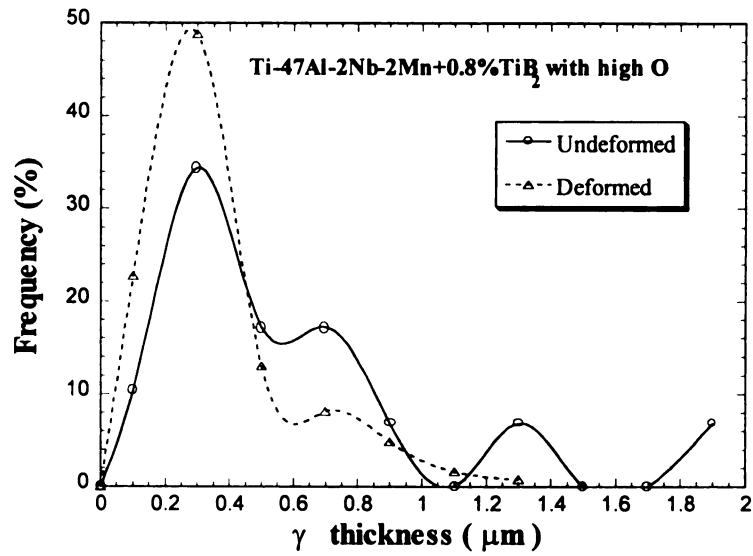


Figure 7.5 Lamellar spacing distribution of high O alloys before and after creep deformation.

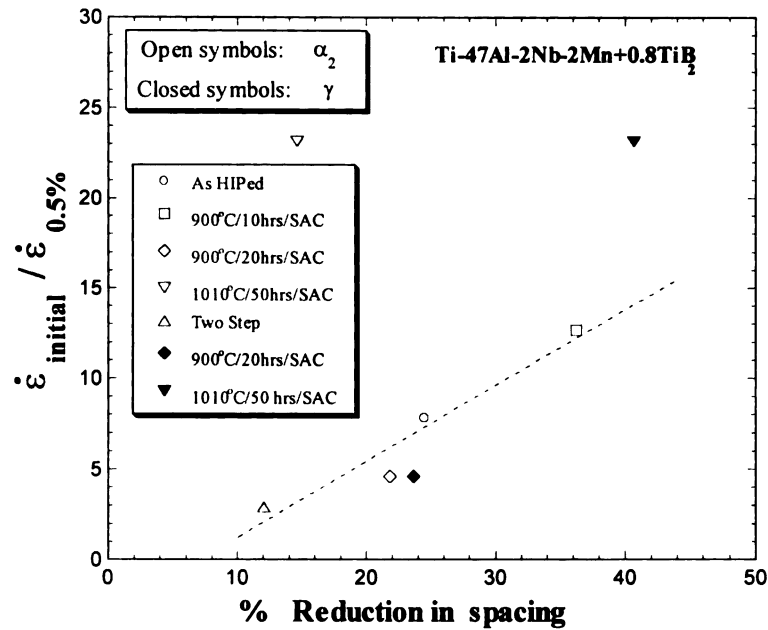


Figure 7.6 Plot of strain-rate ratio vs. % reduction in α_2 spacing and γ thickness in low and high O alloys.

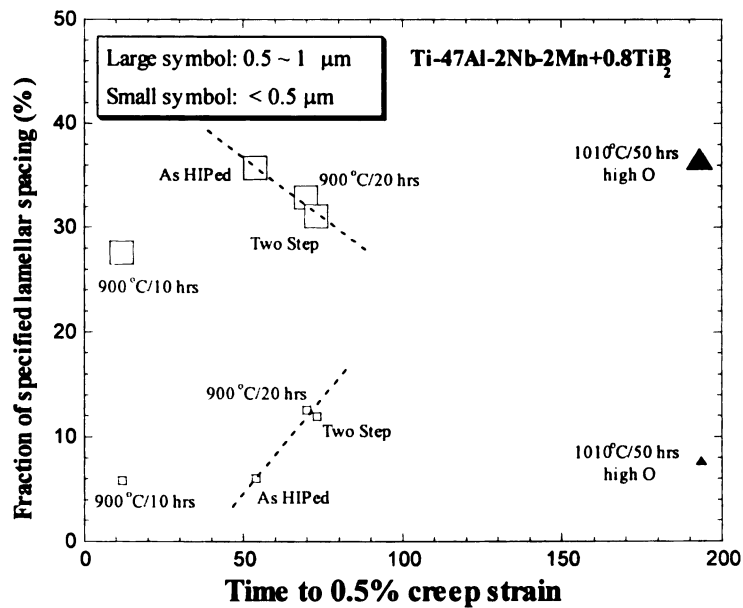


Figure 7.7 Relationship between fraction of specified lamellar spacing and time to 0.5% creep strain.

7.4 CONCLUSIONS

A 10-40% reduction in lamellar spacing was observed within the first 0.5% creep strain, depending on alloy composition and heat treatment. In low O alloys, some limited improvement of creep resistance was obtained with heat treatment. The lamellar volume fraction was about 25%, and this correlated with a smaller decrease in creep rate upon loading. The high O alloy exhibited 40% lamellar grains (in spite of having higher Al content) indicating that O stabilized the α_2 phase. A large decrease in creep rate was observed upon loading, and this caused a 40% decrease in γ thickness. Large reductions in γ thickness can be accomplished by mechanical twinning parallel to the lamellar plane.

CHAPTER 8

CHANGES IN MICROSTRUCTURE DURING PRIMARY CREEP IN A Ti-47Al-2Nb-1Mn-0.5W-0.5Mo-0.2Si ALLOY

ABSTRACT

Cast gamma titanium aluminides are gaining acceptance as potential replacements for superalloy and steel components in many applications. One particular alloy with W, Mo and Si additions has shown exceptional primary creep resistance. Quantitative microscopic comparisons were made between microstructures in undeformed and deformed regions in creep specimens deformed to strains between 0.1 and 1.5 % strain, using optical microscope, scanning electron microscope (SEM), and transmission electron microscope (TEM) techniques. As-hot isostatically pressed (“hipped”) and heat-treated (1010 °C for 50 hours) conditions were compared. The as-hipped specimen had a higher lamellar volume fraction, and it crept more than 100 times faster. The lamellar spacing in the lamellar grains systematically decreased by 15 to 35 %, with increasing stress, during the first 0.1 to 2 % strain. Precipitates containing W, Mo, and/or Si were observed in the deformed gage and undeformed grip sections of the heat-treated specimens. Precipitates are nucleated by heat treatment, but during creep deformation, a more homogeneous and faster growth process occurs in the gage section than in the aged but undeformed grip section. The gage section had a 35 % higher precipitate volume fraction, but their average size was smaller. A lower volume fraction of lamellar grains and the presence of precipitates account for the excellent creep resistance in the heat treated alloy.

8.1 INTRODUCTION

The Ti-Al intermetallic alloys are potential replacements for superalloys in some high-temperature applications in heat engines, turbine engine blades, aerospace and automobile components since it has high specific strength at high temperatures [92,93,128]. The microstructure is affected by composition and heat treatment, and creep properties are sensitive to microstructure. Gamma titanium aluminide can be heat treated to obtain four types of microstructures [110]. The best creep resistance has been observed in fully lamellar microstructures [161]. However, the duplex microstructure is preferred for many applications because it provides a desirable combination of room temperature ductility and toughness [92].

The additions of Cr, Nb, V, Mn, W, Mo and Si, in two phase Ti-Al alloys affect many material properties. 1-3 at% of Cr, V, or Mn can improve the ductility of duplex alloys [143,225-229], but V generally reduces the oxidation resistance[230]. Nb greatly enhances the oxidation resistance [231-233] and slightly improves the creep resistance [232]. The addition of 0.5-1 at.% Si enhances creep strength, the oxidation resistance, and room-temperature fracture toughness of 48at% Al two phase alloys [188,208,234-236]. Si also increases fluidity, and reduces the susceptibility to hot cracking [237]. Mo provides a good balance of strength and ductility in TiAl having very fine equiaxed gamma grains with the α_2 and β phase [210]. Addition of W greatly improves oxidation resistance, and enhances creep resistance [188]. Most of these studies have focused on either room temperature properties, minimum creep rate conditions or stress-rupture properties. However, primary creep resistance is important for practical applications. Gamma based TiAl exhibits primary creep strains that are typical for metals, where the minimum is

reached after about 1% strain. In an effort to decrease the creep rate during primary creep deformation, additions of W, Mo, and Si have significantly increased the time to reach 0.5% strain. A dynamic precipitation process has been indicated in references 231 and 212. Observations of lamellar refinement during primary creep suggest that a significant amount of mechanical twinning occurs parallel to lamellar interfaces as an easy mode of deformation, and this hardens the microstructure [127,205,212,238,239]. In this chapter we analyze microstructural changes during primary creep in Ti-47Al-2Nb-1Mn-0.5W-0.5Mo-0.2Si alloy by characterizing the volume fraction of lamellar and equiaxed microstructures, the distribution of γ thickness and α_2 lath spacing, examination of mechanical twinning, and precipitates with various size, composition, and shapes that interact with dislocations.

8.2 EXPERIMENTAL

The Ti-47Al-2Nb-1Mn-0.5W-0.5Mo-0.2Si alloy was investment cast, hot isostatically pressed (HIPed) at 1260 °C (2300 °F) for 4 hours at 127 MPa in order to eliminate casting porosity at Howmet Corp. Whitehall, MI. The cast 16 mm diameter test bars were heat treated in the two-phase, $\alpha_2 + \gamma$, field at 1010 °C(1850 °F) for 50 hours and air cooled to obtain a duplex microstructure, by the Howmet Corp. The heat treatment is illustrated on the binary phase diagram (see Figure 8.1 [96,97]). Tensile creep specimens with a gage length of 25 mm and 5 mm diameter were machined from the test bars, and creep tests were conducted at the Howmet Corp. One creep specimen (000248) was deformed at 760 °C (1400 °C) at 138 MPa (20ksi) and the other (012784) was deformed at 649 °C (1200 °F) at 276 MPa (40ksi). The specimens were loaded in a few seconds,

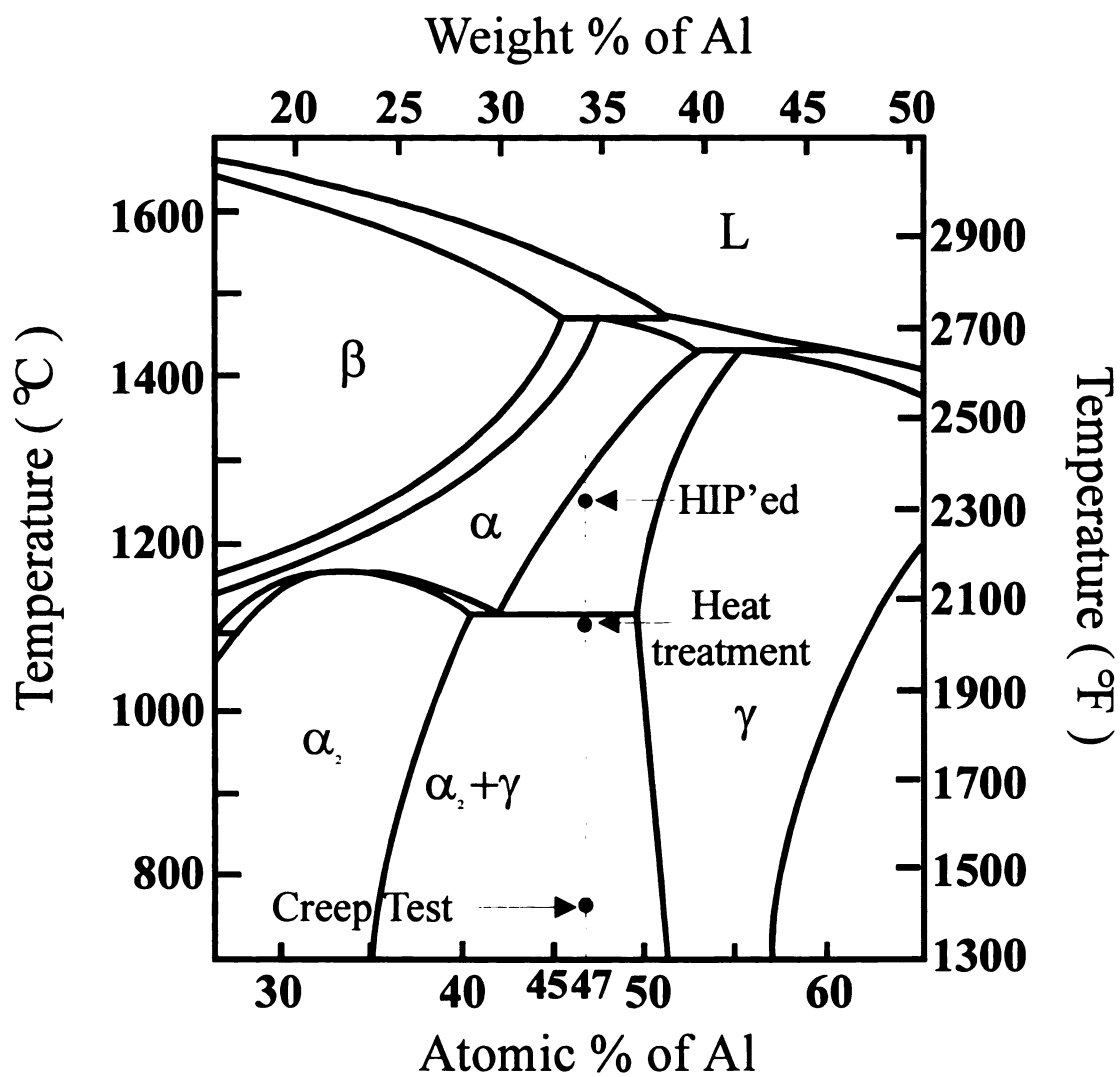


Figure 8.1 A Ti-Al phase diagram near the stoichiometric TiAl composition [96,97]

and data acquisition of one datum each 15 minutes started just after loading. The experiment was stopped when about 0.5% strain was reached, and cooled under load.

Some additional 5x5x3 mm brick shaped specimens were cut using EDM machining from an as-HIPed slice of a 28-mm-square casting gate from a different casting for shear+compression creep tests. The shear+compression experiments were deformed on a 45° inclined stage in an Inconel 718 compression cage fixture developed for evaluating creep in a PST crystal [165,240], as illustrated in Figure 8.2. The top and bottom platens were free to translate in the horizontal direction. Shear+compression creep tests were conducted at 650 and 750 °C in air with equal shear and compression stress components (τ and σ_c) of 61, 91.5 and 122 MPa. They were loaded slowly, to the desired load, in about 3 minutes. Data were recorded using a PC based data acquisition system developed for creep deformation that recorded temperature, load, and displacement. Displacements were measured with an extensometer connected to the compression cage platens with two water cooled external superlinear variable capacitor (SLVC) transducers that were accurate to about 1 μ m. Displacement was converted to shear strain under the assumption of simple shear in the middle of the specimen, where displacement d is related to shear strain $\gamma = \sqrt{2}d / t$, where t is the thickness of the specimen. The principle stresses were determined with Mohr's circle, and they are illustrated in Figure 8.2. The maximum shear stress is 45° from the principle stress state, and it has a value of 1.12 τ . The effective stress for for this loading condition was computed to be $\sigma_e = 1.26\tau$. Since the specimen has compressive stress component with a magnitude equal to the shear stress, there may be some reduction in thickness due to

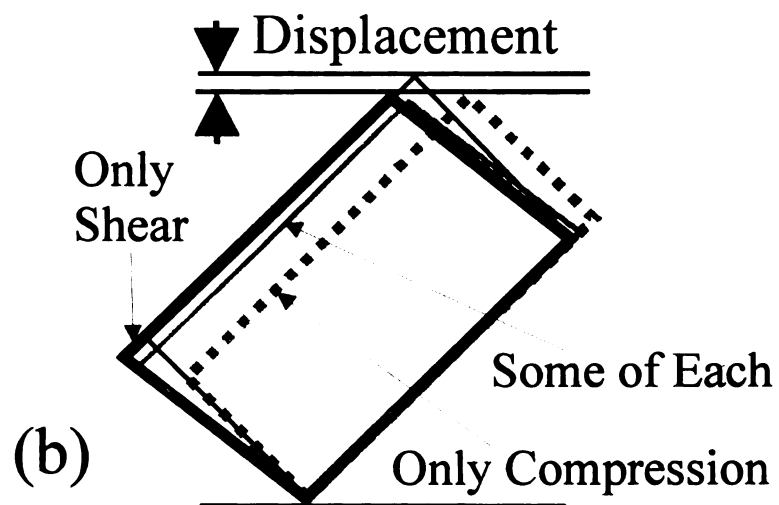
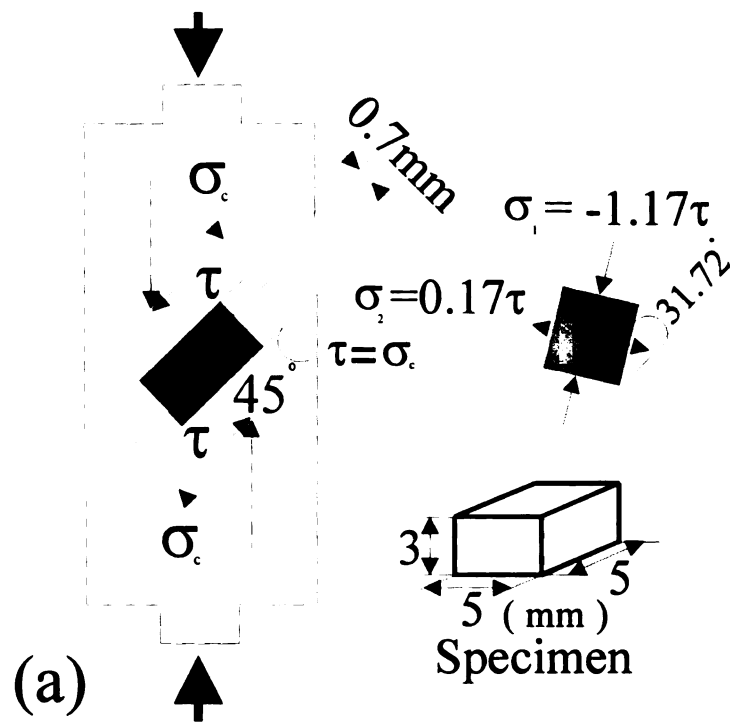


Figure 8.2 Geometry of shear+compression deformation conditions.

deformation. Supposing that all the strain occurred due to compression, then a shape change indicated Figure 8.2.b would occur, and the magnitude of the compressive strain is more than 6 times larger than the shear strain computed by assuming only simple shear (for the measured displacement). If a mixture of shear and compression strain occurred, the resulting shear strain is very nearly the same as obtained using the assumption of only simple shear, as illustrated in Figure 8.2.b. Consequently, the computed simple shear strain is a lower bound on the strain that occurred in the middle of the sample. In order to compare results with tensile experiments, the effective strain was estimated as $\varepsilon_e = \gamma / \sqrt{2}$. Tests were stopped at shear strains of about $\gamma = 0.2, 0.5$ and 1.5% to measure microstructural changes in the middle of the specimen. With such small strains, mechanical measurement of the specimen shape change was not resolvable.

For microstructural analysis of the tensile creep specimens, slices were cut from the middle of the gage and the grip sections of the deformed specimen. For analysis of different phases, polished (unetched) specimens were examined in a JSM-6400V scanning electron microscope (SEM) at 25kV, using the backscattered electron (BSE) technique. LECO 2001 image analyzer software was used to measure the size distribution and volume fraction of precipitates. For optical microscopy, a modified Kroll's reagent (10ml Hydrofluoric acid, 5ml Nitric acid, 35ml Hydrogen peroxide, and 100ml Water, 5 sec., immersion [222]) was used to reveal the microstructure. Lamellar volume fractions were obtained by outlining the shapes of lamellar regions on a piece of transparent plastic covering an optical micrograph, coloring them in, and digitizing the image for image analysis. For micro-analysis by transmission electron microscopy (TEM) the specimens were prepared as follows. First, 0.7 mm thick slices were taken from the specimen using a

diamond saw, and 3 mm discs were produced using an EDM cutting machine such that the foil normal was parallel to the tensile axis. Then, after mechanical polishing, thin foils for electron microscopy were prepared by the twin jet polishing method using a solution of methyl alcohol and 10% sulfuric acid at 20 volts and -25°C. These foils were examined in a Hitachi H-800 TEM operated at 200kV using a double tilt goniometer. Energy dispersive X-ray analysis (EDAX) was conducted on a Philips CM 30 scanning transmission electron microscope (STEM) at Korea Institute of Science and Technology (KIST). X-ray diffraction measurements were made using a Scintag XDS-2000 diffractometer with pole figure goniometers.

8.3 RESULTS

8.3.1 Primary creep behavior

The shear+compression experiments were conducted to examine primary creep behavior in detail. Figures 8.3 and 8.4 illustrate how the creep strain varies with time for the as-HIPed shear+compression and heat-treated tensile deformation conditions investigated. Since zero time represents the time when the creep load is reached, the initial elastic and plastic strain components are not recorded in Figures 8.3 and 8.4. All samples indicate a rapid initial strain rate that decreased rapidly at a strain between 0.1 and 0.3% effective strain. It is common [241] to characterize primary creep deformation using a mathematical model in the form of

$$\epsilon_{\text{primary creep}} = e(1 - \exp(-rt))$$

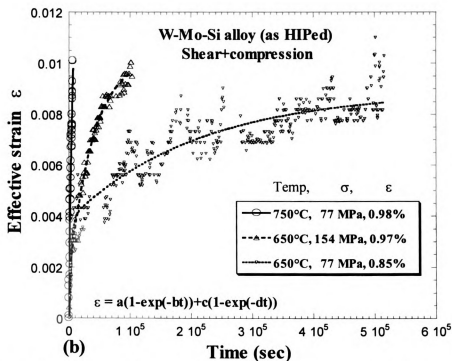
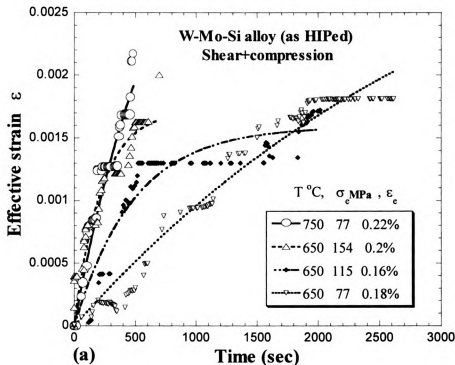


Figure 8.3 Primary creep strains are illustrated a) at low strains (0.2%) in as-HIPed shear+compression specimens, b) at larger strains (1%).

Table 8.1 Curve fit parameters in several experimental conditions

Matl Mode, °C, σ MPa	e_1	r_1	e_2	r_2	R	* R
As-HIP S+C, 750, 77	0.0028287	1.9156e-3	0.097655	1.1681e-5	0.996	0.985
As-HIP S+C, 650, 154	0.0016365	1.7067e-3	0.0086616	2.542e-5	0.990	0.974
As-HIP S+C, 650, 115	0.0015921	7.0764e-3			0.980	0.980
As-HIP S+C, 650, 77	0.0050585	4.7166e-6	0.0038589	3.1558e-4	0.904	0.797
HT Tensile 649, 276	0.0020913	4.6051e-5	0.032154	3.1788e-8	0.998	0.851
HT Tensile 760, 138	0.0013451	2.126e-5	0.066612	5.1683e-7	0.998	0.971

* R for $c=d=0$

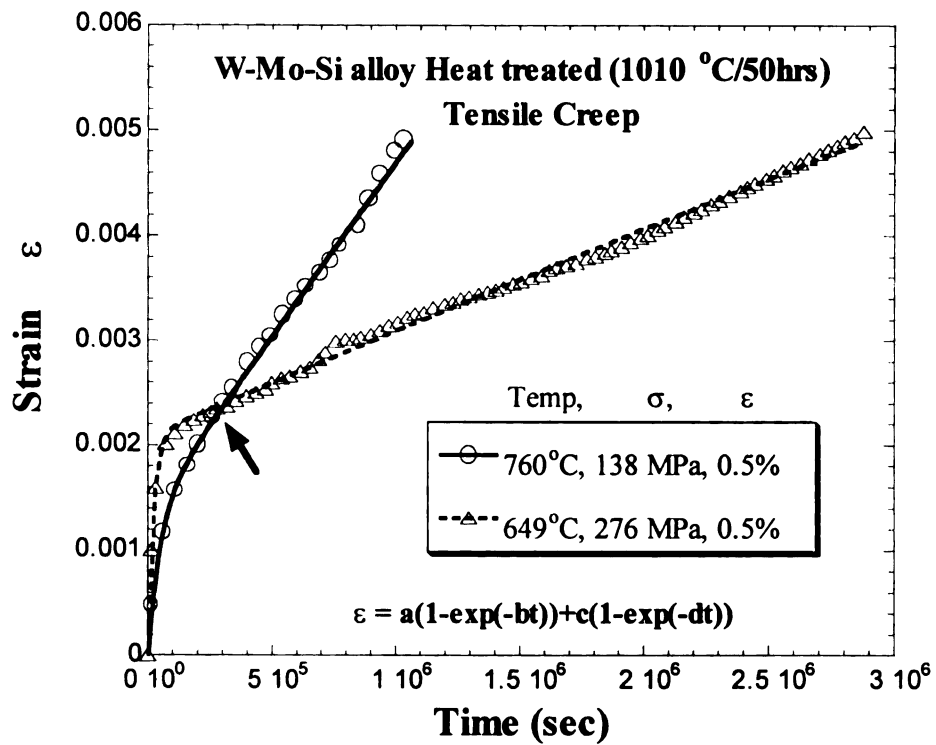


Figure 8.4 Primary creep strains to 0.5% in heat treated tensile specimens with different temperature and stress.

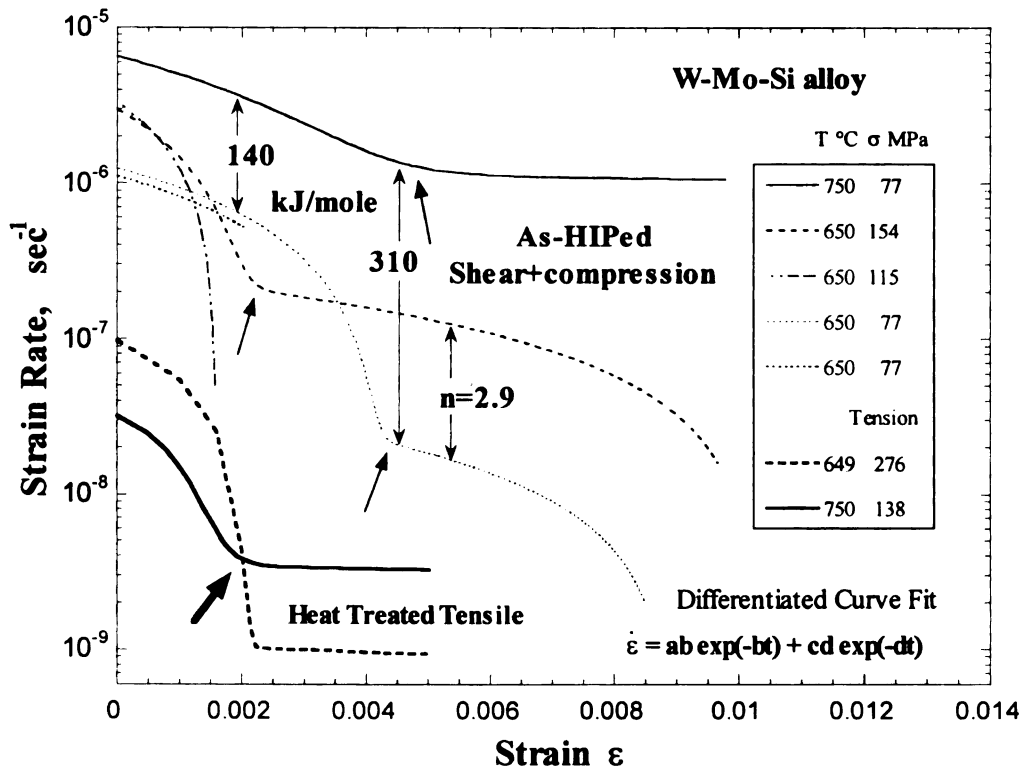


Figure 8.5 Differentiated curve fits (strain rate vs. strain) of data in Figure 8.3 and 8.4.

which describes a process with a rate constant r that slows exponentially with time to reach a saturation strain of e . If the transition in deformation phenomena results from two process that slow down exponentially at different rates, where one saturates earlier than the other, then these two process may be independent and therefore additive, and thus represented by

$$\epsilon_{\text{primary creep}} = e_1(1 - \exp(-r_1t)) + e_2(1 - \exp(-r_2t))$$

This equation was used as a fitting function using Kaleidagraph software to represent the experimental data in a form that can be easily differentiated. The parameters for e_1 and r_1 were determined for the experiments deformed to the lowest strain, and these parameters were used as initial values in the least square fitting process for the larger strain experiments. These fitting parameters are provided in Table 8.1. From the R values, these fitted curves are accurate representations of the primary creep data, and they are more accurate than a curve fit using only one saturation process. The lowest R value obtained was for data taken over many days where room temperature oscillations caused differential thermal expansion strains in the extensometer transducer assembly. This function was then differentiated to represent the creep rate in a smooth manner as shown in Figure 8.5, where the bolder lines represent the creep rates of the heat treated tensile specimens. The effect of these two exponential components of deformation is that a saturation strain is reached for the early e_1 - r_1 process (i.e., the value of e_1) after which creep deformation proceeds at a lower strain rate.

The shape of the strain-rate vs. strain curves in Figure 8.5 is similar for all

specimens, but the details of the shape vary with stress, temperature, heat treatment, and microstructure. At $\sigma_e = 77$ MPa, in the as-HIPed shear+compression specimens, the initial strain rate is about 6 times faster at 760 °C than at 650 °C, and the transition from the early to the later process occurs at a similar strain, near 0.4%. Since these early processes are nearly parallel at the same stress, an apparent activation energy of 140 kJ/mol is obtained. There is a greater decrease in strain-rate in the early process at the lower temperature, so the later process is on the order of 100 times slower at the lower temperature. The apparent activation energy at the beginning of the later process is near 310 kJ/mol. With a stress 2 times higher (154 MPa) at 650 °C, the early process is faster, but it decelerates much more rapidly, and the transition to the later process occurs at a lower strain, near 0.2%. The later process appears to be nearly parallel for the two 650 °C specimens, so a stress exponent of $n \approx 3$ is estimated. At a stress of 115 MPa, between the two other values, the initial creep rate is as high as the specimen at 154 MPa, but it decelerates more rapidly (also evident in Figure 8.3.a). This behavior indicates that the early deformation process at 115 and 154 MPa is different from the early deformation process at 77 MPa.

Similar phenomena are observed for the heat-treated alloy deformed in tension. The specimen deformed at a lower temperature and higher stress (649 °C, 276 MPa) deformed quickly up to 0.2% strain, where the strain rate slowed considerably. At the higher temperature and lower stress (750 °C, 138 MPa), the trend was similar, but the change was less dramatic, leading to a crossover indicated by arrows in Figures 8.4 and 8.5. The stress was higher by a factor of 2, but unlike the comparable data for the as-HIPed material, the initial creep rate of the higher temperature lower stress specimen was

comparatively *slower* for the heat-treated material. Also, the early process exhausted at a strain half as large as in the as-HIPed condition, but this is probably due to the higher stress used in the heat-treated specimens, and the differences in microstructure. This indicates that the heat treatment was very effective in retarding the creep rate, since, in spite of a 60% higher stress, the creep rate was more than 100 times slower.

8.3.2 Microstructures

Optical microstructures for the as-HIPed and heat treated materials are qualitatively very similar, as shown in Figure 8.6. The volume fraction of lamellar grains in the heat treated and creep deformed tensile specimens was about 21% and the as-HIPed specimens had about 59% lamellar grains. In both, equiaxed grains between 5-200 μm were observed, and lamellar grains are on the order of 100-500 μm . Many smaller equiaxed grains are interspersed among the lamellar grain boundaries. Groups of small equiaxed grains are produced during HIP treatment due to large local strains associated with pore closure. The only differences between the two tensile specimens after deformation was that there were more twins in the 649 °C, 276 MPa specimen. There was no other obvious change in the optical microstructure after creep deformation.

Small amounts of β phase were observed in backscattered electron (BSE) image and in X-ray diffraction measurements. The strongest β phase peak (110) was evident in X-ray data shown in Figure 8.7, but higher index β peaks were not detected in any of several diffraction scans on various specimens. The more diffuse peaks are those of the smaller volume fraction phases. In BSE images in Figure 8.8, the brightest phase and the gray phase are β and α_2 phase (Ti_3Al), respectively, and they are located in lamellar

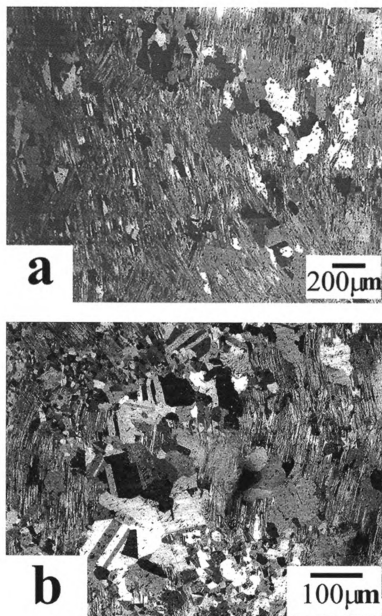


Figure 8.6 Microstructures of Ti-47Al-2Nb-1Mn-0.5W-0.5Mo-0.2Si: (a) As-HIPed condition before deformation (shear vector was subsequently horizontal), (b) Heat Treated tensile gage section deformed at 760 °C, 138 MPa.

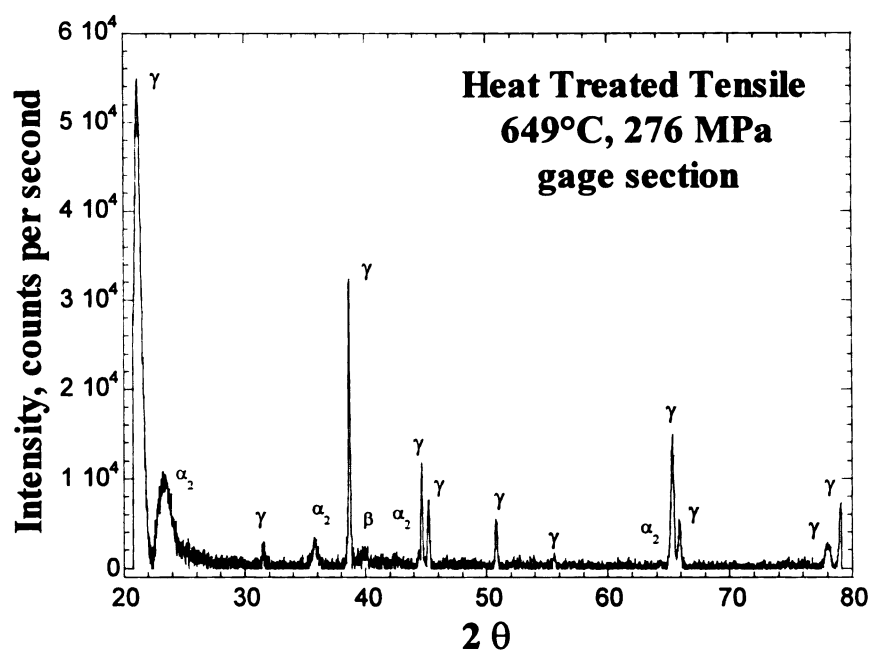


Figure 8.7 X-ray data obtained from the heat treated tensile gage section tested at 649 °C, 276 MPa.

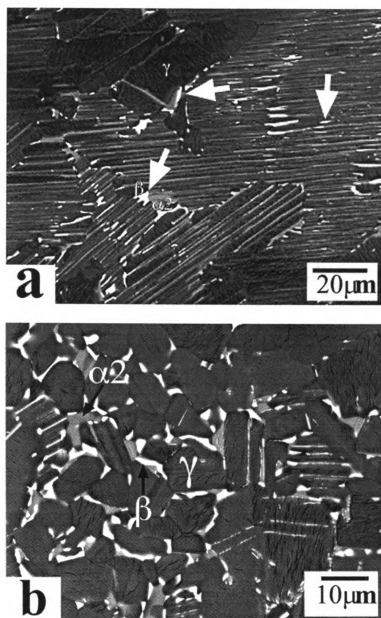


Figure 8.8 BSE image of Ti-47Al-2Nb-1Mn-0.5W-0.5Mo-0.2Si: (a) As-HIPed condition before deformation (b) Specimen tested at 760 °C, 138 MPa (1010 °C/50 hours heat treatment).

boundaries and grain boundaries of equiaxed grains. The dark phase is γ phase (TiAl). The β phase (indicated by arrows) were found in grain boundaries between γ grains and in lamellar grains or in lamellar colony interfaces in both the as-HIPed and heat treated specimens. The β phase has dimensions between 1 and 10 μm , and it is typically angular in shape, or elongated when found in lamellar interfaces. The images in Figures 8.8.a and 8.8.b are typical for comparable regions microstructure in both tensile specimens.

From TEM analysis, Figure 8.9 shows a composite image of a typical region including an equiaxed and a lamellar grain. A number of twins on two twinning planes (white arrows) are evident in the γ grain that appear to have initiated from the lamellar grain boundary. A smaller black arrow shows some more rounded 1-2 μm phases near the lamellar-equiaxed grain boundary. Rounded phases with sizes below 2 μm are denoted hereafter as precipitates, and these are considered as different from the β phase, since they are not only found in interfaces associated with the larger microstructural features. In summary, the important differences between the as-HIPed and heat-treated microstructures are higher lamellar volume fraction in the as-HIPed material and the presence of fine precipitates in the heat treated materials.

a. Precipitates

In higher magnification images from TEM and BSE images, there are many small precipitate phases 2 μm or smaller in the heat-treated microstructure, that are not observed in the as-HIPed microstructure. Precipitates have various shapes with dimensions ranging from 0.05-2 μm . They are evident in lamellar, equiaxed, and interface regions of the deformed microstructure. In lamellar regions they tend to be



Figure 8.9 TEM image of lamellar and equiaxed grains from the specimen tested at 760°C, 138 MPa (1010 °C/50 hours heat treatment).

smaller, and reside in lamellar interfaces, and many of them have a needle shape (Figure 8.10). In equiaxed grains, precipitates are larger, and tend to have an aspect ratio of 2-3 (Figure 8.11). Precipitates always have a high density of dislocations in their vicinity.

In the BSE images in Figure 8.12, they have a brightness (high Z atom content) similar to the β phase, but they are much smaller. They are mostly found in the α_2 phase of lamellar structures. No such precipitates are evident in the as-HIPed lamellar regions as indicated in Figure 8.12.d. The precipitates in lamellar interfaces vary from 0.05-0.45 μm . These precipitates have been identified as Ti_5Si_3 or β in several studies [96,154,185,235]. In comparing the fine precipitates in Figures 8.12.a and 8.12.b, there are more of them in the deformed sample than in the undeformed grip section of the tensile specimen. Figure 8.13 shows the distribution of sizes obtained from precipitates in at least 5 lamellar grains. The area fraction of precipitates in the deformed sample is 35% higher. These observations taken together indicate that precipitation is nucleated by heat treatment, and that a more homogeneous and faster growth process occurs during deformation than in long term static aging at creep temperatures.

On a larger scale, the precipitates are inhomogeneously distributed; some areas seem devoid of precipitates, while in other regions they are readily found. STEM analysis with EDAX of precipitates in various parts of the microstructure indicated some variance in the composition. These measurements are probably sensitive to the size of the precipitate, but in a qualitative sense, there does appear to be more than one composition of precipitate, as some precipitates had significantly different amounts of the refractory elements, and different primitive cell sizes measured in convergent beam electron diffraction [212]. In the larger precipitates, EDAX analysis indicated a higher

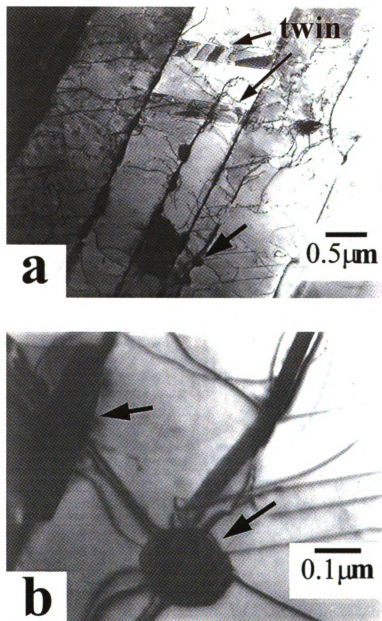


Figure 8.10 Dislocation interactions with particles in lamellar regions. The below image is an enlargement of the precipitate (a) indicated by the arrow (760 °C and 138 MPa).

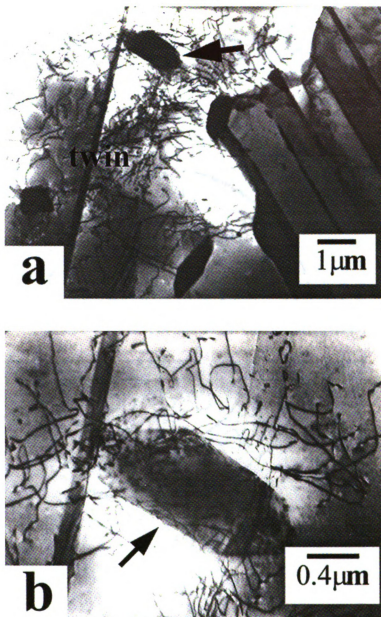


Figure 8.11 Precipitates in equiaxed grains are surrounded by dislocations (649 °C and 276 MPa), (b) an enlargement of the arrowed precipitate in (a).

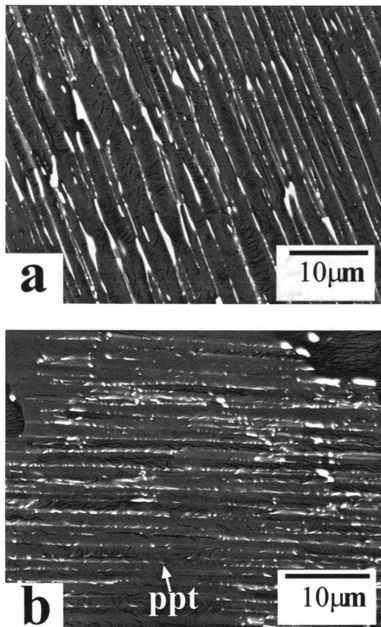


Figure 8.12 BSE images of specimen a) undeformed, b) deformed at 760 °C, 138 MPa (1010 °C/50 hours heat treatment).

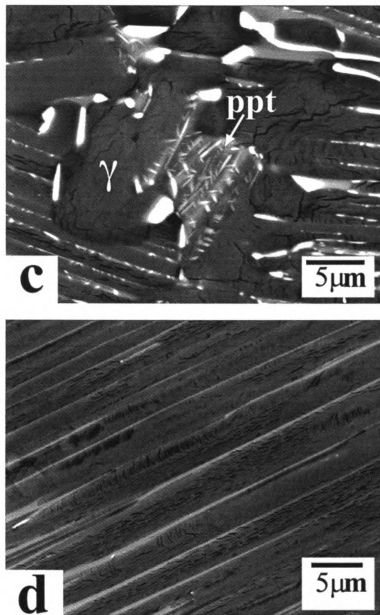


Figure 8.12 BSE images of specimen c) deformed at 760 °C,138 MPa (1010 °C/50 hours heat treatment) d) undeformed as-HIPed condition.

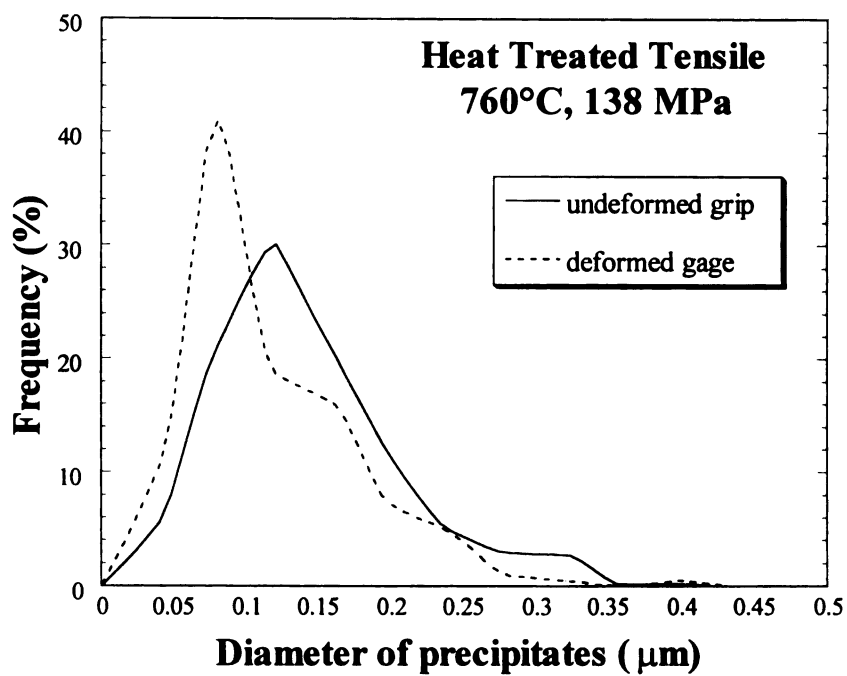


Figure 8.13 Size distribution of precipitates in lamellar grains (tested at 760 °C, 138 MPa).

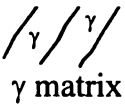
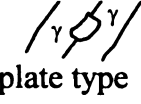
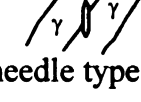



atomic fraction of W, Mo, and Si. Since the silicon peak is adjacent to the aluminum peak, it is difficult to obtain a meaningful estimate of the silicon composition. A summary of the shape and composition of several kinds of precipitates is given in Table 8.2. Figure 8.10.a shows a cross twin in the hard direction within a lamellae. Such twins were rarely seen in these primary creep deformed specimens, though they are more commonly seen at higher strains [47,50,165].

b. Lamellar Spacing

Twinning propagation parallel to the lamellar boundaries is an easy mode of deformation that does not alter the appearance of lamellar microstructures [38]. Figure 8.14 shows a lamellar region where the twin relationship between lamellae is shown at location a. In this figure, two very narrow lamellae are evident in regions marked b and c, where the thin layer has a different contrast from the surrounding lamellae on either side that have the same contrast variations. The similarity on either side of the narrow twin suggests that the thin twin formed in the middle of a pre-existing γ lath. The thin layer is tapered, and thinner toward the left side of the image, suggesting that it was growing from right to left by a mechanical twinning mechanism such as that described by Jin [120,121]. The effect of propagating mechanical twins parallel to the lamellar interface is that two new interfaces are created, and the thickness of the γ lamellae are reduced.

Figure 8.15 shows that the lamellar spacing was refined during creep deformation in the tensile heat treated specimens. The lamellar colony in the undeformed grip section has a lamellar spacing of approximately $1\mu\text{m}$, whereas a lamellar colony in the deformed gage section has a typical spacing less than $0.5\mu\text{m}$ (Figure 8.15.b). Although there are

Table 8.2 Summary of Precipitate Composition and Shapes (at% of element)

Type of precipitate	Ti	Al	Mn	W	Nb	Mo	Si
 γ matrix	45.5	46.0	0.5	0.5	2.9	0.6	
 plate type	54.2	35.0	0.8	3.4	2.3	4.3	*
 needle type	51.3	39.6	0.8	2.4	2.8	3.2	*
 rectangular type	55.2	27.6	1.2	6.1	2.9	7.1	*
 spherical type	54.2	30.0	1.4	6.0	2.6	6.0	*
 needle type	54.1	29.9	1.4	6.0	2.6	6.0	0.2

* Si composition is less than 0.1 at% from Energy Dispersive X-ray analysis.

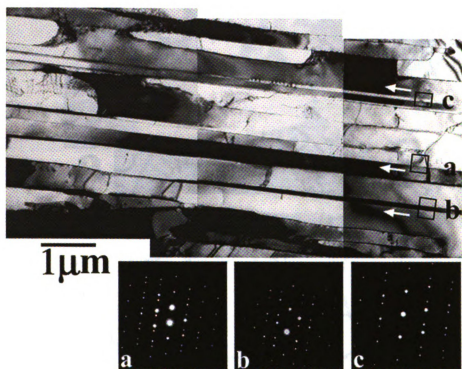


Figure 8.14 Lamellar refinement process is illustrated as indicated by arrows. Diffraction patterns in boxes a, b, and c illustrate true twin relationship.

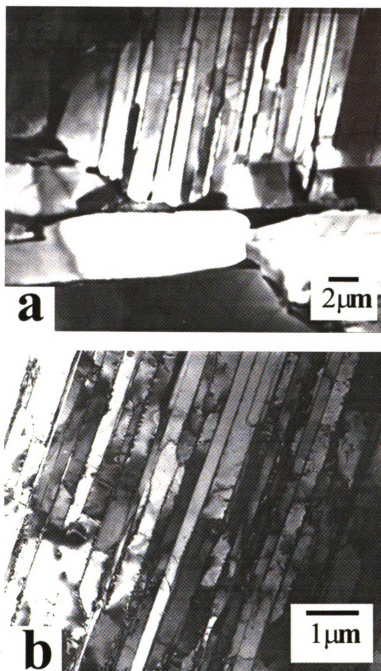


Figure 8.15 Lamellar spacing was refined after creep deformation (760 °C and 138 MPa):
(a) undeformed grip section and (b) deformed gage section.

variations in the lamellar spacing in duplex microstructures, these observations of lamellar refining in the creep deformed lamellae are typical. This indicates that mechanical twinning is an important deformation mode in lamellae of TiAl alloys, as described in Reference 50,141,240,244.

The change in lamellar spacing in the heat-treated tensile specimens was characterized statistically. The α_2 spacing was determined by measuring the distance between two α_2/γ interfaces and the γ thickness was determined by measuring the thickness of γ laths. In regions near grain boundaries, 250-400 α_2 spacing counts in more than 20 lamellar regions and at least 100 γ lamellar interface spacings in about 6 different regions yielded the distributions shown in Figure 8.16. There is a shift of the frequency distribution toward smaller spacings due to small creep strains. This refinement of spacing is consistent with previous studies that include other alloys [141,205,212,239]. The average values are presented in Figure 8.17, where a 34% reduction in α_2 spacing and a 24% reduction in γ thickness occurred for the specimen deformed at 760 °C, 138 MPa.

The lamellar spacing in the as-HIPed shear+compression samples was characterized from about 500 measurements of α_2 spacing in BSE images of 25 lamellar regions that are near grain boundaries, before and after creep deformation. The average lamellar spacing in three undeformed specimens provided average values between 1.32 and 1.43 μm . This 8% variation is representative of this quantification method, which also neglects effects from lamellar plane normals that are not on the surface of the specimen. The distribution of α_2 spacings is represented in Figure 8.18.a for the average

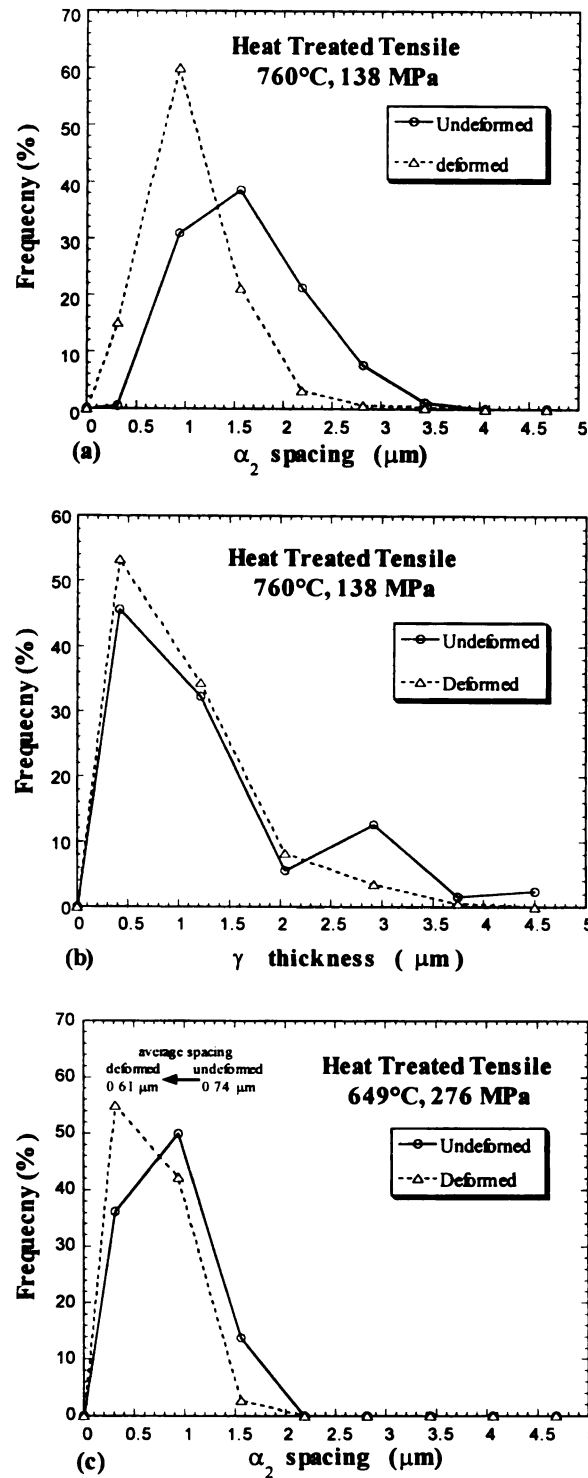


Figure 8.16 a), b) Distribution of α_2 spacing and γ thickness in 750 °C and 138 MPa, and c) α_2 spacing in 649 °C and 276 MPa specimens in undeformed grip and deformed gage section of heat treated tensile creep specimens.

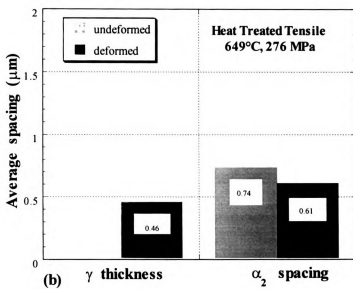
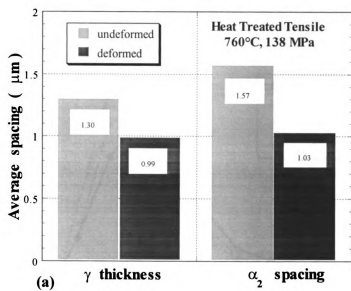


Figure 8.17 Average α_2 spacing and γ thickness in tensile creep specimens a) 760 °C and 138 MPa, and b) 649 °C and 276 MPa before and after creep deformation.

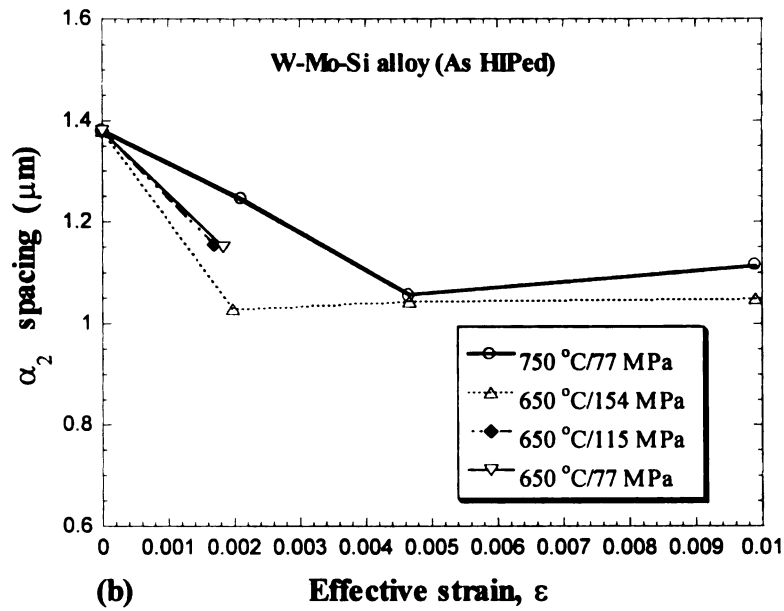
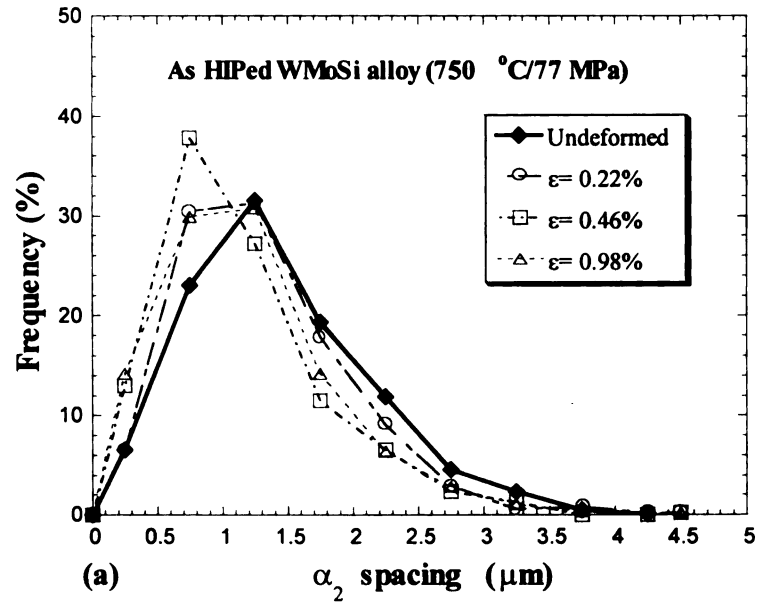


Figure 8.18 a) Frequency of α_2 spacings based on about 500 counts in 25 lamellar regions after compression-shear deformation at 750 °C and 77 MPa, b) α_2 spacing resulting from different effective strains at 650 °C and 750 °C.

of three undeformed specimens, and after three levels of strain at 750 °C and 77 MPa. In every case, there is a nominally similar shift of the frequency distribution toward smaller spacings due to small creep strains. The average α_2 spacing is plotted with respect to effective strain and stress in Figure 8.18.b. There is about 23% reduction in the α_2 lamellar spacing with strain that saturates at effective strains between 0.2 and 0.5%, whereafter the spacing remains relatively constant, or increases slightly. At a strain of 0.2%, the amount of refinement at 750°C is about half of the amount that occurred at 650°C. The amount of refinement at 650°C increases with increasing stresses. At 0.2% strain, where the reduced spacing saturated at 23% at 154 MPa, only 16% reduction was observed at lower stresses (Figure 8.18.b).

Contrary to the observations in the as-HIPed shear+compression specimens, the reduction in α_2 spacing was smaller (18%) in the 650 °C 276 MPa tensile heat treated specimen, but this specimen had a lower undeformed lamellar spacing value. The deformed lamellar spacing (0.61 μm) in this higher stress specimen is much smaller than the spacing for the deformed 760 °C 138 MPa specimen (1.03 μm). Unlike the shear+compression specimens, the undeformed lamellar spacing was measured in the grip section of the creep specimens, which experienced the same thermal history with presumably no stress. The shear+compression specimens all came from the same physical region of the casting, but nothing is known about the relative positions of the two tensile specimens in the casting, where the initial lamellar spacing may have differed due to differences in cooling rates, or other unidentified process parameters. In summary, the lamellar spacing is reduced more quickly and saturates at a smaller value with increasing stress.

8.4 DISCUSSION

The lamellar structure is modified in three ways due to small creep strains, by a reduction in the γ thickness [127,239], which can only occur by mechanical twinning [121], as well as a reduction in the α_2 spacing and thickness due to a strain induced phase transformation [125,127]. The refinement of lamellar spacing presented above is mostly based on α_2 spacing changes during primary creep deformation. These changes correlate with reductions in γ thickness, as indicated in 8. 15 through 8.17 and in Reference 127. Measurements of α_2 spacings is the most convenient way to characterize lamellar refinement, and it serves as an indirect representation of lamellar refinement that also occurs by mechanical twinning in the γ laths.

Mechanical twinning parallel to lamellar interfaces accounts for the lamellar refinement during initial creep deformation. From Figures 8.17 and 8.18, the larger reduction in lamellar spacing with lower temperature and higher stress is consistent with the observation that more twinning was observed with lower temperature deformation in equiaxed grains [50], due to greater self locking behavior of ordinary dislocations at lower temperatures [245]. Since mechanical twinning is limited more by nucleation processes that require large stress concentrations, a lesser stress is also consistent with less twin nucleation [121]. Since mechanical twinning parallel to lamellar interfaces correlates closely with the early process of primary creep deformation, then it is apparent that for a given stress, much of the primary creep strain is taken up by saturation of the easy mode of deformation twinning in lamellar regions. Accommodation of this easy mode of deformation in surrounding γ grains by mechanical twinning is evident in Figure 8.9.

The rate parameters in Figure 8.5 for the early process of $n = 3$ and an activation energy of about 140 kJ/mol is similar to that observed in creep of PST crystals oriented for shear deformation on planes parallel to the lamellar interfaces [165,240]. This low activation energy is consistent with pipe diffusion processes as well as thermally activated glide of ordinary dislocations [245]. Once this initial easy mode has saturated, the relative contribution of mechanical twinning to the total strain is substantially reduced. The apparent activation energy is increased to a value near lattice diffusion, where the rate limiting process for dislocation motion changes. This transition in deformation mode can be easily correlated by comparing Figures 8.5 and 8.18.

Mechanical twinning and dislocation motion are co-deformation mechanisms in the early stages of creep. Twin interfaces and α_2 lamellae are well known to provide barriers to dislocations, so both mechanisms provide a hardening contribution to the alloy. Luster and Morris [142] have shown that deformation modes are restricted to twinning or dislocation motion parallel to the lamellar interface in lamellae thinner than about 0.5 μm . Furthermore, mechanical twinning rotates the crystal into an orientation where only superdislocations have a high Schmid factor for deformation [141]. Thus more twinning refinement results in a harder microstructure, and consequently a greater reduction in strain rate at the saturation of the early process (Figures 8.5 and 8.18).

Jin has shown that the interface of a γ/γ twin boundary actually represents 4 atomic layers with the same stacking arrangement as the α_2 phase [120]. If the twin interface represents a nucleating process for precipitation of α_2 , then these initially 4 layer α_2 films may have grown in thickness, and contributed to the measured reduction in

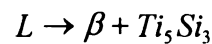
average α_2 spacing. Table 8.3 shows how typical diffusion distances vary with time and temperature [246].

Table 8.3 Diffusion distances of Ti in TiAl

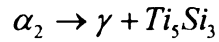
T, °C, condition	t, hr	\sqrt{Dt} , μm
1260 HIP	4	16.36
1010 Heat Treatment	50	6.26
760 Creep 0.5%	289	0.554
760 Creep 0.2%	50	0.231
649 Creep 0.5%	800	0.120
649 Creep 0.2%	50	0.030

For the 760 °C specimen, the average γ thickness is nearly equal to the α_2 spacing, and the typical diffusion distance at the end of the experiment is 54% of the measured α_2 spacing. Since there is a thermodynamic driving force to move Ti out of existing γ layers (see Figure 8.1), the twin interface provides a sink for the rejected Ti atoms. The typical diffusion distance is 20% of the average α_2 spacing for the 650 °C specimen. This is consistent with the final γ thickness being smaller than the α_2 spacing, since fewer Ti atoms could reach a newly created twin interface.

The heat treatment and strain-induced precipitation process during creep deformation in this Si-containing alloy result in the formation of silicide precipitates [185,212]. Two mechanisms for silicide precipitate formation were reported by Noda *et al.* [185]. These precipitates could be produced during solidification through the eutectic reaction:



or nucleated at the interface of γ and α_2 , through the eutectoid reaction:



where the α_2 layer was thinned by consumption via the eutectoid reaction. Since there were no precipitates in the as-HIPed condition, the formation of precipitates during heat treatment in this alloy is more likely to come from the α_2 eutectoid reaction. However, this mechanism cannot be the only one to account for reduction of α_2 thickness since non-Si bearing alloys also exhibit a reduction in α_2 thickness [127,239].

The solute atoms and precipitates interfere with dislocation motion. The existence of precipitates in lamellar interfaces inhibit interfacial dislocation motion [154,247]. The fact that more precipitates and twins were observed in the deformed gage sections suggests that precipitates nucleated during heat treatment grow faster and more homogeneously with the assistance of strain. It is known that W in solution will cause dislocation drag [188]. With deformation, a dislocation impeded by a precipitate will provide a pipe through which the heavier elements can travel more rapidly to the precipitate. The dislocations sweeping through the matrix can thus accelerate and homogenize precipitation by collecting solute elements and then piping them to growing precipitates. This phenomena can account for the more homogeneous and rapid growth of precipitates in the strained material as well as the larger size in the equiaxed grains, where the dislocation pipes sweep a larger volume than they could in the lamellar regions.

The precipitates interfere with deformation processes throughout the microstructure. They have various shapes, and although some precipitates have been

identified as silicides, it is also possible that some are β phase, since they have similar Z content and many morphologies are observed. W and Mo are known as a β phase stabilizers [169,247,248]. The presence of precipitates clearly reduces the creep rate compared to the as-HIPed condition, as illustrated in Figure 8.5, which shows that the creep rates are more than two orders of magnitude smaller due to the heat treatment that causes precipitation. However, the lower creep rate may also result from a smaller volume fraction of lamellar grains because a smaller volume fraction of material would deform by the early mechanical twinning process. The shapes of the creep deformation curves indicate that the same physical mechanical twinning processes occur in both microstructures, regardless of lamellar volume fraction and the precipitate content.

8.5 CONCLUSIONS

TEM analysis of the microstructures of creep deformed Ti-47Al-2Nb-1Mn-0.5W-0.5Mo-0.2Si alloy shows a number of microstructural changes resulting from heat treatment and creep deformation. Refinement of lamellar regions occurs by mechanical twinning and a strain assisted transformation process. Mechanical twins are introduced into both lamellar and equiaxed grains starting from grain boundary interfaces. A rapid initial mechanical twinning process parallel to lamellar interfaces initially hardens the microstructure, and a higher stress increases the amount of mechanical twinning and hardening that occurs. Less mechanical twinning occurs at 760 °C than at 650 °C at the same stress.

Precipitates nucleated by heat treatment grow with the assistance of strain or consumption of α_2 . Many precipitates containing W, Mo and Si are found, but there is

considerable variety in the composition, crystal structure, shape, and size, which all depend on their location in the microstructure. After heat treatment and a 0.5% creep strain, the precipitates vary in size from 0.05 to 2 μm , and larger precipitates are found in the equiaxed regions. The nucleation and growth of these precipitates interferes with dislocation motion, and also hardens the microstructure. Precipitate growth is faster and more homogeneously observed in deforming regions than nonstrained regions, because dislocation pipes provide transport paths for solute elements that homogenize precipitate growth. This precipitation hardening mechanism accounts for much of the excellent creep resistance of this alloy when it was heat-treated.

CHAPTER 9

SHEAR +COMPRESSION CREEP DEFORMATION IN POLYSYNTHETICALLY TWINNED (PST) Ti-47Al-2Nb-2Cr WITH <110> AND <112> ORIENTATIONS

ABSTRACT

Stress and temperature change creep experiments under a compression shear stress state were conducted on Polysynthetically Twinned (PST) crystals prepared from a cast and HIPed Ti-47Al-2Cr-2Nb alloy. Specimens with <110> and <112> directions parallel to the principle resolved shear stress in a shear+compression deformation mode, and the deformation characteristics are compared. Transient creep of the PST crystal after stress and temperature changes (at 9.5~34 MPa and 760~806 °C) exhibited 'normal' behavior and indicates Class M type creep deformation in TiAl. The stress exponent n changes from 3.1 to 5.3 with increasing strain. The activation energy $Q = 137$ kJ/mole at 28 MPa for the <110> PST indicates that dislocation glide aided by pipe diffusion is a likely mechanism of creep deformation in this deformation regime. The activation energy (185 kJ/mole at 13 MPa) of the <112> PST is higher than the <110> PST crystal, but primary creep in the <112> direction occurs much faster than for the <110> direction at a higher stress. Primary creep at 9.5 MPa in the <112> direction caused a 25% refinement of lamellar spacing that hardened the microstructure, indicating that mechanical twinning parallel to the lamellar planes provided an easy initial deformation path during primary creep. At strains near 1%, the creep strength of the two orientations becomes similar.

9.1 INTRODUCTION

Gamma Titanium Aluminide (TiAl) based materials are candidates for high temperature structural applications because of their low density, high specific strength and stiffness at elevated temperature, and high resistance to oxidation and creep. For service at high temperature, it is very important to understand the creep behavior of TiAl based alloys. However, only limited research has been accomplished and there are still many mysteries regarding the creep mechanisms of TiAl. The wide range of values for the apparent stress exponent ($n=2\sim8$) and activation energy (80~600 kJ/mole) [161,163,169,178,183,249] suggest that complicated mechanisms of deformation are involved in TiAl creep behavior. Polysynthetically twinned (PST) crystals provide a fundamental unit of microstructure of the lamellar colonies present in polycrystalline materials. A study of creep in PST crystals should assist in analyzing and developing theories for creep properties of near-gamma alloys. Experiments which remove the effects of microstructure are very helpful to examine the fundamental mechanisms of creep in TiAl.

Stress and temperature change creep tests under compression and shear stress on carefully oriented PST crystals with $\langle 110 \rangle$ and $\langle 112 \rangle$ directions parallel to the principle shear stress were conducted on the alloy Ti-47Al-2Cr-2Nb. The results of stress and temperature change creep tests were analyzed using the power law equation and a modified θ -projection concept equation to examine creep deformation [250]. These experiments covered a limited range of stresses and temperatures so that stress exponents and activation energies can be measured for nominally similar microstructures to examine the fundamental mechanisms for creep deformation. Since lamellar refinement has been

proposed as an important primary creep mechanism [165], microstructures of PST crystals oriented in the $\langle 112 \rangle$ direction were characterized at an early stage of primary creep.

9.2 EXPERIMENTAL DETAILS

9.2.1 Specimen preparation and shear+compression creep test

The PST crystal was grown from a rod of Ti-47Al-2Cr-2Nb that was sectioned into a quarter-circle using EDM machining. The crystals were grown [165] using the ASGAL optical floating zone furnace at the University of Pennsylvania in the LSRM facility. The crystal were grown in a flowing argon environment using the same material as seed and feed crystals. The seed and feed was translated vertically through the hot zone to obtain a growth rate of 5 mm/hr. This PST crystal was oriented using a Laue camera, and a 5 x 5 x 3 mm brick was cut with a diamond saw so that the $\{111\}$ lamellar plane was parallel to the 5 x 5 mm surface as shown in Figure 9.1, and the $\langle 110 \rangle$ and $\langle 112 \rangle$ directions were normal to one of the other faces. By using an X-ray diffractometer with a texture goniometer, the deviation from the desired $\{111\}\langle 110 \rangle$ and $\{111\}\langle 112 \rangle$ orientation was determined to be less than 2° .

A compression cage fixture that imposes a shear traction 45° to the compression axis was developed for evaluating creep in PST crystals under maximum resolved shear stress state [165], as shown in Figure 9.1. The $\{111\}$ lamellar planes were parallel to the 45° surface from the loading axis, and normal dislocation $\langle 110 \rangle$ directions or twin dislocation $\langle 112 \rangle$ directions were consequently parallel to the principle resolved shear stress. Shear and compression stresses of the same magnitude were simultaneously

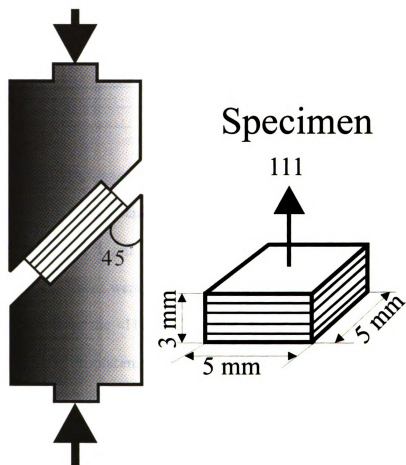


Figure 9.1 Shear+Compression fixture used for creep deformation of 5x5x3 mm PST crystal bricks. PST crystal is shown in soft orientation.

imposed on two PST crystals crept at various temperatures and stresses as shown in Table 9. 1 in air and argon atmosphere using an ATS series 2710 creep testing machine.

Table 9. 1 The conditions for each Shear+Compression creep test.

Specimen	<110> PST	<112> PST
Microstructure	Fully lamellar	Fully lamellar
Test temperature	760 ~ 806°C	760 ~ 806°C
Test stress	$\tau, \sigma = 22 \sim 34$ MPa	$\tau, \sigma = 9.5 \sim 27$ MPa
Final strain	$\gamma = 0.068$	$\gamma = \sim 0.09$
Test atmosphere	Ar	Air

The specimen shape change was measured using external extensometry connected to the compression cage and SLVC transducers located outside of the furnace, providing a displacement resolution of 1 μm . They were loaded to the desired stress in about 3 minutes. The creep specimens were cooled under 80% of the creep load at selected small strains of 0.6%, 1.38% for the <112> PST crystal, and at the final strain. The specimen load, temperature, and displacement-time data were recorded by a PC based data acquisition system developed for creep tests. Assuming simple shear deformation, i.e., no compression strain in the hard direction, $\gamma = (2)^{1/2} \Delta l/t$, where Δl (mm) = $2.54 \times 10^{-4} \Delta V$ (mV) and $t=3$ mm thick sample, the shear stress and strain data were obtained with the aid of spreadsheet and plotting programs.

For microstructure analysis, a JSM-6400 scanning electron microscope was used at 25 kV in the backscattered electron mode. X-ray analysis was conducted by using a Scintag XDS 2000 X-ray diffractometer with a texture goniometer.

9.2.2 Data acquisition and analysis

The automated data acquisition system consists of a PC with a National Instruments AT-MIO-16 board. A resolution of 5 mV provided a shear strain resolution of 0.04%. Multiple-channel scanning was used to obtain 1000 points per second for each channel of data, and these values were averaged. An average value was retained when the value was significantly different from the previously stored datum.

Based on the physical understanding of creep deformation in primary and secondary stages, the θ -projection concept constitutive equation is described in [250]. A variation of the θ -projection constitutive equation was used to analyze creep data. A modification of this equation was used to account for various starting times for a particular deformation condition following a stress or temperature *increase* [251]. The modified equation for transient creep after stress and temperature increase is

$$\varepsilon = \varepsilon_0 + A \{ 1 - \exp(-\alpha (t - t_0)) \} + \dot{\varepsilon}_s (t - t_0) \quad (1)$$

where ε_0 is an adjustable reference strain parameter, t_0 is starting time for a particular loading condition. $\dot{\varepsilon}_s$ is the steady state (or minimum) strain rate, A and α are curve fitting parameters. In the case of transient creep after stress and temperature *decrease*, the constitutive equation is

$$\varepsilon = \varepsilon_0 + B \exp(-\beta (t - t_0)) + \dot{\varepsilon}_s (t - t_0) \quad (2)$$

Differentiating equations (1) and (2),

$$\dot{\epsilon} = A\alpha \exp(-\alpha (t - t_0)) + \dot{\epsilon}_s \quad (3)$$

and

$$\dot{\epsilon} = -B\beta \exp(-\alpha (t - t_0)) + \dot{\epsilon}_s \quad (4)$$

Equation (3) implies that the creep rate during the primary stage decreases gradually towards a “steady state” value, $\dot{\epsilon}_s$, with times greater than t_0 , and equation (4) indicates a gradual increase in creep rate towards a “steady state value”.

9.3 RESULTS AND DISCUSSION

9.3.1 Creep behavior

In general, the stress change experiment is used to evaluate substructure evolution during creep deformation. The temperature change experiment is seldom used because it is not easy to quickly control the temperature fluctuation after temperature changes. From our observations after temperature changes, the temperature generally fluctuated in the range of T_c (creep temperature) $\pm 5^\circ\text{C}$ for a half hour before T_c became stable. This effect may have caused uncertainties in the interpretations of transient behaviors, but the subsequent steady state values are unaffected.

The creep curves of $\langle 110 \rangle$ and $\langle 112 \rangle$ PST crystals with stress and temperature changes are shown in Figures 9.2 and 9.3. The lines through the data represent the curve fit to equations (1) and (2). As the stress or temperature increases, an instantaneous strain is followed by creep which decelerates toward the new (higher) steady-state rate. With stress or temperature decreases, a reduction in strain is followed by transient creep which

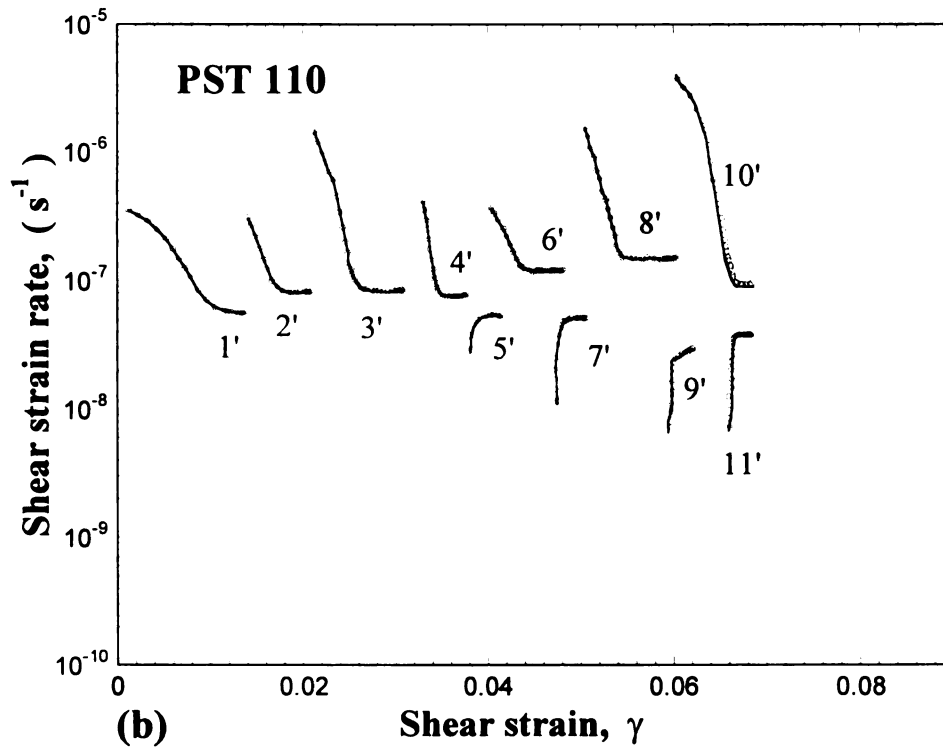
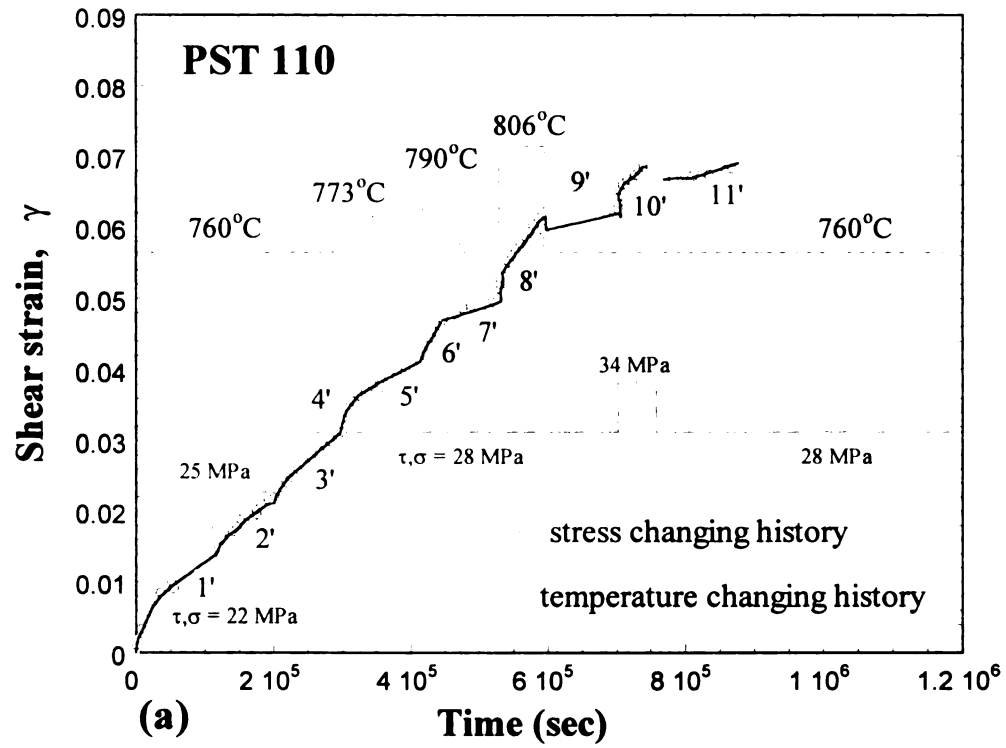


Figure 9.2 Creep deformation of $\langle 110 \rangle$ PST crystal in Ar (with curve fitting)
 (a) strain vs. time curve (b) strain vs. strain-rate curve.

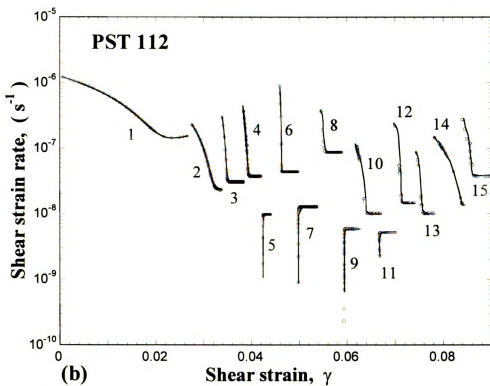
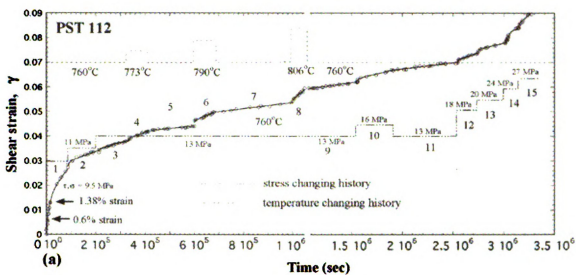


Figure 9.3 Creep deformation of $\langle 112 \rangle$ PST crystal in air (with curve fitting)
 (a) strain vs. time curve (b) strain vs. strain-rate curve.

accelerates to a new (lower) steady state. This typical form of “normal” transient behavior is consistent with the TEM observation of dislocation network observed by many researchers, such as Jin et al. [194] in polycrystalline TiAl. They found that the creep deformation mode in TiAl is pure metal type (Class M) and subgrain boundaries were observed both in equiaxed gamma grains and within gamma laths in lamellar grains in the creep deformed specimen of duplex microstructure. This indicates that stress and temperature have a similar influence on the substructure changes.

By comparing creep curves in the $\langle 110 \rangle$ and $\langle 112 \rangle$ PST crystals, primary creep deformation in the $\langle 112 \rangle$ oriented PST crystal is much faster than the $\langle 110 \rangle$ oriented PST crystal, even though the stress is much lower. Primary creep processes lasted until about 3.5 % shear strain was reached in the $\langle 112 \rangle$ specimen as compared to 1 % shear strain in the $\langle 110 \rangle$ specimen. Since mechanical twinning has the highest resolved shear stress in the $\langle 112 \rangle$ direction it apparently has a lower flow stress in creep than ordinary dislocations, which have the highest resolved shear stress in the $\langle 110 \rangle$ direction.

9.3.2 Activation energy

From the slope of a plot of $\log \dot{\epsilon}_s$ vs. $(1/T)$, the apparent activation energy for creep can be calculated. Figures 9.2.b and 9.3.b show that the transient creep was usually exhausted so that a well defined steady state value could be obtained from the curve fit parameter in equations 1 and 2. The activation energy $Q_C = 137$ kJ/mole for $\langle 110 \rangle$ PST crystal and $Q_C = 185$ kJ/mole was obtained in the temperature range of 760~806 °C, as shown in Figure 9.4.a. Polycrystal samples from which the PST crystals were grown exhibited much higher activation energies between 229 ~ 574 kJ/mole in samples

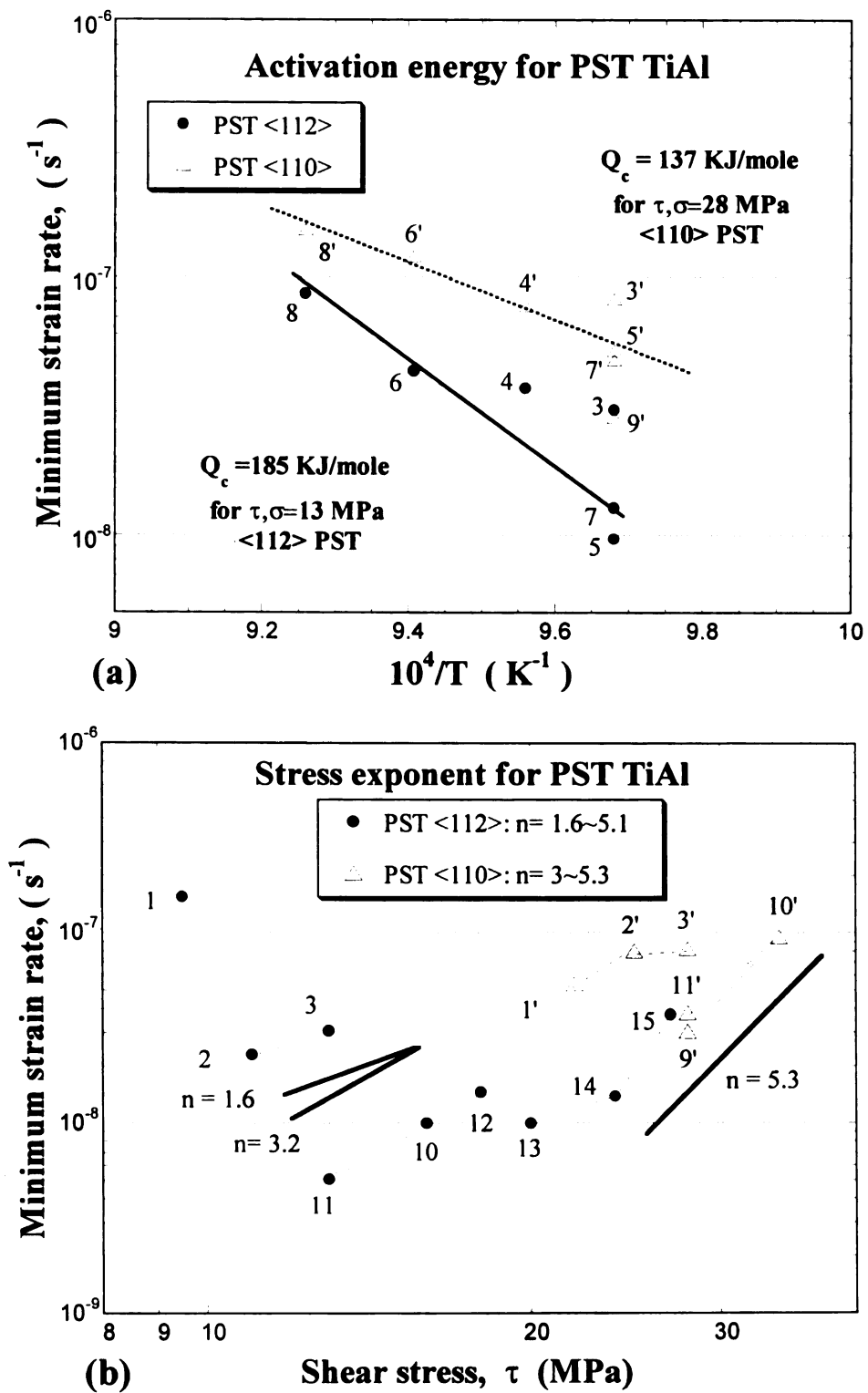


Figure 9.4 a) Temperature and b) Stress dependence of minimum creep rate for PST crystals. Numbers next to datum points refer to Figures 9.2 and 9.3.

deformed in the same way [251]. The lower activation energy may be due to the presence of an easy mode of deformation that is not present in polycrystals which exhibit activation energies typically between 250-450 kJ/mol. The activation energy of the $\langle 110 \rangle$ PST crystal is similar to the activation energy of 150 kJ/mole for interdiffusion in γ -TiAl which was reported by Ouchi et al. [252]. Pipe or grain boundary diffusion is commonly understood to occur with an activation energy of about half of the lattice diffusion energy, which is consistent with the measured values in the PST crystal. Also, an activation energy value of 130 kJ/mole for thermally activated glide of screw dislocations in γ -TiAl at room temperature was reported by Appel et al. [245]. However, the activation energy of $\langle 112 \rangle$ PST crystal is higher than that of $\langle 110 \rangle$ PST crystal, which indicates that the creep deformation mechanisms are either dependent on stress, or significantly different in these orientations.

9.3.3 Stress exponent

According to the power law equation, at each temperature, the stress exponent is given by the gradient of the $\log \dot{\epsilon}_s$ vs. $\log \sigma$ plot. This gradient is shown for each steady-state strain-rate that resulted from the stress changes as the experiment progressed, as shown by the lines in Figure 9.4.b. Thus, by comparing the minimum creep rates following stress changes in the strain range of 1~3% and 6~7%, the stress exponents $n=3.1$ and $n=5.3$ were observed in the $\langle 110 \rangle$ PST crystal, and $n=1.6$, 3.2, and 5.1 were observed at strains of 3~4%, 6~7%, and 7~9% in the $\langle 112 \rangle$ PST crystal, respectively. Furthermore, the $\langle 112 \rangle$ PST crystal is softer than the $\langle 110 \rangle$ PST crystal, since these data

lie above the trend of the $\langle 110 \rangle$ PST crystal data. Both specimens exhibited a hardening trend with increasing strain.

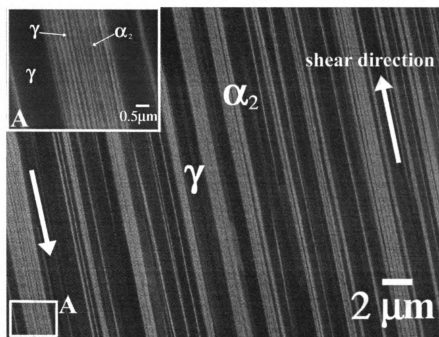
The stress exponent of $n=3$ is characteristic of dislocation glide creep and $n=5$ for dislocation climb creep. In the $\langle 110 \rangle$ PST crystal orientation, there are two possible ways to explain a stress exponent of $n=3$. One is to assume that steady state was not reached in the strain range of 1 ~3%, so as to discredit this measured value. However, minimum strain rates are commonly observed in the range of 1-3% strain in many studies. In the case of the PST crystal deformed in the $\langle 112 \rangle$ direction, $n=1.6$ was measured in the range of 3 ~4% strain. Due to the large primary creep strain in the $\langle 112 \rangle$ specimen, the lack of an early steady state may account for the low n value. Stress exponent values increased with stress, such that both crystals appear to approach $n=5.1\sim 5.3$ mechanism at larger strains.

From the interpretation of the steady-state creep rate and the fitting parameters of equations (1) and (2), the stress exponent of $n=5.3$ for $\langle 110 \rangle$ PST crystal can be rationalized as being due to the dislocation glide ($n\sim 3$) aided by pipe diffusion which increases the stress exponent by 2. The occurrence of pipe diffusion is supported by the low activation energy $Q_c=135$ kJ/mole. In $\langle 112 \rangle$ PST crystal, the stress exponent of $n=3.2$ may result from dislocation glide creep that is not dependent on pipe diffusion, due to the lower stress or strain where $n=3$ was measured. Also, the activation energy may be stress dependent, since a higher activation energy may be needed for pipe diffusion if the stress is lower.

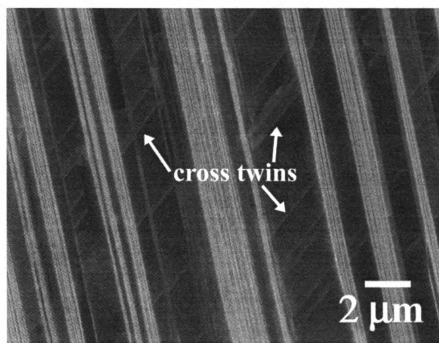
9.3.4 Microstructure and lamellar spacing

Microstructures were examined in the $\langle 112 \rangle$ PST sample. Figure 9.5 shows backscattered electron images of a deformed (about 1.38 % shear strain) $\langle 112 \rangle$ PST crystal. Very fine lamellar microstructures consisted of γ (darker phase) and α_2 laths (brighter phase). Especially fine lamellar features are found in α_2 laths $> 1 \mu\text{m}$, as indicated in the upper left side of Figure 9.5.a. The α_2 spacing (distance between α_2 - γ interfaces) varies between 0.025~4.25 μm . Cross twinning was only observed in the 1.38% shear strain specimen in Figure 9.5.b. This indicated that the easy mode of deformation twinning parallel to lamellar interfaces preceded cross twinning.

The lamellar spacing was characterized from about 500 measurements in more than 20 lamellar regions from the side $\langle 110 \rangle$ surface in the undeformed and deformed samples. There is an increase in smaller α_2 spacings with strain, as shown in the distribution in Figure 9.6.a. The average α_2 spacing decreased from 1.1 to 0.7 μm in Figure 9.6.b. There is a 13% reduction in lamellar spacing at 0.6% and 28% reduction at 1.38% shear strain. However, the average α_2 thickness does not change much during primary strain. This refinement of spacing is consistent with previous studies, and the amount of reduction depends on the composition, interstitial content, heat treatment, and deformation temperature and stress [111,217,141,205,212,239,253]. Figure 9.3 shows that the minimum strain rate at loading condition 2 decreases by one order of magnitude even after increasing the stress from 9.5 to 11 MPa. A similar phenomena occurs at the increase from 18 to 20 MPa. This anomalous reduction in creep rate is probably the result of further reduction of lamellar spacing that further hardens the microstructure. This indicates that initially, twinning strain in the $\langle 112 \rangle$ direction is very easy, but with the consequent lamellar refinement, the $\langle 112 \rangle$ crystal hardens dramatically, as compared to



(a)



(b)

Figure 9.5 Backscattered electron images of deformed $\langle 112 \rangle$ PST crystal (1.38% shear strain at 760°C and 13 MPa).

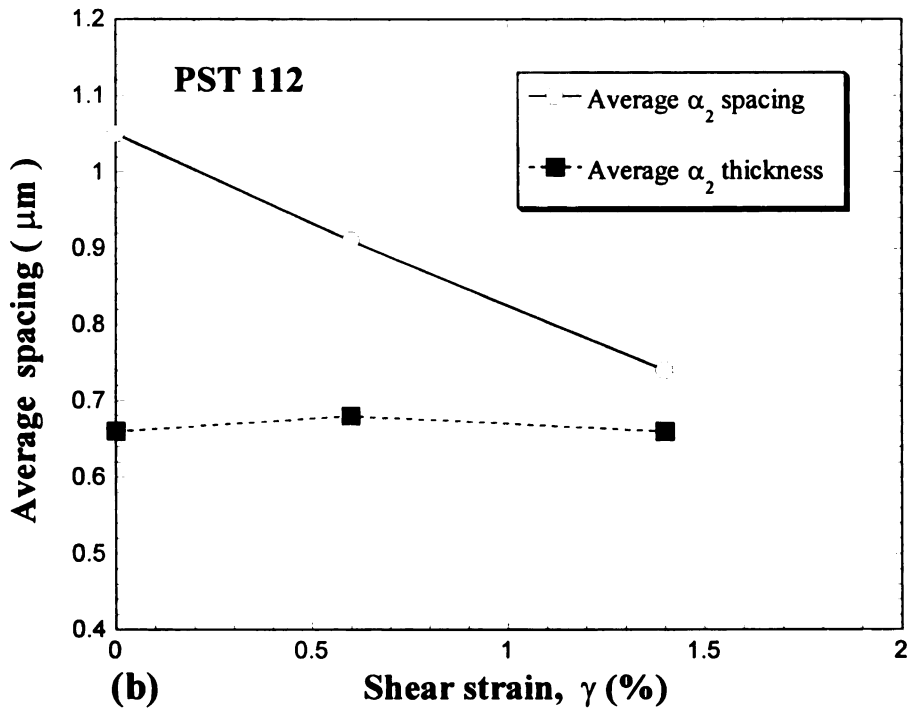
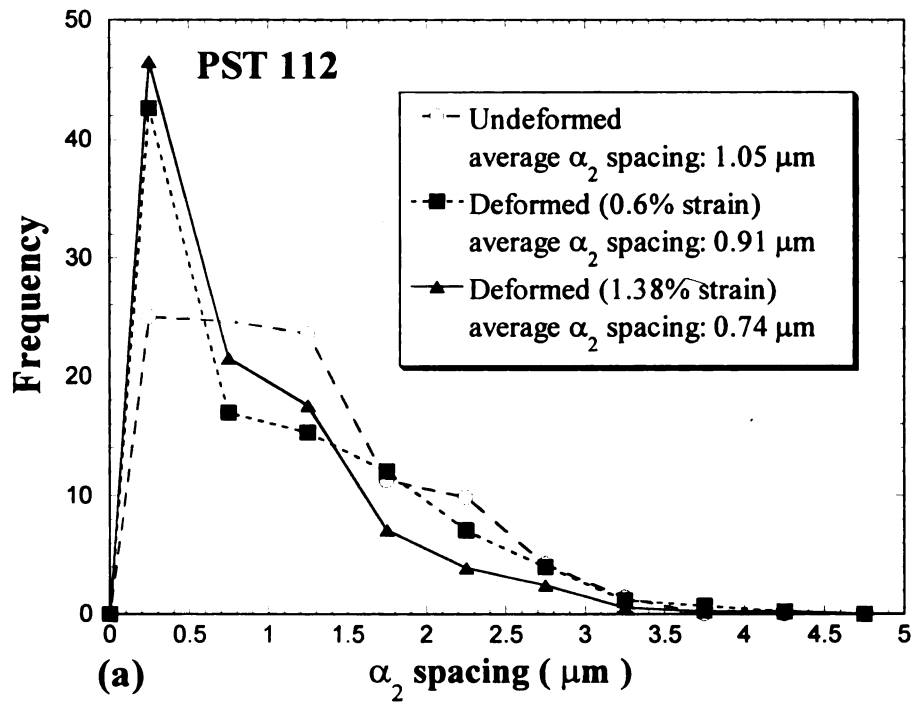


Figure 9.6 (a) α_2 spacing distribution, and (b) average α_2 spacing and thickness with different primary creep strain levels in the $\langle 112 \rangle$ PST crystal.

the $\langle 110 \rangle$ crystal.

Luster and Morris have shown that only deformation modes parallel to the lamellar planes are operative in γ lamellae thinner than about $0.5 \mu\text{m}$, which makes thin lamellae more resistant to deformation [142]. Improvements in creep resistance have been correlated with initial lamellar spacing that was reduced by heat treatment [127]. These results indicate that refining the lamellar spacing is desirable for improving primary creep resistance. Recent results indicating that primary creep deformation is retarded by pre-straining [159] can be easily understood in terms of the lamellar refinement observations discussed above.

9.4 CONCLUSION

‘Normal’ transient creep after stress and temperature changes were observed in the $\langle 110 \rangle$ and $\langle 112 \rangle$ PST crystals. This indicates that Class M type creep deformation and subgrain structures were formed during the transient creep processes. The stress exponent of $n=5.3$ at 22~34 MPa and activation energy $Q_c=137$ kJ/mole (in Ar) at 760~806°C for the $\langle 110 \rangle$ PST crystal suggest that dislocation glide is aided by pipe diffusion in this microstructure and crystallographic orientation. For the $\langle 112 \rangle$ PST crystal, the stress exponent of $n=3.1$ at 13~18 MPa and $Q_c=185$ kJ/mole (in Air) at 760~806 °C suggest that the creep deformation mechanism is limited by dislocation glide. However, at a higher shear stress glide limited by pipe diffusion can account for an increase in the stress exponent to $n=5.3$. The activation energy of the $\langle 112 \rangle$ PST crystal at 13 MPa is higher than that of $\langle 110 \rangle$ PST crystal at 28 MPa, suggesting that the apparent activation energy may depend on stress. The refinement of lamellar spacing

(13~23 % reduction) during primary stage was observed. Reduction of lamellar spacing contributes to strain in the early primary stage, and also hardens the crystal. After 1.38% shear strain, hard mode deformation (cross twins) was activated in some lamellar laths.

CHAPTER 10

THE EFFECT OF HEAT TREATMENTS ON MICROSTRUCTURES AND PRIMARY CREEP DEFORMATION OF FOUR INVESTMENT CAST TITANIUM ALUMINIDE ALLOYS

ABSTRACT

Several heat treatments were developed and applied to investment cast Ti-45Al-2Nb-2Mn(at%)+0.8v%TiB₂ XDTM, Ti-47Al-2Nb-2Mn(at%) + 0.8v%TiB₂ XDTM, Ti-47Al-2Nb-2Cr(at%), and Ti-47Al-2Nb-1Mn-0.5W-0.5Mo-0.2Si alloys in an effort to enhance creep properties and decrease heat treatment time compared to current practices. Results show that the creep resistance of WMoSi can be improved by 10 times with heat treatment, and 47-2-2 can be improved by 3 times, and the XD alloys can be improved slightly, or not at all with lower Al level. The variation, or lack of variation, in creep resistance with heat treatment can be explained by differences observed in the microstructures and textures produced by the various heat treatments. Quantitative microscopic comparisons were made between microstructures in undeformed and deformed regions in creep specimens deformed to strains between 0.1 and 1.5% strain, using optical, SEM and TEM techniques. The lamellar spacing in lamellar grains systematically decreased by 15-35%, with increasing stress, during the first 0.1-2% strain. Precipitates containing W, Mo, and/or Si nucleated and grew at a faster rate in the deformed part of the specimen, as compared to the grip section, with approximately twice the volume fraction in the deformed region, and the precipitates were generally smaller

and more homogeneously dispersed. These observations indicate that strain assisted nucleation of precipitates accounts for much of the excellent creep resistance of the WMoSi alloy.

10.1 INTRODUCTION

Cast near gamma titanium aluminides are gaining acceptance as potential replacements for superalloy and steel components in aerospace, automotive and industrial applications since it has high specific strength at high temperatures [92,93,128]. Components cast from these alloys can operate at temperatures up to 815 °C (1500 °F) at half the weight of the components they replace. Most applications of cast gamma components require good primary creep resistance to meet component life requirements.

The microstructure is an important factor that is sensitive to composition, heat treatment, and strongly affects creep properties. Gamma titanium aluminide can be heat treated to obtain four types of microstructures [110]. The best creep resistance has been observed in fully lamellar microstructures [161]. However, the duplex microstructure is preferred for many applications since it provides desirable room temperature ductility [92].

The addition of Cr, Nb, V, Mn, W, Mo and Si, in two phase Ti-Al alloys is also an important factor in order to control the material properties. Cr can improve the ductility of duplex alloys with additions of 1~3% at%. [225,226]. The additions of 1~3 at% V and Mn are the most common elements for improving plasticity in two phase TiAl alloys [143,227-229] but V generally reduces the oxidation resistance[230]. Nb greatly enhances the oxidation resistance [231-233] and slightly improves the creep resistance

[232]. The addition of 0.5~1 at.% Si enhances creep strength, the oxidation resistance, and room temperature fracture toughness of 48 at% Al two phase alloys [208,234-236]. Si also increases fluidity, and reduces the susceptibility to hot cracking [237]. Mo provides a good balance of strength and ductility in TiAl having very fine equiaxed gamma grains with the α_2 and β phase [210,254]. Addition of W greatly improves oxidation resistance, and enhances creep resistance [169].

Most of these studies have focused on either room temperature properties, minimum creep rate conditions or stress-rupture properties. However, primary creep resistance is important for practical applications. Gamma based TiAl exhibits primary creep strains that are typical for metals, where the minimum is reached after about 1% strain. In an effort to decrease the creep rate during primary creep deformation, additions of W, Mo, and Si have increased the time to reach 0.5% strain due to a dynamic precipitation process [231,238]. In several related studies, observations of lamellar refinement indicate that primary creep deformation includes a significant amount of mechanical twinning parallel to lamellar interfaces that occurs as an easy mode of deformation that hardens the microstructure at low strains [50,165,212,213]. In this chapter, the primary creep resistance (time to 0.5% creep strain) is compared between four alloys having different kinds of strengthening strategies, including ceramic particles, solid solution elements and precipitates, which affect the ways the microstructure can be manipulated by heat treatment. After primary creep to 0.5% we quantify changes in the different lamellar and equiaxed microstructures, γ thickness and α_2 spacing, mechanical twinning, interstitial composition, precipitate size, composition, shapes, and dislocation interactions with precipitates.

10.2 MATERIALS AND EXPERIMENTAL PROCEDURE

The investment cast gamma TiAl alloys used are described in Table 10.1. Some specimens with varying interstitial content were investigated and they are hereafter identified as med-O or high-O alloys. All materials were hot isostatically pressed (HIPed) at 1260 °C for 4 hours at 172 MPa (2300 °F, 25 ksi) in order to eliminate casting porosity. The heat treatments used were in the $\alpha_2+\gamma$ phase field at 900 or 1010 °C (1650 or 1850 °F) for 10, 20 or 50 hours, and cooled in a static argon atmosphere (SAC). A two step heat treatment was also used consisting of 1177 °C (in the $\alpha+\gamma$ phase field) for 5 hours and then in the $\alpha_2+\gamma$ field for 10 hours at 1010 °C (2150 and 1850 °F), respectively, and cooled in static argon. These heat treatments all provided duplex microstructures. These specimens were then subjected to creep tests at 760 °C, 138 MPa (1400 °F, 20 ksi) and 649 °C, 276 MPa (1200 °F, 40ksi). The creep specimens were cooled under load once 0.5 % strain was reached. Some additional 5x5x3 mm brick shaped specimens of Ti-47Al-2Nb-1Mn-0.5W-0.5Mo-0.2Si alloy were cut using EDM machining from a piece of an as-HIPed casting gate for compression-shear creep tests. They were deformed on a 45° inclined stage in a compression cage fixture developed for evaluating creep in a PST crystal [165].

Compression-shear creep tests were conducted at 650 and 750 °C with shear and compression stress components of 61, 91.5 and 122 MPa in air using an ATS series 2710 creep testing machine. Tests were stopped once 0.2-1.5% creep strains were reached. The creep data were recorded by a PC based data acquisition system developed for creep tests. The specimen shape change was measured using external extensometry connected

Table 10.1 Nominal chemical composition of investment cast TiAl alloys (at%)

Abbreviation	Ti	Al	Si	Nb	Mn	Cr	Mo	W	B	O	N	H	Fe
47-2-2	Balance	47		2		2							
47Al XD (low O)	48.54	46.19	0.04	1.87	1.86	0.02			1.15	0.203	0.026	0.012	0.07
med-O	48.55	45.43	0.04	2.02	1.95	0.02			1.14	0.227	0.032	0.012	0.10
high-O	47.66	47.16	0.04	1.81	1.88	0.02			1.07	0.289	0.037	0.012	0.03
45Al XD	Balance	45		2	2				0.8*				
WMoSi	Balance	47	0.2	2	1		0.5	0.5					

* Vol. Fraction of TiB₂

to the compression cage and SLVC transducers located outside of the furnace. Specimen load, temperature, displacement, and time data were reduced, assuming simple shear deformation with the aid of spreadsheet and plotting programs.

For optical and SEM analysis, deformed samples were obtained from the gage section of the creep deformed specimen. Some undeformed samples were also cut from the grip section of tensile test specimens. A modified Kroll's reagent [222] was used to reveal the microstructure in this material. For analysis of different phases, polished and unetched specimens were used in a JSM-6400V scanning electron microscope (SEM) at 25kV, using the Backscattered electron (BSE) technique. For micro-analysis by transmission electron microscopy (TEM) the specimens were prepared as follows: 0.7 mm thick slices were taken from the specimen using a diamond saw. 3 mm discs were produced using an EDM cutting machine such that the foil normal was parallel to the tensile axis. After mechanical polishing thin foils for electron microscopy were prepared by the twin jet polishing method using a solution consisting of methyl alcohol and 10% sulfuric acid at 20 volts at -25 °C. These foils were examined in a Hitachi H-800 transmission electron microscope operated at 200kV. Texture measurements were made on selected specimens and analysis was made using popLA software [214].

10.3 RESULTS AND ANALYSIS

10.3.1 Primary creep behavior

Tensile creep

The time to 0.5% creep of the four alloys varies with composition and heat

treatment as shown in Figure 6.2 and 7.1. The average value of three samples is plotted with the line, and high and low values are also plotted. From this plot, it is apparent that the 45 Al composition is insensitive to heat treatment. The 47 Al (low O) samples exhibit different responses to heat treatment. With TiB_2 , the heat treatment for 10 hours at 900 °C is damaging to primary creep resistance, but otherwise there is no significant improvement with increasing time at temperature in heat treatment, other than a beneficially smaller range of values with the two step heat treatment. But for the 47Al with high O alloys, creep resistance is significantly improved with increasing amounts of O. The alloys with medium and high O exhibit creep times to 0.5% that are more than twice as long. The scatter is similar in magnitude for all alloys except the low O alloy after the two-step heat treatment. For the 47-2-2 alloy, the creep resistance is substantially improved with increasing amounts of time and temperature in heat treatment, but the variability in the samples is not significantly improved with heat treatment. For the WMoSi alloy, the primary creep resistance is the best (295 hours). In WMoSi alloy, tensile creep deformation at low temperature and high stress (649 °C, 276 MPa), the material deformed quickly up to 0.2% strain, where the strain rate slowed considerably. At the higher temperature and lower stress, (750 °C, 138 MPa) the trend was similar, but the change was less dramatic. This effect is clearly shown in Figure 8.5, and 10.1. The strain rate vs strain curve was obtained by differentiating a least squares curve fit of the creep data using the equation $(\epsilon = a(1 - \exp(bt)) + c(1 - \exp(dt)))$ [205]. All alloys exhibit a rapid decrease in strain-rate below about 0.2%. The creep rates of the higher O alloys were lower and decreasing more rapidly at 0.5% strain. At low strains, the creep curves for both higher O alloys cross at a strain of 0.1%, indicating that the high O alloy had a

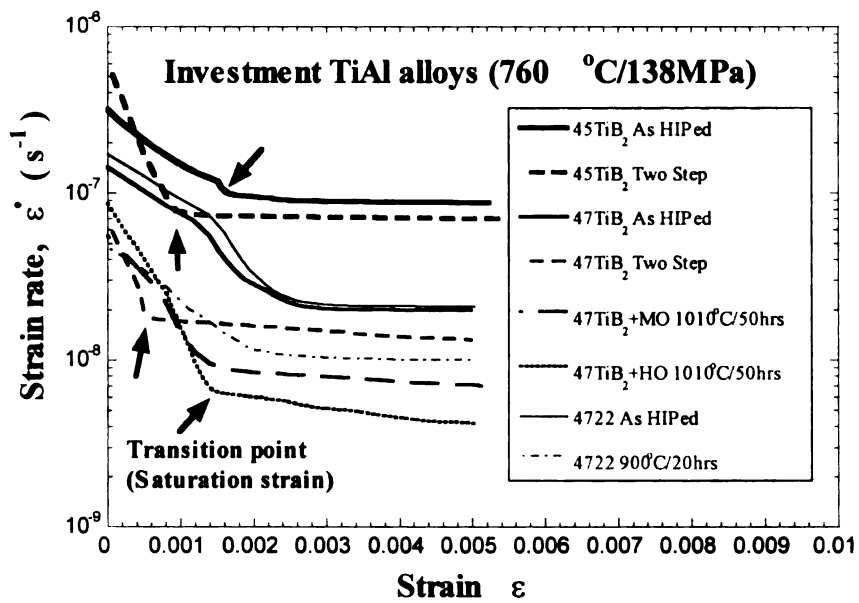


Figure 10.1 Differentiated curve fits of creep data exhibit a decreasing strain rate to a saturation strain between 0.1 and 0.5% strain, whereafter the decrease in strain rate is less rapid.

faster initial creep rate. The WMoSi alloy also shows a cross over in the curve creep around at 0.2% strain due to different stress and temperature conditions shown in Figure 8.5. The most dramatic reductions of strain rate occurred in the alloys having better primary creep resistance.

Compression-shear creep

For the larger strain compression-shear creep conditions in Figure 8.3.b, the initial creep rates are similar, but the 750 °C specimen reached 0.8% about 20 times faster than the 650 °C specimen at the same stress. From Figure 8.5. the initial creep rate and shape of the creep deformation curve for stresses larger than 77 MPa is similar, indicating a rapid decrease in the creep rate. At 77 MPa, the strain rate decreases more slowly to an initial saturation strain that is reached at a larger strain. At the lower temperature, the saturation of the initial creep rate is reached at a smaller strain, and the decrease in strain rate is larger.

The initial saturation strains depend on the temperature and stress. A higher stress at the same temperature or a higher temperature with same stress make the saturation strain shift toward smaller strain. The curvature of the creep curves is similar at the same temperature or stress level. A higher stress results in a greater drop in the strain rate at the saturation strain. The effect of heat treatment on the creep rate for the WMoSi alloy reduces the creep rate by more than a factor of 10.

10.3.2 Microstructures

Ti-45Al-2Nb-2Mn-0.8TiB₂

From optical micrographs, a very fine duplex microstructure was observed in all specimens as shown in Figure 10.2.a, regardless of heat treatment. There is a homogeneous distribution of 10-50 μm equiaxed and 20-100 μm lamellar grains. The volume fraction of lamellar grains generally decreases with increasing amounts of heat treatment (Figure 10.3).

From analysis of backscattered images of undeformed and deformed specimens obtained in the SEM, there are no distinguishable changes in the microstructure resulting from creep deformation. Optical micrographs of the crept specimen show that many TiB₂ particles are distributed randomly. There are several types of particles such as equiaxed, needle, and irregular shaped precipitates with a spacing of 30-50 μm , and they are located inside gamma grains, in grain boundaries between gamma (dark phase) and α_2 (bright phase) grains and in lamellar grains, but not inside α_2 grains, as shown in Figure 6.4.d. As annealing time increased no distinct change in the particles was observed, but in the case of the two-step heat treatment there appeared to be fewer particles. Single phase γ and α_2 grains represent about 40% of the volume fraction. The α_2 grains have angular shapes, but the γ grains tend to be more round and equiaxed. This indicates that equiaxed γ grains nucleate in several places in a given parent α_2 grain, and that some of the parent α_2 region transform into lamellar grains, but others do not. Very fine lamellar features are observed in some α_2 grains in both deformed and undeformed specimens (see arrows in Figure 6.4.d). These regions also exhibit contrast indicating formation of extremely fine

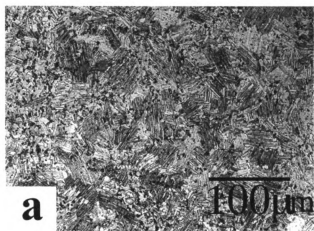


Figure 10.2 Microstructures of As HIPed 45Al XD (a) optical micrographs before creep test.

lamellar microstructures consisting of both α_2 and γ lathes. Since they are much finer than the obvious lamellar grains, they are not likely to have resulted from thermally induced transformation, so they are more likely to have resulted from local stress concentrations [47,50,213]. These features were observed in all heat treatments. Since the α_2 grains have an angular shape, stress concentrations are more likely to be focused at triple points in α_2 grains, where fine mechanical twinning is most often observed [47,50,213]. The fine twinned regions are also observed in TEM images. They occur in the angular shaped α_2 grains, as illustrated in Figure 6.5.a. Regions of extremely fine mechanical twinning are also observed in some lathes of the lamellar grains (Figure 6.5.b).

Ti-47Al-2Nb-2Mn-0.8TiB₂

Microstructures of as-HIPed specimens exhibit a heterogeneous microstructure illustrated in Figure 10.4 a. There are clusters of small equiaxed grains in some regions where there are fewer lamellar grains, and conversely, a few fine γ grains are observed in regions dominated by lamellar grains. After heat treatment the microstructures exhibit fewer small grain clusters. The volume fraction of equiaxed grains changes, and after the two step heat treatment, the lamellar volume fraction increased slightly as described in Figure 10.3. As time and temperature of heat treatment increase, microstructures became more homogeneous. The equiaxed grain size distribution becomes more homogeneous, and fewer clusters of finer γ grains were observed. The microstructures of medium O alloys are similar to that of the low O alloy shown in Figure 10.4. a. The low and medium O alloy has a lower volume fraction of lamellar grains than the high O alloy (25%, 22% and causes more lamellar grains. However, this result is consistent with the observation

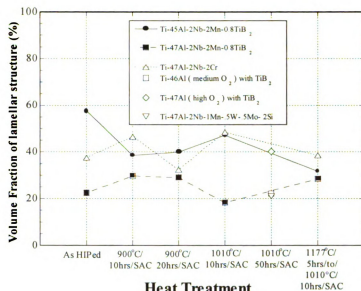


Figure 10.3 Volume fraction of lamellar grains in TiAl alloys with respect to heat treatment.



Figure 10.4 (a) optical micrographs of As HIPed 47Al XD before creep test.

that oxygen is an alpha phase stabilizer in Ti alloys [143,223]. From Table 10.2 the higher O levels have fewer small grains, which correlates with improved creep resistance [127].

Backscattered electron (BSE) images of the higher O alloys after creep deformation in Figure 7.4.a and b illustrate differences in α_2 morphology (white phase, see arrows). The largest α_2 regions in the high O alloy are smaller than those in medium O alloy, and angular shaped 3-7 μm α_2 grains (arrow) were commonly observed in the medium O alloy (it also has lower aluminum). Angular α_2 grains correlate with faster primary creep [127]. In the alloys with boron, two types of boride particles were found, needle and round.; the round type is 1.5-3.5 μm , and the needle type is 3-60 μm long. The needle particles have been identified as TiB and equiaxed particles as TiB₂ [224]. The heat treatment or interstitial content did not affect the size and distribution of these particles.

From analysis of SEM BSE images and TEM images, these particles appear to provide nucleation sites for lamellar lathes (fine lamellar colonies were frequently found near particles), and they also block and entangle dislocations.

Ti-47Al-2Nb-2Cr

In contrast to the microstructures containing TiB₂, the as-HIPed microstructure exhibits very large (up to 500 μm) lamellar grains and about 200 μm pockets of equiaxed 10-20 μm equiaxed γ grains (Figure 10.5 a). The microstructure is extremely heterogeneous, and it exhibits some of the same types of heterogeneities (clusters of small equiaxed grains) observed in Figure 10.5 a. As shown in Figure 10.3, with heat treatment, the volume fraction of the lamellar grains increases and decreases with increasing time

Table 10.2 Grain sizes of four investment TiAl alloys (unit: μm).

Alloys	lamellar	equiaxed
Ti-45Al-2Nb-2Mn-0.8TiB ₂	20~50	10~50
Ti-47Al-2Nb-2Mn-0.8TiB ₂ (low O)	20~200	10~50
Ti-46Al-2Nb-2Mn-0.8TiB ₂ (medium O)	20~200	10~50
Ti-47Al-2Nb-2Mn-0.8TiB ₂ (high O)	100~200	25~100
Ti-47Al-2Nb-2Cr	50~500	20~200
Ti-47Al-2Nb-1Mn- 0.5W-0.5Mo-0.2Si	100~500	5~200



Figure 10.5 Microstructures of As HIPed 47-2-2 (a) optical micrographs before creep test (b) BSE images after creep test.

and temperature, and the microstructure becomes less heterogeneous. The pockets of equiaxed grains become fewer and there are fewer fine grains in the pockets.

In the backscattered electron SEM images of this alloy there is a smaller volume fraction of angular equiaxed α_2 grains between gamma grains (Figure 10.5 b). The very fine twins seen in the 45 Al sample (Figures 6.4.d, and 6.5.a and b) were not observed in the smaller α_2 equiaxed grains in the 47 Al specimens. Very small bright phases can be seen either in α_2 equiaxed grains or boundaries of gamma grains (indicated by arrows) and these phases are β phase which is produced by addition of Cr. They have an orientation relationship of $(0001) \alpha_2 // \{111\} \gamma // \{110\} \beta$, and $\langle 1120 \rangle \alpha_2 // \langle 110 \rangle \gamma // \langle 111 \rangle \beta$ [215]. Since Cr is known to strengthen the α_2 and γ phases, this may account for the lack of mechanical twinning observed in the α_2 phase in the Ti-47Al-2Nb-2Cr alloy [215]. There appears to be a decrease in the amount of β phase with the increasing amounts of heat treatment.

TEM investigations indicate that a 170° angle relationship between lamellae is frequently observed in the as-HIPed and heat treated conditions. Typically, one of the two lamellar lathes has a finer spacing described in the reference [127]. Subboundaries developed in larger regions of lamellar grains during high temperature deformation. No subgrains had developed fully in equiaxed grains even though there were regions exhibiting a dislocation density greater than $2 \times 10^{12}/\text{m}^2$. After the two-step heat treatment, dynamic precipitation was observed in grain interiors and interfaces, and this may account for some the improved creep resistance [212].

Ti-47Al-2Nb-1Mn-0.5W-0.5Mo-0.2Si

The microstructure of the undeformed as-HIPed alloy showed a similar feature as shown in Figure 8.6.b. Since the strains were small, there was no obvious change in the microstructure after creep deformation. However, reductions in the lamellar spacing were systematically observed in higher magnification observations after deformation. Figure 8.8.b shows the microstructure of the tensile crept specimen in the gage section with equiaxed grains ranging from 5-200 μm . The lamellar colonies are on the order of 100-500 μm , but many have smaller equiaxed grains interspersed among the lamellar grain boundaries. These groups of small equiaxed grains are produced during HIP treatment due to large local strains associated with pore closure. The volume fraction of lamellar grains in the two crept tensile specimens are $21 \pm 2\%$ and with the balance being equiaxed grains. Macroscopically the only differences between specimens deformed at 750 °C, 138 MPa and 649 °C, 276 MPa, were the observation of more twins in the larger equiaxed grains of the deformed sample compared to the microstructure in the undeformed grip section. Also, there appeared to be more twinning at the lower temperature, higher stress condition.

Backscattered electron images in Figure 8.8.b indicated that the β phase (whitest phase) were found in grain boundaries between γ grains and lamellar grains or in lamellar colony interfaces in both the as-HIPed and heat treated specimens as observed in a related study [185,212,236]. As shown in Figure 8.12.b, precipitates in the heat treated alloy after HIPing are located in various places such as lamellar interfaces, grain boundaries, and within equiaxed grains, and precipitates were found only in the heat treated alloy. The as-HIPed deformed specimens exhibited no precipitates. This indicates that subsequent heat

treatment facilitates the formation of the precipitates. The precipitates in lamellar interfaces vary from 0.05-0.45 μm and tend to be smaller, and many of them have a needle shape (Figure 8.12.b). In equiaxed grains, precipitates are larger, and tend to have an aspect ratio of 2-3. Thus the precipitates have various shapes with dimensions ranging from 0.2-2 μm . These precipitates have been identified as Ti_5Si_3 in several studies [185,212,236]. After analyzing the distribution of precipitates in at least 5 lamellar grains, about 35% more precipitates were found in the deformed sample. This observation suggests that precipitates were formed with the assistance of strain during creep deformation. These observations taken together indicate that precipitation is facilitated by heat treatment, and that a more homogeneous nucleation and growth process occurs in the presence of strain. As with TiB_2 particles, the precipitates always have a high density of dislocations in their vicinity.

10.3.3 Lamellar spacing

From TEM analysis, twins appear to have initiated from a grain boundary at the boundary region between an equiaxed and a lamellar grain and propagated through equiaxed grains. 250-500 α_2 spacing counts in more than 20-25 lamellar regions and at least 100 γ thickness in about 6 different regions near grain boundaries before and after creep deformation were used to compute the average of α_2 spacing and γ thickness before and after creep deformation. The α_2 spacing was measured by using BSE imaging. These measurements are upper bounds of the actual spacing, since the lamellar plane normal direction was not determined to make the parallax correction needed to determine the actual α_2 spacing. However, this is a systematic way to compare α_2 spacings in

specimens with similar microstructures. The TEM was used for measuring the true γ thickness and α_2 thickness (by tilting the foil so that a $\langle 110 \rangle$ direction in a lamellar plane was parallel to the beam) and about 50 α_2 laths were counted in several lamellar regions for this measurement.

In the case of Ti-47Al-2Nb-2Cr alloy, by using the dark field method and tilting techniques, the γ thickness, α_2 spacing and the thickness of α_2 laths in several lamellar grains were measured. The data was obtained by measuring about 100-350 laths and taking the average.

Ti-47Al-2Nb-2Mn-0.8TiB₂

The α_2 spacing was reduced in these alloys after creep deformation and this reduction varies with heat treatment and interstitial content [127,239]. The average α_2 spacing before deformation in the alloy with high O is 1.37 μm , which is nearly as large as the 1.57 μm spacing of the low O alloy which showed the poorest creep resistance. The average α_2 thickness is larger (0.2 μm) in the high O alloy than the low O alloy (0.15 μm). This also suggests that oxygen stabilizes the α_2 phase.

The distribution of α_2 spacing and γ thickness before and after creep deformation are shown in Figure 10.6.a. From this plot, the reduction of the α_2 spacing and γ thickness after deformation at the early stage of creep can be easily visualized since the dashed line shows the highest frequency of lamellae with fine spacing. During the first 0.5% strain, more reduction in the strain-rate correlates with more reduction in lamellar spacing in the low O alloy. The high O alloy does not follow the same relationship between the

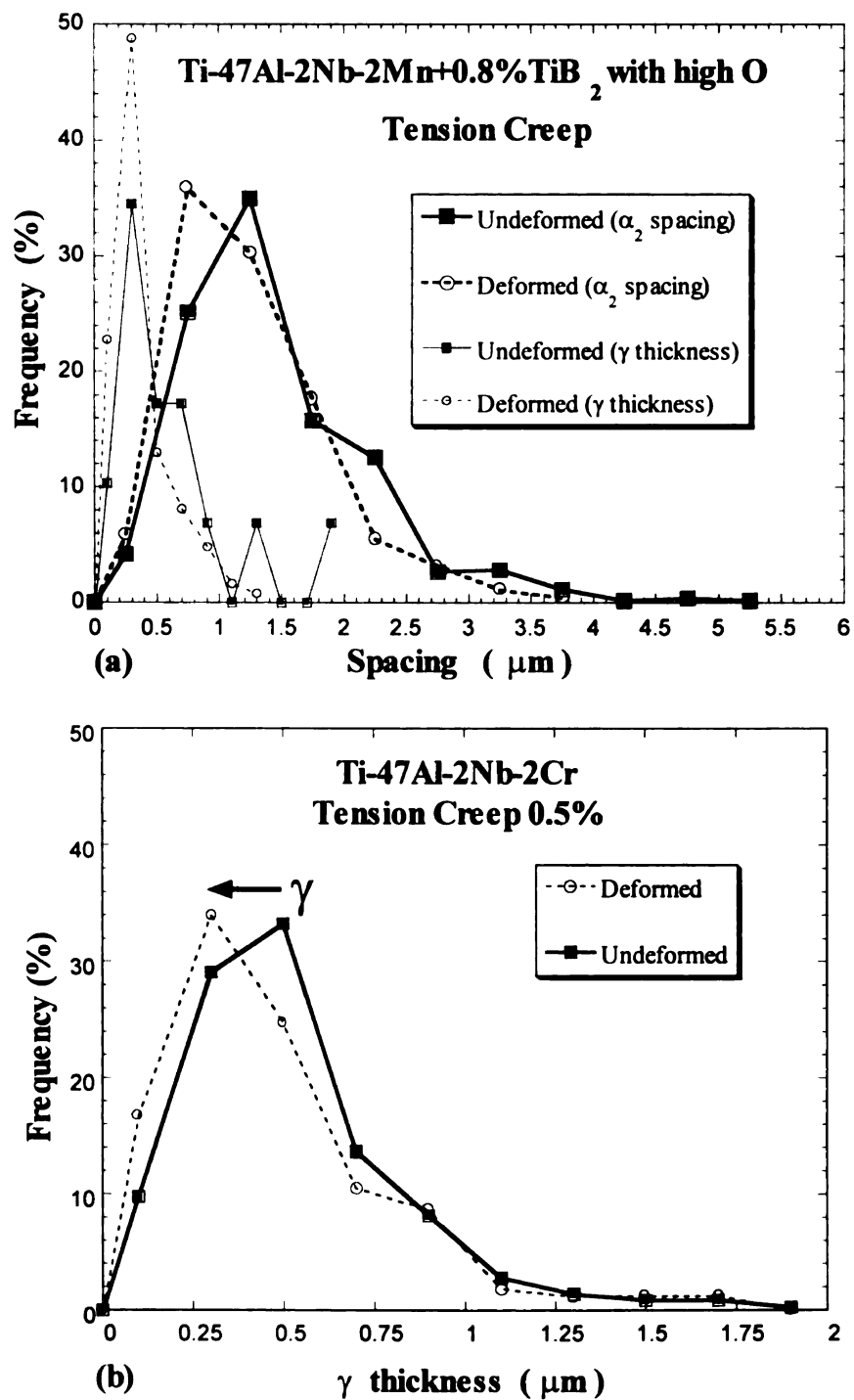


Figure 10.6 Distribution of α_2 spacing and γ thickness in TiAl alloys before and after creep deformation (a) high O (b) 47-2-2.

reduction in spacing and the reduction in strain-rate: The high O alloy exhibits a larger reduction in strain-rate, and a greater amount of reduction in the γ thickness. The high O alloy exhibits more reduction of γ thickness than the alloy heat treated at 900 °C for 10 hours, which gave poor creep resistance. If the reduction in lamellar spacing occurs by mechanical twinning, then more twinning appears to cause a greater amount of strain at early times. The effect of the high O is that more refinement in the γ thickness occurs in primary creep, but it occurs more slowly.

Ti-47Al-2Nb-2Cr

The α_2 spacing and γ thickness decrease with heat treatment and after creep deformation [127]. In the case of γ thickness, there was only 8% reduction of thickness from heat treatment and a 4% reduction of γ thickness after creep deformation in the 900 °C/20hr heat treated alloy as determined from Figure 10.6.b. From the reference 34, measured averaged α_2 spacing shows that the spacing decreases from about 5% to 18% from the As HIPed condition to the one and two-step heat treatments. From Table 10.3, after deformation, in the one-step heat treatment there was a 22% reduction of the α_2 spacing, and a 10% reduction in the α_2 thickness. This may result from nucleation of new α_2 lamellae initiated by mechanical twinning, since a mechanical twin has the crystal structure of the α_2 phase for three layers in each interface [213]. In general, heat treatment and creep deformation cause the lamellar scale to become more refined.

Ti-47Al-2Nb-1Mn-0.5W-0.5Mo-0.2Si

a. lamellar spacing in compression-shear creep deformation

The distribution of α_2 spacings before and after deformation is represented in Figure 8.18.a. The undeformed representation shows the same trend for three samples characterized before deformation, and the average is indicated by a bold line. In every case, there is a nominally similar shift of the frequency distribution toward smaller spacings due to small creep strains. The average of about 500 observations of α_2 spacings is plotted with respect to effective strain and load in Figure 10.7. There is a 23% reduction in lamellar spacing with strain that saturates at effective strains between 0.1 and 0.3%, whereafter the spacing remains relatively constant. For the same strain of 0.1%, the amount of refinement at 750 °C is about half of the amount that occurred at 650°C. The amount of refinement at 650 °C decreases with decreasing stresses.

b. lamellar spacing in tensile creep deformation

From Table 10.3, there was a reduction in spacing of 34 % in α_2 and 24 % in γ thickness for the specimen deformed at 760 °C, 138 MPa. Contrary to the observations in the compression-shear specimens, the reduction in α_2 spacing was smaller (18%) in the 650 °C 276 MPa specimen, in part, due to a lower undeformed lamellar spacing. However, the deformed lamellar spacing for this specimen (0.9 μm) is smaller than the spacing for the deformed 760 °C 138 MPa specimen (1.03 μm).

Unlike the compression shear specimens, the undeformed lamellar spacing was measured in the grip section of the creep specimens, which experienced the same thermal history with presumably no stress. The compression-shear specimens all came from the

Table 10.3 Average lamellar spacing and reduction % of TiAl alloys

	γ thickness	α_2 spacing	α_2 thickness	Creep test condition
4722	0.49 μm , 4 %* 900 °C /20 hrs	1.29 μm , 22 % 900 °C /20 hrs	0.11 μm , 10 % 900 °C /20 hrs	Tension 760 °C /138 MPa
47Al XD (low O)	0.38 μm , 24 % 900 °C /20 hrs	1.33 μm , 22 % 900 °C /20 hrs 1.42 μm , 24 % As HIPed	0.15 μm	Tension 760 °C /138 MPa
high O	0.59 μm , 40 % 1010 °C /50 hrs	1.37 μm , 14 % 1010 °C /50 hrs	0.2 μm	Tension 760 °C /138 MPa
WMoSi	1.30 μm , 24 % 1010 °C /50 hrs	1.57 μm , 14 % 1010 °C /50 hrs		Tension 760 °C /138 MPa
WMoSi	0.46 μm	0.74 μm , 18 %** 1010 °C /50 hrs		Tension 649 °C /276 MPa
WMoSi		1.38 μm , 23 % As HIPed		Compression-shear 760 °C /138 MPa

* about 3 lamellar regions sampled, more than 3 in other specimens. ** initial lamellar spacing was fine in this specimen.

• initial values of α_2 spacing and γ thickness, and α_2 thickness are indicated before %.

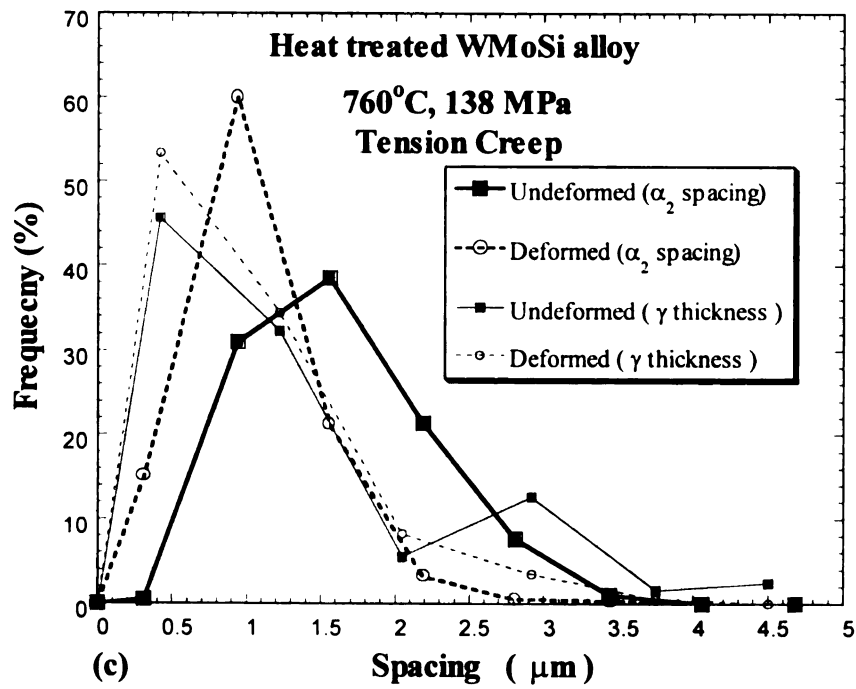


Figure 10.6 Distribution of α_2 spacings and γ thickness in TiAl alloys before and after creep deformation (c) WMoSi alloys under tension mode.

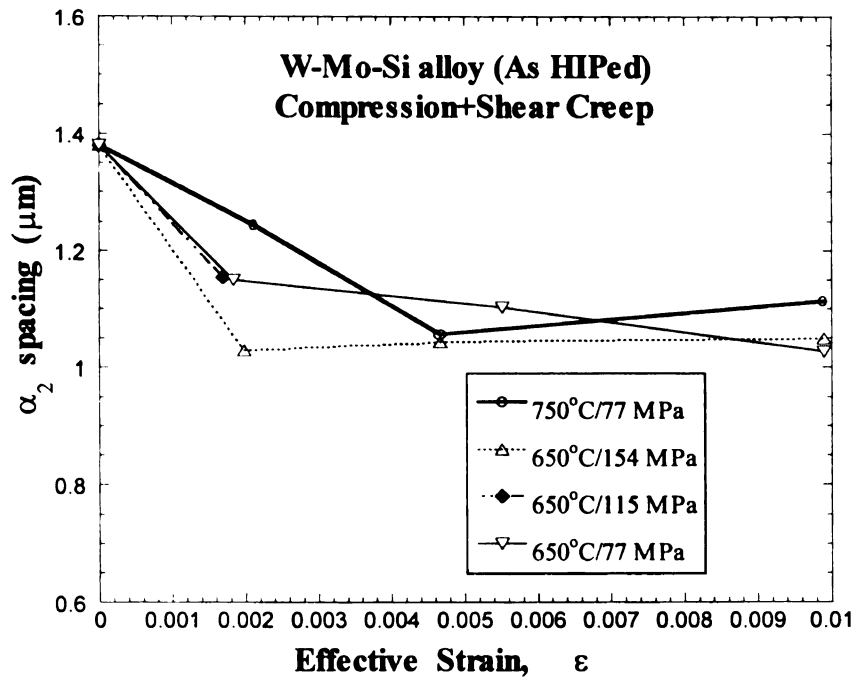


Figure 10.7 The plot of α_2 spacing respect to different effective strains and different loads at 650 °C and 760 °C.

same physical region of the casting, but nothing is known about the relative positions of the two tensile specimens in the casting, where the initial lamellar spacing may have differed due to differences in cooling rates, or other unidentified process parameters. The α_2 spacing and γ thickness distribution curves before and after deformation are represented as a bold and a dotted line, respectively, in Figure 10.6.c. As with the compression-shear specimens, there is a nominally similar shift of the frequency distribution toward smaller spacing due to small creep strains.

10.3.4 Effect of Anisotropic Crystal Structure on Deformation

Figure 3.8 a shows the maximum Schmid factor for true $\langle 112 \rangle$ twinning and dislocation deformation systems. A high Schmid factor indicates that a deformation system will operate to carry strain. The operation of true twinning depends strongly on the orientation of a crystal with respect to the loading axis. In tension, orientations close to $\langle 441 \rangle$ (near tail of arrow) are likely to twin. However, upon twinning, the crystal rotates to an orientation near $\langle 118 \rangle$ (near head of arrow). Once the crystal is twinned, the Schmid factor for true twinning is zero. The same phenomena occurs in compression, in the opposite sense. In the twinned orientation, the Schmid factor for ordinary dislocations is also small, and only superdislocations have a high Schmid factor, so twinning increases the volume fraction of crystals where only super dislocations can operate. Luster and Morris observed that superdislocations were active only in crystals having a Schmid factor greater than 0.35, and they only nucleated from interfaces where efficient slip transfer from neighboring crystals was possible [142]. Ordinary dislocations and true twinning were observed in grains where the Schmid factor was larger than 0.25. In

lamellae thinner than 0.5 μm , only deformation systems with Burgers vectors in the lamellar plane were operative. These criteria were applied in Figure 3.8. b to determine the volume fraction of a set of randomly oriented crystals that could deform with 4 or more deformation systems active, excluding superdislocations. Deformation in tension has only 19 vol% of crystals with 4 Schmid factors operative, while in compression, 28 vol % have 4 systems active. In contrast, 33 vol % of crystals in a FCC metal have 4 systems with $m > 0.32$ (inverse Taylor factor). These observations imply that compression of TiAl should be less prone to cracking than tension, since superdislocation activity is restricted as indicated above.

10.4 DISCUSSION

The above review of several investigations indicate that many microstructure features affect primary creep. The impact of the following microstructural features will be assessed for the alloys investigated: Lamellar refinement, reduction of lamellar volume fraction, removal of small equiaxed gamma grains, effect of heat treatment, and the effect of dynamic precipitation. With understanding of how these microstructural changes affect creep properties, optimal microstructural design criteria for creep resistance can be balanced with other design constraints.

10.4.1 Lamellar refinement

Lamellar refinement occurs in all materials examined. Lamellar refinement can only occur by a mechanical twinning process, or by a strain induced transformation similar to twinning [121,125]. These processes cause new interfaces to be created as

strain occurs. Most of the refinement occurs in the first 0.1-0.2% of strain, where the strain rate is high. Comparing Figure 8.5 with 10.7 shows that the initial fast strain rate drops rapidly as the lamellae are refined, and that the strain rate decreases more slowly with strain after the initial refinement process has saturated, as indicated by the discontinuity in the strain rate in Figure 8.5. The amount of refinement depends on the initial lamellar spacing, stress and temperature. A greater amount of lamellar refinement occurs in materials with higher initial lamellar spacing, and consequently, the time to reach 0.5% is reduced, since more of the 0.5% strain occurs in the initial high strain rate process of lamellar refinement. Therefore, reducing the lamellar spacing will reduce the initial amount of strain that can be accommodated by lamellar refinement, and it will take longer to reach 0.5% strain. Heat treatment can be used to reduce initial lamellar spacing; more heat treatment reduces lamellar spacing [127]. Pre-straining can also refine the lamellar spacing in exactly the same way as in creep deformation, by taking up the easy refinement strain before the creep process begins. The most creep resistant TiAl based alloys developed to date have extremely fine lamellar spacings of 0.1 μm [159].

Lamellar refinement hardens the material in two ways, by orientation hardening due to twinning, and by restriction of deformation to modes parallel to the lamellar plane. The volume fraction of hard orientations, where only superdislocations have a high Schmid factor increases with the amount of strain accommodated by mechanical twinning. In addition to orientational hardening, creation of more finely spaced interfaces strengthens the material by a Hall-Petch effect. In addition to strengthening, very fine lamellaer regions have been shown to deflect cracks propagating across lamallae [255]. The greatest amount of lamellar refinement observed in the studies described above

occurred in the high oxygen XD alloy. From Figure 10.6.a and Table 10.3, the reduction in γ thickness was 40%. The high interstitial content may restrict ordinary dislocation mobility more than in the other alloys, and the more difficult operation of ordinary dislocations would increase the probability for strain accommodation by mechanical twinning. Even though mechanical twinning has a lower critical resolved shear stress than ordinary dislocations in binary TiAl single crystals [256], twin nucleation requires a high stress concentration, which exists in grain boundary regions [120].

The reduction in the spacing between α_2 layers and the reduction in α_2 thickness indicated in Table 10.3 indicates that new α_2 layers are being formed in the process of lamellar refinement. This is possible by a strain induced phase transformation that required subsequent diffusion of Ti into the transformed crystal structure, which has been proposed by [205]. A true twin interface can serve as a nucleus for this process, since a true twin interface consists of 4 atomic layers of α_2 crystal structure [213]. Strain accomplished by a moving ledge mechanism has been proposed by Wang and Nieh [159]

10.4.2 Effects of Heat Treatment on Grain size and Lamellar Volume Fraction

Heat treatments shown in Figures 6.2, 7.1 indicate that more heat treatment improves or does not adversely affect creep resistance (with one notable exception for the 10 hr 900°C in the 47Al XD alloy in Figure 7.1). A major source of this improvement is due to removal of fine equiaxed grains that provide regions where boundary diffusional processes are more significant. The presence of the TiB_2 inhibits grain growth, which causes a limiting effect on improving creep resistance. However the degrading effect of

larger grain size on room temperature ductility is well established, so the improved creep resistance in the 47-2-2 alloy in Figure 6.2 may occur at the expense of ductility

Since the lamellar grains are the source of the lamellar refinement deformation mechanism, a higher lamellar volume fraction should cause a greater amount of strain at the initial high strain rate. In low temperature, low stress creep of duplex microstructures, the steady state creep rate was observed to increase with lamellar volume fraction [257]. A larger strain at the high strain rate will reduce the time to 0.5%. Evidence for this is effect is found in Figures 6.2, 7.1, and 10.3. Figure 10.3 shows that the lamellar volume fraction is affected by heat treatment, though it is difficult to ascertain how intrinsic microstructural variations may obscure these measurements. The data in Figure 10.3 were taken from several regions and multiple cross sections of a sample, and they are nominally similar to the trends observed when fewer observations were used. The most consistent feature was the differences in volume fraction between the 10 hrs 1010 °C and the 2 step heat treatment conditions. The 47-2-2 alloy exhibits the best improvement in creep resistance with the 2-step heat treatment, and correspondingly, the lamellar fraction was reduced by this heat treatment. The same thing occurred in the 45Al XD alloy, and the effect of reducing the lamellar volume fraction was a big reduction in the experimental scatter in the times to 0.5%, but no substantial improvement was measured with any heat treatment in this alloy. Conversely, the lamellar volume fraction increased with the 2 step heat treatment in the 47 Al XD alloy, and this would suggest a degrading effect on creep resistance. Since the 2 step heat treatment also reduced the number of fine grains, these two changes apparently balanced each other so that no net improvement in creep resistance was obtained.

10.4.3 Effects of Heat Treatment on Precipitation, and Dynamic Precipitation

The most creep resistant alloy is the heat treated WMoSi alloy. The heat treatment causes nucleation of precipitates. The growth of the precipitates is affected by the stress state, where the stressed region of the material stimulates a more homogeneous and faster growth of the precipitates. Moving dislocations acting as pipes for transport of solute atoms to precipitates enhance and homogenize their growth. This effect is beneficial for developing a creep resistant microstructure that does not develop larger harder inclusions that would degrade ductility. The 47-2-2 alloy also developed fine precipitates with the two-step heat treatment, but the substantial improvement in creep resistance is also correlated with a much larger grain size.

The WMoSi alloy in the as-HIPed condition exhibited strain rates more than 10 times faster with a smaller stress, giving it a creep resistance similar to the 45Al XD alloy. The lack of precipitates in this alloy indicates that most of the silicon is still in solution, which implies that Si in solution degrades creep resistance. This has also been demonstrated by Wang and Nieh [258]. They showed that Si in solution would facilitate ledge mobility in lamellar interfaces, which was proposed as a rate limiting creep deformation process.

10.5 CONCLUSION

Changes in the microstructure have been analyzed to determine how heat treatment and alloy composition affect primary creep resistance in several near- γ TiAl alloys.

All alloys exhibit lamellar refining that causes an initially rapid creep rate up to strains between 0.1 and 0.2%. This undesirable rapid creep strain can be reduced by refining the lamellar spacing by heat treatment or pre-straining.

Lamellar refining occurs by mechanical twinning or similar processes that transform the crystal orientation by a moving interface. The microstructure is hardened by a Hall-Petch effect which results in prevention of deformation across thin lamellae when they are smaller than 0.5 μm , and by orientation hardening, since mechanical twinning rotates crystals into hard orientations where only superdislocations have a high Schmid factor.

Heat treatment homogenizes the grain size distribution by removing fine grains. This results in a more homogeneous creep deformation that can reduce the scatter in some alloys. There is limited evidence for degraded primary creep resistance with higher lamellar volume fraction.

Precipitation provides a large benefit for creep resistance. The use of silicon can be detrimental to creep resistance if it is kept in solution. Precipitation is complex, and heat treatment can provide appropriate conditions for a desirable homogeneous dynamic growth of precipitates during creep deformation.

CHAPTER 11

THE EFFECT OF CARBON CONCENTRATION ON PRIMARY CREEP OF AN INVESTMENT CAST Ti-47Al-2Mn-2Nb+0.8vol.%TiB₂ ALLOY

ABSTRACT

Creep experiments in investment cast XDTM alloys with carbon additions in the as-HIPed duplex microstructure exhibit up to a 10 fold improvement in primary creep resistance compared to the same alloy with low carbon. The carbon levels examined are 0.006, 0.037, 0.065 and 0.110 wt% and creep experiments were done at 138 MPa at 760 and 815 °C, and at 276 MPa at 649 °C. A ten-fold increase in time to 0.5% strain was observed under all conditions tested with a carbon concentration between 0.037 and 0.065 wt%, with no additional benefit from higher carbon concentrations (in contrast, oxygen levels of 0.1wt% yielded only a two-fold increase in creep resistance). The microstructures were investigated in selected tensile creep specimens deformed to about 0.5% strain at 650 °C and 276 MPa. Primary creep deformation in alloys containing carbon are similar to other alloys in that primary creep is divided into two stages, an initial rapid process that refines lamellar spacing through strain levels between 0.2 and 0.5%, and a second primary creep process, where no lamellar refinement occurs. Carbon refines the grain size, alters dislocation configurations in a way that suggests that solute pinning occurs, and carbides are present in the vicinity of interfaces.

11.1 INTRODUCTION

Recent studies made on the effect of interstitials (hydrogen, nitrogen, carbon, and oxygen) on creep properties of TiAl have focused on secondary creep or tertiary creep properties [164,221,259,260]. These interstitials strongly affect microstructural transformation, deformation mechanisms and consequently, mechanical properties [221]. Few studies, however, have been made on the effect of interstitials on primary creep [239,260].

Investment cast Ti-47Al-2Nb-2Mn+0.8TiB₂ XDTM alloys with low interstitial content (about 0.03 at% N, 0.02 at% C, and 0.2 at% O) have been developed at Howmet Corp. Recent investigations motivated by reducing the process cost by reducing the HIPing temperature and/or time and temperature of subsequent heat treatments has yielded some improvement in primary creep resistance [127,239]. Alloys with higher interstitial element concentrations were also investigated to examine the effects on primary creep and process cost reduction. In this chapter, the effect of carbon concentration on primary creep deformation and microstructures of investment cast and HIPed TiAl alloys with no further heat treatment are examined and compared to the same alloy with low interstitial content. Microstructures and primary creep deformation mode are analyzed in terms of grain size, distribution of α_2 , volume fraction of lamellar grains, and carbon concentration.

11.2 EXPERIMENTAL PROCEDURE

Four alloys of near- γ TiAl with the nominal composition of Ti-47Al-2Nb-2Mn-0.8TiB₂XDTM were prepared with varying carbon contents. The same master heat was

used to make all four alloys, by adding measured amounts of aluminum carbide to the crucible prior to by VAR (Vacuum Arc Remelting) and investment casting that provided the compositions given in Table 11.1. The master heat had a low carbon content (0.006 wt%) typical of normal production capability. All alloys were hot isostatically pressed (HIPed) at 1260 °C for 4 hours at 127 MPa (2300 °F, 25 ksi) to eliminate casting porosity and to establish the duplex microstructure. Tensile creep specimens with a gage length of 25 mm and 5 mm diameter were machined from test bars. These specimens were then subjected to creep tests at 649 °C, 276 MPa (1200 °F, 40 ksi), 760 °C, 138 MPa (1400 °F, 20 ksi), and 815 °C, 138 MPa (1500 °F, 20 ksi). The creep specimens were cooled under load after creep strains between 0.4 - 4% were reached.

Table 11.1 Al and C content in as-HIPed investment cast alloys.

C wt%	0.006 (low)	0.037	0.065	0.110
C at%	0.020	0.12	0.21	0.36
Al at%	46.1	46.4	46.6	47.0

For microstructure analysis, only the low carbon, 0.065, and 0.110 wt% alloys deformed at **649 °C, 276 MPa** were examined. Samples were obtained from the grip section of crept specimens to examine the undeformed microstructure and from the gage section of crept specimens to examine the deformed microstructure. A modified Kroll's reagent was used to etch for optical microstructure analysis [222]. For scanning electron microscopic analysis, samples were cut from the grip and gage section of crept samples and then electropolished using a 350 ml Methanol, 175 ml Butyl alcohol, and 30 ml Perchloric acid solution at 20 volt and -50 °C. TEM specimens were sliced from the gage section and the final thinning process was performed in a twin jet electropolishing system

using a 10% sulfuric acid + methanol solution at -20 °C. All microscopy samples were prepared so that the sample normal was parallel to the tensile axis. Microscopy was conducted in a JSM 6400V scanning electron microscope (SEM) operated at 25 kV, and a Hitachi H-800 transmission electron microscope (TEM) operated at 200 kV.

11.3 RESULTS AND DISCUSSION

11.3.1 Microstructures

Figure 11.1 illustrates the grain refinement resulting from addition of carbon. The lamellar grain size is more refined than the equiaxed grain size (see Table 11.2). Figure 11.2(a), shows the needle and round shaped particles arising from the XD process are evenly distributed (equiaxed type: TiB_2 and needle type: TiB) [224]. They are known to be located inside of γ and α_2 grains and in grain boundaries from previous studies [111,127,239]. As shown in Figure 11.2(b-d), all alloys show duplex microstructures having different amount of lamellar volume fractions. Most equiaxed grains are located around grain boundaries of lamellar grains. Some equiaxed grains can also be seen in the middle of lamellar grains. The different grain size and lamellar volume fractions strongly influence primary creep behavior [127].

The reduction of grain size from the addition of interstitials was similar to that in a cast gamma TiAl alloy with nitrogen (Ti-48.5Al-1.5Mo-1N) studied by Cho *et al.* [260]. They suggested that the Ti_2AlN particles suppress the grain growth and refine the microstructure. Chen *et al.* (600-700C ppm), Tian and Nemoto (0.5C mol%), and Whittenberger and Ray (0.025-0.4C at%)[220,261,262] showed that the fine precipitation of carbides as plate-shaped particles (Ti_2AlC : 0.06~0.2 μm) or perovskite type particles

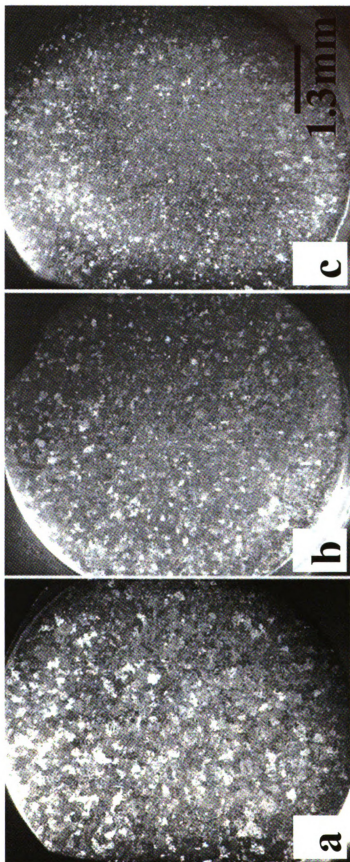


Figure 11.1 Optical micrographs of Ti-47Al-2Nb-2Mn+0.8 vol%/TiB₂ alloys having (a) Low carbon, (b) 0.065 wt% carbon, (c) 0.11 wt% carbon.

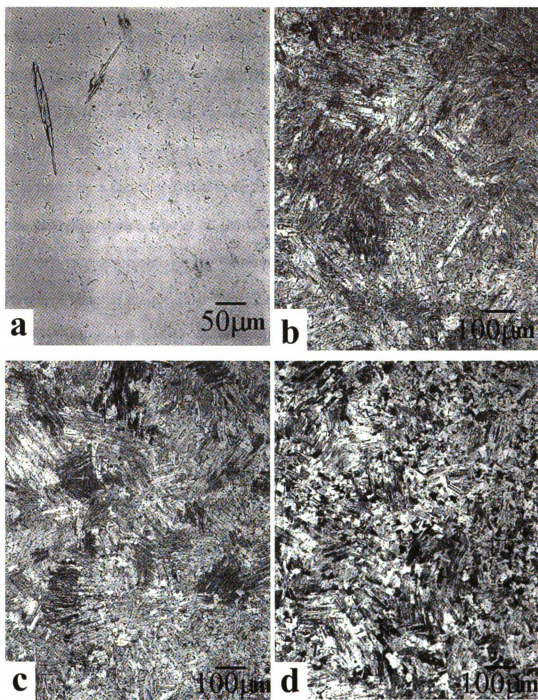


Figure 11.2 Optical micrographs of Ti-47Al-2Nb-2Mn+0.8 vol%TiB₂ alloys having (a,b) Low carbon, (c) 0.065 wt% carbon, (d) 0.11 wt% carbon.

(Ti₃AlC: 0.008~0.2 μm) were formed by cooling after HIPing and/or aging treatment. Such Ti₂AlC or Ti₃AlC precipitates could retard the grain growth. Optical micrographs shown in Figure 11.2 indicate a smaller range of grain sizes in the higher carbon alloys (Table 11.2). Also, there is a high volume fraction of lamellar grains in the alloys having low and 0.065 wt% carbon, but in the 0.110 wt% C alloy the volume fraction of lamellar grains is lower by a factor of 2 (Table 11.2), and more equiaxed grains are developed at lamellar grain boundaries. Cho *et al.* [260,263] also mentioned that the addition of more than 0.3 at% nitrogen results in the development of some equiaxed grains at the grain boundaries of lamellar grains. Since the carbides and nitrides have similar stoichiometry, morphology, and atomic weight, the effect of carbon may be similar to that of nitrogen. Although interstitials such as carbon and nitrogen can change the α transus in the $\alpha + \gamma$ region (where the phase transformation from α to lamellar grains occurs during cooling), this cannot account for the large difference in the lamellar volume fraction observed in the 0.110 wt% alloy.

Table 11.2 The lamellar volume fraction and grain size in TiAl alloys

TiAl alloys	volume fraction of lamellar grains*	lamellar grain size	equiaxed grain size
0.006 wt% C	68 \pm 7%	100 ~ 350 μm	5 ~ 30 μm
0.065 wt% C	70 \pm 10%	50 ~ 200 μm	3 ~ 20 μm
0.110 wt% C	29 \pm 10%	50 ~ 150 μm	3 ~ 20 μm

* average values from at least four images having areas of $1.02 \times 10^{10} \mu\text{m}^2$ in each image. The italic number represents standard deviation.

In equiaxed grain regions, thin layers of α_2 phase exist in some boundaries of γ grains having less than 10 μm grain size in the backscattered electron (BSE) images in Figure 11.3. These layers are thicker and brighter in the alloys containing more carbon.

The greater amount of retained α_2 may be due to the presence of the higher carbon concentration since the solubility of interstitial elements in α_2 is greater than that of γ [264,265]. Fine precipitates are often observed in or near these α_2 areas. From Figure 11.4, the thickness of α_2 in the alloy with 0.110 wt% C is as large as 2 μm , while the thickness is less than 0.5 μm in the alloys with low carbon and 0.065 wt% C. These thicker α_2 features in the 0.110 wt% C are similar to angular α_2 grains which have been correlated with poorer creep properties from previous studies [11,127,239,253].

Fine precipitates are also observed near grain boundaries of equiaxed grains and in lamellae. In Figure 11.5 very fine precipitates (see arrow) ranging from 0.08 μm to 0.2 μm are observed preferentially in α_2 layers of lamellar laths and in equiaxed α_2 grains. A few precipitates are also observed in γ grains. These fine precipitates can be a barrier to moving dislocations during deformation, and their presence in α_2 may impede slip transfer through the α_2 phase. Fine particles also are observed in grain boundaries of equiaxed grains, as shown in the bright field image in Figure 11.5(c). Chen *et al.*, and Tian and Nemoto [220,261] observed homogeneous distributions of plate-shaped (Ti_2AlC) or perovskite type particles (Ti_3AlC) in γ grains, but such homogeneous precipitate distributions could not be found in the current as-HIPed alloys. These fine particles can harden the grain boundaries during high temperature deformation.

Particularly in deformed samples, as shown in Figure 11.6, many deformation twins are found in gamma grains after small creep strains. From prior studies [11,127,239,253], such fine twins are common features in investment cast TiAl alloys crept only in the primary stage.

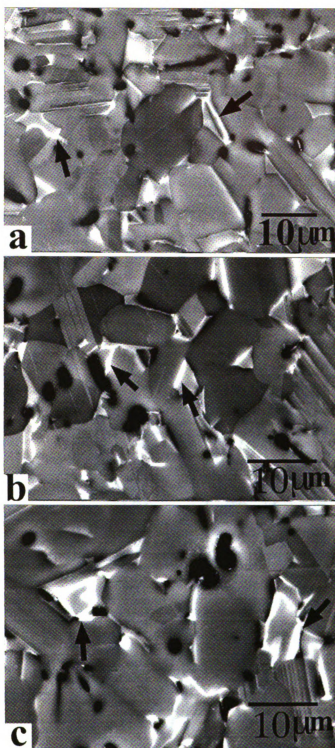


Figure 11.3 Backscattered electron images of Ti-47Al-2Nb-2Mn+0.8 vol%TiB₂ alloys having (a) Low carbon, (b) 0.065 wt% carbon, (c) 0.11 wt% carbon. The arrows indicate the thin layers of α_2 phase.

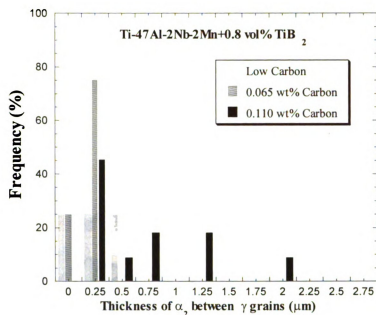


Figure 11.4 Distribution of thin α_2 layers surrounded by γ grains in TiAl alloys.

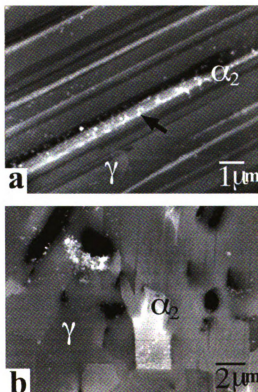


Figure 11.5 a and b: Backscattered electron images of Ti-47Al-2Nb-2Mn+0.8 vol%TiB₂ alloys having 0.065 wt% carbon.

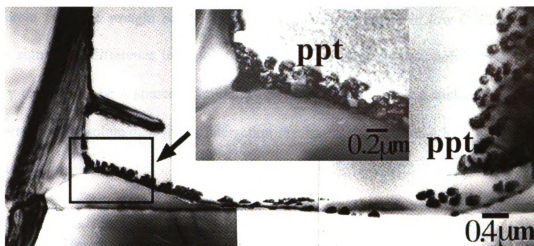


Figure 11.5.c Precipitates along the grain boundaries of γ grains in creep tested Ti-47Al-2Nb-2Mn+0.8 vol%TiB₂ alloys having 0.065 wt% carbon.

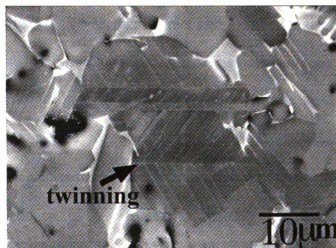


Figure 11.6 Backscattered electron images of Ti-47Al-2Nb-2Mn+0.8 vol%TiB₂ alloys having 0.11 wt% carbon.

Intensive dislocation activity can be seen in the vicinity of a TiB particle, and dislocations and bowed dislocations along with their pinning points can be easily seen ((Figure 11.7), indicated by arrows). The general shape of these dislocation lines is different from the straight screw segments commonly observed in low C alloys [266]. This significant difference in dislocation morphology suggests that carbon dissolved in the γ matrix can be a source of pinning points that retard moving dislocations during deformation by solute/dislocation interaction mechanisms, rather than by a barrier effect of carbide precipitates.

11.3.2 Lamellar spacing

Lamellar spacing was characterized by tabulating 300 to 370 α_2 spacing measurements (i.e., distance between α_2 - γ interfaces using backscattered electron (BSE) imaging) in more than 20 lamellar regions near grain boundaries. Measurements were taken from the grip and gage section of crept samples to compute the average α_2 spacing of undeformed and deformed material. These measurements are upper bounds of the actual spacing, since the lamellar plane normal direction was not determined to make the parallax correction needed to determine the actual α_2 spacing. However, this is a systematic way to compare α_2 spacings in specimens with similar microstructures.

The distribution of α_2 spacings in undeformed and deformed material is represented as solid and dashed lines, respectively in Figure 11.8. In every case, there is a shift of the frequency distribution toward higher frequencies at lower spacing values after creep. For example, the average α_2 spacing in 0.065 wt% C changed from 1.17 to 0.84 μm due to a small creep strain of 0.42%. This reduction of α_2 spacing can be explained

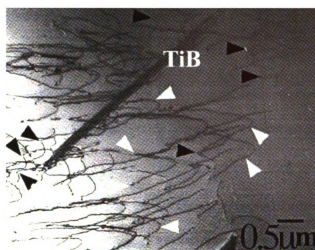


Figure 11.7 Dislocation activity near TiB particles in creep deformed Ti-47Al-2Nb-2Mn+0.8vol%TiB₂ alloys having 0.065 wt% carbon. White arrows show bowing, and black arrows show pinning points.

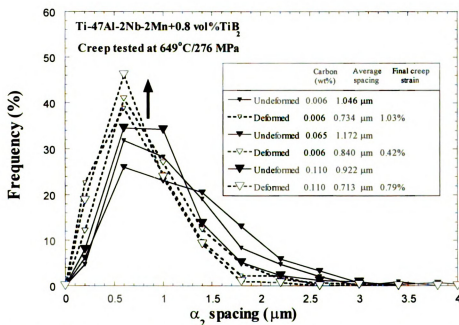


Figure 11.8 Distribution plot of α_2 spacing in undeformed grip and deformed gage section of tensile creep specimens.

indirectly by the easy mode deformation twinning parallel to lamellar boundaries. This refinement trend is similar to that found in prior studies [11,127,239,253].

11.3.3 Primary Creep behavior

Primary creep resistance increased with increasing carbon content up to a value of 0.065 wt%, as shown in Figure 11.9(a). This plot shows that an increase in creep resistance by an order of magnitude can be obtained with small carbon additions at all temperatures in a systematic manner. Figure 11.9(b) shows data for specimens deformed at 649°C and 276 MPa (40 ksi and 1200°F) as a function of time. The alloys with low carbon reach 0.60% creep strain in 100 hours, while the alloys with 0.037, 0.065, and 0.110 wt% C show lower strains of 0.22, 0.15, and 0.25% creep strains, respectively at 100 hours creep time. Thus carbon concentrations up to 0.065 wt% increase the primary creep resistance increase, but a 0.110 wt% carbon addition results in a decrease in creep resistance. The 0.037 and 0.065 wt% specimens exhibit the lowest primary creep rates after 100 hours, but the 0.065 and 0.110 wt% specimens exhibit the lowest early primary creep rates (at 20 hours). Thus the 0.065 wt% alloy is near an optimum carbon concentration for primary creep resistance.

The θ -projection concept constitutive equation described in [250,267] is based on the phenomenological understanding of creep deformation in primary and secondary stages. A variation of the θ -projection constitutive equation was used to characterize the present creep data. The equation used for curve fitting the creep data is

$$\varepsilon(t) = e_1 (1 - \exp(-r_1 t)) + e_2 (1 - \exp(-r_2 t)) + \dot{\varepsilon}_s t \quad (1)$$

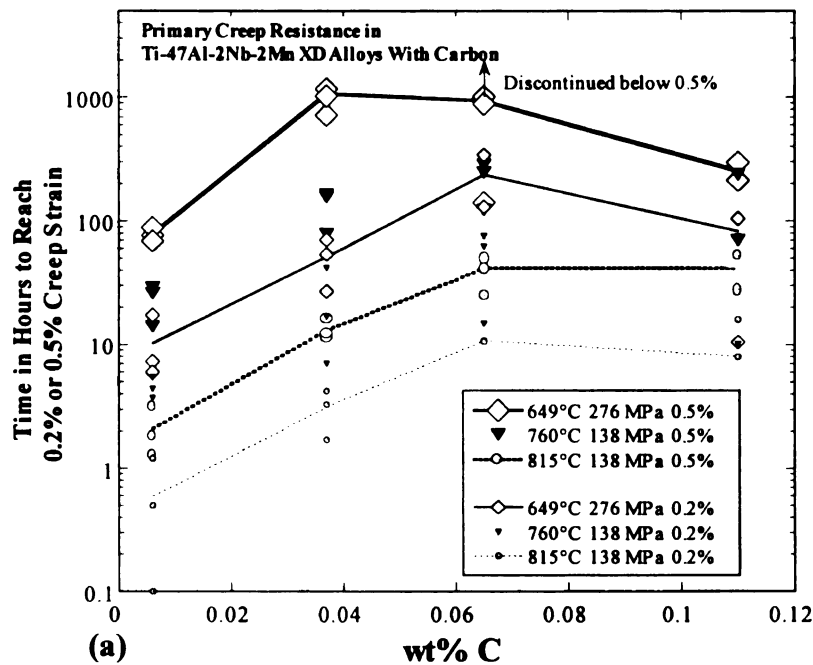
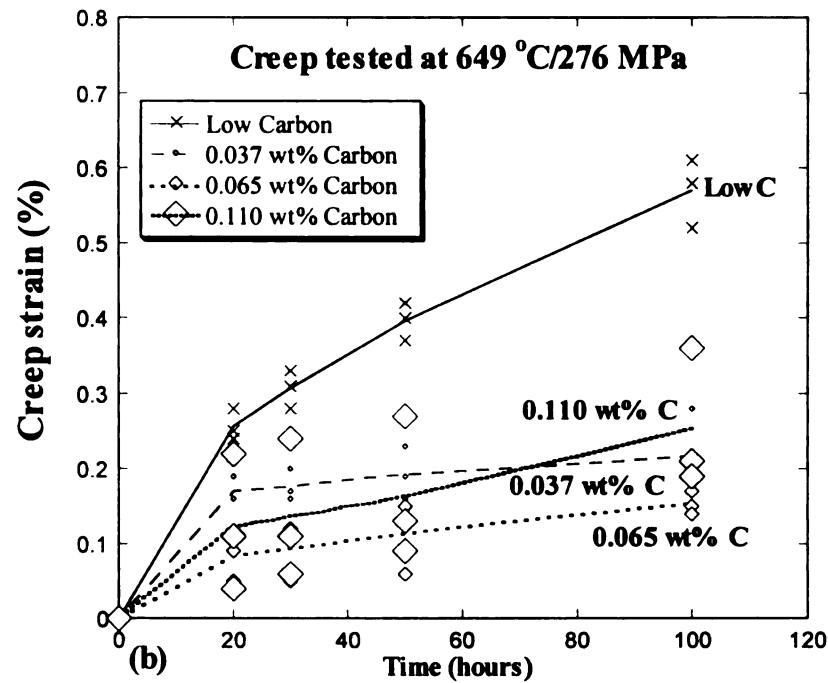


Figure 11.9 (a) Creep times to 0.2% and 0.5% strain as a function of carbon concentration for specimens deformed at three deformation conditions. (b) Creep strain to 0, 20, 30, 50, and 100 hours in Ti-47Al-2Nb-2Mn+0.8 vol%TiB₂ alloys. Lines go through the average of 3 samples.

where ϵ is creep strain, t is creep time, e_1 , r_1 , e_2 , and r_2 are curve fitting parameters, and $\dot{\epsilon}_s$ is the steady state (or minimum) strain rate. Equation (1) was used as a fitting function using Kaleidagraph in software to represent the experimental data in a form that can be easily differentiated. These fitting parameters are provided in Table 11.3. These fitted curves are accurate representations of the creep data as indicated by the R values. By differentiating equation (1), the strain rate can be calculated from following equation

$$\dot{\epsilon}(t) = e_1 r_1 (-r_1 t) + e_2 r_2 (-r_2 t) + \dot{\epsilon}_s \quad (2)$$

Table 11.3 Curve Fit Parameters in Creep tests shown in Figure 11.10

TiAl Alloys	e_1	r_1	e_2	r_2	R
0.006 wt%	0.0017058	1.0053×10^{-4}	0.0027975	2.7965×10^{-6}	0.9997
0.065 wt%	0.0008675	3.1575×10^{-4}	0.0012788	2.5094×10^{-6}	0.9992
0.110 wt%	0.0017167	1.7173×10^{-4}	0.0007673	6.8842×10^{-6}	0.9995

- R represents Least Squares Curve fits

The trends illustrated by the data in Figure 11.9(b) are also evident in the strain rate vs. strain plot in Figure 11.10. The minimum strain rate of 0.065 wt% C is lower than the low C alloy by more than one order of magnitude. The minimum strain rate of 0.110 wt% C is between the Low C and 0.065 wt% C. The transition points which indicate a change in the dominant primary creep mechanism [253] are indicated by arrows in Figure 11.10. A slower strain rate at the transition point implies better primary creep resistance. This transition point is strongly related to microstructure features such as

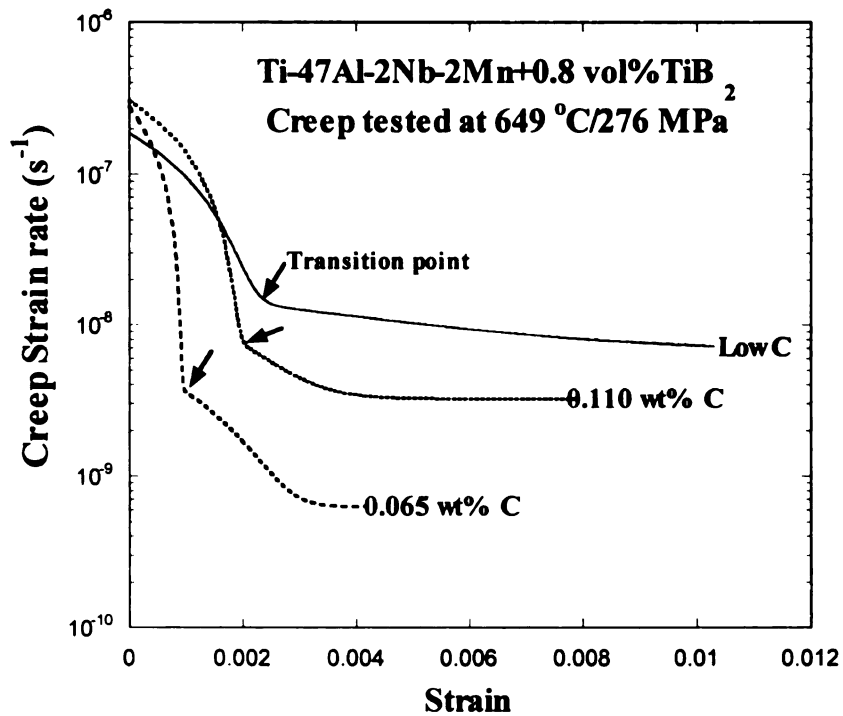


Figure 11.10 Creep strain rate as a function of creep strain in Ti-47Al-2Nb-2Mn+0.8vol%TiB₂ alloys.

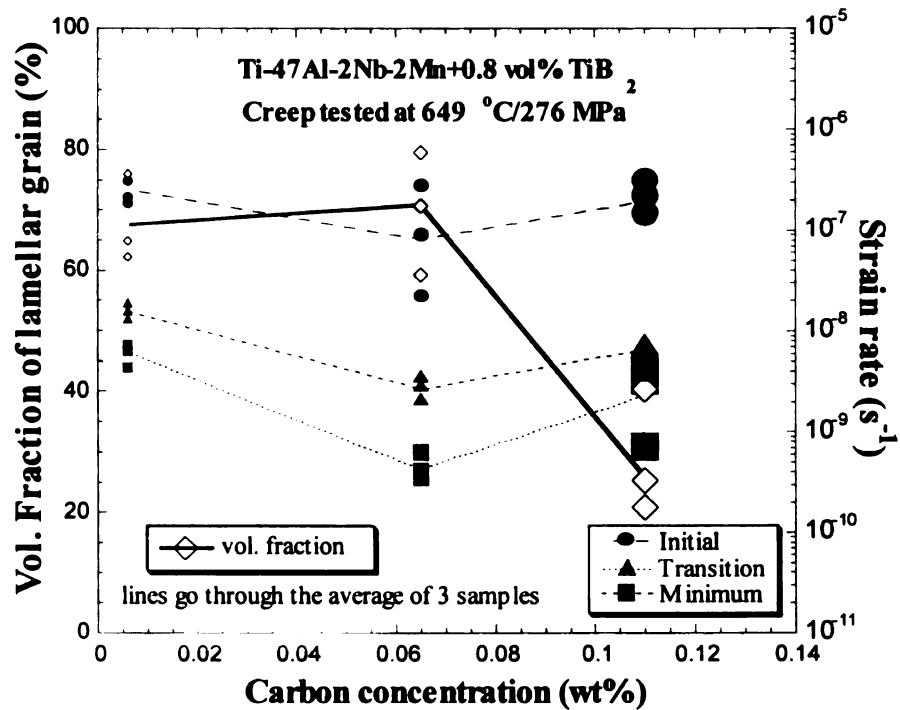


Figure 11.11 The relationship between lamellar vol. fraction and strain rates with carbon concentration. On this and subsequent plots, the size of the symbol represents carbon concentration.

lamellar volume fraction and deformation twinning [111,253,205].

As indicated in Table 11.2 and Figure 11.11, the volume fraction of lamellar grains is affected by carbon concentration, and the impact of carbon on several characteristic strain rates denoted as initial, transition, and minimum is shown. The volume fraction of lamellar grains increases slightly with increasing carbon but it drops dramatically with more than 0.065 wt% C. All characteristic strain rates decrease with increasing carbon concentration up to 0.065 wt% and then the strain rates increase slightly with additional carbon. Although the alloys having 0.110 wt% C have the lowest lamellar volume fraction (~29 %), its minimum creep rate is still much lower than low C alloys with high lamellar volume fractions.

Figure 11.12 shows that the initial strain rate, strain rate at the transition point, and minimum strain rate decrease linearly as the volume fraction of lamellar grains increase. The two higher carbon alloys are on the same line, while the low carbon alloy exhibits the same slope but the transition strain rate is almost an order of magnitude faster. This suggests that once a saturation level of carbon is added, the transition strain rate is not reduced further. A higher volume fraction of lamellar grains is beneficial for creep resistance, since a larger volume fraction of lamellar interfaces will block dislocations during deformation. Worth et al. [164,221] indicated that 30% lamellar volume fraction in a duplex microstructure gave poorer creep resistance than the equiaxed γ microstructure (0% lamellar volume fraction) due to the increase in dislocation mobility in the duplex alloy γ phase. The fully lamellar microstructure gave the best creep resistance because the fine lamellar spacing impeded dislocation motion on {111} planes not parallel to the lamellar interface. The addition of carbon did not have a dramatic

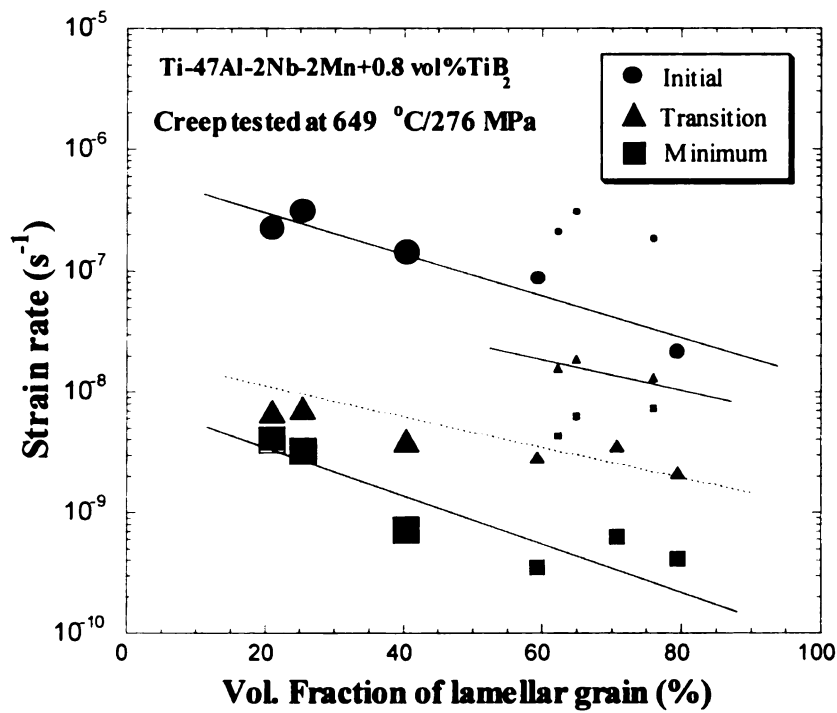


Figure 11.12 The relationship between lamellar vol. fraction and initial strain rates and strain rate at minimum and transition points. Symbol size represents carbon concentration (small, medium, and large size symbol: Low carbon, 0.065 wt%, and 0.110 wt% carbon).

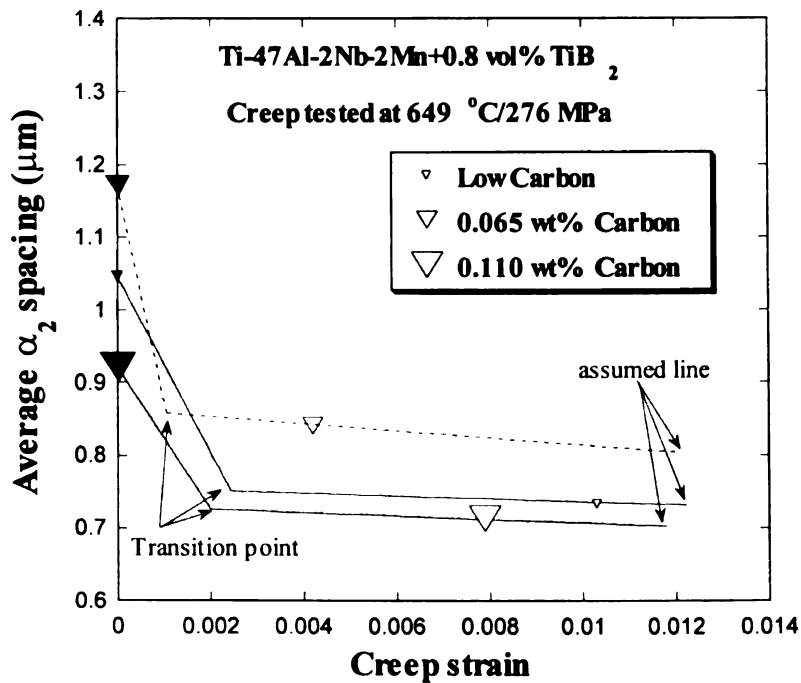


Figure 11.13 α_2 spacing as function of creep strain.

effect on the lamellar spacing, as the 0.065 wt% alloy exhibited the best primary creep resistance, yet it also had the largest average lamellar spacing (Figure 11.8). As a result of microstructural analysis in Figures 11.5 and 11.7, the improvement in primary creep resistance with addition of carbon is probably due to a solute atmosphere drag mechanism along with precipitates that interfere with slip near or across boundaries. The mild decrease in creep resistance in the 0.110 wt% C alloy correlates with the small volume fraction of lamellar grains and the increased presence of angular α_2 as described in Figures 11.3.c and 11.4.

Based on prior work, it is known that lamellar spacing was refined due to easy mode deformation twinning that occurs below the transition strain, whereafter the α_2 spacing remains constant [205,253]. Using the strain values at the transition for the specimens in Figure 11.10, and the measured lamellar spacing, the rate of lamellar refinement can be estimated as shown in Figure 11.13. The 0.065 wt% C alloy exhibits the fastest rate of lamellar reduction that correlates closely with the greatest deceleration of strain rate in Figure 11.10, and hence the best primary creep resistance. Also, these data indicate that the smallest lamellar spacing does not necessarily lead to superior primary creep resistance. The greatest deceleration of primary creep occurs with the highest initial α_2 spacing, since an increase in lamellar interfaces due to lamellar refinement will increase the number of barriers to dislocations during early creep deformation. This is consistent with the case of oxygen additions in TiAl alloys, where the high O alloy exhibited a greater reduction of the thickness of γ lathes (from TEM) than lower O alloys, due to mechanical twinning parallel to the lamellar plane [239].

The relationship between reduction of α_2 spacing and the strain rate at the

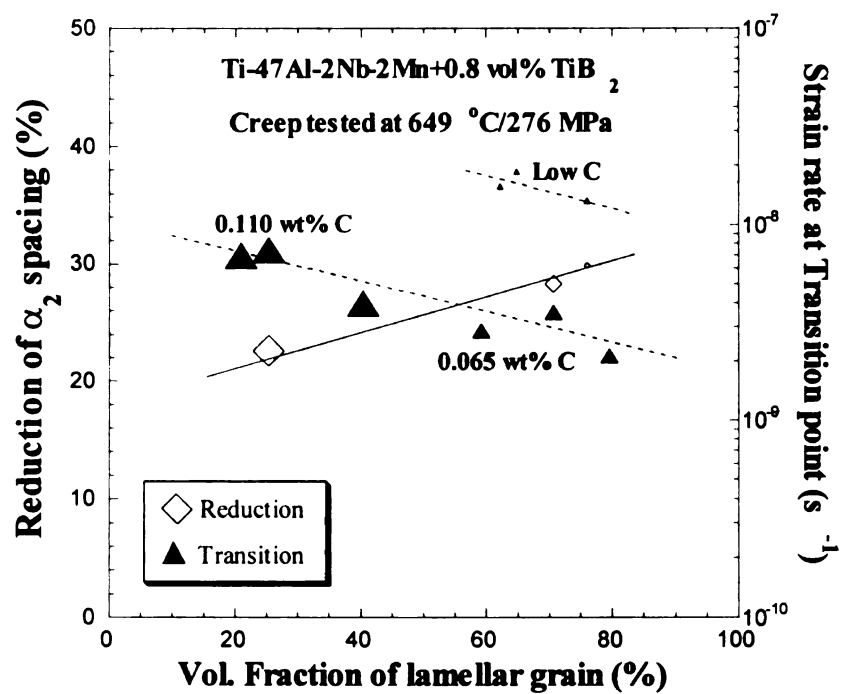


Figure 11.14 Lamellar refinement and strain rates at transition point as a function of lamellar vol. fraction.

transition point (with respect to lamellar volume fraction) is plotted in Figure 11.14. A higher lamellar volume fraction results in greater reduction of lamellar spacing and a lower strain rate at the transition. These two qualities taken together are effective in reducing the initial fast mode of primary creep.

From the above, a limited amount of carbon (0.065 wt% C) gives the best primary creep property for several reasons: the carbon dissolved in γ grains can impede the moving dislocations, and precipitates at grain boundaries and interfaces block slip transfer and harden the grain boundary. The carbon causes a smaller lamellar grain size that gives the better primary creep resistance similar to extruded fully lamellar alloys [160]. The addition of carbon does not cause any fundamental difference in the reduction of lamellar spacing in the lamellar grains due to the easy mode twin deformation, which is observed in low carbon alloys.

10.4 CONCLUSIONS

The addition of carbon in investment cast Ti-47Al-2Nb-2Mn-0.8TiB₂ results in a grain size refinement, and the lamellar volume fraction is reduced from 70% to 30% by adding more than 0.065 wt% C. In 0.110 wt% C alloys, thick layers of α_2 , which are similar to angular α_2 grains that correlate with poorer creep resistance, are observed. In the 0.065 wt% C alloy, bowed dislocations along with pinning points in γ grains and precipitates at grain boundaries are observed. This suggests that carbon dissolved in γ matrix can be a source of pinning points and can cause drag on the moving dislocations. Precipitates at grain boundaries and interfaces block slip transfer and harden the grain boundary. The reduction of lamellar spacing occurs due to the easy mode deformation

twinning parallel to lamellar boundaries at the early stage of primary creep in a way that is similar to other low carbon alloys. Higher lamellar volume fraction results in a greater reduction of lamellar spacing and a lower strain rate at the transition point that separates an initial fast mode and a slower mode of primary creep. The increase in lamellar interfaces impedes dislocation motion on $\{111\}$ planes that are not parallel to the lamellar interface. These results indicate a limited carbon addition (0.065 wt% C) to Ti-47Al-2Nb-2Mn-0.8TiB₂ gives the best primary creep resistance.

CHAPTER 12

MECHANISMS OF LAMELLAR REFINEMENT DURING PRIMARY CREEP OF NEAR-GAMMA DUPLEX TiAl

Primary creep has been investigated in a number of near-gamma TiAl alloys with duplex microstructures from previous studies [111,127,205,239,253]. These studies show that two stages of primary creep deformation occur, an early and rapid process that exhausts itself after about 0.2-0.5% strain, and a different process that dominates the deformation up through the minimum creep rate that is more similar to minimum or secondary creep deformation. When creep data are fit to functions that are complex enough to accurately represent the measured strain-time data, these two stages are easily observed in a strain-rate vs. strain plot. From interrupted creep tests, the early process causes lamellar refinement, i.e. a reduction of lamellar spacing, and the second process does not alter the lamellar spacing significantly. The primary creep resistance is dominated by the rate at which the early process is exhausted. The refinement of lamellar spacing due to small creep strains could be explained by a reduction in the γ thickness [127,239], which can only occur by mechanical twinning [121], as well as a reduction in the α_2 spacing due to a strain induced γ - α_2 shear transformation [125,127].

In this study, a simulation of the refinement process has been made to examine possible mechanisms that could account for the observed refinement (see appendix). The lamellar distributions obtained from the simulation are compared with the measurements in TiAl alloys, and the resulting local strains in the lamellar microstructure are computed to consider how different deformation histories affect the resulting deformed distribution.

Investment cast TiAl alloys, such as Ti-47Al-2Nb-2Mn+0.8TiB₂ XDTM with oxygen (XD high O), Ti-47Al-2Nb-2Mn+0.8TiB₂ XDTM alloys with different HIP conditions (XD low HIPed and XD high HIPed), and Ti-47Al-2Nb-1Mn-0.5W-0.5Mo-0.2 Si alloy were tested at 760 °C and 138 MPa creep conditions, and the W-Mo-Si alloy was also tested at 649 °C and 276 MPa at Howmet Corp. All creep tests were stopped at about 0.5% creep strain. The simulation code is developed using Quick-Basic (see appendix). The code starts with data from a distribution plot from an undeformed specimen. A set of 100 lamellar spacings that represent the undeformed lamellar spacing frequency distribution is generated in a random order. The simulation is started by following assumptions: The thickest lamellae in the undeformed condition are subdivided in a manner that changes the frequency distribution in the thicker bins to match the deformed distribution by assuming that strain induced α_2 shear transformations parallel to lamellar planes with a thickness of 0.2 μm occur. No more than one twin can occur in one lamellar lath. When a lath is divided, one lath from the original bin is removed, and two smaller laths are added to the appropriate smaller bins. The refinement process starts in the thickest lamellae and continues until the lamellar distribution matches the deformed distribution in the larger bins. The simulation is finished, when the last bin that has a larger fraction than the deformed distribution is reached, as illustrated in Figure 12.1. From the 0.2 μm thickness of each shear transformation, a cumulative shear displacement is evaluated, assuming a shear strain of 0.3535 in the 0.2 μm layer. This strain corresponds to a particular dislocation moving on every other plane in a manner to generate the α_2 structure [268]. The output file has a calculated local shear strain, lamellar spacings and lamellar spacing frequency distribution at each simulation step, and the total

number of transformed layers and lamellae is created. This file is opened with Microsoft Excel and the distribution plot was created by using *KaleidaGraphTM* software.

From the simulation, the resulting distribution of thinner lamellae in two different TiAl alloys match the measured distribution quite closely, as illustrated in Figure 12.1. From this mechanism described above, the local shear strain in lamellar grains due to α_2 shear transformation can be computed from this simulation as illustrated in Figure 12.2. On the horizontal axis, each original lamellae is indicated by a short vertical line. A place where the α_2 shear transformations took place is indicated by an arrow, and the lamellar distribution line is displaced up due to this shear transformation in several lamellae. From the slope where the shear transformation occurs, in the simulated sample overall of strain in the lamellar region can be calculated as indicated by the dashed line. The computed local shear strains ($>0.7\%$) in lamellar microstructure were similar or higher than effective shear strains ($\gamma_{\text{eff}}=1.0\%=2 \bullet 0.5\% \epsilon$) from specimens simulated in Figure 12.3. For computed shear strains less than about 2%, the amount of lamellar refinement is about the same. One datum suggests that more reduction of lamellar spacing would occur if more than 2% local shear strain develops in lamellar microstructures.

In general, there are two stages in the primary creep deformation, and the first stage is rapid drop of creep strain rate, and then the later stage is slower process that controls the deformation up through the minimum creep rate (see Figures 8.5, 10.1, and 11.10). The transition points which indict a changes in the dominant primary creep mechanism [253] are indicated by arrows in these Figures. A slower strain rate at the transition point implies better creep resistance, and this transition point is strongly correlated with microstructure features such as lamellar volume fraction and deformation

twinning [111,205,253,269]. There is also a correlation between the computed local shear strain and the lamellar volume fraction, creep strains, and strain at transition points in most TiAl alloys as shown in Figure 12.4, 12.5, and 12.6. A linear relationship between the transition strain rate and the minimum creep rate in XD alloys vs. computed local shear strains can be seen in Figure 12.4. This trend is strongly correlated with lamellar volume fraction as shown in Figure 12.5 and 12.6. As the volume fraction of lamellar grains increases, the computed local shear strain decreases, and the strain rate at transition point decreases, too. From experimental measurements, the strain at the transition point increases with increasing lamellar volume fraction. The higher volume fraction of lamellar grains implies less lamellar refinement per lamellar grain, but with more lamellar grains, there is more strain accomplished by refinement, so the transition strain is larger. However, the observation in Figure 12.3, lamellar refinement not being proportional to local shear strain is difficult to rationalize. Further analytical efforts in simulation are required.

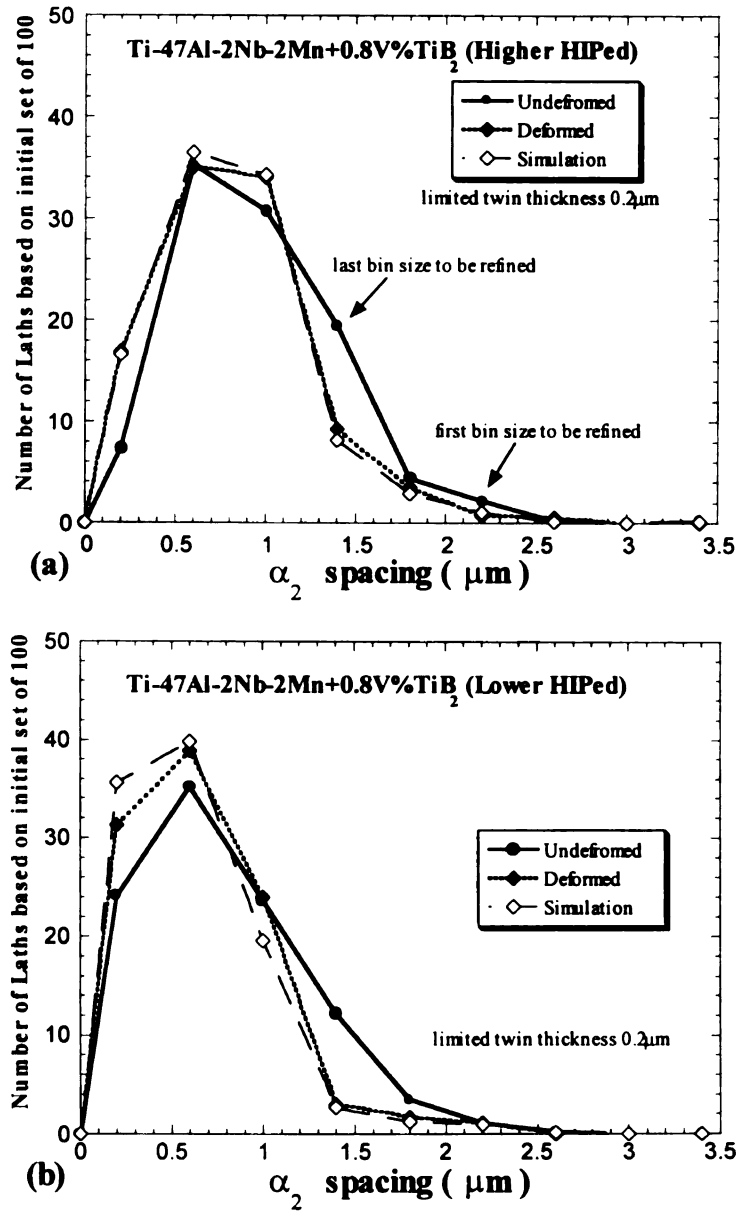


Figure 12.1 The distribution of α_2 spacing is shifted to a greater fraction of finer spacing as a result of early stage primary creep deformation. A simulation based on the undeformed room temperature grip that generates 0.2 μm thick α_2 layers within thicker γ lamellae matches the deformed distribution.

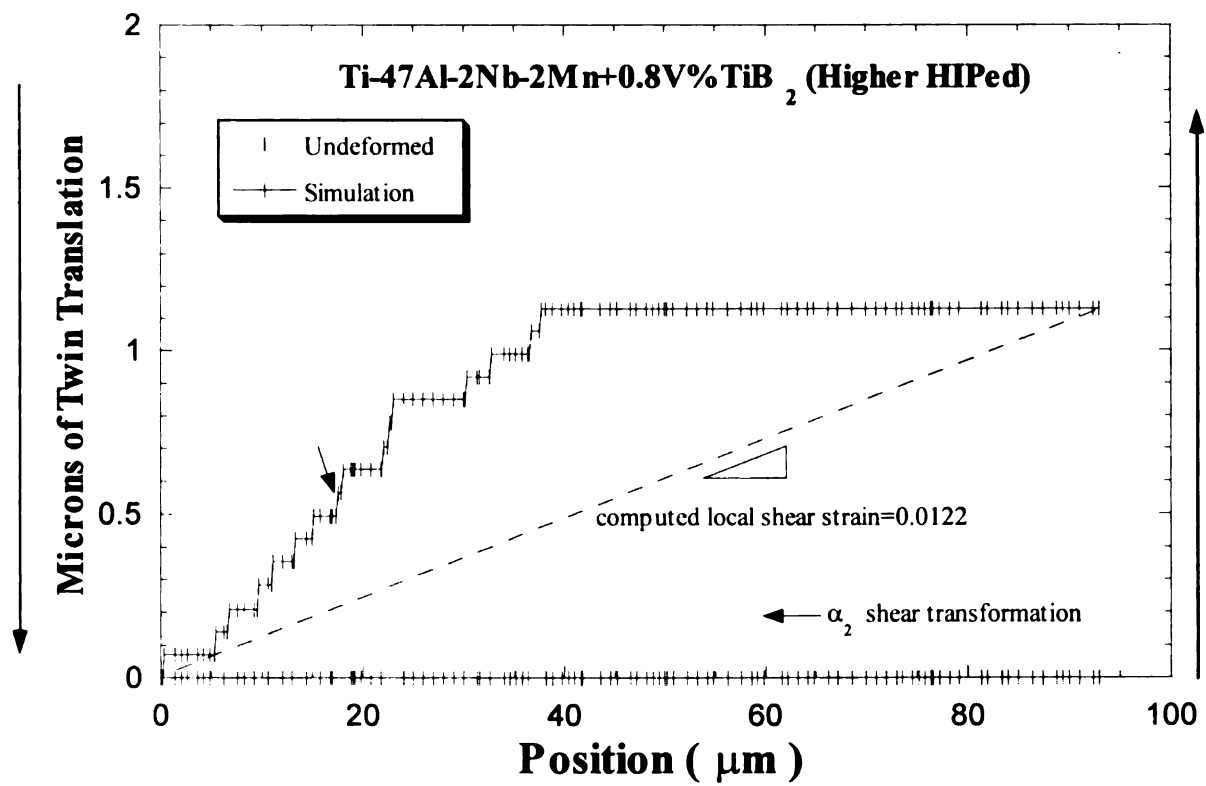


Figure 12.2 Lamellar laths configuration in undeformed and deformed case from simulation.

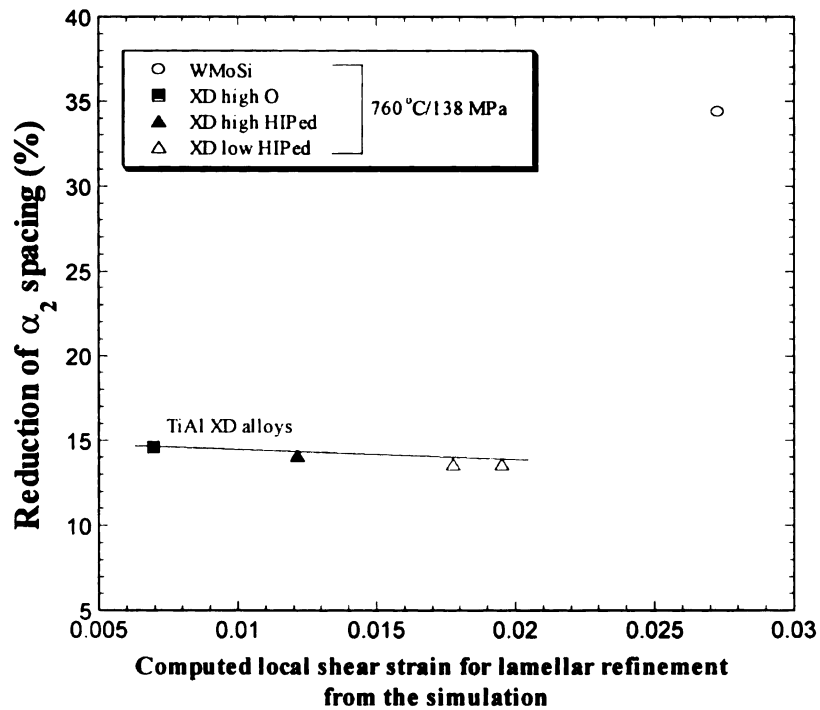


Figure 12.3 The relationship between computed local shear strains and reduction of α_2 spacing.

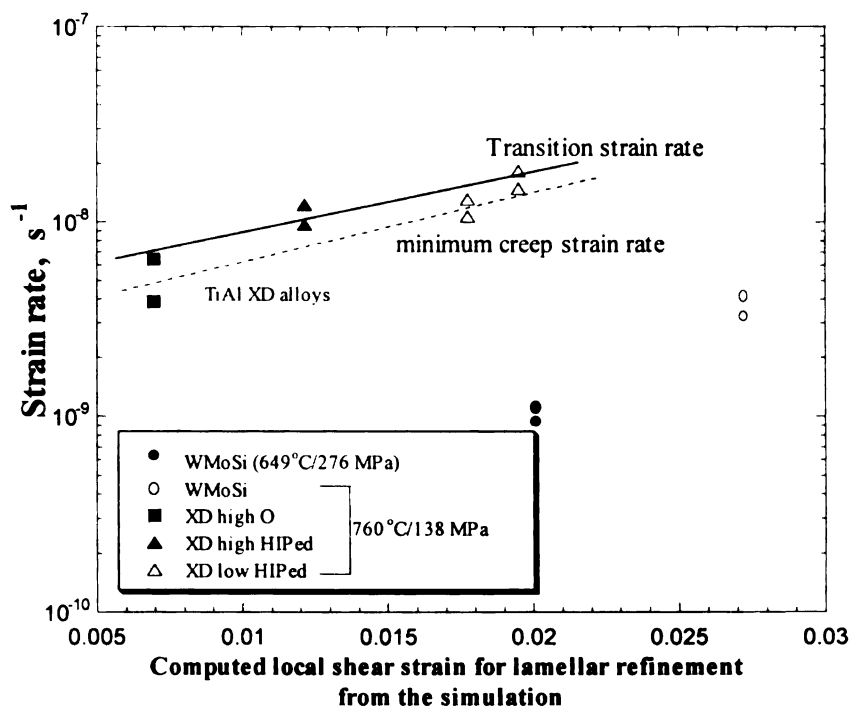


Figure 12.4 The relationship between computed local shear strains and strain rates at transition points.

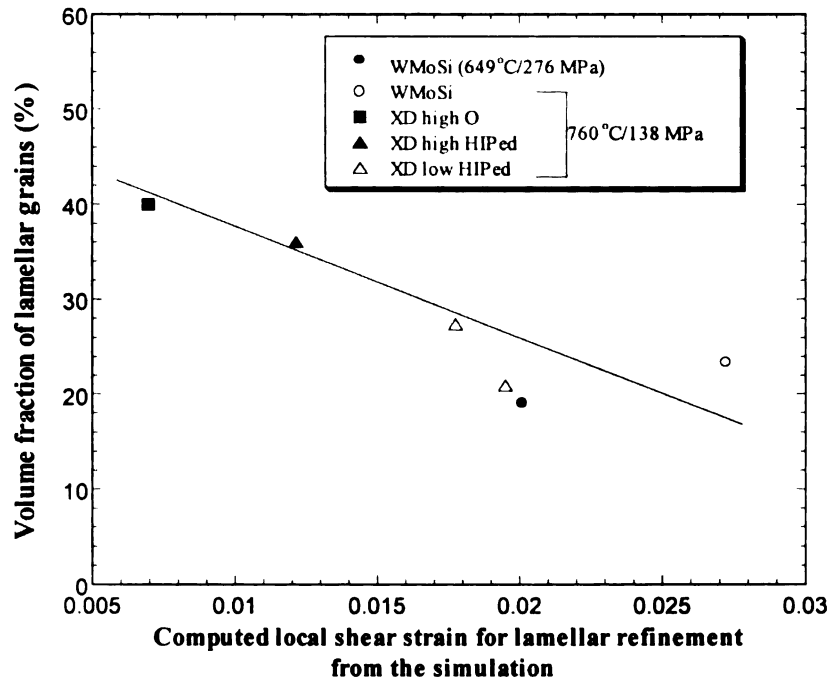


Figure 12.5 The relationship between computed local shear strains and volume fraction of lamellar grains.

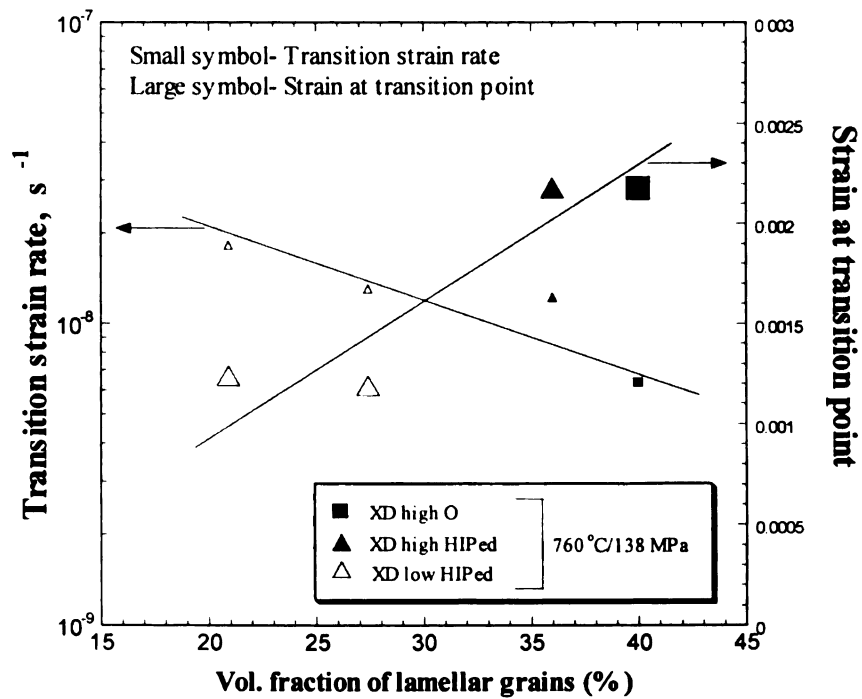


Figure 12.6 The relationship between strain rates and strains at transition point with volume fraction of lamellar grains.

CHAPTER 13

SUMMARY

Changes in the microstructure have been analyzed to determine how heat treatment and alloy composition affect primary creep resistance in several investment cast TiAl alloys. Creep behavior in PST crystals with different orientations was investigated to determine how different orientations affect creep behavior in lamellar microstructure by changing stresses and temperatures. The creep behavior of these alloys and the influence of heat treatment are summarized.

Ti-45Al-2Nb-2Mn-0.8TiB₂ did not show much difference in primary creep resistance after various heat treatments because no difference in the microstructures was caused by heat treatment. The creep resistance was poor, due to very fine microstructures and large angular α_2 grains. Some limited improvement in the Ti-47Al-2Nb-2Mn-0.8TiB₂ alloy was obtained with heat treatment. The XD alloys with high O showed better primary creep property than low O alloys. The high O alloy exhibited 40% lamellar grains (in spite of having higher Al content) indicating that O stabilized the α_2 phase. The addition of carbon in investment cast Ti-47Al-2Nb-2Mn-0.8TiB₂ improved primary creep resistance, refined grain sizes, and reduced the lamellar volume fraction from 70% to 30% by adding more than 0.065 wt% C. Thick layers of α_2 , which are similar to angular α_2 grains that correlate with degraded creep resistance, are observed in 0.110 wt% C alloys. The heat treatments (especially the two step heat treatment) significantly improved the creep resistance of the Ti-47Al-2Nb-2Cr alloy. This heat treatment led to the smallest volume fraction (18%) of lamellar grains, a homogeneous microstructure, the

least amount of pockets of small equiaxed grains, large equiaxed grains, and it caused precipitation of some small particles in interfaces. The texture is strengthened with heat treatment (the desirable texture to minimize mechanical twinning is to have crystals oriented near 001 with the tensile axis and away from 441) and it may contribute to the excellent creep resistance obtained from the two-step heat treatment. Ti-47Al-2Nb-1Mn-0.5W-0.5Mo-0.2Si alloy shows the best primary creep resistance (~300 hrs to 0.5% creep strain). Precipitates (size from 0.05 to 2 μm) were nucleated by heat treatment, and they grew with the assistance of strain or transformation of α_2 to γ . Many precipitates in this alloy have considerable variety in the composition, crystal structure, and shape and size, depending on their location in the microstructure. The nucleation and growth of these precipitates interferes with dislocation motion, and they harden the microstructure. This precipitation hardening mechanism accounts for much of the excellent creep resistance of this alloy when it was heat-treated. Thus precipitation in TiAl alloys provide a large benefit for creep resistance.

From quantitative microscopic comparisons between microstructures in undeformed and deformed regions (with various strains, stresses, and temperatures) using SEM and TEM techniques, all alloys exhibit lamellar refining that causes an initially rapid creep rate up to strains between 0.1 and 0.5% during deformation. The reduction of lamellar spacing is a consistent microstructural feature during primary creep deformation in all investment cast TiAl alloys, and this refinement process occurs by mechanical twinning (easy mode deformation) and/or α_2 shear transformation parallel to lamellar boundaries. The refinement process at the early stage of primary creep results in a rapid drop of creep rate, because of limited dislocation motion on $\{111\}$ planes not parallel to

the lamellar interface, and orientational hardening due to mechanical twinning or α_2 shear transformation. Primary creep in TiAl alloys is divided into two stages, an initial rapid process that refines the lamellar spacing through strain levels between 0.2 and 0.5%, and a second primary creep process, where no lamellar refinement occurs. More lamellar refinement occurs with a higher volume fraction of lamellar grains and with lower temperature and higher stress. The best primary creep resistance occurs when the transition occurs at a lower strain rate. This research shows that microstructural variance has a large impact on primary creep resistance, but that the lamellar refinement process occurs similarly in all microstructural variations. Thus a higher volume fraction of lamellar grains is beneficial for creep resistance because a larger volume fraction of lamellar interfaces will block overall dislocation motion during deformation.

From the investigation of PST crystals with different orientations for shear in $\langle 110 \rangle$ or $\langle 112 \rangle$ directions, the orientation dependence of the activation energy for creep and the stress exponent was examined ($Q_c = 135$ and 185 kJ/mol for the $\langle 110 \rangle$ and the $\langle 112 \rangle$ direction, respectively). These values are about half of the 290 kJ/mol activation energy measured for Ti diffusion. Furthermore, the amount of primary creep strain was several times larger in the $\langle 112 \rangle$ direction than in the $\langle 110 \rangle$ direction, and this greater amount of strain occurred at a much lower stress. The stress exponent of $n=5.3$ at higher shear stress regions in both directions suggests that viscous dislocation glide ($n=3$) controlled by pipe diffusion ($n+2$) can account for secondary creep in this microstructure and lamellar orientation. Similar to the lamellar refinement in TiAl alloys, refinement of lamellar spacing was also observed. In comparing activation energies of the early process in primary creep experiments in the W-Mo-Si alloy with creep in the soft orientation in a

PST crystal ($Q_c=140$ and $137\sim185$ kJ/mole in the W-Mo-Si, and PST crystals, respectively), the activation energies are similar: it is near 150 kJ/mol. The early mechanism for primary creep in polycrystals is correlated with creep kinetics of easy deformation in PST crystals that causes lamellar refinement.

The lamellar refinement process has been simulated to determine how much twinning or shear transformation contributed to the reduction of lamellar spacing after deformation under some limited assumptions. When several variations of initial lamellar spacing distribution are considered, the resulting deformed distribution, and the resulting local strains in the lamellar microstructure can be computed. The simulated lamellar spacing distribution was quite close to the actual spacing distribution from the measurements, when refinement was assumed to occur by α_2 shear transformation into layers $0.2\text{ }\mu\text{m}$ thick in the thicker lamellae. The computed local shear strains (0.7%) in lamellar microstructure were similar to or higher than the specimen (1%). The higher volume fraction of lamellar grains implies less lamellar refinement per lamellar grain, but with more lamellar grains, there is more strain accomplished by refinement, so the transition strain is larger. Lamellar refinement not being proportional to local shear strain is difficult to rationalize. There is a correlation between the computed local shear strain, the lamellar volume fraction, and the strain at transition points between the early and later primary creep process in most TiAl alloys.

APPENDIX

APPENDIX

PROGRAM CODES FOR SIMULATION OF LAMELLAR REFINEMENT

```
'program LAMDIST.BAS simulates lamellar refinement process
```

```
,
```

```
    DIM SPACINGS(20, 500), CUR(250), DST(13, 10)
```

```
    DEFINT I-N
```

```
    RANDOMIZE
```

```
    LUND = 100
```

```
    TITLE$ = SPACE$(100)
```

```
    SPEC$ = SPACE$(8)
```

```
    KEY OFF
```

```
'10  PRINT
```

```
'    PRINT "choose 0 to exit; "
```

```
'    PRINT "      1 Normal simulation with true twinning"
```

```
'    INPUT IOPT
```

```
'    IF IOPT = 1 THEN GOSUB 100
```

```
'    IF IOPT = 0 THEN CLOSE : END
```

```
'    GOTO 10
```

```
.....
```

```
' input initial and final distributions NUMBIN = number of bins
```

```
' B,U,D are bin size and fraction for undeformed, deformed distribution.
```

```
.....
```

```
100  PRINT "Enter name of normalized distrib file, having 1 line header, binsize, undef,  
deform"
```

```
'    INPUT DIST$
```

```
    DIST$ = "file name from raw data"
```

```
    OPEN DIST$ FOR INPUT AS #3
```

```
    INPUT #3, TITLE$: TITLE$ = DIST$ + " " + TITLE$
```

```

PRINT "Bin size undef deformed starting value"
NUMBIN = 0: SUMTHICK = 0!: DIS(0, 0) = 0!: SUMUND = 0!: SUMDEF = 0!
*****

' input distribution data
*****

WHILE NOT EOF(3)
INPUT #3, B, U, D
NUMBIN = NUMBIN + 1
DST(0, NUMBIN) = B: IBZ = 0
DST(1, NUMBIN) = U * LUND: IUND = 1
DST(2, NUMBIN) = D * LUND: IDEF = 2
DST(3, NUMBIN) = U * LUND: ICUR = 3
SUMUND = SUMUND + DST(IUND, NUMBIN)
SUMDEF = SUMDEF + DST(IDEF, NUMBIN)
PRINT NUMBIN;
FOR I = 0 TO 3
PRINT USING "#####.#"; DST(I, NUMBIN);
NEXT I: PRINT
WEND
CLOSE #3
DISTOUT$ = DIST$ + ".OUT"
OPEN DISTOUT$ FOR OUTPUT AS #2
PRINT TITLE$
PRINT NUMBIN; "Bins,"; LUND; "Lamellae in undeformed problem (LUND)"
PRINT #2, TITLE$; NUMBIN; "Bins,"; LUND; "Lamellae in undeformed
problem (LUND)"
PRINT "Sum of undeformed and deformed distributions are"; SUMUND;
SUMDEF; "OK ? ? ";
INPUT K
PRINT #2, "Sum of undeformed and deformed distributions are"; SUMUND;
SUMDEF

```



```
PRINT #2, " Bin # sumdisp sumshear #twins total #lamellae Distribution..."
```

```
.....  
' Fill CUR(N) matrix randomly using undeformed distribution
```

```
' LUND = # lamellae in undeformed condition
```

```
' LBIN = # lamellae in a given bin
```

```
' NRAND = random position among available positions in CUR()  
.....
```

```
FOR N = 0 TO LUND
```

```
  CUR(N) = 0!
```

```
  NEXT N: I = 0
```

```
  FOR NB = 1 TO NUMBIN
```

```
    BINSIZE = DST(IBZ, NB)
```

```
    LBIN = DST(IUND, NB)
```

```
    PRINT "NB; LBIN | # rand# -> pos:.."; NB; LBIN;
```

```
    FOR N = 1 TO LBIN
```

```
      NRAND = RND * (LUND - I)
```

```
      PRINT "|"; N; NRAND;
```

```
      IF I = LUND THEN 145
```

```
      J = 0
```

```
      FOR K = 1 TO LUND
```

```
        IF CUR(K) <> 0 THEN 135
```

```
        J = J + 1
```

```
        IF J < NRAND THEN 135
```

```
        PRINT "->"; K;
```

```
        CUR(K) = BINSIZE
```

```
        SUMTHICK = SUMTHICK + BINSIZE
```

```
        I = I + 1: GOTO 140
```

```
135    NEXT K
```

```
140    NEXT N: PRINT : INPUT K
```

```
145    NEXT NB
```

```
      SPACINGS(0, 0) = 0!: SPACINGS(1, 0) = 0!
```

```

FOR NC = 1 TO LUND + 2
  SPACINGS(0, NC) = SPACINGS(0, NC - 1) + CUR(NC)
  SPACINGS(1, NC) = 0!
  PRINT CUR(NC);
NEXT NC

PRINT " ---- Sumthick ="; SUMTHICK
.....

' Start looping with strain, refining lamellae in the largest bins first
' LBIN = number of lamellae in given bin, NUB = number of bins
' LCUR = # lamellae in CUR(), LUND = INITIAL # lamellae in CUR()
' NREFIN = number of refinement episodes for given bin
' LREFIN = cumulative total number of refinement episodes
' NSHRMAX = used to determine maximum number of columns for position-shear
output
' Will not subdivide the lamellae in the smallest bin
.....

  LCUR = LUND: LREFIN = 0: NSHRMAX = 0
  FOR NB = NUMBIN TO 2 STEP -1
    NREFIN = 0
    IF DST(IUND, NB) < DST(IDEF, NB) - .5 THEN 300
'above prevents refinement of lamellae for bin sizes below the crossover point
    FOR NC = 1 TO LCUR
      IF DST(ICUR, NB) <= DST(IDEF, NB) + .5 THEN GOTO 200
'above prevents distribution from going below the deformed distribution for current bin
      IF CUR(NC) <= (DST(IBZ, NB) + DST(IBZ, NB - 1)) / 2 THEN GOTO 190
'above skips lamellae that are smaller than the current bin size indicated by NB
      NREFIN = NREFIN + 1: LREFIN = LREFIN + 1
      A = RND * CUR(NC): B = RND * CUR(NC)
      IF A > B THEN
        D(1) = B: D(2) = .2
        D(3) = CUR(NC) - D(1) - D(2)
        ' thick lamellae divided

```

```

ELSE
    D(1) = A: D(2) = .2
    D(3) = CUR(NC) - D(1) - D(2)
    END IF
FOR K = 1 TO NUMBIN
    PRINT USING "####.#"; DST(ICUR, K);
NEXT K: PRINT " = Current Distrib"
FOR K = 1 TO NUMBIN
    PRINT USING "####.#"; DST(ICUR, K) - DST(IDEF, K);
NEXT K: PRINT " = Cur-Def Distrib"
PRINT "Bin"; NB; "DST(IUND, NB) & DST(IDEF, NB) ="; DST(IUND, NB);
DST(IDEF, NB);
PRINT "Found lath at NC ="; NC; "at/near"; DST(ISZ, NB)
PRINT "=> D(1)+D(2)+D(3) ="; D(1); D(2); D(3); "="; CUR(NC); "=
CUR(NC)"
.....

' -----find condition to accept adding one to the minimum sized bin - later
' Adjust distrib; NI = index for bins NB and smaller
.....

    DST(ICUR, NB) = DST(ICUR, NB) - 1
    FOR NI = NB TO 1 STEP -1
        FOR I = 1 TO 3
            IF NI = NB THEN
                IF ABS(D(I)) > (DST(ISZ, NI) + DST(ISZ, NI - 1)) / 2 THEN 160
            ELSE
                IF ABS(D(I)) > (DST(ISZ, NI) + DST(ISZ, NI + 1)) / 2 THEN 165
            END IF
            IF NI = 1 THEN GOTO 160
            IF ABS(D(I)) < (DST(ISZ, NI) + DST(ISZ, NI - 1)) / 2 THEN 165
160      DST(ICUR, NI) = DST(ICUR, NI) + 1
165      NEXT I

```

170 NEXT NI

.....
' Shift lamellae down in CUR(), put refined lamellae into correct position

' compute shear displacements and strain
.....

FOR NI = LCUR + 2 TO NC + 3 STEP -1

CUR(NI) = CUR(NI - 2)

NEXT NI: LCUR = LCUR + 2

CUR(NC) = D(1): CUR(NC + 1) = -D(2): CUR(NC + 2) = D(3)

SUMDISP = SUMDISP + D(2) * .7071: shear = SUMDISP / SUMTHICK

FOR K = 1 TO LCUR

PRINT CUR(K);

NEXT K: PRINT "----"; LCUR; "lamellae"

PRINT "Sum of displacements, Shear strain ="; SUMDISP; shear; NREFIN;
"twins,"; LREFIN; "total"

INPUT K

190 NEXT NC

200 IF NREFIN = 0 THEN 220

PRINT "---> Finished bin"; NB; "writing distribution to file": PRINT

PRINT #2, USING "###.####"; NB; SUMDISP; shear;

PRINT #2, USING "##### "; NREFIN; LREFIN; LCUR;

FOR K = 1 TO NUMBIN

PRINT #2, USING "#####.##"; DST(ICUR, K);

NEXT K: PRINT #2,
.....

' Create cumulative arrays for plotting stages of lamellar refinement

' NPOS is position in lamellare crystal, NTWTR is twin shear translation
.....

SPACINGS(NB + 1, 0) = 0!: SPACINGS(NB, 0) = 0!

NPOS = NB * 2: NTWTR = NPOS + 1: IF NTWTR > NSHRMAX THEN
NSHRMAX = NTWTR

```

FOR NC = 1 TO LCUR
SPACINGS(NPOS, NC) = SPACINGS(NPOS, NC - 1) + ABS(CUR(NC))
IF CUR(NC) > 0 THEN
SPACINGS(NTWTR, NC) = SPACINGS(NTWTR, NC - 1)
ELSE
SPACINGS(NTWTR, NC) = SPACINGS(NTWTR, NC - 1) - CUR(NC) * .7071
END IF
NEXT NC
220 NEXT NB
*****

' Output results
*****

300 PRINT "writing shear data...":
PRINT #2, "Bin # Bin size undef deform computed"
FOR NB = 1 TO NUMBIN
PRINT #2, USING "#####.##"; NB; DST(0, NB); DST(1, NB); DST(2, NB);
DST(3, NB)
NEXT NB: PRINT NSHRMAX + 1; "columns printed for shear-position data"
PRINT #2, "Position Displace @Bin 1 @Bin 2 @Bin 3 ";
PRINT #2, " @Bin 4 @Bin 5 @Bin 6 @Bin 7 "
FOR NC = 0 TO LCUR
FOR I = 0 TO NSHRMAX
PRINT #2, USING "#####.##"; SPACINGS(I, NC);
NEXT I: PRINT #2,
NEXT NC
PRINT "-----DONE-----"
END

```

LIST OF REFERENCES

REFERENCES

1. R.W. Evans and B. Wilshire, Introduction to Creep, The Institute of Materials, 1993, p. 2.
2. R.W. Evans and B. Wilshire, Introduction to Creep, The Institute of Materials, 1993, p. 18.
3. William D. Callister, Materials Science and Engineering an Introduction, 4th edition, John Wiley & Sons, Inc., 1997, p. 220.
4. W. Blum, Materials Science and Technology, Eds. R.W. Cahn, P. Haasen and E. J. Kramer, vol. 6, VCH, Weinheim, 1993, p. 367.
5. Harry Kraus, Creep Analysis, Wiley-interscience, 1980, pp. 8-9.
6. R.E. Smallman, Metallurgy Modern Physical, 4th Edition, Butterworth, 1985, p. 450.
7. R.W. Evans and B. Wilshire, Introduction to Creep, The Institute of Materials, 1993, p. 20.
8. R.W. Evans and B. Wilshire, Creep of Metals and Alloys, The Institute of Materials, 1985, p. 79.
9. O.D. Sherby and P.M. Burke, Prog.Mater. Sci., 1967, (13), p. 327.
10. R.W. Evans and B. Wilshire, Introduction to Creep, The Institute of Materials, 1993, p. 22.
11. R.W. Evans and B. Wilshire, Creep of Metals and Alloys, The Institute of Materials, 1985, p. 95.
12. MarcAndre Meyers, and Krishan Kumar Chawla, Mechanical Metallurgy Principles and applications, Prentice-Hall, Inc., 1984, p. 662.
13. C. Zener and J.H. Hollomon, J. Appl. Phys. 15, 1944, p. 22.
14. J.E. Dorn, in Creep and Recovery, ASM, Cleveland, OH, 1957, p. 255.
15. J.E. Dorn, in Creep and Fracture of Metals at High Temperatures; Proc. NPL Symposium, HMSO, London, 1956, p. 89.
16. R.W. Evans and B. Wilshire, Creep of Metals and Alloys, The Institute of Materials, 1985, p. 81.
17. R.W. Evans and B. Wilshire, Introduction to Creep, The Institute of Materials, 1993, p. 25.

18. B. Burton and G.W. Greenwood, *Acta Metall.*, 1970, (18), p. 1237.
19. R.W. Evans and B. Wilshire, *Introduction to Creep*, The Institute of Materials, 1993, p. 26.
20. P. Feltham and J.D. Meakin, *Acta Metall.*, 1959, (7), p. 614.
21. R.W. Evans and B. Wilshire, *Introduction to Creep*, The Institute of Materials, 1993, p. 27.
22. R.W. Evans and B. Wilshire, *Introduction to Creep*, The Institute of Materials, 1993, p. 31.
23. F.R.N. Nabarro, *Report of a Conference on Strength of Solids*, Physical Society, London, 1948, p. 75.
24. C. Herring, *J. Appl. Phys.*, 21, 1950, p. 437
25. R.L. Coble, *J. Appl. Phys.*, 34, 1963, p. 1679.
26. Josef Cadek, *Creep in Metallic Materials*, Elsevier Science Publishing Co., 1988, p. 210
27. B. Burton, *Diffusional Creep in Polycrystalline Materials*, Trans. Tech. Publ., Bay village, OH, 1977
28. Puttick and King, *J. Inst. Metals*, 1952, 81, p. 537.
29. A.E. Aigeltinger and R.C. Gifkins, *J. Mater. Sci.*, 1975, 10, p. 1889.
30. R.C. Gifkins, *Fracture*, Technological Press, courtesy of John Wiley & Sons.
31. R. Raj and M. F. Ashby, *Metall. Trans.*, 1971, 2, p. 1113.
32. W. Beere, *Met. Sci.*, 1976, 10, p. 133.
33. M.V. Speight, *Acta Metall.*, 1975, 23, p. 779.
34. N.F. Mott, in *Creep and Fracture of Metals at High Temperatures*, Proc. NPL Symp., HMSO London, 1956, p. 21.
35. L. Raymond and J.E. Dorn, *Trans. AIME* 230, 1964, p. 560.
36. C.R. Barrett and W.D. Nix, *Acta Metall.*, 1965, 13, p. 1247.
37. J. Weertman, *J. Appl. Phys.*, 1957, 28, p. 1185.
38. A.H. Cottrell and M.A. Jaswon, *Proc. R. Soc., London*, 1949, A199, p. 104.
39. J. Weertman, *J. Appl. Phys.*, 1957, 28, p. 362.
40. J. Weertman and J.R. Weertman, in *Physical Metallurgy*, R.W. Cahn (Ed.), North Holland, Amsterdam, 1965, p. 736.

41. J. Weertman, Trans. ASM 61, 1968, p. 681.
42. J. Weertman, in Proc. J.E. Dorn Symp. Rate Processes in Plastic Deformation of Materials, J.C.M. Li and A.K. Mukherjee (Ed.), ASM, Metals Park, OH, 1975, p. 315.
43. F.R.N. Nabarro, Philos. Mag., 1967, 16, p. 231.
44. M.A. Meyers and K.K. Chawla, Mechanical Metallurgy principles and applications, published by Prentice-Hall Inc., New Jersey, 1984, pp. 284-287.
45. R.E. Smallman, Modern Physical Metallurgy 4th Edition, Butterworth & Co Ltd, London, 1985, pp. 284-285.
46. M. Yamaguchi, and Yukichi Umakoshi, Progress in Materials Science, vol. 34, 1990, pp. 69-73.
47. Z. Jin, R. Beals, and T.R. Bieler, Structural Intermetallics, edited by R. Darolia, et al., TMS, 1993, p. 275.
48. C.R. Feng. D.J. Michel and C.R. Crowe, Scripta Metall., vol. 22, 1988, pp. 1481-1486.
49. C.R. Feng. D.J. Michel and C.R. Crowe, Scripta Metall., vol. 23, 1989, pp. 1135-1140.
50. Z. Jin, S.W. Chung, and T.R. Bieler, Gamma Titanium Aluminides edit by Y-W. Kim et al., TMS, 1995, pp. 975-983.
51. O.D. Sherby and P.M. Burke, Prog.Mater. Sci., 1967, (13), p. 325.
52. P. Yavari, F.A. Mohamed and T.G. Longdon, Acta metall. 29, 1981, p. 1945.
53. Josef Cadek, Creep in Metallic Materials, Elsevier Science Publishing Co., 1988, pp. 161-162.
54. O.D. Sherby and P.M. Burke, Prog.Mater. Sci., 1967, (13), p. 1505.
55. K. Maruyama and S. Karashima, Trans. Japan Inst. Metals, 16, 1975, pp. 671-678.
56. K. Abe, H. Yoshinaga and S. Morozumi, J. Japan Inst. Metals, 40, 1976, pp. 393-399.
57. W.D. Nix, Intern. Symp. On Advances in Metal Deformation, Cornell Univ., Oct., 1976.
58. H. Oikawa and K. Sugawara, Scripta Metall., vol. 12, 1978, p. 89.
59. H. Oikawa and K. Sugawara, Scripta Metall., vol. 12, 1978, p. 85.
60. J. Weertman, Trans. AIME 218, 1960, p. 207.
61. J. Weertman, Acta Metall., 1977, (25), p. 1393.

62. T.R. Bieler, D.Y. Seo, T.R. Everard, and P.A. McQuay, Creep behavior of Advanced Materials for the 21st Century, eds R.S. Mishra, A.K. Mukherjee, and K. Linga Murty, TMS, San Diego Annual Meeting, March, 1999, in press.
63. Oehlert and A. Atrens, *Acta metall. mater.* 42, 1994, p. 1493.
64. J.C. Gibeling, *Acta metall.* 37, 1989, p. 3183.
65. R.S. Mishra^a, T.K. Nandy, P.K. Sagar, A.K. Gogia, D. Banerjee, *Trans IIM (India)*, 49, 1996, p. 331.
66. R.S. Mishra and D. Banerjee, *Scripta Metall. et Mater.* 31, 1994, p. 1555.
67. S.V. Raj and T. G. Langdon, *Acta metall.*, 39, 1991, p. 1823.
68. T.H. Alden, *Metall. Trans.*, 18A, 1987, p. 811.
69. E. Krempl, *J. Eng. Mater. Tech. (Trans. ASME)*, 101, 1979, p. 380.
70. E.N. da C. Andrade and K.H. Jolliffe, *Proc. R. Soc. A* 254, 1960, p. 211.
71. G.S. Daehn, X.J. Xin and R.H. Wagoner, *Creep and Fracture of Engineering Materials and Structures*, eds. J.C. Earthman and F. A. Mohamed, (TMS, Warrendale, PA, 1997), p. 257.
72. R.L. Bagley, D.E.G. Jones, and A.D. Freed, *Metall Mater. Trans.* 26A, 1995, p. 829.
73. B.C. Odegard and A.W. Thompson, *Met al. Trans.* 4, 1974, p. 1207.
74. S. Suri, T. Neeraj, G.S. Daehn, D.H. Hou, J.M. Scott, R.W. Hayes, and M.J. Mills, *Creep and Fracture of Engineering Materials and Structures*, eds. J.C. Earthman and F. A. Mohamed, (TMS, Warrendale, PA, 1997), p. 119.
75. R.W. Hayes, *Scripta Metall. Mater.* 29, 1993, p. 1229.
76. R.C. Ecob, *Acta Metall.* 34, 1986, p. 257.
77. H. Zhou, Q.P. Kong, *Scripta Mater.* 34, 1996, p. 269.
78. A.S. Argon, A.K. Bhattacharya, *Acta metall.* 35, 1987, p. 1499.
79. Orlova, *Mater. Sci. and Eng. A*, A163, 1993, p. 61.
80. M. Heilmaier, *Modeling the Mechanical Response of Structural Materials*, eds. EM Taleff and RK Mahidhara, (TMS, Warrendale, PA, 1998), p. 137.
81. V. Sass, U. Glatzel, M. Feller-Kneipmeier, *Acta mater.* 44, 1996, p. 1967.
82. T.M. Pollock, A.S. Argon, *Acta Metal. et Mater.*, 40, 1992, p. 1.
83. S-U. An, *J. of the Korean Institute of Metals and Materials*, 30, 1992, p. 247.

84. R.S. Mishra and A.K. Mukherjee, Creep and Fracture of Engineering Materials and Structures, eds. J.C. Earthman and F. A. Mohamed, TMS, Warrendale, PA, 1997), p. 237.
85. J.D. Parker, B. Wilshire, Scr. Metall., 13, 1979, p. 669.
86. P.R. Bhowal, E.F. Wright, E.L. Raymond, Metal Trans. 21A, 1990, p. 1709.
87. J. Weertman, Trans. AIME 227, 1963, p. 1475.
88. M.F. Ashby, Acta Metall., 1972, (20), p. 887.
89. R.W. Evans and B. Wilshire, Creep of Metals and Alloys, The Institute of Materials, 1985, p. 13.
90. R.W. Evans and B. Wilshire, Introduction to Creep, The Institute of Materials, 1993, p. 47.
91. H.A. Lipsitt, D. Shechtman and R.E. Schafrik, Metall. Trans. 6A, 1975, p. 1991.
92. Y-W. Kim, JOM, vol. 41, No.7, 1989, p. 24.
93. Y-W. Kim and F.H. Froes, High Temperature Aluminides and Intermetallics, eds. S.H. Whang, et al., TMS, 1990, p. 465.
94. J.C. Chesnutt, Superalloys 1992, eds S.D. Antolovich, R.W. Stusrud et al., 1992, pp. 381-389.
95. S.C. Huang and J.C. Chestnutt, in Intermetallic Compounds, ed., J. H. Westbrook and R.L. Fleischer, John Wiley & Sons Ltd. press, 1994, p. 73.
96. C. McCullough, J.J. Valencia, H. Mateos, C.G. Levi and R. Mehrabian, Scripta Metall., 22, 1988, p. 1131.
97. C. McCullough, J.J. Valencia, H. Mateos, C.G. Levi and R. Mehrabian, Acta Metall. Mater., 37, 1989, p. 1321.
98. M. Yamaguchi, and Y. Umakoshi, Progress in Materials Science, vol. 34, 1990, p. 13.
99. M. Yamaguchi, and Y. Umakoshi, Progress in Materials Science, vol. 34, 1990, pp. 75-83.
100. M. Yamaguchi, and Y. Umakoshi, Progress in Materials Science, vol. 34, 1990, p.24.
101. Y.W. Kim, Acta Metall., 1992, vol. 40, No. 6, pp. 1121-1134.
102. S.M. L. Sastry and H.A. Lipsitt, Metall. Trans. A 8, 1977, p. 299.

103. M. Yamaguchi, and Y. Umakoshi, *Progress in Materials Science*, vol. 34, 1990, p. 65.
104. M. Yamaguchi, *Metals and Technology* 60, 1990, p. 34.
105. Y. Yamabe, K. Sugawara and M. Kikuchi, *Proc. 1990 Tokyo Meeting, Japan Inst. of Metals. Sendai: the Japan Institute of Metals, 1988*, p. 409.
106. Y.S. Yang and S.K. Wu, *Scripta Metall.*, 1990, vol. 24, pp. 1801-1806.
107. M. Yamaguchi, and Y. Umakoshi, *Progress in Materials Science*, vol. 34, 1990, p. 66.
108. Y.W. Kim, *Acta Metall.*, vol. 40, No.6, 1992, pp. 1121-1134.
109. M. Yamaguchi, and Y. Umakoshi, *Progress in Materials Science*, vol. 34, 1990, pp. 73-74.
110. Y-W. Kim and D.M. Dimiduk, *JOM*, vol. 43, No. 8, 1991, p. 40.
111. D.Y. Seo, T.R. Bieler and D.E. Larsen, *Structural Intermetallics*, edited by M.V. Nathal et al., TMS, 1997, p. 137.
112. D.Y. Seo and T.R. Bieler, unpublished research
113. T. Fujiwara, A. Nakamura, M. Hosomi, S.R. Nishitani, Y. Shirai, and M. Yamaguchi, *Phil. Mag.* 61, 1990, p. 591.
114. E.S. Bumps, H.D. Kessler and M. Hansen, *Trans. AIME*, 194, 1952, p. 1609.
115. P. Duwez and J.L. Taylor, *JOM*, January 1952, p. 70.
116. S.C. Huang, E.L. Hall and M.F.X. Gigliotti, *High Temperature Ordered Intermetallic Alloys II*, ed. N.S. Stoloff, C.C. Koch, C.T. Liu and O. Izumi, MRS, Pittsburgh, PA, 1987, p. 481.
117. J.W. Christian and D.E. Laughlin, *Acta Metall.* 36, 1988, p. 1617.
118. D.W. Pashley, J.L. Robertson and M.J. Stowell, *Phil. Mag.* 19, 1969, p. 83.
119. M.H. Yoo, *J. Mater. Res.* 4, 1989, p. 50.
120. Z Jin and T.R. Bieler, *Phil Mag. A.* 71, 1995, pp. 925-47.
121. Z Jin and T.R. Bieler, *Phil Mag. A.* 72, 1995, pp. 1201-19.
122. S. Farenc, A. Coujou, and A. Coret, *Phil Mag A.* 67, 1993, p. 127.
123. Z Jin, Ph.D. thesis, Michigan State University, 1994, pp. 98 and 108.
124. D. Shechtman, M.J. Blackburn and H.A. Lipsitt, *Metall. Trans.* 5, 1974, p. 1373.

125. C.R. Feng, D.J. Michel and C.R. Crowe, *Scripta Metall.*, vol. 23, 1989, pp. 241-246.
126. M.J. Blackburn, in *The Science, Technology and Application of Titanium*, eds. R.T. Jaffee and N.E. Promisel, Pergamon Press, London, 1970, p. 633.
127. D.Y. Seo, T.R. Bieler and D.E. Larsen, *Advances in the Science and Technology of Titanium Alloy Processing*, eds. I. Weiss, R. Srinivasan, P. Bania, and D. Eylon, (TMS Warrendale, PA, 1997), pp. 603-622.
128. H.A. Lipsitt, D. Shechtman and R.E. Schafrik, *Metall. Trans. A6*, 1975, p. 1991.
129. G. Hug, A. Loiseau and A. Lasalmone, *Phil. Mag. A54*, 1986, p. 47.
130. G. Hug, A. Loiseau and A. Lasalmone, *Phil. Mag. A57*, 1988, p. 499.
131. E.L. Hall and S-C. Huang, *High Temperature Ordered Intermetallic alloys III* (edited by C.T. Liu, A.I. Taub, N.S. Stoloff and C.C. Koch) *MRS Symposia Proceedings*, Vol. 133, 1989, p. 693.
132. S.H. Whang and Y.D. Hahn, *High Temperature Aluminides and Intermetallics* (edited by S.H. Whang, C.T. Liu, D.P. Pope and J.O. Stiegler) TMS, Warrendale, PA, 1990, p. 91.
133. V.K. Vasudevan, M.A. Stucke, S.A. Court, H.S. Fraser, *Phil. Mag. Lett.*, 59, 1989, p. 299.
134. S. Sriram et al., *Mat. Res. Soc. Symp. Proc. vol.364*, 1995, p. 647.
135. S.H. Whang, Z.M. Wang, and Z.X. Li, *Gamma Titanium Aluminides* edit by Y-W. Kim et al., TMS, 1995, p. 245.
136. S.H. Whang, Q. Feng, and Z.M. Wang, *Proc. of 7th Int. conf. on Creep and Fracture of Engrg. Mat.& structure* edit by J. C. Earthman et al, TMS, 1997, p. 319.
137. B. Viguier, et al., *Gamma Titanium Aluminides* edit by Y-W. Kim et al., TMS, 1995, p. 275.
138. B. Viguier, et al., *Mat. Res. Soc. Symp. Proc. vol.364*, 1995, p. 653.
139. Z.M. Wang , and S.H. Whang, *Sym. on Gamma Titanium Aluminides*, TMS Annual Meeting, Orlando, FL, 1997, To be published in *Met. Trans. A*.
140. D.M. Dimiduk, *Sym. on Gamma Titanium Aluminides*, TMS Annual Meeting, Orlando, FL, 1997, To be published in *Met. Trans. A*.

141. T.R. Bieler and D.Y. Seo, Deformation and Fracture of Ordered Intermetallic Materials, eds. W.O. Soboyejo, H.L. Fraser, T.S. Srivatsan, (TMS, Warrendale, PA 1996), pp. 89-100.
142. J. Luster and M.A. Morris, Metall. Trans. A, 26A, 1995, pp. 1745-1756.
143. M. Yamaguchi and H. Inui, Structural Intermetallics, edited by R. Darolia, et al., TMS, 1993, p. 127.
144. M. Yamaguchi and H. Inui, Ordered Intermetallics-Physical Metallurgy and Mechanical Behavior (Proc. NATO Advanced Research Workshop), ed. C.T. Liu, R.W. Cahn and G. Sauthoff (Kluwer Academic Publishers, Dordrecht, 1992), p. 217.
145. H. Inui, K. Kishida et al., submitted to Phil. Mag. A in December 1994.
146. M. Yamaguchi, H. Inui, and K. Kishida et al., Mat. Res. Soc Symp. Proc. vol.364, 1995, p. 3.
147. T. Fujiwara, A. Nakamura, M. Hosomi, S.R. Nishitani, Y. Shirai, and M. Yamaguchi, Phil. Mag. 61, 1990, p. 600.
148. Z. Jin, G.T. Gray III and M. Yamaguchi, Mat. Res. Soc. Symp. Proc. vol.460, 1997, p. 189.
149. Y. Ishikawa, K. Maruyama, and H. Oikawa, Mater. Trans., JIM, 33, 1992, pp. 1182-1184.
150. H. Oikawa, Mat. Sci. & Eng., A153, 1992, pp. 427-432.
151. M. Lu and K.J. Hemker, Acta Metall., 1997, vol. 45, No. 9, pp. 3573-3585.
152. B.D. Worth, J.W. Jones, and J.E. Allison, Met. and Mat. Trans. A, vol. 26A, 1995, pp. 2947-2959.
153. J. Triantafillou, J. Beddoes, and W. Wallace, Canadian Aeronautics & Space Journal, 42, 1996, p. 108.
154. J. Beddoes, L. Zhao, J. Triantafillou et al., Gamma Titanium Aluminides edit by Y-W. Kim et al., TMS, 1995, pp. 959-966.
155. M. Es-Souni, A. Bartels, and R. Wagner, Mat. Sci. and Eng. A171, 1993, pp. 127-141.
156. M. Es-Souni, A. Bartels, and R. Wagner, Structural Intermetallics, edited by R. Darolia, et al., TMS, 1993, pp. 335-343.

157. D.I. Kimm, and J. Wolfenstine, *Scripta Met. et Mat.*, vol. 30, 1994, pp. 615-619.
158. U. Hofmann and W. Blum, *Scripta Met. et Mat.*, vol. 32, 1995, pp. 371-376.
159. T.G. Nieh and J.N. Wang, *Scripta Met. et Mat.*, vol. 33, 1995, pp. 1101-1106.
160. J.N. Wang, A.J. Schwartz, et al., *Mat. Sci. and Eng. A206*, 1996, pp. 63-70.
161. J.S. Huang and Y.W. Kim, *Scripta Met. et Mat.*, vol. 25, No.8, 1991, pp. 1901-1906.
162. R.W. Hayes, *Scripta Met. et Mat.*, vol. 29, 1993, pp. 1229-1233.
163. D.A. Wheeler, B. London, and D.E. Jr. Larsen, *Scripta Met. et Mat.*, vol. 26, 1992, pp. 939-944.
164. B.D. Worth, J.W. Jones, and J.E. Allison, *Met. and Mat. Trans. A*, vol. 26A, 1995, pp. 2961-2972.
165. T.R. Bieler, D.Y. Seo et al., *Gamma Titanium Aluminides* edit by Y-W. Kim et al., TMS, 1995, pp. 795-802.
166. C.H. Wu, Master Thesis in Michigan State University, 1995, pp. 80-99.
167. M.F. Bartholomeusz, Q. Yang and J.A. Wert, *Scripta Met. et Mat.*, vol. 29, 1993, pp. 389-394.
168. T. Takahashi and H. Oikawa, *Mat. Res. Soc. Symp. Proc.* vol.213, 1991, p. 721.
169. P. L. Martin, M. G. Mendiratta, and H. A. Lipsitt, *Metall. Trans. A*, A14, 1983, p. 2170.
170. H. Oikawa, *Proceedings of High Temperature Aluminides and Intermetallics*, ed. by S. H. Whang, C. T. Liu, D. P. Pope, and J. O. Stiegler, TMS, 1990, p. 353.
171. H. Nagai, T. Takahashi, and H. Oikawa, *J. Mat. Sci.*, 25, 1990, p. 629.
172. T. Takahashi, H. Nagai, and H. Oikawa, *Mat. Sci. and Eng.*, A128, 1990, p. 195.
173. T. Takahashi, and H. Oikawa, *Proceedings of Microstructure/Property Relationships in Titanium Aluminides and Alloys*, ed. By W.Y. Kim and R. Boyer, TMS, 1991, p. 227.
174. H. Oikawa, and T. Takahashi, *Proceedings of Creep and Fracture of Engineering Materials and Structure*, ed. By B. Wilshire and R. Evans, The Institute of Metals, London, 1990, p. 237.
175. Loiseau, and A. Lasalmonie, *Mat. Sci. Eng.*, 67, 1984, p. 163.

176. V. Seetharaman, S. Semintin, C. Lombard, and N. Frey, *Mat. Res. Soc. Symp. Proc.* vol.288, 1992, p. 513.
177. G. Viswanathan and V. Vasudevan, *Mat. Res. Soc. Symp. Proc.* vol.288, 1992, p. 787.
178. R. W. Hayes and B. London, *Acta. Metall. et Mater.*, 40, 1992, pp. 2167.
179. W. O. Soboyejo and R. J. Lederich, *Structural Intermetallics*, ed. by R. Darolia, J. J. Lewandowski, C. T. Liu, P. L. Martin, D. B. Miracle, and M. V. Nathal (TMS, Warrendale, PA, 1993), p. 353.
180. M. Es Souni, A. Bartels, and R. Wagner, *Acta. Metall. et Mater.*, 43, 1995, pp. 151-161.
181. A. Bartels, J. Seeger, and H. Mecking, *Mat. Res. Soc. Symp. Proc.* vol.288, 1992, p. 1179.
182. C.R. Feng, and K. Sadananda, *Mat. Res. Soc. Symp. Proc.* vol.288, 1992, p. 1155.
183. R. W. Hayes and P. A. McQuay, *Scripta Metall. et Mater.*, 30, 1994, p. 259.
184. D. Shih, et al, *Proceedings of Microstructure/Property Relationships in Titanium Aluminides and Alloys*, ed. By W.Y. Kim and R. Boyer, TMS, 1991, p. 135.
185. T.O. Noda, M. Isobe, and M. Sayashi, *Mat. Sci. and Eng.*, A192/193, 1995, pp. 774-779.
186. Li, J. Wolfenstine, J.C. Earthman, and E.J. Lavernia, *Metall. Trans. A*, Vol. 28A, 1997, p. 1849.
187. S. Kampe, J.D. Brayant and L. Christodoulou, *Metall. Trans. A*, 22A, 1991, p. 447.
188. P. L. Martin, et al., *Proceedings of Creep and Fracture of Engineering Materials and Structure*, ed. By B. Wilshire and R. Evans, The Institute of Metals, London, 1990, p. 265
189. S. Cheng, J. Wolfenstine and O. Sherby, *Metall. Trans. A*, 23A, 1992, p. 1509.
190. S.C. Huang, *Structural Intermetallics*, edited by R. Darolia, et al., TMS, 1993, pp. 299-307.
191. M. Es Souni, A. Bartels, and R. Wagner, *Mat. Sci. and Eng.* A192/193, 1995, pp. 698-706.
192. R.V. Ramanujan, P.J. Maziasz, and C.T. Liu, *Acta. Met.*, vol.44, No.7, 1996, p. 2611.

193. L.M. Hsiung and T.G. Niech, *Scripta Met. et Mat.*, vol. 36, 1997, pp. 323-330.
194. Z. Jin, R. Beals, and T.R. Bieler, *Mat. Res. Soc. Symp. Proc.* vol.364, 1995, p. 505.
195. D.Y. Seo, T.R. Bieler and D.E. Larsen, Data from Howmet Corp. 1995.
196. C.H. Wu, Master Thesis in Michigan State University, 1995, p. 102.
197. C.H. Wu, Master Thesis in Michigan State University, 1995, pp. 48-57.
198. Colin Thomas and Mark Behrendt, *Advanced Materials and Processes*, Vol. 150, No.3, Sept., 1996, pp. 29-31.
199. J. B. Conway, *Numerical Methods for Creep and Rupture Analysis*, Gordon and Breach, New York, 1967.
200. R.W. Evans and B. Wilshire, *Creep of Metals and Alloys*, The Institute of Materials, 1985, pp. 197-243.
201. R.W. Evans and B. Wilshire, *Introduction to Creep*, The Institute of Materials, 1993, p. 80.
202. K. Maruyama, C. Harada, and H. Oikawa, *Journal of the Society of Materials Science, Japan*, 34 (1985), p. 1289.
203. K. Maruyama, and H. Oikawa, *Scripta Metall.*, vol. 21, 1987, p. 233.
204. C.H. Wu, Master Thesis in Michigan State University, 1995, p. 30.
205. D. Y. Seo, T.R. Bieler and D.E. Larsen, *Proceedings of 7th International Conference on Creep and Fracture of Engineering Materials and Structures in Irvine, CA, Aug. 1997*, p. 577.
206. J. Beddoes, W. Wallace, and L. Zhao, *Intl. Mater. Rev.*, 40, 1995, p. 197.
207. S. Tsuyama, S. Mitao and K. Minakawa, *Mater. Sci. Eng.*, A153, 1992, p. 427.
208. S.C. Huang, D.W. McKee, D.S. Shih and J.C. Chestnutt, *Intermetallic Compounds-Structure and Mechanical Properties*, ed. O. Izumi, (The Japan Institute of Metals, Sendai, 1991), p. 363.
209. T. Maeda, M. Okada, Y. Shida and M. Nakanishi, *Proc. 1989 Sapporo Meeting*, (The Japan Institute of Metals, Sendai, 1989), p. 238.
210. T. Maeda, M. Okada and Y. Shida, *MRS Symp. Proc.*, vol 213, (MRS Pittsburgh, PA, 1991), p. 555.
211. P.R. Bhowal, H.F. Merrick and D.E. Larsen, *Mater. Sci. Eng.*, A192/193, 1995, pp. 685-690.

212. D.Y. Seo, S.U. An, T.R. Bieler, D.E. Larsen, P. Bhowal, H. Merrick, *Gamma Titanium Aluminides*, ed. Y-W. Kim, et al. (TMS, Las Vegas, NV 1995), p. 745.
213. Z. Jin and T.R. Bieler, *Phil Mag.*, 70,(1995), pp. 819-836.
214. T.S. Kallend, U.F. Kocks, A.D. Rollett, and H.R. Wenk, *Mater. Sci. Eng.*, A132, 1991, pp. 1-11.
215. Y. Zheng, L. Zhao and K. Tangri, *Scripta Metall.*, 26, (1992), p. 291.
216. S.C. Huang and E.L. Hall, *MRS Symp. Proc.*, 133, 1989, p. 373.
217. V.K. Vasudevan, S.A. Court, P. Kurath and H.L. Fraser, *Scripta Metall.*, 23(6), 1989. p. 907.
218. M. Aindow, K. Chaudhuri, S. Das and H.L. Fraser, *Scripta Metall.*, 24, 1990, p. 1105.
219. S. Sriram, V.K. Vasudevan and D.M. Dimiduk, *MRS Symp. Proc.*, 213, 1991, p. 375.
220. W.H. Tian and M. Nemoto, *Gamma Titanium Aluminides*, ed. Y-W. Kim,, R. Wagner, and M. Yamaguchi, (TMS, Warrendale, PA, 1995), p. 689.
221. B.D. Worth, J.W. Jones and J.E. Allison, *Gamma Titanium Aluminides*, eds. Y.W. Kim, R. Wagner, and M. Yamaguchi, (TMS, Warrendale, PA, 1995), pp. 931-938.
222. K. Muraleedharan and T.M. Pollock, unpublished research, PRET home page, <http://titan.mems.cmu.edu/etch.html>.
223. S. Yamauchi and H. Shiraishi, *Mater. Sci.Eng.*, A152, 1992, p. 283.
224. D.E. Larsen, S.L. Kampe, Christodoulou, *MRS Symp. Proc.*, 194, 1990, p. 285.
225. S.C. Huang and E.L. Hall, *Metall. Trans. A*, 22A 1991, p. 1619.
226. T. Kawabata, T. Tamura, and O. Izumi, *Metall. Trans. A*, 24A, 1993, p. 141.
227. M.J. Blackburn and M.P. Smith, U.S. Patent 4294615, 1981.
228. S.C. Huang and E.L. Hall, *Acta Metall. Mater.*, 6, 1991, p. 1053.
229. T. Tsujimoto and K. Hashimoto, *Mat. Res. Soc. Symp. Proc.*, 133, 1989, p. 391.
230. G.H. Meier, D. Appalonia, R.A. Perkins, and K.T. Chiang, in *Oxidation of High-Temperature Intermetallics*, ed. T. Grobstein and J. Doychak (TMS, Warrendale, PA 1988), p. 185.
231. D.W. McKee and S.C. Huang, *Corrosion Sci.*, 33, 1992, p. 1899.
232. J. B. McAndrew and H.D. Kessler, *J. Metals*, 8, 1956, p. 1348.

233. W. Zhang, G. Chen, and Z. Sun, *Scripta Metall.*, 28, 1993, p. 563.
234. S. Tsuyama, S. Mitao and K. Minakawa, *Mater. Sci. Eng.*, A153, 1992, p. 427.
235. S. Tsuyama, S. Mitao, and K. Minakawa, *Mater. Sci. Eng.*, A153, 1992, p. 451.
236. K. Kasahara, K. Hashimoto, H. Doi, and T. Tsujimoto, *J. Japan Inst. Metals*, 53, 1990, p. 948
237. Y. G. Nakagawa, S. Yokoshima, and K. Matsuda, *Mater. Sci. Eng.*, A153, 1992, p. 722.
238. R.A. Perkins, K.T. Chiang, and G.H. Meier, *Scripta Metall.*, 21, 1987, p. 1505.
239. D. Y. Seo, T.R. Bieler and D.E. Larsen, *Mater. Res. Soc. Symp. Proc. Vol. 460* (Pittsburgh, PA, 1997) p. 281.
240. D.Y. Seo, C.H. Wu, and T.R. Bieler, *Mater Sci. and Eng.* A239-40, 1997, p. 450.
241. R.W. Evans and B. Wilshire, *Introduction to Creep*, The Institute of Materials, London, 1993.
242. M. Yamaguchi and Y. Umakoshi, *Progress in Materials Science*, 34, (1990), p. 71.
243. S. Farenc, A. Coujou and A. Couret, *Mater. Sci. Eng.*, A164, 1993, p. 438.
244. T. Hanamura and M. Tanino, *J. Mater. Sci. Lett.* 8, 1989, p. 24
245. F. Appel and R. Wagner, *Gamma Titanium Aluminides*, (TMS, Warrendale, PA, 1995), pp. 231-244.
246. S. Kroll, H. Mehrer, N.N. Stolwijk, C. Herzig, R. Rosenkranz, G. Frommeyer, *Z. Metallkde*, 83, (1992), pp. 591-595.
247. L.M. Hsiung and T.G. Nieh, *Mater Sci and Eng.* in press.
248. T. Maeda, M. Okada and Y. Shida, in *Proc. 6th Int. Conf. on 'Mechanical behavior of Materials VI'*, Oxford, Pergamon Press, 1992, p. 199.
249. H. Oikawa, *Mater. Sci. and Eng.*, A153 (1992), p. 427.
250. F. Garofalo, *Fundamentals of Creep and Creep-Rupture in Metals*, The MacMillan Co., New York, Chap. 2.
251. Chih-Huei Wu, Master Thesis, Michigan state University, 1995, p. 31
252. K. Ouchi, Y. Iijima, and K. Hirano, *Titanium '80-Science and Technology*, (TMS Warrendale, PA, 1981), p. 559.
253. D.Y. Seo, T.R. Bieler, S.U. An, and D.E. Larsen, *Mater. Trans. A*, vol. 29A (1998), pp. 89-98.

254. T. Maeda, M. Okada, Y. Shida and M. Nakanishi, Proc. 1989 Sapporo Meeting, (The Japan Institute of Metals, Sendai, 1989), p. 238.
255. Z. Jin and G.T. Gray III, TMS symposium on Fundamentals of Gamma Titanium Aluminides, Feb. 1997, eds. K.S. Chan, V.K. Vasudevan, Y.-W. Kim, to be published in Mater. Trans.
256. R. Mahapatra, A. Girshick, D.P. Pope, V. Vitek, Scripta Metall. et Mater. 33, 1995, pp. 1921-1927).
257. R. A. MacKay and I. E. Locci, unpublished research, NASA Lewis.
258. Wang and Nieh, TMS symposium on Fundamentals of Gamma Titanium Aluminides, Feb. 1997, eds. K.S. Chan, V.K. Vasudevan, Y.-W. Kim, to be published in Mater. Trans.
259. P.I. Gouma, S.J. Davey, and M.H. Loretto, Materials Science and Engineering, A241(1998), pp.151-158.
260. H.S. Cho et al., submitted to Materials Science and Engineering (1998).
261. S. Chen, P.A. Beaven, and R. Wagner, Scripta Metall., 26 (1992), pp.1205-1210.
262. J.D. Whittenberger and Ranjan Ray, Scripta Metall., 33 (1992), pp.1505-1512.
263. H.S. Cho and S.W. Nam, private communication, 1998.
264. Denquin et al., Scripta Metall., 28 (1993), pp.1131-1136.
265. Menand, A. Huguet, and A. Nerac-Partaix, Acta Metall. Mater., 44 (1996), pp. 4729-4737.
266. H.S. Cho, and D.Y. Seo, unpublished research, 1998.
267. R.W. Evans and B. Wilshire, Introduction to Creep, The institute of Materials, London, 1993.
268. Kad, B.K., P.M. Hazzledine, H.L. Fraser, Defect-Interface Interactions , MRS Symp. Proc. Vol. 319, (MRS, Pittsburgh, PA 1994), p. 311.
269. D.Y. Seo and T.R. Bieler and P.A. McQuay, Interstitial and Substitutional Solute Effects in Intermetallics, eds. I. Baker, R.D. Noebe, and E.P. George, (TMS, Warrendale, PA, 1998) p. 227